Universidade de Aveiro
2017

Departamento de Engenharia de Materiais e Cerâmica

Ana Catarina Fernandes Marques

Desenho e processamento de estruturas porosas de fosfatos de cálcio por robocasting para engenharia de tecido ósseo

Design and processing of porous scaffolds based on calcium phosphates by robocasting for bone tissue engineering

Universidade de Aveiro
2017
Departamento de Engenharia de Materiais e Cerâmica

Ana Catarina Fernandes Marques

Desenho e processamento de estruturas porosas de fosfatos de cálcio por robocasting para engenharia de tecido ósseo

Design and processing of porous scaffolds based on calcium phosphates by robocasting for bone tissue engineering

Tese apresentada à Universidade de Aveiro para cumprimento dos requisitos necessários à obtenção do grau de Doutor em Ciência e Engenharia de Materiais, realizada sob a orientação científica do Professor Doutor José Maria da Fonte Ferreira, Professor Associado com Agregação do Departamento de Engenharia de Materiais e Cerâmica da Universidade de Aveiro e da Doutora Aureliana Filipa Sousa, Investigador Assistente pós doutorado, i3S- Instituto de Investigação e Inovação em Saúde, /INEB- Instituto Nacional de Engenharia Biomédica da Universidade do Porto.

Apoio financeiro da FCT e do POPH/FSE no âmbito do III Quadro Comunitário de Apoio.
SFRH/BD/78355/2011

Aos meus pais...

À minha irmã Mariana...

Ao Luís...

o júri

presidente

Prof. Doutor Eduardo Anselmo Ferreira Da Silva
Professor Catedrático no Departamento de Geociências da Universidade de Aveiro

Prof. Doutor João Filipe Colardelle Da Luz Mano
Professor Catedrático no Departamento de Química da Universidade de Aveiro

Prof. Doutora Maria Ascensão Ferreira Da Silva Lopes
Professora Auxiliar no Departamento de Engenharia Metalúrgica e de Materiais da Faculdade de Engenharia da Universidade do Porto

Prof. Doutora Meriem Lamghari Moubarrad
Investigadora Principa do INEB - Instituto de Engenharia Biomédica e Professora Auxiliar Convidada da Faculdade de Engenharia da Universidade do Porto

Prof. Doutor João Carlos Tomás Ramos
Professor Auxiliar da Faculdade de Medicina da Universidade de Coimbra

Prof. Doutor José Maria Da Fonte Ferreira
Professor Associado c/ Agregação do Departamento de Engenharia de Materiais e Cerâmica da Universidade de Aveiro

agradecimentos

Em primeiro lugar quero expressar o meu sincero agradecimento ao Professor Doutor José Maria Ferreira (orientador) e à Doutora Aureliana Filipa Sousa (co-orientadora) pela excelência científica e pela partilha de conhecimentos Agradeço a motivação, a dedicação e a disponibilidade constantes.

Para agradecer à Doutora Susana Olhero as palavras que poderei dizer nunca serão suficientes, o meu MUITO OBRIGADA, pela amizade, disponibilidade, pelo interesse manifestado por este trabalho, pelo saber que me transmitiu, pelas opiniões e críticas, pela total colaboração no solucionar de dúvidas e problemas que foram surgindo ao longo da realização deste trabalho e por todas as palavras de incentivo. Sem dúvida que a sua bondade genuína fez desta jornada um caminho muito mais fácil.

Aos meus colegas de laboratório no DEMAC pela ajuda e por todo o apoio. Agradeço, de forma especial, à Doutora Paula Torres, pelo tempo despendido e pela partilha de conhecimentos, que me permitiram que cada dia fosse encarado com particular motivação. As suas palavras de encorajamento e de grande amizade revelaram-se determinantes nesta etapa que agora termina.

A todos os técnicos e pessoal da secretaria do DEMAC, Dr.ª Alexandra, Luísa, Ana Ribeiro, Célia Miranda, Marta Ferro, Tiago Silva, Artur Sarabando, Octávio e Sr. Jacinto, por tão atenciosamente me terem auxiliado sempre que necessitei da sua colaboração.

Ao Professor Doutor Pedro Granja agradeço a disponibilidade com que me recebeu no i3S e me integrou no seu grupo de trabalho desde o primeiro momento, a oportunidade e a confiança. A sua simpatia, boa disposição, plena dedicação e interesse serviram de exemplo e de impulso adicional numa das fases mais complicadas deste trabalho. Aos meus colegas do laboratório 107 do i3S pela maneira com que me acolheram e me apoiaram, estando sempre disponíveis para me ajudarem.

À Doutora Sandra Vieira e Ana Marote, do Departamento de Biologia da Universidade de Aveiro, por todo o tempo que abdicaram do seu trabalho para me poder acompanhar na fase inicial deste trabalho.

Ao Professor João Abrantes pelas inúmeras análises de DRX por refinamento de Rietveld.

Ao Professor Pedro Miranda e ao Doutor Hugo Perera, do Departamento de Ingeniería Mecánica, Energética y de los Materiales da Universidad de Extremadura, pela hospitalidade, pela transmissão de conhecimento e pela disponibilidade que demonstraram durante a minha estadia em Badajoz.

À Doutora Ana Bettencourt, da Faculdade de Farmácia da Universidade de Lisboa, pelo trabalho desenvolvido, apoio científico e disponibilidade.

A todos os meus amigos e familiares pelos bons momentos, apoio, paciência e amizade.

Aos meus pais pelo apoio incondicional, carinho e paciência, que me permitiram concluir mais esta etapa da minha vida. À minha irmã por ter "segurado as pontas" nos momentos mais difíceis, pelos sorrisos, abraços e pela motivação constante.

Ao Luís o meu muito obrigada pela paciência, companheirismo, tendo sempre uma piada pronta para me fazer sorrir e por permitir que ao longo deste anos o "nós" tenha sido tantas vezes esquecido.

palavras-chave

Fosfatos de cálcio bifásicos, iões dopantes, fabrico aditivo, *robocasting*, *scaffolds* porosos, *scaffolds* não sinterizados, libertação de fármacos, regeneração óssea

resumo

A presente dissertação teve como foco principal o desenvolvimento de estruturas 3D porosas (*scaffolds*) para regeneração óssea por *robocasting*. Esta técnica de fabrico aditivo permite a produção de *scaffolds* com morfologia e estrutura predefinidas e sem a necessidade de maquinagem subsequente, podendo ser usada para o fabrico de implantes personalizados com estrutura interna semelhante à do osso que se pretende substituir.

Como materiais de partida, foram utilizados pós de fosfatos de cálcio bifásicos (hidroxiapatite + β-fosfato tricálcico) não dopados, e dopados com diferentes iões (Sr, Ag, Cu, Mg e Zn), obtidos por precipitação em meio aquoso. A substituição parcial de iões Ca pelos iões dopantes induziu alterações na composição de fases cristalinas e resultou em partículas com características morfológicas distintas e em materiais com desempenhos biológicos diferentes.

Os pós foram dispersos em meio aquoso com a ajuda de aditivos de processamento adequados (um dispersante e um ligante) de modo a obter suspensões com elevada concentração de sólidos, requisito essencial para o fabrico de componentes por robocasting. O tamanho e a morfologia das partículas e a concentração dos aditivos de processamento desempenharam os papéis cruciais no comportamento reológico das suspensões. A adição de agente floculante modificou drasticamente as propriedades reológicas do sistema e permitiu a obtenção de pastas com comportamento viscoelástico adequado para o processo de extrusão. Os *scaffolds* com diferentes tamanhos de poro foram produzidos pela deposição de um filamento com 410 µm de diâmetro. A resistência à compressão dos *scaffolds* sinterizados a 1100°C foi comparável ou mesmo superior à do osso esponjoso.

Scaffolds com diferentes tamanhos de poro (120-500 µm) foram testados *in vitro* usando células estaminais mesenquimais humanas (hMSCs). Pretendeu-se avaliar a influência do tamanho dos poros na adesão celular inicial, na atividade metabólica e no potencial osteogénico. Os resultados obtidos mostraram que os poros com maior dimensão proporcionam condições favoráveis para a diferenciação osteogénica das hMSCs. Além disso, os fosfatos de cálcio co-dopados com Sr e Zn melhoraram o desempenho biológico, incluindo adesão, atividade metabólica e proliferação das hMSC.

A última parte da tese foi dedicada à preparação de *scaffolds* não sinterizados incorporando um fármaco (levofloxacina) de forma a obter componentes com capacidade de regeneração óssea e de tratamento local de infeções. A pasta utilizada foi obtida através da dispersão dos pós de CaP numa solução de quitosano na presença do fármaco e de um agente de reticulação (genipin).

Os *scaffolds* 3D à base de fosfatos de cálcio produzidos por *robocasting* no âmbito desta tese revelaram-se muito promissores para aplicações na engenharia de tecidos, particularmente regeneração de tecido ósseo e administração de fármacos.

keywords

Biphasic calcium phosphate, dopant ions, additive manufacturing, robocasting, porous scaffolds, sintering-free scaffolds, drug delivery, bone regeneration

abstract

The main focus of this thesis was the development of novel 3D porous scaffolds for bone regeneration by robocasting. This additive manufacturing technique allows the production of scaffolds with predefined morphology and structure without the need for subsequent machining and can be used for the manufacture of customized implants with an internal structure similar to that of the bone to be replaced.

Biphasic calcium phosphates (hydroxyapatite + β-tricalcium phosphate), undoped and doped (with Sr, Ag, Cu, Mg and Zn), obtained through aqueous precipitation process were used as starting powders. The partial substitution of Ca ions by doping ions induced changes in the crystalline phase assemblages and resulted in particles with distinct morphological characteristics and in materials with different biological outcomes.

The powders were dispersed in aqueous medium with the aid of suitable processing additives (a dispersant and a binder) in order to obtain suspensions with high solids loading, an essential requirement for the manufacture of components by robocasting. The size and morphology of the particles and the concentration of the processing additives played crucial roles in the rheological behaviour of the suspensions. The addition of a flocculating agent drastically modified the rheological properties of the systems and allowed obtaining pastes with viscoelastic behaviour suitable for the extrusion process. The scaffolds with different pore sizes were produced by the controlled deposition of filaments with 410 μm in diameter. The compressive strength of scaffolds sintered at 1100 ° C was comparable or even superior to that that of spongy bone.

Scaffolds with different pore sizes (120-500 μm) were tested in vitro using human mesenchymal stem cells (hMSCs). The aim was to evaluate the influence of pore size on initial cell adhesion, metabolic activity and osteogenic potential. The results showed that larger pores provide favourable conditions for osteogenic differentiation of hMSCs. In addition, calcium phosphates co-doped with Sr and Zn improved the biological performance, including adhesion, metabolic activity and proliferation of hMSC.

The last part of the thesis was devoted to the preparation of sintering-free scaffolds incorporating a drug (levofloxacin) in order to obtain components with capacity for bone regeneration and local treatment of infections. The paste used was obtained by dispersing the CaP powders in a solution of chitosan in the presence of the drug and a crosslinking agent (genipin).

The 3D scaffolds produced by robocasting in the frame of this thesis program revealed to be very promising for tissue engineering applications, particularly bone tissue regeneration and drug delivery.

TABLE OF CONTENTS

LIST OF FIGURES

CHAPTER 1

CHAPTER 2

CHAPTER 3

CHAPTER 4

LIST OF TABLES

CHAPTER 1

CHAPTER 2

CHAPTER 3

CHAPTER 5

LIST OF ABBREVIATIONS

3D	Three-Dimensional
AE	Adsorption Efficiency
ALP	Alkaline Phosphatase
AM	Additive Manufacturing
ATCC	American Type Culture Collection
BCP	Biphasic Calcium Phosphates
BET	Brunauer–Emmett–Teller Method
BMP	Bone Morphogenetic Proteins
BSA	Bovine Serum Albumin
BTE	Bone Tissue Engineering
CAD	Computer-Aided Design
CaP	Calcium Phosphate
CLSI	Clinical & Laboratory Standards Institute
DIV	Days In Vitro
DLS	Dinamic Light Scattering
DL	Drug Delivery
DNA	Deoxyribonucleic Acid
DTA	Differential Thermal Analysis
DWA	Direct Write Assembling
EBSS	Eagle's Balanced Salt Solution
ECM	Extracellular Matrix
FBS	Fetal Bovine Serum
FDM	Fused Deposition Modelling
FT-IR	Infrared Spectroscopy by Fourier Transform
HA	Hydroxyapatite
hDNFs	Human Dental Neonatal Fibroblasts
hMSCs	Human Mesenchymal Stem Cells
HPMC	Hydroxypropyl Methylcellulose
HPLC-UV	High Performance Liquid Chromatography - Ultraviolet
ICDD	International Centre for Diffraction Data
ICP	Inductively Coupled Plasma

IEP	Isolectric Point
LEV	Levofloxacin
LVR	Linear Viscoelasticity Region
MIC	Minimum Inhibitory Concentration
MRSA	Methicillin resistant *S. aureus*
MSSA	Methicillin susceptible *S. aureus*
OD	Optical Density
O.D.f	Final optical density
PBS	Phosphate-Buffered Saline
PEI	Polyethylenimine
PS	Particle Size
PSD	Particle Size Distribution
RT	Room Temperature
SEM	Scanning Electron Microscopy
SFF	Solid Free-form Fabrication
SLS	Selective Laser Sintering
SSA	Specific Surface Area
TCP	Tricalcium Phosphate
TG	Thermo gravimetric analysis
UV	UltraViolet
VEGF	Vascular Endothelial Growth Factor
XRD	X-Ray Diffraction
ZP	Zeta Potential

THE PRESENT THESIS IS BASED ON THE FOLLOWING PUBLICATIONS (SCI JOURNALS):

Catarina. F. Marques, Ana C. Matos, Isabel A. C. Ribeiro , Lídia M. Gonçalves, Ana Bettencourt, José M. F. Ferreira**. Insights on the properties of levofloxacin-adsorbed Sr- and Mg-doped calcium phosphate microparticles**. Journal of Materials Science: Materials in Medicine (2016) 27:123.

Catarina F. Marques, Susana Olhero, J.C.C. Abrantes, Ana Marote, Sónia Ferreira, Sandra I. Vieira, José M.F. Ferreira, **Biocompatibility and antimicrobial activity of biphasic calcium phosphate powders doped with metal ions.** Journal Ceramics International 43(17) (2017) 15719-15728.

Catarina F. Marques, Fidel Hugo Perera, Ana Marote, Sónia Ferreira, Sandra I. Vieira, Susana Olhero, Pedro Miranda, José M.F. Ferreira. **Biphasic calcium phosphate scaffolds fabricated by direct write assembly: Mechanical, anti-microbial and osteoblastic properties**. Journal of the European Ceramic Society 37 (2017) 359-368.

Catarina F. Marques, Aureliana Sousa, Fidel Hugo Perera, Susana Olhero, Pedro Miranda, Pedro L. Granja, José M.F. Ferreira. **The effect of porosity of biphasic calcium phosphate scaffolds fabricated by robocasting on osteogenic differentiation of hMSCs.** Submitted to Journal of Materials Science and Engineering C.

Catarina F. Marques, Susana Olhero, Paula M. C. Torres**,** João C.C. Abrantes, Sara Fateixa, Helena I.S. Nogueira, Isabel Ribeiro, Ana Bettencourt, Aureliana Sousa, Pedro L. Granja, José M.F. Ferreira. **Sintering-free scaffolds obtained by additive manufacturing for concurrent bone regeneration and drug delivery.** Submitted to publication in Journal of Advanced Functional Materials.

AIM AND STRUCTURE OF THE THESIS

With the increase of the average life expectancy, tissue engineering became an area of great interest. Every year, there are millions of people who need some kind of prostheses, and the need for all kind of implants became very well known in our society. In recent years, particular attention was paid to the synthesis of bioceramics with porous morphology since most strategies to regenerate bone depend on 3D porous structures (scaffolds) to support cell attachment, proliferation, and differentiation. Diverse conventional techniques, such as the polymeric sponge method, starch consolidation, the use of porogens and foaming agents, have been used to build porous ceramic scaffolds. However, a precise control of pore size, geometry and spatial distribution is essential to satisfy the greatest challenges in this area. Such a target can be properly achieved by using additive manufacturing (AM) techniques that enable producing customized scaffolds with predefined shape and internal architecture according to a computer design, without the need for subsequent machining. Robocasting, as one of these techniques, combines the extrusion of a continuous filament with a computer-guided positioning system in a layer by layer fashion to build 3D structures.

The main target of this PhD thesis was developing novel 3D porous scaffolds similar to the human cancelous bone for bone regeneration by robocasting technique. Porosity was tailor-made in order to evaluate the influence of porous structure in the formation of bone tissue in a cellular environment, enabling the prediction of scaffolds behaviour after implantation. Thereby, all the relevant properties (chemical, structural, mechanical and biological) were considered and balanced in order to get the best compromise for the proposed aim.

For this purpose, firstly calcium phosphate powders with co-substituted elements were developed in order to find a material holding anti-microbial or/and osteoblastic stimulation properties. These properties could enable them acting in specific situations, as excellent alternatives to traditional un-doped calcium phosphate powders. Lastly, a hybrid system that allows the release of an antibiotic for bone regeneration by diffusion was also developed.

Accordingly, the first chapter of this thesis consists in a brief overview of bone tissue and calcium phosphate as bone regeneration materials, and a description of the state of the art, specifically results compilation presented in literature related to the scaffolds production and their performance in tissue engineering.

Chapter 2 and Chapter 3 present studies related to synthesis and characterization of calcium phosphate powders, undoped and co-substituted with ions that have important roles in biological processes. The first study, Chapter 2, introduces the results of ionic substitution in the HA lattice, which are crucial for understanding the importance of dopant ions in obtaining biphasic calcium phosphate powders. Subsequently, Chapter 3 presents the assessment of substitution elements that could confer anti-microbial properties and/or osteoblast proliferation in the biphasic calcium phosphate powders. Rietveld refinement was used to determine composition and structural parameters of the phases formed. Evaluation of the anti-microbial and/or osteoblast proliferation properties of the synthesized powders was also studied.

Chapter 4 describes 3D porous scaffolds fabrication using robocasting as direct write assembly technique. The powders were thoroughly characterized and their *in vitro* biocompatibility and antibacterial activities were evaluated. Colloidal inks with high solids loading and appropriate rheological properties were prepared, enabling the successful production of 3-D structures with improved mechanical properties, suitable for bone tissue engineering.

In Chapter 5, the effect of varying internal architectural scaffold designs on the mechanical and biological performance was investigated, in an attempt to devise an "ideal scaffold", with ability for inducing bone formation. *In vitro* osteogenic potential of human mesenchymal stem cells (hMSCs) in the scaffolds was studied and the best compromise between scaffolds macroporosity and *in vitro* performance was evaluated by different cell parameters, such as morphology, viability, adhesion and proliferation

The preparation and characterization of the macroporous hybrid scaffold (chitosan/biphasic calcium phosphate) is described in Chapter 6. In an attempt to produce a scaffold with a practical application, the ability of porous scaffolds to be used as controlled drug delivery systems for osteomyelitis treatment was studied.

In Chapter 7 are presented the general conclusions that could be drawn from the discussions of all the results presented throughout the thesis, and future work perspectives.

Chapter 1

LITERATURE REVIEW

BONE – OVERVIEW

Bone is a highly specialized form of connective tissue whose primary functions are to provide a mechanical support system for muscular activity, provide for the physical protection of organs and soft tissues, and act as a storage facility for systemic mineral homeostasis [1]. It is a complex living tissue in which the extracellular matrix is mineralized, conferring marked rigidity and strength to the skeleton while still maintaining some degree of elasticity. In addition to its supportive and protective functions, bone is a major source of inorganic ions, actively participating in calcium homeostasis in the body. There is increasing evidence that the central control of development and renewal of the skeleton is more sophisticated than previously appreciated [2]. Bone extracellular matrix is composed of approximately 70% inorganic phase, in the form of crystals of a calcium phosphate (hydroxyapatite [$Ca_{10}(PO_4)_6(OH)_2$)], for structural reinforcement and stiffness, 25% organic phase (~90% type I collagen, ~5% noncollagenous proteins (NCPs), ~2% lipids by weight), that provides flexibility and toughness, and 5% of water [3,4].

The structural-functional unit of the bone is an osteon, a microscopic system of osseous tubes inserted in one another (Fig. 1). In the centre of the system, there is a nutrient canal 10 to 100 μm in diameter, containing a blood capillary. The number of osseous tubes constituting an osteon may vary from 4 to 20. Bone is covered with a thin layer of connective tissue (periosteum), containing vessels and nerves. The inner layer of periosteum contains a large amount of osteoblasts [5,6].

Morphologically, the bone of the mature skeleton consists of cortical (or compact) bone (80%) and cancellous (or trabecular) bone (20%) (Fig.1). In cortical bone, densely packed collagen fibrils form concentric lamellae, and the fibrils in adjacent lamellae run in perpendicular planes as in plywood. Cancellous bone has a loosely organized, porous matrix. Differences between cortical and cancellous bone are both structural and functional, related to their primary functions cortical bone provides mechanical and protective functions and cancellous bone provides metabolic functions [1].

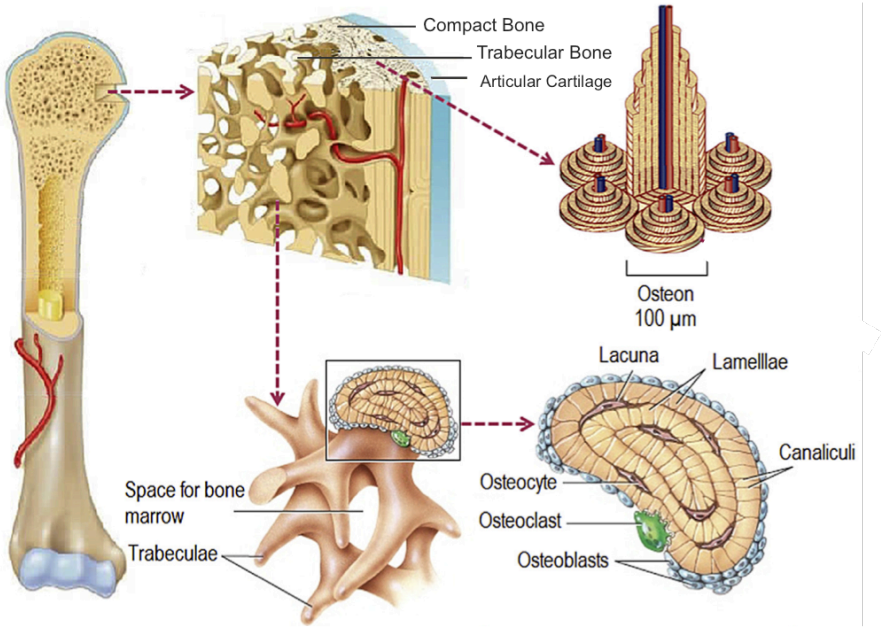

Fig. 1. Structure organization of bone: cortical (compact) bone and cancellous (or trabecular) bone [Adapted from 7].

The mechanical strength of the two architectures varies depending on the type of bone and its porosity [8]. The apparent density of cancellous bone varies from 0.1 to 1 gcm^{-3} according to the porosity that changes from 50%–90% resulting in its modulus and ultimate compressive strength being around 20 times less than that of cortical bone [9,10]. Table 1 shows the summary differences between the two types of bone.

Table 1- Differences between cortical bone and cancellous bone [1,11].

Properties	Cortical Bone	Cancellous Bone
Bone mass (%)	80	20
Main functions	Mechanical support and physical protection	Mineral homeostasis
Porosity (%)	5–10	75–90
Elastic modulus (GPa)	17	0.1–2
Stiffness modulus (GPa)	8.7–14.1	0.02–0.5
Compressive strength (MPa)	131–224	2–12
Flexural strength (MPa)	135–195	–
Tensile strength (MPa)	50–151	1–5

Bone is a highly dynamic organ composed by four types of cells: osteoblasts, osteoclasts, bone lining cells presented on bone surfaces and bone lining permeating the mineralized interior (osteocytes) [1].

Osteoblasts are cuboidal differentiated cells found on the surface of new bone responsible for the production of the extracellular matrix (ECM) of bone, and its subsequent mineralization process [12,13]. Osteoblasts produce the organic matrix of bone, called osteoid. Some of the osteoblasts become trapped in the lacunae within the matrix of bone and differentiate into osteocytes [14]. Old osteoblasts become inactive, thin and elongated lining cells which lies on the bone surface [15]. The repair process and formation of new bone requires the differentiation and the proliferation of osteoblasts. Genes must be activated in the osteoblasts in order to signal cell division and ECM production that is capable of mineralizing to become bone [16].

The osteocyte is a mature osteoblast inside the bone matrix and is responsible for its maintenance, through the growth of new arms on the cell and the packing of osteoblasts and osteoclasts [14,15]. They become responsible for communication between other analogous cells and bone lining cells by developing long branches, forming a wide network of intercellular communication. Osteocytes are mature bone cells, uniform in shape and size, smaller than osteoblasts and greater in number; they form more than 90% of bone cells in the skeleton of an adult human.

Bone lining cells are flat, elongated, inactive cells that cover bone surfaces that are undergoing neither bone formation nor resorption. Little is known regarding the function of these cells; however, it has been speculated that bone lining cells can be precursors for osteoblasts [1].

Osteoclasts originate from hematopoietic stem cells, they are large multinucleated cells, responsible for resorbing the mineralized bone matrix and they move from different locations on the bone surface dissolving the bone [17]. Osteoclasts contain a stockpile of lysosomal enzymes, which are secreted and are able to resorb 200,000 μm^3/day during 15–20 days of lifetime [14].

Bone remodelling is a dynamic process of bone formation and bone destruction,

accounts for its growth during the development stages of the body, preserving its shape and consistency, and enabling its regeneration in case of fracture, however, for larger defects, human intervention is required to aid or stimulate the healing. Bone remodelling is linked to bone growth and is influenced by genetic factors, nutrition and hormones and is composed of four consecutive phases: activation, resorption, reversal and formation [18]. An unbalanced ratio between the formation of new bone and resorption of old bone, can lead to several osseous diseases.

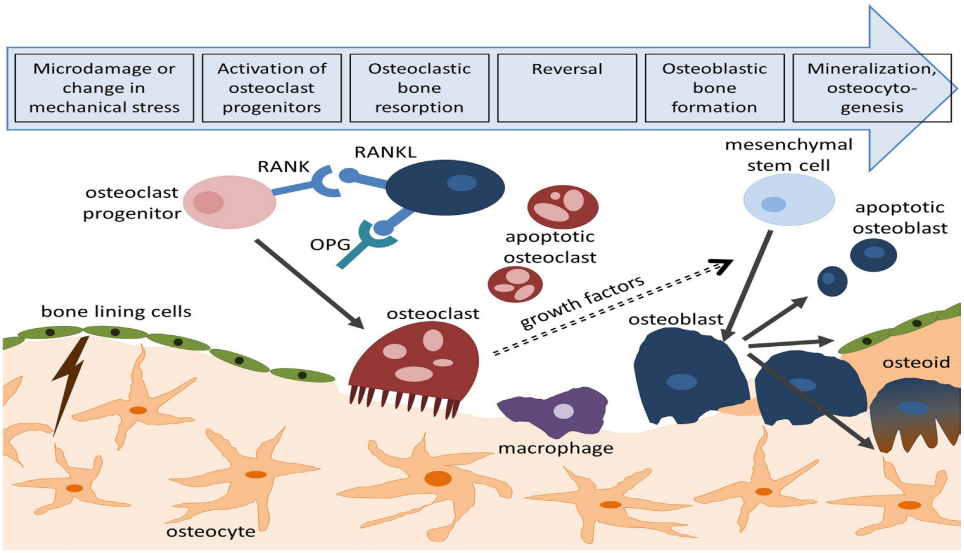

Fig. 2. Bone remodelling process that consists of four consecutive steps: activation, resorption, reversal, and formation [18].

BONE GRAFTS

Bone graft is the second most commonly transplanted tissue [19], approximately 2.2 million bone grafting procedures are performed annually worldwide [20]. Bone tissue regeneration remains an important challenge in the field of orthopaedic and craniofacial surgery. Bone grafts are crucial for the treatment of a number of conditions, including segmental bone defects caused by trauma or by pathological diseases as tumour excision, chronic osteomyelitis, osteoarthritis, osteogenesis imperfecta and Paget's disease, non-unions, avascular necrosis and spinal fusions [21,22]. Current clinical treatments found for large defects are challenging, and

despite the natural capacity of bone for healing, if an injury is beyond a critical limit (critical size defect), it cannot heal by regeneration. Traditional tissue engineering treatment options in reconstructive surgery include autologous bone grafts and allografts bone grafts (tissue from another patient) to repair large bone defects [23]. Autologous bone grafting remains the gold standard to fill a bone defect with the highest success rates for bone regeneration [24,25] but autografting may be restricted by donor site morbidity, bone availability, secondary surgery cost and burden and potential risk of disease transmission [26,27]. Using the allografts, which accounts for 34% of the current bone grafts, appears as an alternative to autografts, but also has drawbacks including availability, disease transmission and risks of infection and rejection by the immune system [28,29]. Xenografts are another option for bone grafts. In this case, animal bone is supplied as a powder, granules or blocks, but disease transmission and immune rejection are major risks [30]. The limitations with conventional grafting approaches can be overcome by the use of synthetic bone substitutes/scaffolds. A large number of synthetic bones have been developed, which can vary in composition, mechanical of action, and special characteristics. Althoutgh they should be biocompatible, they are still unable to provide an osteogenic capacity as good as the autografts [31,32].

Along the last years the bone graft biomaterials have evolved and can be categorized, according Hench, into three different generations [16]. The first generation bone graft require the biomaterial to match the physical properties of the tissue to be replaced, these include metals and alloys which have excellent mechanical properties but are neither bioresorbable nor bioactive and because their limited lifetime it needs to be removed and replaced surgically. The second generation of bone grafts include bioactive ceramics and bioresorbable polymers that were developed with bioactive interfaces which would elicit a specific biological response. The third generation bone grafts try to get closer to the autograft, made up of polymer–ceramic composite scaffolds, with the incorporation of osteogenic cells, growth factors or bone morphogenetic proteins, capable of inducing specific cellular responses at the molecular level.

BONE TISSUE ENGINEERING

Tissue engineering has emerged as a promising approach for the repair and regeneration of tissues and organs lost or damaged as a result of trauma, injury, disease or aging [33,34]. Tissue engineering has been defined as an interdisciplinary field that incorporates principles of engineering and the life sciences to produce biological substitutes that restore, maintain or improve tissue function [35]. This innovative technology has attracted increasing attention as an alternative strategy to treat damaged organs and tissues that cannot be self-regenerated, such as full-thickness skin burn, over critical-sized bone defects, and chronic cartilage disease. In contrast to classic biomaterials approach, it is based on the understanding of tissue formation and regeneration, and aims to induce new functional tissues, rather than just to implant new spare parts [9]. Tissue engineering aims to eliminate the disadvantages of the conventional clinical treatments associated with donor-site morbidity and scarcity in autografting and allografting. Developed as an artificial bone matrix, a tissue engineering scaffold plays an essential role in regenerating bone tissue. Bone tissue engineering (BTE) has emerged to regenerate damaged bone and therefore to recover its malfunctions rather than replacing it. There are three basic elements required for bone tissue engineering: osteogenic cells, growth factors and an osteoconductive scaffold matrix [36-38]. The main principle of BTE strategy is to cultivate cells in a designed artificial 3D porous matrix, working as a scaffold to sustain cell proliferation, differentiation and to provide guidance for tissue regeneration and growth. The culture of these cells, under controlled stimulation with growth factors *in vitro*, leads to new extracellular matrix (ECM) generated by the cells that may be implanted into the body when matured. After implantation the natural tissue regeneration processes will ideally take place, integrating the implant, leading to blood vessel formation. The structure of the scaffold dissolves while new tissue is formed in its place [39].

BIOMATERIALS FOR BONE TISSUE ENGINEERING

According to the American National Institute of Health, Biomaterial can be defined as "any substance or combination of substances, other than drugs, synthetic or natural in origin, which can be used for any period of time, which augments or replaces partially or totally any tissue, organ or function, in order to maintain or improve the quality of life of the individual" [40].

In general, these can be classified according two aspects: chemical composition and biological behaviour. The first subdivided biomaterials in four main classes of materials as ceramics, metals, polymers, and composites, with varied degree of bioactivity. Therefore, biomaterials can be classified into four categories according to the nature of their interaction with the surrounding tissue; these are: bioinert, when introduced to the body do not cause any reaction or interact with the biological tissue, meaning that the host won´t recognized them as a strange body (ex: titanium, zirconia and alumina); biotolerant, not necessarily rejected by the host but rather moderately accepted by the recipient tissue which encapsulates the implant with a fibrous interface (ex: stainless steel, glass, chromium-cobalt fibres and polymethylmethacrylate (PMMA)); bioactive, may cause a reaction or have an effect on the living environment, also due to their composition are capable of forming a direct link with the tissue (ex: hydroxiapatite, bioactive glasses); biodegradable/reabsorbable, those that suffer of slow degradation and gradual substitution of the host tissue (ex: tricalcium phosphate and bioactive glass) **[**40**].**

The basic requirements of a scaffold material are high cell/tissue biocompatibility, non-toxicity, capability of promoting cell proliferation and differentiation, and sufficient mechanical properties [41,42]. However, in order to achieve an excellent restoration of a bone implant, three different processes must take place, osteoinduction, osteoconduction and osseointegration [43]. Osteoinduction is the ability of a material to recruit and induce progenitor or undifferentiated cells to differentiate towards the osteoblastic lineage, thus, is the process by which osteogenesis is induced. Osteoconduction means that bone grows on a surface, for this, the materials allowing the bone cells adhere, proliferate and form extracellular matrix on its surface or down into pores and channels. Osseointegration is the stable anchorage of an implant achieved by direct bone-to-implant contact, materials bonded

with surrounding bone without growth fibrous tissue at the bone-implant interface.

CALCIUM PHOSPHATES

Among several synthetic bone substitutes options, there are ceramics, glasses and glass ceramics that have been used to produce are synthetic scaffolds for applications in dentistry and orthopaedics since 1980s [44,45]. Being a major constituent of bone, calcium phosphates (CaPs) have been extensively studied as scaffold materials for bone tissue engineering. Among different CaPs, the majority of research has been focused on hydroxyapatite (HA, $Ca_{10}(PO_4)_6(OH)_2$), β-tricalcium phosphate (β-TCP, $Ca_3(PO_4)_2$) or biphasic calcium phosphate (BCP, a mixture of HA and β-TCP) [32].

Among the various monophasic calcium phosphate ceramics, HA ($Ca_{10}(PO_4)_6(OH)_2$) is the most stable, the most dense and the most insoluble, possessing a K_{sp} value of around 2.9×10^{-58} over a pH range of ~4.5 to ~9.7 [46-48]. From a chemical and structural point of view it is the material most similar to the mineralized constituents of hard tissue (bones and teeth). Moreover, stoichiometric HAP has a Ca/P ratio of 1.67 and is considered to be osteoconductive but not osteoinductive [49]. HA can be easily prepared by different methods, precipitation, thermal treatments at high temperature or hydrothermal conversion from coral [50].

Of the two known crystal forms of HA—monoclinic, space group $P2_1/b$, and hexagonal, space group $P6_3/m$—only the hexagonal phase is of practical importance because the monoclinic form is destabilized by the presence of even small amounts of foreign ions [51]. The hexagonal structure contains two different cation sites, Ca(I) and Ca(II), but only one phosphate environment (Ca(I), Ca(II) are used for stoichiometric apatite; M(I), M(II) are the general symbols for substituted apatites). The structure can be roughly described as a phosphate assembly crossed by parallel channels filled by OH^- ions and parallel to the crystallographic *c*-axis (Fig. 3 (a)). The channel walls are formed of Ca(II) atoms arranged in staggered triangular arrays. Ca(I) atoms have a different environment and are positioned in columns parallel to the OH^- channels [52]. A unit cell accommodates a formula unit $Ca_{10}(PO_4)_6(OH)_2$. Among the 10 cations, the 4 Ca(I)s are tightly bonded to 6 oxygens and less strongly

to the other 3 oxygens (mean Ca(I)–O distance 0.255 nm), whereas the 6 Ca(II) atoms are surrounded by 7 oxygens (mean Ca(II)–O distance 0.245 nm). Ca(I) atoms are strictly aligned in columns and any small change in the metal–oxygen interactions affects the entire lattice. However, the Ca(II) atoms belonging to consecutive layers are staggered, allowing random local misplacements without compromising the whole structure. As a consequence, cations smaller than Ca or also low concentrations of slightly larger cations are preferably accommodated in site Ca(I) where stronger interactions are present, while larger cations should be accommodated in position Ca(II), even at high concentrations.

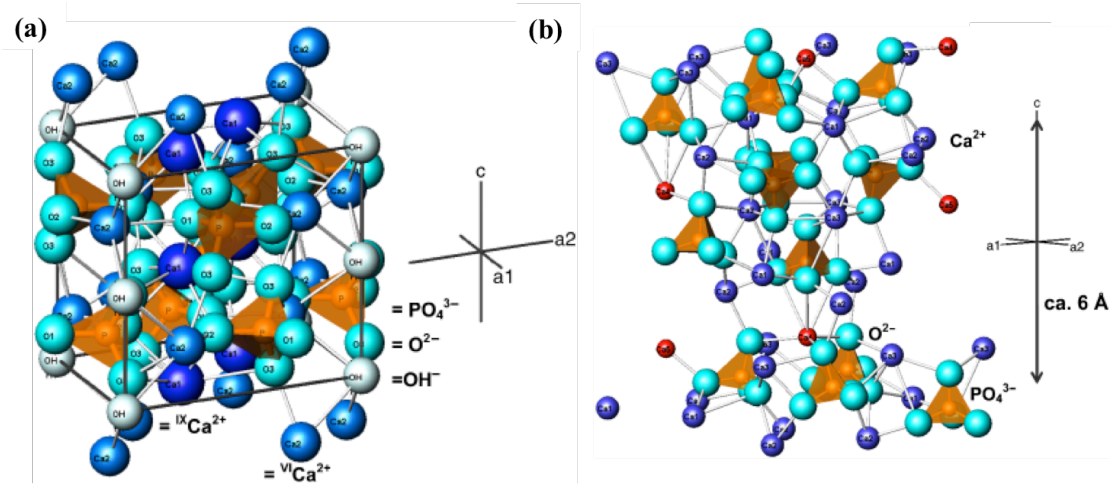

Fig. 3 Crystal structure of hydroxyapatite (a) and β-tricalcium phosphates (b) projected perpendicular to c-axis. [Adapted from 53].

Stoichiometric tricalcium phosphates (TCP) ($Ca_3(PO_4)_2$) possesses a Ca/P ratio of 1.5 and occurs in two phases, α and β; these phases possess identical chemistries but different crystal structures [54]. The rhombohedral β-TCP, space group *R*3*c* (Fig. 3 (b)), can be obtained only at high temperature, by solid-state reaction or by thermal conversion of other phosphates, and is stable up to 1125 ºC. Moreover, β-TCP form cannot be obtained by direct precipitation and it results from the calcining at 700-800 ºC of Ca deficient apatite, with the loss of water, according to the equation [55]:

$$Ca_9(HPO_4)(PO4)_5(OH) \rightarrow 3Ca_3(PO_4)_2 + H_2O$$

Above 1125 ºC β-TCP converts into α-TCP, which unit cell is monoclinic, space group $P2_1/a$. [51]. Both phases are less stable than HAP and hence more soluble in aqueous environments [47]: Ksp values of 10−25.5 for α-TCP and 10−28.9 for β-TCP at 25 ºC have been reported [56]. The principal disadvantage of the use of HA and related calcium phosphates as bone scaffold is that the slow degradation of these inorganic ceramics in the body limits their utility for bone-regeneration application. Sintered hydroxyapatite can take more than five years to be reabsorbed by the body, while tricalcium phosphate can be completely degraded in one or two years [57]. β-TCP has been used more extensively in bone regeneration than α-TCP and is considered to be both osteoconductive and osteoinductive [58].

Biphasic calcium phosphate

Biphasic calcium phosphate (BCP) ceramics are a mixture of hydroxyapatite and β-tricalcium phosphate that combines the great biodegradability of β-TCP with the strong mechanical properties of HA [59] and were developed to better control the process of biomaterials resorption and bone substitution. BCPs are considered better when compared to either single phase HA or β-TCP components because of their unique dissolution characteristics which promote new bone formation at the implant site [60].

Increasing the β-TCP/HA ratio will give a more biodegradable material since β-TCP dissolves preferentially from its matrix, releasing calcium and phosphate ions to the media, enhancing the *in vivo* activity and decreasing the resorption time. Simultaneously, a higher β-TCP/HA ratio will diminish the mechanical strength in the BCP material. However, it has been proved that the mixture of calcium phosphates turns out to be the ideal choice [59].

Daculsi found an optimum balance of the more stable phase of HA and more soluble TCP, enabling to gradually control the dissolution in the body, seeding new bone formation as it releases calcium (Ca^{2+}) and phosphate (PO_4^{3-}) ions into the biological medium [61].

Some authors have defended the superior properties of the BCP materials directly prepared over those obtained by mixing two single phases [62]. Therefore, there are several synthesis routes that can be employed in preparation of BCPs, being the most widely used the precipitation [63].

Dopant ions of calcium phosphates

Bone is not a homogenous material. Besides Ca and P, it also incorporates various trace elements playing vital roles in the formation, growth, and repair of bone. In recent years various studies demonstrated that adding trace elements to CaP materials, such as strontium, magnesium, zinc, copper and even silver, can lead to controlled degradation, increase the mechanical strength of the materials, and positively influence the biological response, improving the performance process after implantation [50,64].

Orthopaedic implants can cause post-operative infections owing to the adhesion of bacteria on their surface, being a serious problem with awful consequences [65]. Open fractures, in particular, involving large segmental bone defects filled with artificial bone grafts are prone to such infections [66-68]. The infection rate on orthopaedic implants restoration was reported to be 72.9% [69]. Such infections significantly increase the treatment costs due to additional surgery required and extended recovery of the patient [70,71]. It has been reported that incorporation of trace ions such as Ag, Zn, and Cu into synthetic materials improves their antimicrobial properties, preventing the adhesion of bacteria at the site of implantation [72,73]. There are three main mechanisms for the antimicrobial activity of these ions [74-77]. Firstly, metal ions bind to proteins deactivating them. Secondly, metal ions can interact with microbial membrane and induce structural and permeability changes. Finally, metal ions interact with microbial nucleic acids, preventing microbial replication.

Small quantities of copper and zinc ions are essential for various metabolic processes in most of the living organisms, while higher amounts are potentially toxic. Besides its antimicrobial activity, copper, is an essential trace element for mammalian life,

with its highest abundance in the liver tissue [78], playing a cross-linking role for collagen and elastin of bone [79-81]. It also induces a stimulatory effect on endothelial cells towards angiogenesis, probably caused by upregulation of VEGF expression [82,83]. On the other hand, zinc is present in all biological tissues, especially in bone, which accounts for 28% of the total Zn content in the body. Zn also plays a vital role in the maintenance of membrane structure, function, protein synthesis, DNA synthesis, mitosis, and cell proliferation [84,85]. Several important metalloenzymes utilize zinc for structure, catalytic, or regulatory actions, including alkaline phosphatase (ALP) that is absolutely vital for the maturation of new bone formation. Zinc stimulates bone formation and mineralization [86,87] having a direct specific proliferative effect on osteoblastic cells *in vitro* and it is thought to possess a potent and selective inhibitory effect on osteoclastic bone resorption *in vivo* [88,89]. Zinc-doped CaP materials have shown increased osteoblastic response *in vitro* as well as new bone formation *in vivo* [88,90]. Zinc phosphate cements are some of the oldest and most widely used cements in dental industry [91].

Strontium is a non-essential element, present in mineral phase of bone, especially at regions of high metabolic turnover [92]. Sr has bone-seeking behaviour and favours bone growth [93]. Low Sr doses are beneficial in the treatment of osteoporosis [94] and its administration as Sr ranelate showed significant reduction of fractures in osteoporotic patients [95]. In addition, Sr decreases bone resorption by inhibition of osteoclast-resorbing activity and osteoclastic differentiation, and it promotes bone formation by enhancing pre-osteoblastic cell replication and osteoblastic differentiation [92,93]. The evidences of the beneficial effects of strontium on bone regeneration justify the increasing interest in addition it into calcium phosphate bioceramics [96-98].

Magnesium (Mg^{2+}) has been often associated with the mineralization of calcified tissues and indirectly influences mineral metabolism [99,100]. Its ability to stimulate the formation of biphasic HA-TCP mixtures upon heating [101] by enhancing the thermal stability of TCP is an added benefit from Mg-doping HA, making the resulting bone grafts more biodegradable.

The use of multiple ionic doping has been attempted to get further biological benefits from synthetic CaP bone grafts, but their physical properties can also be

altered [102-104]. The changes in mechanical properties and biological responses reflect the effects of doping on the physicochemical properties of CaPs such as phase, crystallinity, microstructure, solubility, grain size, mechanical strength, and strength degradation kinetics caused by cation substitution [102].

Most of the ion doping reported on literature was accomplished through methods of chemical precipitation, sol-gel, and ion-exchange process [105-107]. The physicochemical properties of CaP might vary depending on whether the dopant is substituting 'Ca' or 'P' site in the crystal lattice and/or staying in its respective salt form. Depending on the ionic radius, the substitution of the added dopant can either stabilize or destabilize the crystal structure of CaPs [108].

SCAFFOLDS IN TISSUE ENGINEERING

In bone tissue engineering scaffolds play a fundamental role; they can provide a temporary three-dimensional (3D) system for initial cell proliferation, differentiation and extracellular matrix production and, in addition, providing a template for new tissue regeneration [35,109]. Both the scaffold material and its architectural design (pore size, porosity and interconnectivity) play a significant role in governing tissue regeneration and define the ultimate shape of newly grown soft or hard tissue [39,110]. The ideal scaffold must have certain properties and characteristics to occur effective bone formation, such as:

(i) Be biocompatible (non-toxic), described as its ability to support normal cellular activity, including molecular signalling systems without any local and systematic toxic effects to the host tissue [111]. An ideal bone scaffold must be osteoconductive where the scaffold allows the bone cells to adhere, proliferate, and form ECM on its surface and pores. The scaffold should also be able to induce new bone formation through biomolecular signalling and recruiting progenitor cells, a property known as osteoinduction. Furthermore, an ideal scaffold needs to form blood vessels in or around the implant within few weeks of implantation to actively support nutrient, oxygen, and waste transport [112];

(ii) Exhibit, after *in vitro* tissue culture, mechanical properties comparable to those of the tissue to be replaced. Mechanical properties of bone vary widely from cancellous

to cortical bone. Young's modulus of cortical bone is between 15 and 20 GPa and that of cancellous bone is between 0.1 and 2 GPa. Compressive strength varies between 100 and 200 MPa for cortical bone, and between 2 and 20 MPa for cancellous bone. Therefore, the large variation in mechanical property and geometry makes it difficult to design an 'ideal bone scaffold' [112];

(iii) Have a porous three-dimensional (3D) architecture and interconnected open porosity to allow cell proliferation, vascularization and diffusion of nutrients between the cells seeded within the matrix and the surroundings. A must have property for scaffolds is interconnected porosity where the pore size should be at least 100 μm in diameter for successful diffusion of essential nutrients and oxygen for cell survival [113]. The optimum pore size range for bone tissue in-growth is within 200–350 μm [114]. Recent studies indicated that multi-scale porous scaffolds involving both micro (pore size <20 μm) and macro porosities (pore size >100 μm) can perform better than only macro porous scaffolds [115];

(iv) Bioresorbability is another fundamental factor for scaffolds in bone tissue regeneration, to degrade at a rate that matches the production of new tissue, into nontoxic products that can be easily resorbed or excreted by the body;

(v) Capable of being processed economically into anatomically relevant shapes and dimensions, and be sterilized for clinical use [116].

FABRICATION TECHNIQUES

In an organ, cells and their ECM are usually organized into 3D tissues. Therefore, in tissue engineering, a highly porous 3D matrix (scaffold) is often necessary to accommodate cells and to guide their growth and tissue regeneration in three dimensions. A variety of techniques, conventional or advanced processing methods, have been used to fabricate 3D porous ceramics scaffolds for tissue engineering and regenerative medicine.

Conventional techniques are relatively simple methods, including solvent casting and particulate leaching, gas foaming, fibre meshes and fibre bonding, phase separation,

melt molding, emulsion freeze drying, solution casting and freeze drying [109,117]. However, there are inherent limitations in these processing methods, most of them are incapable of producing fully continuous interconnectivity and uniform pore morphology within a scaffold, it is difficult to accurately control the pore geometry, pore size, spatial distribution cannot be controlled, and overall porosity of the scaffolds [118]. In addition, the use of organic solvents may cause toxic effects on cells during subsequent culture [119,120]. Recently, to overcome these obstacles, advanced additive manufacture (AM) techniques, also known as Rapid Prototyping (RP) or Solid Free-form Fabrication (SFF), have been successfully used to fabricate porous 3D structures with customized external shapes and predesigned internal microarchitecture. Additive manufacturing is a fabrication method using 3D multi-layered constructs to build porous biocompatible scaffolds of pre-defined shapes with excellent mechanical and osteoconductive properties [121]. AM techniques used to fabricate 3D ceramic structures can be classified as [122]: (1) laser assisted sintering (e.g., SLS and LENS), (2) extrusion (e.g., fused deposition of ceramics, FDC), (3) polymerization (e.g., SLA), and (4) direct writing-based processes (e.g., ink-jet 3DP).

In all AM techniques, a 3D model is created by computer-aided design (CAD) program and then is converted to an STL (standard tessellation language) file. The 3D object is then sliced to two-dimensional (2D) cross sections and fabrication of the part is started from the base in alternating layers. Manufacturing is continued layer by layer until the entire part is fabricated. Compared to traditional manufacturing processes, the primary advantage of AM is its ability to create complex designs with high accuracy in dimensions and structural features without the need for specific tooling or dies. In addition, almost all AM techniques are faster than traditional processes without the need for further surface finishing. However, not all the AM techniques are useful for fabrication of similar ceramic structure due to the limitations of each technique [122].

A brief overview of the most important AM techniques including 3D printing (3DP), stereolithography (SLA), fused deposition modelling (FDM), and selective laser sintering (SLS) is presented below.

3D printing

3D printing technology was developed at the Massachusetts Institute of Technology in 1995 by Sachs *et al.* [123] and it is considered one of the most attractive AM system. With a high application potential for bone tissue engineering, 3D printing can be adapted to produce porous ceramic-based bone scaffolds with well-defined inner and external structures [124]. 3DP is a power-based freeform fabrication method in which using a regular ink-jet printed-head, binders are printed on to loose powders in a powder bed. Fig. 4 shows a schematic representation of the 3DP process. A first layer of powder is laid on the building platform and a liquid binder is sprayed on the surface of the powder layer bonding together the powder granules. Once the layer is completed, the platform is lowered the height of one layer and a new one is laid over the precedent one. This process is repeated until all of the layers have been printed. The printed structure, embedded in the loose powder, must be extracted from the powder bed after it has been printed, and the unbound powder must be removed from its pores and cavities, a crucial step in the printing process that is referred to as depowdering. The scaffold can then be sintered [125-128]. In general, a large variety of ceramic, metallic, polymeric, and composite materials can be processed using 3DP, being binder selection and process parameter optimization the keys to successful part fabrication.

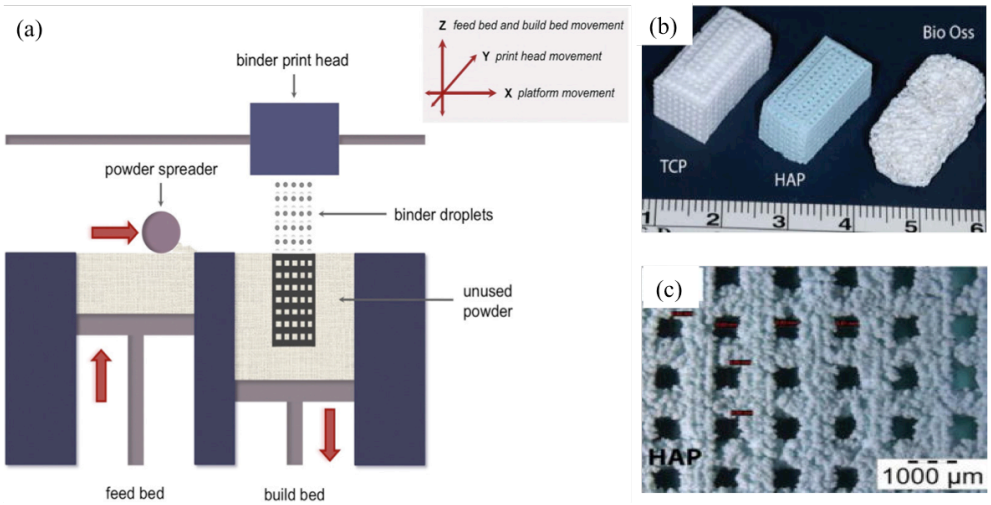

Fig. 4. (a) Schematic drawing representing the 3D printing process [128]. Examples of bioceramic scaffolds produced by 3DP: (b) TCP and HA photograph and (c) SEM image of HA [124].

Stereolithography

The manufacturing of 3D objects by stereolithography (SLA) is based on the spatially controlled solidification of a liquid resin by photo-polymerisation. This technique was developed, at the same time, by Kodama (1981) and Nakai and Marutani (1986), in two different laboratories [129,130]. SLA uses a computer-controlled laser beam or a digital light projector with a computer-driven building stage, where a pattern is illuminated on the surface of a resin. As a result of this, the resin in the pattern is solidified to a defined depth, causing the adherence to a support platform. After photo-polymerisation of the first layer, the platform is moved away from the surface and the built layer is recoated with liquid resin. A pattern is then cured in this second layer [129]. Figure 5 shows a schematic representation of the stereolithography process.

The possibility to fabricate flexible, submicron/decimetre-sized accurate structures as well as components with different geometries with high efficiency level is the main advantage of SLA [122].

The limited number of resins that are commercially available for processing by stereolithography has often been considered the main limitation of the technique. The resin should be a liquid that rapidly solidifies upon illumination with light [140].

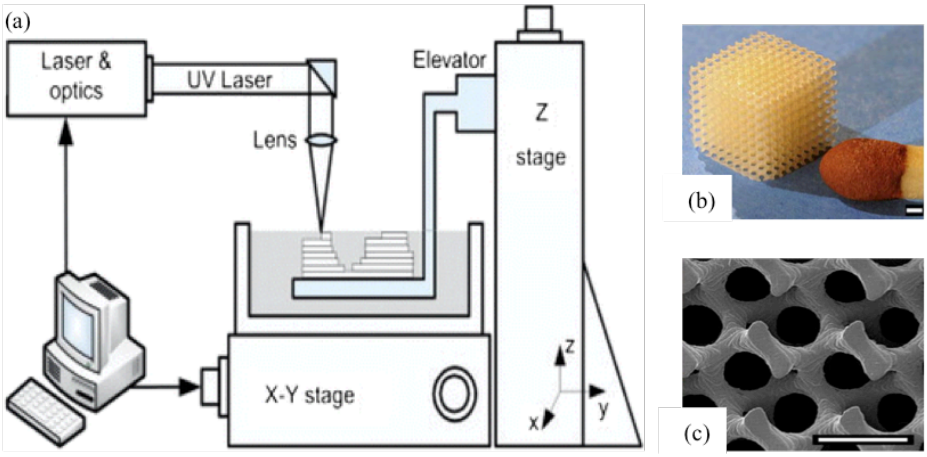

Fig. 5. (a) Schematic drawing representing of an SLA system. [131] (b) Photograph of PDLLA scaffolds built by SLA and SEM micrograph (c). Bar: 500 μm [132].

Fused deposition modeling

Fused deposition modelling (FDM) is an AM technique that utilizes thermoplastic fibre that is heated and selectively extruded out of nozzles, moving within the x- and y-axes layer-by-layer, Figure 6. The semi-molten polymer is extruded onto a base plate following a path predetermined by CAD specifications. When a layer is completed, the base platform is lowered vertically on the z-axis and another layer of thermoplastic polymer is delivered. This process is repeated until the structure has been completed [125,133,134]. Fused deposition modelling was used to produce novel scaffolds with honeycomb-like pattern, fully interconnected channel network, and controllable porosity and channel size. In comparison with other AM techniques, the FDM method does not require any solvent and offers great ease and flexibility in material handling and processing. However, the resolution of FDM is relatively low, at 250 μm [120,133].

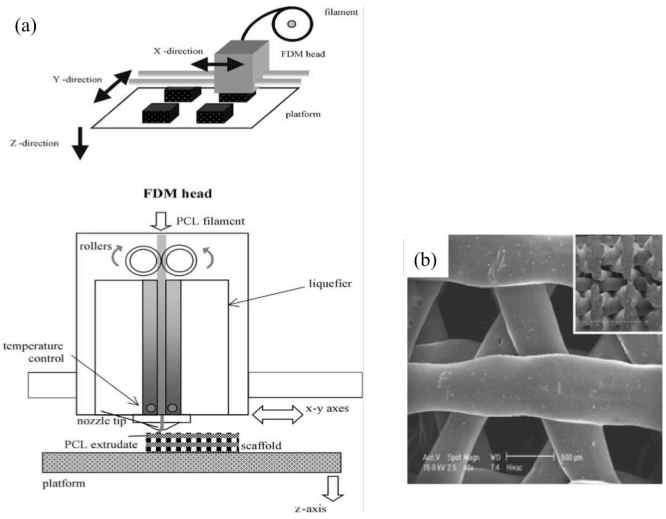

Fig. 6. (a) A schematic diagram of the FDM extrusion and deposition process [135], (b) SEM images of PCL/TCP composite scaffolds obtained from FDM [136].

Selective laser sintering

Selective laser sintering (SLS) is one of the most established and widely used additive manufacturing techniques. This technique was developed and patented by Deckard

and Beaman from the University of Texas at Austin. In this process, an object is created layer-by-layer from heat-fusible powdered material with heat generated from a scanning laser beam [127].

The laser beam selectively fuses powders following the cross-sectional information carried by the CAD data. During sintering, the laser beam-powder interaction increases the temperature inducing fusion of adjacent particles. After a layer is created, the powder bed is lowered and another layer of powder is rolled over it; the process is repeated layer after layer until the scaffold is completed. Unlike what happens with SLA, temporary support structures are not needed during the process, as support is provided by the unbound powder and, just as in 3DP, all remaining powder is removed after the scaffold has been completed [125,137].

Although the potential of scaffolds fabricated via SLS for bone tissue engineering has been recognized from a relatively wide range of powder materials such as poly(lactic acid), PCL and bioceramics, this technique needs high operating temperatures during manufacturing process, being the main disadvantage [137].

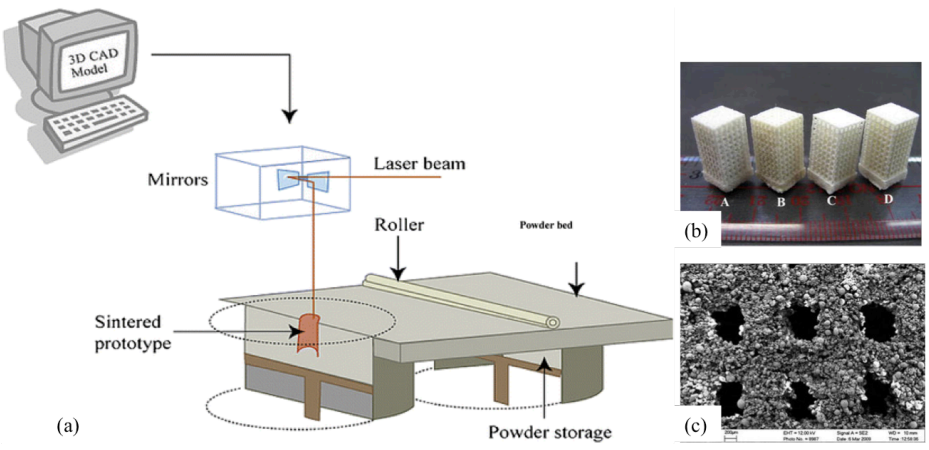

Fig. 7. (a) Schematic representation of the SLS system [131]. (b) Photograph of PHBV/TCP composite scaffolds built by SLS, and (c) a SEM morphology [138].

Robocasting

Robocasting, also called direct-write assembly, is a versatile AM technique [139-145]. This new AM technique was developed at Sandia National Laboratories, Albuquerque, New Mexico. It consists of a computer controlled robotic deposition of highly concentrated pastes (containing water, trace amounts of chemical modifiers, and ceramic powder), capable of fully supporting their own weight during assembly, allowing precise control of pore size (100 μm to 2 mm), shape and alignment [122,141,146]. Scaffold designs are created in a computer-aided design (CAD) program, which is then used to control the movements of the robocaster. A colloidal paste is loaded into a syringe mounted on a z -axis motion control stage and extruded through fine nozzles onto a moving x–y stage. Complex 3D parts are built in a layer-by-layer sequence. Figure 8 shows a schematic representation of the robocasting process. Compared with other AM technologies for ceramic materials, the most obvious advantage of robocasting is that the entire process, including fabrication, drying and sintering, can be complete in less than 24 hours [122,147].

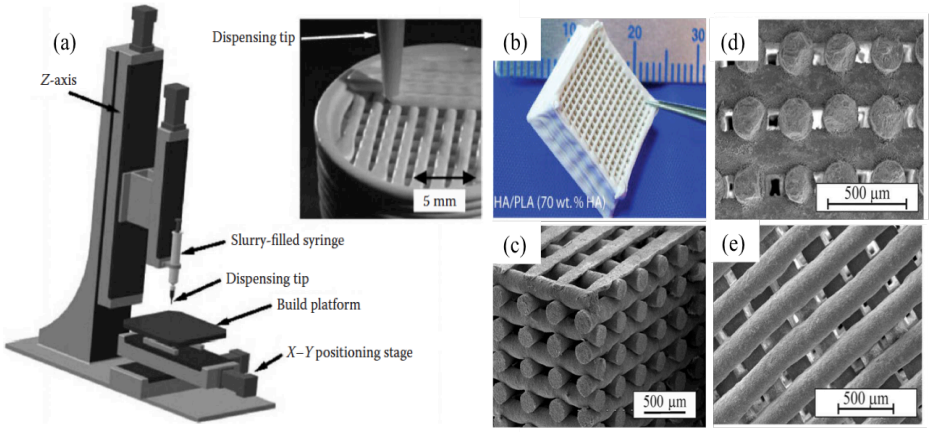

Fig. 8. (a) Schematic of robocasting process [141]. Examples of scaffolds produced by robocasting: (b) low magnification picture showing HA/PLA scaffold [148] and SEM micrographs showing the morphology of HA (c, d) and β -TCP (e) scaffolds after sintering [149,150].

Robocasting requires careful characterization and control of viscoelastic properties of the paste being deposited, commonly denominated as inks [141,146]. Colloidal inks must satisfy two important criteria: (i) exhibit a well-controlled viscoelastic response, i.e., they must be able to flow through a deposition nozzle and then "set" immediately to facilitate shape retention of the deposited features even as they span gaps in the underlying layer(s), and (ii) contain high solids volume fractions to minimize drying-induced shrinkage after assembly, meaning that particle network must be able to resist compressive stresses arising from capillary tension [145,151-153]. These criteria require careful control of colloidal forces to generate a highly concentrated, stable dispersion. These conditions are usually achieved by selecting an appropriate dispersant and exerting some mechanical action (stirring, milling), or ultrasonic agitation, to break down the agglomerates. Additionally, particle size and particle size distribution are also relevant factors that determine the rheological properties of the suspensions [146,154,155]. After the preparation of high solids loading suspensions, a system change is induced by several ways (e.g., ΔpH, ionic strength, or solvent quality) that promotes a fluid-to-gel transition [146]. Until now, several ink proposals have been explored, however, since the main challenge in robocasting is developing ceramic slurries with suitable viscoelastic properties for the deposition process, the research for new ceramic inks has never stopped.

Porosity in robocast scaffolds can be tailored on three length scales: macro- (greater than 100 μm), micro- (1–30 μm), and submicron (less than 1 μm). Macroscale porosity is introduced directly by the robocasting process as it draws successive layers. Robocast rods, arranged in latticed patterns, create macroporous pathways in three dimensions. Varying the rod spacing and size, pathways can be precisely constructed to produce highly uniform macropores. This technique has been used to produce porous ceramic and composite scaffolds with different architectures [149,156-158]. The size and fraction of submicron porosity can be controlled by sintering conditions [159-162].

The appearance of robocasting as AM technology opened the opportunity to construct medical devices and scaffolds for tissue engineering, particularly, orthopaedic applications by using bioceramic powders. Porous bioceramic scaffolds are widely regarded as promising candidates for bone tissue regeneration, since the pore

architecture in such materials must exhibit an appropriate level of interconnectivity [163-165] to allow vascularization and diffusion of nutrients in order to promote cell ingrowth. This requirement implies the fabrication of scaffolds with large and higher total porosity when compared to ones fabricated by conventional techniques [166-168]. In recent years, different studies have been done in the fabrication of calcium phosphate scaffolds [59,148,149,156,169,170], remaining the possibility to explore new compositions such as HA, β-TCP and BCP.

Using the robocasting technique, Dellinger *et al.* [170] produced model HA scaffolds of various architectures, including periodic, radial, and superlattice structures with macropores (100–600 μm), micropores (1–30 μm), and submicron pores (< 1 μm). This study indicates that by precise control of scaffold features, these model scaffolds may be used to systematically study the effects of scaffold porosity on bone ingrowth processes both *in vitro* and *in vivo*.

Russias *et al.* also reported the preparation of tissue engineering scaffolds by robocasting with HA or bioglass/polylactide or polycaprolactone. The mechanical property was characterized before and after submerging in simulated body fluid for 20 days. It was strongly dependent on the ratio of the organic and inorganic phase, and could be controlled based on different applications [148]. All these scaffolds showed encouraging biological response in *in vitro* evaluations.

Miranda and co-workers optimized the particle size and morphology of TCP powders, in order to prepare suitable inks for robocasting. Reducing particle size and increasing specific surface area of the TCP powders could be appropriate procedures for successful slurry preparation [156]. Therefore, through the analysis of microstructure and heat treatment, scaffolds fabrication via robocasting with tailored performance could be achieved for bone tissue engineering applications as well [156].

Heo *et al.* [171] produced HA/PCL composite scaffolds using the robocasting process. The macropores in the scaffolds were well interconnected, with a porosity of 73 % and a pore size of 500 μm. The compressive modulus of the nano-HA/PCL and micro-HA/PCL scaffolds was 3.2 and 1.3 MPa, respectively. The higher modulus of nano-HA/PCL was to be likely caused by the well-dispersed nanosized HA particles. In addition, the more hydrophilic surface of nano-HA/PCL, which resulted from the

greater surface area of HA of nano size, could promote cell attachment and proliferation compared with micro-HA/ PCL. Martinez-Vazquez *et al.* [158] reported the infiltration of PCL or PLA into β-TCP porous scaffolds fabricated by robocasting increased their compressive strength compared with pure calcium phosphate scaffolds.

The incorporation of biomolecules in the scaffolds, such as growth factors, antibiotic or anti-inflammatory drug with the aim to accelerate local bone healing, is promising and currently under extensive research. The usage of the robocasting offers opportunities for fabricating scaffolds a broad range of materials, however, the green bioceramics should be submitted to a sintering step at high temperatures to obtain the desired mechanical properties of the scaffolds, barring the incorporation of temperature sensitive bioactive molecules in the extrudable ink, hence before sintering. Martinez-Vazquez *et al.* [172] studied the processing conditions to fabricate, by robocasting, composite scaffolds with a high content of ceramic, and with no sort of additive (dispersant, binder, etc.), in order to obtain ideal synthetic scaffolds of gelatin and silicon-doped hydroxyapatite (HASi) for bone regeneration and drug release, in a single step, without the need for sintering.

REFERENCES

[1] J.P. Bilezikian, L.G. Raisz, T.J. Martin, Principles of Bone Biology 3rd Edition, Academic Press, 2008.

[2] P. Ducy, T. Schinke, G. Karsenty, The osteoblast: A sophisticated fibroblast under central surveillance, Science 289 (2000) 1501–1504.

[3] A. Boskey, Mineralization of bones and teeth, Elements Mag 3 (2007) 385 – 392.

[4] M.F. Young, Bone matrix proteins: their function, regulation, and relationship to osteoporosis, Osteoporos Int 14 (2003) S35 – S42.

[5] R.B. Martin, Bone as a Ceramic Composite Material, Materials Science Forum 293 (1999) 5 –16.

[6] W. Suchanek, M. Yoshimura, Processing and properties of hydroxyapatite-based biomaterials for use as hard tissue replacement implants, Journal of Materials Research 13(1) (1998) 94 –117.

[7] X. Wang, S. Xu, S. Zhou, W.Xu, M. Leary, P. Choong, M. Qian, M. Brandt, Y.M. Xie, Topological design and additive manufacturing of porous metals for bone scaffolds and orthopaedic implants: A review, Biomaterials 83 (2016) 127 –141.

[8] D.R. Carter,W. Hayes, The Compressive behaviour of bone as a two-phase porous structure, J. Bone and Joint Surgery 59 (1977) 954–962.

[9] A.J. Salgado, O.P. Coutinho, R.L. Reis, Bone tissue engineering: State of the art and future trends , Macromolecular Bioscience 4 (2004) 743–765.

[10] M.J. Yasemski , R.G. Payne , W.C. Hayes , R. Langer , A.G. Mikos, Evolution of bone transplantation strategies, molecular and cellular tissue for human bone engineer, Biomaterials. 17 (2) (1996) 175–185.

[11] F. Barrère, C. a. van Blitterswijk, K. de Groot, Bone regeneration: Molecular and cellular interactions with calcium phosphate ceramics, Int. J. Nanomedicine 1(3) (2006) 317–332.

[12] J. Zhang, M. Wang, M.C. Jae, M. Athanasios, The incorporation of 70S bioactive glass to the osteogenic differentiation of murine embryonic stem cells in 3D bioreactors, J. Tissue Engineering Regeneration Medicine 3 (2009) 63–71.

[13] A.S. Mistry, A.G. Mikos, Tissue engineering strategies for bone regeneration,

Advanced Biochemical Engineering/Biotechnology 94 (2005) 1–22.

[14] D.W. Sommerfeldt, C.T. Rubin, Biology of bone and how it orchestrates the form and function of the skeleton, European Spine Journal 10 (2001) S86-–S95.

[15] P.D. Downey, M.I. Siegel, Bone biology and the clinical implications for osteoporosis, J. Physical Therapy 86 (2006) 77–91.

[16] L.L. Hench, J. Polak, Third-generation biomedical materials, Science 295(5557) (2002) 1014–1017.

[17] K.A. Hing, Bone repair in the twenty-first century: biology, chemistry or engineering, Philosophical Transactions of the Royal Society A, 362 (2004) 2821–2850.

[18] C. Wittkowske, G.C. Reilly, D. Lacroix, C.M. Perrault, In Vitro Bone Cell Models: Impact of Fluid Shear Stress on Bone Formation, Front Bioeng Biotechnol 4:87 (2016) 1–24

[19] P.V. Giannoudis, H. Dinopoulos, E. Tsiridis, Bone substitutes: an update, Injury 36 (3) (2005) S20–S27.

[20] C. Laurencin, Y. Khan, S.F. El-Amin, Bone graft substitutes, Expert Rev Med Devices 3 (2006) 49–57.

[21] P.N. Soucacos, Z.T. Kokkalis, M. Piagkou, E.O. Johnson, Vascularized bone grafts for themanagement of skeletal defects in orthopaedic trauma and reconstructive surgery, Injury 44 (1) (2013) S70–S75.

[22] E. Guerado, C.H. Fuerstenberg, What bone graft substitutes should we use in posttraumatic spinal fusion? Injury 42 (2) (2011) S64–S71.

[23] E.M. Bueno, J. Glowacki, Cell-free and cell-based approaches for bone regeneration, Nat Rev Rheumatol 5 (2009) 685–697.

[24] M.A. Fernandez-Yague, S.A. Abbah, L. McNamara, D.I. Zeugolis, A. Pandit, M.J. Biggs, Biomimetic approaches in bone tissue engineering: integrating biological and physicomechanical strategies, Adv Drug Deliv Rev 84 (2015) 1–29.

[25] J.T. Marino, B.H. Ziran. Use of solid and cancellous autologous bone graft for fractures and nonunions. Orthop Clin North Am 41 (2010) 15–26.

[26] U. Kneser, D.J. Schaefer, E. Polykandriotis, R.E. Horch, Tissue engineering of

bone: the reconstructive surgeon's point of view, J Cell Mol Med 10 (2006) 7–19.

[27] C.G. Finkemeier, Bone-grafting and bone-graft substitutes, J Bone Joint Surg Am 84A (3) (2002) 454–464.

[28] L.G. Zhang, A. Khademhosseini, T. Webster (Eds.), Tissue and Organ Regeneration: Advances in Micro- and Nanotechnology, CRC Press, 2014.

[29] A. Oryan, S. Alidadi, A. Moshiri, N. Maffulli, Bone regenerative medicine: classic options, novel strategies, and future directions, J. Orthop. Surg. Res. 9 (18) (2014) 1–27.

[30] A. Woesz, Rapid prototyping to produce porous scaffolds with controlled architecture for possible use in bone tissue engineering. In: Virtual Prototyping and Manufacturing in Medical Applications, Springer, Chapter 9, 2008.

[31] C. Szpalski, J. Barr, M. Wetterau, P.B. Saadeh, S.M. Warren, Cranial bone defects: current and future strategies, Neurosurg Focus 29 (2010) E8.

[32] S. Bose, M. Roy, A. Bandyopadhyay, Recent advances in bone tissue engineering scaffolds, Trends Biotechnol 30 (2012) 546–554.

[33] R.M. Nerem, Cellular engineering, Ann Biomed Eng 19 (1991) 529–45.

[34] R. Langer, J.P. Vacanti, Tissue engineering, Science 260 (1993) 920–926.

[35] L. Moroni L, J.R. Dewijn, C.A. Van Blitterswijk, Integrating novel technologies to fabricate smart scaffolds, J. Biomaterials Science, Polymer Edition 19(5) (2007) 543–572.

[36] M. Matsuno, K. Omata, Y. Hashimoto, Y. Tabata, T. Satch, Alveolar bone tissue engineering using composite scaffold for drug delivery, Japanese Dental Science Review 46 (2010) 188–192.

[37] M. Schieker, H. Seitz, I. Drosse, S. Seitz, W. Mutschler, Biomaterials as scaffold for bone tissue engineering, European Journal of Trauma 32(2) (2006) 114–124.

[38] Q. Fu, E. Saiz, M. Rahaman, A.P. Tomsia, Toward strong and tough glass and ceramic scaffolds for bone repair, Advanced Functional Materials 23 (2013) 5461–5476.

[39] C.Z. Liu, J.T. Czernuszka, Development of biodegradable scaffolds for tissue engineering: a perspective on emerging technology, Materials Science and Technology 23(4)a (2007) 379–391.

[40] TW. Bauer. Bone graft materials: and overview of the basic science. Clinical Orthopaedics and Related Research 37 (2000) 10–27.

[41] J.R. Jones, M.E. Lisa, L.L. Hench, Optimising bioactive glass scaffolds for bone tissue engineering, Biomaterials 27 (2006) 964–973.

[42] K.F. Leong, C.M. Cheah, C.K. Chua, Solid free form fabrication of three-dimensional scaffolds for engineering replacement tissues and organs, Biomaterials 24 (2003) 2363–2378.

[43] T. Albrektsson, C. Johansson, Osteoinduction, osteoconduction and osseointegration, European Spine Journal 10 (2001) S96–S101.

[44] M. Bonher, Calcium orthophosphates in medicine: from ceramics to calcium phosphate cements, Injury 31:4 (2000) 37–47.

[45] J.O. Hollinger, J. Brekke, E. Gruskin, D. Lee, Role of bone substitutes, Clin Orthop Relat Res 324 (1996) 55–65.

[46] C.P. Klein, J.M. de Blieck-Hogervorst, J.G. Wolke, K. de Groot, Studies of the solubility of different calcium phosphate ceramic particles in vitro, Biomaterials 11 (1990) 509–512.

[47] P. Ducheyne, S. Radin, L. King, The effect of calcium phosphate ceramic composition and structure on in vitro behavior I. Dissolution, J Biomed Mater Res 27 (1993) 25–34.

[48] L.C. Bell, H. Mika, B.J. Kruger, Synthetic hydroxyapatite-solubility product and stoichiometry of dissolution, Arch Oral Biol 23 (1978) 329–336.

[49] K. Ogata, S. Imazato, A. Ehara, S. Ebisu, Y. Kinomoto, T. Nakano, Y. Umakoshi, Comparison of osteoblast responses to hydroxyapatite and hydroxyapatite/soluble calcium phosphate composites, J Biomed Mater Res A 72 (2005) 127–135.

[50] E. Boanini, M. Gazzano, A. Bigi, Ionic substitutions in calcium phosphates synthesized at low temperature, Acta Biomaterialia 6:6 (2010) 1882–1894.

[51] C. Elliott, Structure and chemistry of the apatites and other calcium orthophosphates, Elsevier, Amsterdam (1994).

[52] J. Terra, E.R. Dourado, J.G. Eon, D.E. Ellis, G. Gonzalez, A. Malta Rossi, The structure of strontium-doped hydroxyapatite: an experimental and theoretical study, Phys Chem Chem Phys 11 (2009) 568–577.

[53] S. Kannan, F. Goetz-Neunhoeffer, J. Neubauer, J.M.F. Ferreira, Ionic Substitutions in Biphasic Hydroxyapatite and β-Tricalcium Phosphate Mixtures: Structural Analysis by Rietveld Refinement, J Am Ceram Soc 91 (1) (2008) 1–12.

[54] S.V. Dorozhkin, M. Epple, Biological and medical significance of calcium phosphates, Angew Chem Int Ed 41 (2002) 3130–3146.

[55] I.R. Gibson, I. Rehman, S.M. Best, W. Bonfield, Characterization of the transformation from calcium-deficient apatite to β-tricalcium phosphate, J Mater Sci Mater Med 12 (2000) 799–804.

[56] E. Fernandez, F.J. Gil, M.P. Ginebra, F.C.M. Driessens, J.A. Planell, S.M. Best, Calcium phosphate bone cements for clinical applications—Part I: solution chemistry, Mater Sci-Mater M 10 (1999) 169–176.

[57] D. Tadic, F. Beckmannb, K. Schwarz, M. Epple, A novel method to produce hydroxyapatite objects with interconnecting porosity that avoids sintering, Biomaterials 25 (2004) 3335–3340.

[58] M. Bohner, J. Lemaitre, Can bioactivity be tested in vitro with SBF solution?, Biomaterials 30 (2009) 2175–2179.

[59] J. Franco, P. Hunger, M.E. Launey, A.P. Tomsia, E. Saiz, Direct write assembly of calcium phosphate scaffolds using a water-based hydrogel, Acta Biomaterialia 6 (2010) 218–228.

[60] S. Kannan, J.M.G. Ventura, A.F. Lemos, A. Barba, J.M.F. Ferreira, Effects of sodium addition on the precipitation of hydroxyapatites and biphasic ceramics, Ceram Int 34 (2008) 7–13.

[61] G. Daculsi, Biphasic calcium phosphate concept applied to artificial bone, implant coating and injectable bone substitute, Biomaterials 19 (1998) 1473–1478.

[62] O. Gauthier, J.M. Bouler, E. Aguado, R.Z. LeGeros, P. Pilet, G. Daculsi, Elaboration conditions influence physicochemical properties and in vivo bioactivity of macroporous biphasic calcium phosphate ceramics, J Mater Sci Mater Med 10(4) (1999) 199–204.

[63] R.Z. LeGeros, S. Lin, R. Rohanizadeh, D. Mijares, J.P. LeGeros, Biphasic calcium phosphate bioceramics: Preparation, properties and applications, J Mater Sci Mater Med 14 (2003) 201–209.

[64] S. Bose, G. Fielding, S. Tarafder, A. Bandyopadhyay, Understanding of dopant-induced osteogenesis and angiogenesis in calcium phosphate ceramics, Trends in Biotechnology 31 (10) (2013) 594–605.

[65] A.D. Pye, D.E.A. Lockhart, M.P. Dawson, C.A. Murray, A.J. Smith, A review of dental implants and infection, Journal of Hospital Infection 72 (2009) 104–110.

[66] W.T.M. Jansen, J.T. van der Bruggen, J. Verhoef, A.C. Fluit, Bacterial resistance: a sensitive issue: complexity of the challenge and containment strategy in Europe, Drug Resistance Updates 9 (2006) 123–133.

[67] L. Crémet, S. Corvec, P. Bémer, L. Bret, C. Lebrun, B. Lesimple, A-F. Miegeville, A. Reynaud, D. Lepelletier, N. Caroff, Orthopaedic-implant infections by Escherichia coli: molecular and phenotypic analysis of the causative strains, Journal of Infection 64 (2012) 169–175.

[68] F. Jenny, Fighting bacterial infections—future treatment options, Drug Resistance Updates 14 (2011) 125–139.

[69] A.D. Khosravi, F. Ahmadi, S. Salmanzadeh, A. Dashtbozorg, E. Abasi Montazeri, Study of Bacteria Isolated from Orthopedic Implant Infections and their Antimicrobial Susceptibility Pattern, Res J Microbiol 4 (2009) 158–163.

[70] W. Harris, C.B. Sledge, Total hip and total knee replacement (Part II), N Engl J Med 323(1990) 801–807.

[71] S. Nasser, Prevention and treatment of sepsis in total hip replacement surgery, Orthop. Clin. North Am. 23 (1992) 265–277.

[72] F. Bir, H. Khireddine, A. Touati, D. Sidane, S. Yala, H. Oudadesse, Electrochemical depositions of fluorohydroxyapatite doped by Cu^{2+}, Zn^{2+}, Ag^{+} on stainless steel substrates, Applied Surface Science, 258 (2012) 7021–7030.

[73] S. Saidin, P. Chevallier, M. R. Abdul Kadir, H. Hermawan, D. Mantovani, Polydopamine as an intermediate layer for silver and hydroxyapatite immobilisation on metallic biomaterials surface, Materials Science and Engineering C 33:8 (2013) 4715–4724.

[74] G. Borkow, J. Gabbay, Copper as a biocidal tool, Curr Med Chem 12 (2005) 2163–2175.

[75] B. Sugarman, Zinc and infection, Rev Infect Dis 5 (1983) 137–147.

[76] S. Atmaca, K. Gül, R. Çiçek, The effect of zinc on microbial growth, Turk J Med Sci 28 (1998) 595–597.

[77] T.N. Phan, T. Bucker, J. Sheng, J.D. Baldeck, R.E. Marquis, Physiologic actions of cinc related to inhibition of acid and alkali production by orl streptococci in suspensions and biofilms, Oral Microbiol Immun 19 (2004) 31–38.

[78] B.R. Stern, Essentiality and toxicity in copper health risk assessment: overview, update and regulatory considerations, J Toxicol Environ Health A 73 (2010) 114–127.

[79] M. Hunt, Copper and boron as examples of dietary trace elements important inbone development and disease, Curr Opin Orthop 9 (1998) 28–36.

[80] W. Opsahl, H. Zeronian, M. Ellison, D. Lewis, R.B. Rucker, R.S. Riggins, Role of copper in collagen cross-linking and its influence on selected mechanical properties of chick bone and tendon, J Nutr 112 (1982) 708–716.

[81] N.M. Lowe, W.D. Fraser, M.J. Jackson, Is there a potential therapeutic value of copper and zinc for osteoporosis?, Proc Nutr Soc 61 (2002) 181–185.

[82] R. Barbucci, S. Lamponi, A. Magnani, F.M. Piras, A. Rossi, E. Weber. Role of the Hyal-Cu (II) complex on bovine aortic and lymphatic endothelial cells behavior on microstructured surfaces, Biomacromolecules 6 (2005) 212–219.

[83] C. Wu, Y. Zhou, M. Xu, P. Han, L. Chen, J. Chang, Y. Xiao, Copper-containing mesoporous bioactive glass scaffolds with multifunctional properties of angiogenesis capacity, osteostimulation and antibacterial activity, Biomaterials 34 (2013) 422–433.

[84] L.C. Ann, S. Mahmud, S.K.M. Bakhori. Electron spectroscopy imaging and surface defect configuration of zinc oxide nanostructures under different annealing ambient. Surface Science 265 (2013) 137–144.

[85] E.S. Thian, T. Konishi, Y. Kawanobe, P.N. Lim, C. Choong, B. Ho, M. Aizawa, Zinc-substituted hydroxyapatite: a biomaterial with enhanced bioactivity and antibacterial properties, Journal of Materials Science: Materials in Medicine 24 (2013) 437–445.

[86] M. Yamaguchi, H. Oishi, Y. Suketa, Stimulatory effect of zinc on bone-formation in tissue-culture, Biochem Pharmacol 36 (22) (1987) 4007–4012.

[87] M. Yamaguchi, R. Yamaguchi, Action of zinc on bone metabolism in rats – increases in alkaline-phosphatase activity and DNA content, Biochem Pharmacol 35 (5) (1986) 773–777.

[88] X. Li, Y. Sogo, A. Ito, H. Mutsuzaki, N. Ochiai, T. Kobayashi, S. Nakamura, K. Yamashita, R.Z. LeGeros, The optimum zinc content in set calcium phosphate cement for promoting bone formation in vivo, Mater Sci and Eng C 29 (2009) 969–975.

[89] M. Otsuka, S. Marunaka, Y. Matsuda, A. Ito, P. Layrolle, H. Naito, N. Ichinose, Calcium level-responsive in vitro zinc release from zinc containing tricalcium phosphate (ZnTCP), J Biomed Mater Res 52 (2000) 819–824.

[90] A. Ito, H. Kawamurab, M. Otsukac, M. Ikeuchia, H. Ohgushia, K. Ishikawad, K. Onumaa, N. Kanzakia, Y. Sogoa, N. Ichinosee**,** Zinc-releasing calcium phosphate for stimulating bone formation, Mater Sci Eng C 22 (2002) 21–25.

[91] S. Pina, S.I. Vieira, P. Rego, P.M.C. Torres, O.A.B. da Cruz e Silva, Cruz e Silva EF, J.M.F. Ferreira, Biological responses of brushite-forming Zn- and ZnSr-substituted β-tricalcium phosphate bone cements, eCM 20 (2010) 162–177.

[92] S.G. Dahl, P. Allain, P.J. Marie, Y. Mauras, G. Boivin, P. Ammann, Y. Tsouderos, P.D. Delmas, C. Christiansen, Incorporation and distribution of strontium in bone, Bone, 28 (2001), 446–453.

[93] S.P. Nielsen. The biological role of strontium, Bone 35 (2004) 583–588.

[94] E. Shorr, A.C. Carter, The usefulness of strontium as an adjuvant to calcium in the remineralization of the skeleton in man, Bull Hosp Jt Dis Orthop Inst 13 (1952) 59–66.

[95] P.J. Meunier, C. Roux, E. Seeman, S. Ortolani, J.E. Badurski, T.D. Spector, J. Cannata, A. Balogh, E.M. Lemmel, S. Pors-Nielsen, R. Rizzoli, H.K. Genant, J.Y.

Reginster, The effects of strontium ranelate on the risk of vertebral fracture in women with postmenopausal osteoporosis, N Engl J Med 350 (2004) 459–468.

[96] E. Landi, A. Tampieri, G. Celotti, S. Sprio, M. Sandri, G. Logroscino, Sr-substituted hydroxyapatites for osteoporotic bone replacement, Acta Biomater 3 (2007) 961–969.

[97] S. Panzavolta, P. Torricelli, L. Sturba, B. Bracci, R. Giardino, A. Bigi, Setting properties and in vitro bioactivity of strontium enriched gelatin-calcium phosphate bone cements, J Biomed Mater Res A 84 (2008) 965–972.

[98] C.F. Marques, A. Lemos, S.I. Vieira, O.A.B. da Cruz e Silva, A. Bettencourt, J.M.F. Ferreira, Antibiotic-loaded Sr-doped porous calcium phosphate granules as multifunctional bone grafts, Ceramics International 42 (2) Part A (2016) 2706–2716.

[99] R.Z. LeGeros, Calcium Phosphates in Oral Biology and Medicine, Monogr Oral Sci 15 (1991) 1–201.

[100] F. Ren, Y. Leng, R. Xin, Synthesis, characterization and ab initio simulation of magnesium-substituted hydroxyapatite, Acta Biomater 6 (2010) 2787–2796.

[101] I.R. Gibson, W. Bonfield, Preparation and characterization of magnesium/carbonate co-substituted hydroxyapatites, J Mat Sci: Mater Med 13 (2002) 685–693.

[102] S. Bose, S. Tarafder, S.S. Banerjee, N.M. Davies, A. Bandyopadhyay, Understanding *in vivo* response and mechanical property variation in MgO, SrO and SiO_2 doped β-TCP, Bone 48 (2011) 1282–1290.

[103] M. Roy, G.A. Fielding, A. Bandyopadhyay, S. Bose, Effects of zinc and strontium substitution in tricalcium phosphate on osteoclast differentiation and resorption, Biomater Sci 1 (2012) 74–82.

[104] S. Tarafder, N.M Davies, A. Bandyopadhyay, S. Bose, 3D printed tricalcium phosphate bone tissue engineering scaffolds: effect of SrO and MgO doping on *in vivo* osteogenesis in a rat distal femoral defect model, Biomater Sci 1 (2013) 1250–1259.

[105] V. Stanić, S. Dimitrijević, J. Antić-Stanković, M. Mitrić, B. Jokić, I.B. Plećaš, S. Raičević, Synthesis, characterization and antimicrobial activity of copper and zinc-doped hydroxyapatite nanopowders, Applied Surface Science 256 (2010) 6083–6089.

[106] X. Chen, Q-L. Tang, Y-J. Zhu, C-L. Zhu, X-P. Feng, Synthesis and antibacterial property of zinc loaded hydroxyapatite nanorods, Materials Letters 89 (2012) 233–235.

[107] R-J. Chung, M-F. Hsieh, K-C. Huang, L-H. Perng, F-I. Chou, T-S. Chin, Anti-microbial hydroxyapatite particles synthesized by a sol–gel route, Journal of Sol–Gel Science and Technology 33 (2005) 229–239.

[108] S. Bose, G. Fielding, S. Tarafder, A. Bandyopadhyay, Understanding of dopant-induced osteogenesis and angiogenesis in calcium phosphate ceramics, Trends in Biotechnology 31(10) (2013) 594–605.

[109] D.W. Hutmacher, Scaffolds in tissue engineering bone and cartilage, Biomaterials 21 (2000) 2529–2543.

[110] S.J. Hollister, Porous scaffold design for tissue engineering, Nature Materials 4 (2005) 518–524.

[111] D.F. Williams, On the mechanisms of biocompatibility, Biomaterials 29 (2008) 2941–2953.

[112] M.J. Olszta, X.G. Cheng, S.S. Jee, B.R. Kumar, Y.Y. Kim, M.J. Kaufman, E.P. Douglas, L.B. Gower, Bone structure and formation: A new perspective, Mater. Sci. Eng. R: Rep. 58 (2007) 77–116.

[113] J. Li, J. Hong, Q. Zheng, X. Guo, S. Lan, F. Cui, H. Pan, Z. Zou, C. Chen, Repair of rat cranial bone defects with nHAC/PLLA and BMP-2-related peptide or rhBMP-2, J. Orthop. Res 29 (2011) 1745–1752.

[114] C.M. Murphy, M.G. Haugh, F.J. O'Brien, The effect of mean pore size on cell attachment, proliferation and migration in collagen–glycosaminoglycan scaffolds for bone tissue engineering, Biomaterials 31 (2010) 461–466.

[115] J.R. Woodard, A.J. Hilldore, S.K. Lan, C.J. Park, A.W. Morgan, J.A. Eurell, S.G. Clark, M.B. Wheeler, R.D. Jamison, A.J. Wagoner Johnson, The mechanical properties and osteoconductivity of hydroxyapatite bone scaffolds with multi-scale porosity, Biomaterials 28 (2007) 45–54.

[116] M.N. Rahaman, D.E. Day, B.S. Bal, Q. Fu, S.B. Jung, L.F. Bonewald, A.P. Tomsia, Bioactive glass in tissue engineering, Acta Biomaterialia 7 (2011) 2355–2373.

[117] E. Sachlos, J. T. Czernuszka, Making tissue engineering scaffold work. Review on the application of solid freeform fabrication technology to the production of tissue engineering scaffolds, European Cells and Materials 5 (2003) 29–40.

[118] E.L.W. de Mulder, P. Buma, G. Hannink, Anisotropic porous biodegradable scaffolds for musculoskeletal tissue engineering, Materials 2 (2009) 1674–1696.

[119] D.W. Hutmacher, Scaffold designed fabrication technologies for engineering tissues-state of art and future perspectives, J Biomaterials Science, Polymer Edition 12(1) (2001) 107–124.

[120] Y.-J. Seol, T.-Y. Kang, D.-W. Cho, Solid freeform fabrication technology applied to tissue engineering with various biomaterials, The Royal Society of Chemistry, Soft matter 8 (2012) 1730–1735.

[121] M. Vaezi, H. Seitz, S. Yang, A review on 3D micro-additive manufacturing technologies, Int J Adv Manuf Technol 67 (2013) 1721–1754.

[122] A. Bandyopadhyay, S. Bose, Additive Manufacturing - 1st Edition (2016) by Taylor & Francis Group, LLC.

[123] E.M. Sachs, J.S. Haggerty, M.J. Cima, P.A. Williams, Three-dimensional printing techniques, US Patent # 5204055 A (1993).

[124] P.H. Warnke, H. Seitz, F. Warnke, S.T. Becker, S. Sivananthan, E. Sherry, Q. Liu, J. Wiltfang, T. Douglas, Ceramic scaffolds produced by computer-assisted 3D printing and sintering: characterization and biocompatibility investigations, J Biomed Mater Res B Appl Biomater 93 (2010) 212–217.

[125] J.W. Lee, J.Y. Kim, D.W. Cho, Solid free-formfabrication technology and its application to bone tissue engineering, Int J Stem Cells 3 (2010) 85–95.

[126] H. Seitz, W. Rieder, S. Irsen, B. Leukers, C. Tille, Three-dimensional printing of porous ceramic scaffolds for bone tissue engineering, J Biomed Mater Res B Appl Biomater 74 (2005) 782–788.

[127] G. Brunello, S. Sivolella, R. Meneghello, L. Ferroni, C. Gardin, A. Piattelli, B. Zavan, E. Bressan, Powder-based 3D printing for bone tissue engineering, Biotechnology Advances 34 (2016) 740 –753.

[128] S. Bose, S. Vahabzadeh, A. Bandyopadhyay, Bone tissue engineering using 3D

printing, Metrials Today 16(12) (2013) 496–504.

[129] H. Kodama, Automatic method for fabricating a three-dimensionalplastic model with photo-hardening polymer, Rev Sci Instrum 52 (1981) 1770–1773.

[130] T. Nakai, Y. Marutani, Shaping 3-D solid objects using a UV laser and photopolymer, Conference on Lasers and Electro-Optics. Optical Society of America, p. ME2 (1986).

[131] P.J. Bartolo, H.A. Almeida, R.A. Rezende, T. Laoui, B. Bidanda (2008). Advanced processes to fabricate scaffolds for tissue engineering. In: Bidanda B, Bartolo PJ (eds) Virtual prototyping of biomanufacturing in medical application. Springer, New York, 149–170.

[132] F.P.W. Melchels, J. Feijen, D.W. Grijpma, A poly(D, L-lactide) resin for the preparation of tissue engineering scaffolds by stereolithography, Biomaterials 30 (2009) 3801–3809.

[133] J.R. Meakin, D.E. Shepherd, D.W. Hukins, Short communication: fused deposition models from CT scans, Br J Radiol 77 (2004) 504–507.

[134] J. Korpela, A. Kokkari, H. Korhonen, M. Malin, T. Närhi, J. Seppälä, Biodegradable and bioactive porous scaffold structures prepared using fused deposition modelling, J Biomed Mater Res B Appl Biomater 101 (2013) 610–619.

[135] I. Zein, D.W. Hutmacher, K.C. Tan, S. H. Teoh, Fused deposition modeling of novel scaffold architectures for tissue engineering applications, Biomaterials 23 (2002) 1169–1185.

[136] Y. Zhou, D.W. Hutmacher, S.-L. Varawan, T.M. Lim, In vitro bone engineering based on polycaprolactone and polycaprolactone– tricalcium phosphate composites, Polym Int 56 (2007) 333–342.

[137] H.N. Chia, B.M. Wu, Recent advances in 3D printing of biomaterials, J Biol Eng 9 (2015) 1–14.

[138] B. Duan, M. Wang, Encapsulation and release of biomolecules from CaP/PHBV nanocomposite microspheres and three-dimensional scaffolds fabricated by selective laser sintering, Polym Degrad Stab 95 (2010) 1655–1664.

[139] J. III Cesarano, P.D. Calvert, Freeforming objects with lowbinder slurry, US Pat

6027326 (2000).

[140] J. III Cesarano, R. Segalman, P.D. Calvert, Robocasting provides moldless fabrication from slurry deposition, Ceram Ind 148 (1998) 94–102.

[141] J.N. Stuecker, J. III Cesarano, D.A. Hirschfeld, Control of the viscous behavior of highly concentrated mullite suspensions for robocasting, J Mater Process Technol 142 (2003) 318–325.

[142] J.N. Stuecker, J.E. Miller, R.E. Ferrizz, J.E. Mudd, J. Cesarano, Advanced support structures for enhanced catalytic activity, Ind Eng Chem Res 43 (2004) 51–55.

[143] J.E. Smay, J. Cesarano, B.A. Tuttle, J.A. Lewis, Directed colloidalassembly of linear and annular lead zirconate titanate arrays, J Am Ceram Soc 87 (2004) 293–295.

[144] B.A. Tuttle, J.E. Smay, J. III Cesarano, J.A. Voight, T.W. Scofield, W.R. Olson, J.A. Lewis, Robocast Pb $(Zr_{0.95}Ti_{0.05})O_3$ ceramic monoliths and composites, J Am Ceram Soc 84 (2001) 872–874.

[145] J.E. Smay, G.E. Gratson, R.F. Shepherd, J. III Cesarano, J.A. Lewis, Directed colloidal assembly of 3D periodic structures. Adv Mater 14 (2002) 1279–1283.

[146] J.E. Smay, J. III Cesarano, J.A. Lewis, Colloidal inks for directed assembly of 3-D periodic structures, Langmuir 18 (2002) 5429–5437.

[147] J. Cesarano, Recent developments in robocasting of ceramics and multimaterial deposition, Solid Free Fabr Proc, Austin, TX, (1998) 697–703.

[148] J. Russias, E. Saiz, S. Deville, K. Gryn, G. Liu, R.K. Nalla, A.P Tomsia, Fabrication and in vitro characterization of three-dimensional organic/inorganic scaffolds by robocasting, J Biomed Mater Res A 83A (2007) 434–445.

[149] P. Miranda, A. Pajares, E. Saiz, A.P. Tomsia, F. Guiberteau, Mechanical properties of calcium phosphate scaffolds fabricated by robocasting, J Biomed Mater Res A 85A (2008) 218–27.

[150] F.J. Martínez-Vázquez, F.H. Perera, I. van der Meulen, A. Heise, A. Pajares, P. Miranda, Impregnation of β-tricalcium phosphate robocast scaffolds by in situ Polymerization, Journal of Biomedical Materials Research A 101A (11) (2013) 3086–3096.

[151] J.N. Stuecker, Freeform fabrication and near net shape processing of composites from Mullite and Kaolin Ceramics, Master's Thesis. NM: New Mexico Institute of Mining and Technology; 1999.

[152] J.A. Lewis, Direct-write assembly of ceramics from colloidal inks, Current Opinion in Solid State and Materials Science 6 (2002) 245–250.

[153] J.J.Guo, J.A. Lewis, Aggregation effects on the compressive flow properties and drying behavior of colloidal silica suspension, J Am Ceram Soc 82 (1999) 2345–2358.

[154] D.J. Shanefield, Organic additives and ceramic processing (2nd ed), Kluwer Academic Publishers, Boston (1996).

[155] D.R. Dinger, J.E. Funk, Particle-packing phenomena and their application in materials processing, Mater Res Soc Bull (1997)19–23.

[156] P. Miranda, E. Saiz, K. Gryn, A.P. Tomsia, Sintering and robocasting of β-tricalcium phosphate scaffolds for orthopaedic applications, Acta Biomater 2 (2006) 457–66.

[157] D.J. Hoelzle, A.G. Alleyne, A.J.W. Johnson, Micro-robotic deposition guidelines by a design of experiments approach to maximize fabrication reliability for the bone scaffold application, Acta Biomater 4 (2008) 897–912.

[158] F.J. Martínez-Vázquez, F.H. Perera, P. Miranda, A. Pajares, F. Guiberteau, Improving the compressive strength of bioceramic robocast scaffolds by polymer infiltration, Acta Biomater 6 (2010) 4361–4368.

[159] F.F. Lange, Sinterability of agglomerated powders, J Am Ceram Soc 67 (1984) 83–89.

[160] J. Zheng, J.S. Reed, The different roles of forming and sintering on densification of powder compacts, Am Ceram Soc Bull 71 (1992) 1410–1416.

[161] W.D. Kingery, Francois B, The sintering of crystalline oxides. I. Interactions between grain boundaries and pores, In: Kuczynske GC, Hooton NA, Gibbon GF, editors. Sintering and Related Phenomena. New York: Gordon and Breach; 1967. 471–498.

[162] G. Heimke, P. Griss, Tissue interactions to bone replacement materials. In: de

Groot K, editor, Bioceramics of Calcium Phosphate. Boca Raton, FL: CRC Press; 1983, 79–97.

[163] B. Flautre, M. Descamps, C. Delecourt, M. Blary, P. Hardouin, Porous HA ceramic for bone replacement: Role of the pores and interconnections—Experimental study in the rabbit, J Mater Sci Mater Med 12 (2001) 679–682.

[164] V. Karageorgiou, D. Kaplan, Porosity of 3D biornaterial scaffolds and osteogenesis, Biomaterials 26 (2005) 5474–5491.

[165] H. Cheung, K. Lau, T. Lu, D. Hui, A critical review on polymer-based bio-engineered materials for scaffold development. Compos Part B Eng 38 (2007) 291–300.

[166] K.A. al Ruhaimi, Bone graft substitutes: A comparative qualitative histologic review of current osteoconductive grafting materials, Int J Oral Maxillofac Implant 16 (2001) 105–114.

[167] A. Uchida, A. Nade, E. McCartney, W. Ching, The use of ceramics for bone-replacement—A comparative-study of 3 different porous ceramics, J Bone Jt Surg Br 66 (1984) 269–275.

[168] N. Tamai, A. Myoui, T. Tomita, T. Nakase, J. Tanaka, T. Ochi, H. Yoshikawa, Novel hydroxyapatite ceramics with an interconnective porous structure exhibit superior osteoconduction *in vivo*, J Biomed Mater Res 59 (2002) 110–117.

[169] E. Saiz, L. Gremillard, G. Menendez, P. Miranda, K. Gryn, A.P. Tomsia, Preparation of porous hydroxyapatite scaffolds, Materials Science and Engineering: C 27 (3) (2007) 546–550.

[170] J.G. Dellinger, J. III Cesarano, R.D. Jamison, Robotic deposition of model hydroxyapatite scaffolds with multi architectures and multiscale porosity for bone tissue engineering. J Biomed Mater Res 82A (2006) 383–394.

[171] S.-J. Heo, S.-E. Kim, J. Wei, Y.-T. Hyun, H.-S. Yun, D.-H. Kim, J.W. Shin, J.-W. Shin, Fabrication and characterization of novel nanoand micro-HA/PCL composite scaffolds using a modified rapid prototyping process, J Biomed Mater Res 89A (2009) 108–116

[172] F.J. Martínez-Vázquez, M.V. Cabañas, J.L. Paris, D. Lozano, M. Vallet-Regí, Fabrication of novel Si-doped hydroxyapatite/gelatine scaffolds by rapid prototyping for drug delivery and bone regeneration, Acta Biomaterialia 15 (2015) 200–209.

Chapter 2

INSIGHTS ON THE PROPERTIES OF LEVOFLOXACIN-ADSORBED Sr- AND Mg-DOPED CALCIUM PHOSPHATE POWDERS

Catarina F. Marques[1], Ana C. Matos[2], Isabel A. C. Ribeiro [2], Lídia M. Gonçalves[2], Ana Bettencourt[2], José M. F. Ferreira[1]

[1] Department of Materials and Ceramics Engineering, CICECO, University of Aveiro, 3810-193 Aveiro, Portugal.

[2] Research Institute for Medicines (iMed.ULisboa), Faculty of Pharmacy, University of Lisbon, Av. Prof. Gama Pinto, 1649-003 Lisbon, Portugal.

Journal of Materials Science: Materials in Medicine (2016) 27:123.

Abstract

Several types of biodegradable materials have been investigated for the treatment of osteomyelitis. Calcium phosphate (CaP) ceramics are among the most performing materials due to their resemblance to human hard tissues in terms of mineralogical composition, and proven ability to adsorb and deliver a number of drugs. This research work was intended to study the suitability of modified calcium phosphate powders loaded with a fluoroquinolone as drug delivery systems for osteomyelitis treatment. Levofloxacin (LEV) was chosen due to the well-recognized anti-staphylococcal activity and adequate penetration into osteoarticular tissues. Substituted calcium phosphate powders (5 mol% Sr^{2+} or 5 mol% Mg^{2+}) were synthesised through aqueous precipitation. The obtained powders were characterised by X-ray diffraction, SEM and FTIR analysis. The X-ray diffraction patterns confirmed the presence of HA and β-tricalcium phosphates (β-TCP) phases in doped compositions, especially in the case of Mg-doped system. The fixation of LEV at the surface of the particles occurred only by physisorption. Both the *in vitro* microbiological susceptibility, against *Staphylococcus spp,* and biocompatibility of LEV-loaded CaP powders have not been compromised.

Keywords: osteomyelitis, calcium phosphate, fluoroquinolone, drug delivery

1. Introduction

Osteomyelitis is a difficult-to-treat progressive infection of the bone, caused by bacteria or sometimes by fungus, characterized by bone destruction, bone necrosis, and may progress to a chronic and persistent state [1,2]. The traditional treatment of chronic osteomyelitis involves operative debridement of the dead infected tissue, obliteration of dead space, osseous repair, adequate soft tissue coverage and long-term systemic antibiotic therapy [3]. However, the inability to maintain high antibiotic concentrations at the site of infection for an extended period of time is considered as the major reason for failure in the treatment of this disease [4,5]. Thus, it has been recognized that antibiotic local delivery offers several advantages compared to oral or systemic treatment, including higher concentrations of drug at the target site while avoiding systemic toxicity [6]. Antibiotic-impregnated implants are particularly attractive because they not only deliver high levels of drug but also help to obliterate the dead space that follows bone debridement [7, 8].

Polymethylmethacrylate (PMMA) beads loaded with gentamicin are the most widely studied material for osteomyelitis treatment. But the surgical removal of the beads after antibiotic release is a drawback [9,10]. Coping with this limitation, a number of recent research works focused on biodegradable bone filler systems for local delivery of antibiotics [8, 11-13]. Besides not requiring surgical removal, such systems also act as guides for bone repair as the implant is gradually resorbed and replaced by the newly formed bone.

Antibiotic-loaded resorbable CaP ceramics have been suggested as potential materials for the treatment of osteomyelitis [14-16]. HA deserved a particular attention because of its chemical and structural similarities with the inorganic phase of human bone and its biocompatibility, osteoconductive and osteophilic nature [17,18]. Moreover, the crystalline lattice of HA is able to easily incorporate foreign substituting ions that enhance osteointegration and mechanical properties of the grafts [19-23]. Magnesium (Mg^{2+}) has been often associated with the mineralization of calcified tissues and indirectly influences mineral metabolism [24,25]. Its ability to stimulate the formation of biphasic HA-TCP mixtures upon heating [26] by enhancing the thermal stability of TCP is an added benefit from Mg-doping HA, making the resulting bone grafts more biodegradable. Strontium (Sr^{2+}) is another interesting doping ion since it increases

osteoclast apoptosis and enhances preosteoblastic cell proliferation and collagen synthesis, with consequent depression in bone resorption and maintained bone formation [23].

Considering the importance of LEV in osteomyelitis treatment due to its broad antibacterial spectrum and excellent bone penetration properties [27,28], the present aims at studying the adsorption and release kinetics of this drug by CaP powders doped with Mg^{2+} and Sr^{2+}. The interactions between levofloxacin and CaP powders were studied by X-ray diffraction and FTIR spectroscopy. The adsorption efficiency of LEV and its *in vitro* releasing kinetics from the different doped powders were determined by high-performance liquid chromatography-UV **(**HPLC-UV). The LEV minimum inhibitory concentration (MIC) from different powders was evaluated for *Staphylococcus aureus*, *Staphylococcus epidermidis* and *Escherichia coli* cultures. The *in vitro* biocompatibility was evaluated using MG63 and L929 cell lines.

2. Materials and Methods

2.1. Preparation of CaP powders

Powders of pure and HA-doped (with Mg^{2+} and Sr^{2+}) were synthesized via aqueous precipitation. Diammonium hydrogen phosphate [$(NH_4)_2HPO_4$, Quality Chemicals, Spain], calcium nitrate tetrahydrate [$Ca(NO_3)_2 \cdot 4H_2O$, Quality Chemicals, Spain], magnesium nitrate hexahydrate [$Mg(NO_3)_2 \cdot 6H_2O$, Sigma-Aldrich, Darmstadt, Germany] and strontium nitrate [$Sr(NO_3)_2$, Sigma-Aldrich, Darmstadt, Germany] were used as reagents. The concentrations of the starting precursor solutions were set in order to have total (Ca + M)/P molar ratio = 1.67 (M = Sr or Mg) for all the compositions, as reported in Table 1. For each composition, the $(NH_4)_2HPO_4$ solution was slowly added to the continuously stirred (1000 rpm) cationic solution and the pH of the system was then increased to 9 and maintained at this value by adding the required amounts of 8 M ammonium hydroxide [NH_4OH, Sigma-Aldrich, Darmstadt, Germany] solution. After the completion of addition, the reaction was performed at 90 ºC for 2 h under constant stirring conditions (1000 rpm). In parallel, a standard material of Ca/P molar ratio of 1.67 (pure HA) was also prepared under similar

conditions and used as control. After the completion of the reaction, the suspension was poured out from the reactor and the precipitate was separated through vacuum filtration and dried at 100 ºC overnight. The dried powders were calcined at 800 ºC temperature in a Thermolab furnace (Pt30%Rh/Pt6%Rh thermocouple) using a heating rate of 5 ºC·min^{-1} followed by a dwelling time of 1 h at that temperature, and then cooled to room temperature (RT). The calcined powders were then dry milled for 30 min in a high energetic ball milling up to achieving mean particle sizes <500 nm and labelled according to the compositions as HA, Sr-HA and Mg-HA.

Table 1. Planned concentrations of the Ca, P and Sr and Mg precursors used in the synthesis, and experimental compositions as determined from ICP analysis.

	Planned compositions							**Experimental compositions (from ICP analysis (± 0.02)**		
Sample Code	(Ca+M)/P molar ratio	Molar concentrations of the percursors				M (mol%)		(Ca+M)/P molar ratio	M (mol%)	
		Ca	P	Sr	Mg	Sr	Mg		Sr	Mg
[HA]	1.67	2	1.2	0	0	0	0	1.67	0	0
[Sr-HA]	1.67	1.9	1.2	0.1	0	5	0	1.66	5.04	0
[Mg-HA]	1.67	1.9	1.2	0	0.1	0	5	1.65	0	4.83

2.2. Calcium phosphate powders characterization

The characteristics of the CaP powders prior to LEV adsorption were assessed by different complementary techniques. Dynamic light scattering (DLS) (Zetasizer Nano ZS, Malvern Instruments, UK) was used to determine particle size. The specific surface area was measured through the gas adsorption BET method using a Micromeritis Gemini 2370 V5.00 (Norcross, USA) after degassing the powders in a Micromeritis Flow prep 060 (Norcross, USA). The morphological features were observed by scanning electronic microscopy (SEM – Hitachi SU-70, Hitachi High-Technologies Europe, GmbH, Germany) using 25 kV acceleration voltage and beam current of 10 μA. The mineral phases formed upon heat-treating at 800 ºC were

identified by X-ray diffraction using a High Resolution X-ray Diffractometer (PANalytical X'Pert PRO) with Cu Kα radiation (λ = 1.5406 Å) produced at 45 kV and 40 mA, which scanned the diffraction angles (2θ) between 20º and 80º with a step size of 0.01º, time per step 198,6450 s. Spectra-fitting software called HighScorePlus was utilised to quantify the percentages of crystalline phases for the calcined powders. This software requires crystallographic information files to fit and quantify each specific phase within a XRD spectrum. The database utilized was PDF-47 2015 RDB, and the files utilised in the evaluation of the powders were; HA (# 04-015-7245) [29], β–TCP (# 04-006-9376) [30].

Zeta-potential measurements (Malvern Zeta sizer, Nano ZS, Malvern, Worcestershire, UK) were performed before and after LEV adsorption at the surface of CaP powders heat treated at 800 ºC at several pH values. The aim was obtaining information about the effects of LEV adsorption on the solid/liquid interface. The powders were firstly dispersed ultrasonically, and allowed to stand for 30 min to let larger particles to settle. An aliquot taken from the supernatant was used to measure the zeta potentials. The pH of the suspensions was adjusted with 0.1 M HCl and 0.1 M NaOH. For comparison purposes, the measurements were also performed for solid LEV particles.

Elemental analyses for Ca, P and doped ions (Sr and Mg) were determined for all powders using inductively coupled plasma (ICP) spectrometry (ICP-OES Jobin Yvon Activa M., USA). For this purpose, nitric acid with double-distilled water was used to dissolve the powders prior to ICP analysis.

2.3. Drug loading, adsorption efficiency, *in vitro* release

2.3.1. Drug loading (DL) and adsorption efficiency (AE)

Aqueous LEV solutions were prepared in distilled water with suitable antibiotic concentrations (determined through preliminary tests) to allow the incorporation of an approximate amount of ~2.5 w% of drug into the powders. The impregnation process consisted in immersing 3 g of each kind of CaP powders into 5 mL solutions containing 400 mg of LEV, meaning a theoretical *DL* of 13.3 %. The mixtures were

kept under stirring in the absence of light for 24 h. The LEV-loaded CaP powders were then centrifuged, frozen at –80 ºC (Hettich, Germany) for 4 h, and freeze-dried at –51 ºC under a pressure of 1.5 Pa (Labconco, USA) for 48 h. According to the compositions, the LEV-loaded powders are hereafter labelled as LEV[HA], LEV[Sr-HA] and LEV[Mg-HA].

Drug loading efficiency (*DL,* or *AE*) was determined as the percentage of LEV incorporated relative to dry mass of CaP [($w_{LEV}/w_{particles}$)*100]. For this, 6.0 mg (±5 %) of each LEV-loaded powder was completely dissolved in 2 mL HCL (0.1 N). After adequate dilution, the drug content was determined by HPLC-UV (Shimadzu LC-6A and SPD-6A, Kyoto Japan), using an adjusted method described in literature [31]. Briefly, the chromatographic analysis was performed using a 125-4, 5 μm LiChrosphere® 100 RP-18 (Merck, Darmstadt, Germany) column, a degassed mobile phase of water:acetonitrile and triethylamine (85:15(*V/V)*; 0.6%(*V/V)*), and adjusted to pH 3 using ortho-phosphoric acid, a 1.2 mL·min^{-1} flow rate and UV detection at 294 nm (at 25 ºC). All chromatographic separations were carried out in triplicate for each independent batch.

2.3.2. Drug release studies

Levofloxacin release was determined after a previous dispersion of the different LEV[HA], LEV[Sr-HA] and LEV[Mg-HA] powders in the release medium during a predefined time period. Briefly, 6.0 mg (±5%) of particles were dispersed in propylene tubes containing 2 mL of a solution of NaCl 0.9%(*w*/*V*) with 0.05%(*V/V*) Tween20® (hereinafter release medium) in a shaking water-bath at 37 ºC. At pre-determined time points throughout a 1-week period (0 h, 0.5 h, 1 h, 2 h, 6 h, 24 h, 48 h and 168 h) samples were collected and analysed for LEV content by the HPLC-UV method as described earlier. Between collections, and throughout that release period, the withdrawn aliquots were replaced with equal volume of fresh release medium solution and sink conditions were guaranteed.

Furthermore, to determine the LEV kinetic mechanism of release of either LEV[Mg-HA] and LEV[Sr-HA], experimental data was fitted to a first order model equation

presented on Equation (1).

$$M_t = 1 - e^{-kt} \qquad \text{Eq. (1)}$$

where M_t denotes the fraction of drug released up to time t, and k is the constant of the mathematical model.

2.4. Antimicrobial susceptibility testing

The antimicrobial susceptibilities of selected strains to LEV standard solution and to 48 h release medium supernatants, were obtained by the Broth Microdilution Method described by the Clinical and Laboratory Standards Institute (CLSI) [32]. All assayed samples were two-fold diluted in Müeller-Hinton broth (Biokar Diagnostics, France) and final LEV concentration ranged from 2 μg·mL^{-1} to 0.015 μg·mL^{-1}. The medium supernatants recovered by centrifugation after 48 h of LEV release (LEV[HA], LEV[HA-Sr] and LEV[HA-Mg]), were also tested for antimicrobial susceptibility. *Staphylococcus aureus* (ATCC 25923), *Staphylococcus epidermidis* (ATCC 12228) and *Escherichia coli* (ATCC 25922) obtained from American Type Culture Collection (ATCC) were first cultured in Tryptic Soy Agar (TSA) (Liofilchem, Italy) and the inoculum was prepared according to CLSI (CLSI, 2012) in Müeller-Hinton broth. Minimum inhibitory concentration (MIC) results were obtained by measurement of absorbance at 595 nm in a spectrofluorometer (Anthos, Zenyth 3100) after 24 h of incubation at 37 ºC. All assays were performed with negative controls (not inoculated media) and positive controls (inoculated media). *E coli* ATCC®25922 was used as a quality control strain to guarantee that the test system performed as expected [34]. Assays were carried out in three independent experiments.

2.5. Cytotoxicity evaluation of the CaP powders

The cytotoxicity of the LEV loaded CaP powders was assessed using a general cell viability endpoint MTT (3-(4,5-dimethyl-2-thiazolyl)-2,5-diphenyl-2H-tetrazolium

bromide) [35, 36]. MTT is a yellow, water-soluble tetrazolium dye that is converted by viable cells to a water-insoluble, purple formazan. Two cell lines were chosen for cytotoxicity evaluation, L929 (Mouse fibroblast cell line, ATCC® CCL-1™) and MG63 (human osteoblast cell line, ATCC CRL-1427™).

Cell viability was assessed after 24 h of incubation of the two cell lines with a powders concentration at 300 $\mu g \cdot mL^{-1}$. The day before experiment, cells were seeded in sterile flat bottom 96 well tissue culture plates (Greiner, Germany), in RPMI 1640 culture medium, supplemented with 10% (*V/V*) fetal serum bovine, 100 $units \cdot mL^{-1}$ of penicillin G (sodium salt), 100 $\mu g \cdot mL^{-1}$ of streptomycin sulphate, and 2 mM L-glutamine, at a cell density of 2×10^5 $cells \cdot mL^{-1}$ (L929) and 1×10^5 $cells \cdot mL^{-1}$ (MG63) 100 µL per well. All the mentioned products were purchased from Life Technologies (UK). Cells were incubated at 37 ºC and 5% CO_2.

On the next day, culture medium was replaced by fresh medium containing the different samples to be analysed. Each sample was tested in six wells per plate. Culture medium was used as negative control and sodium dodecyl sulphate (SDS) at 1 $mg \cdot mL^{-1}$ as positive control. After 24 h the culture medium was removed and replaced by medium containing 0.5 $mg \cdot mL^{-1}$ of MTT. The cells were further incubated for 3 h. Medium was removed from the plates containing reduced MTT, and the intracellular formazan crystals were solubilized and extracted with 100 µL dimethylsulfoxide. After 15 min at room temperature the absorbance was measured at 570 nm in Microplate Reader (FLUOstar Omega, BMGLabtech, Germany).

The relative cell viability (%), compared to control cells, was calculated by $[Absorvance_{570\ nm}]_{sample}/[Absorvance_{570\ nm}]_{control}*100$.

Data was expressed as mean and standard deviation (mean ± SD) of six independent experiments (n=6). Statistical evaluation of data was performed using one-way analysis of variance (ANOVA). Tukey–Kramer multiple comparison test (GraphPad PRISM 5 software, USA), was used to compare the significance difference between groups, a $p < 0.05$ was accepted as significant.

3. Results

3.1. Characterisation of CaP powders

The morphological features of all CaP powders are shown in the SEM images of Figure 1. The powders consist of small and tightly agglomerated regular shaped particles. No significant morphological differences could be perceived among the three compositions. The physical properties of the calcined CaP powders, namely the specific surface area (SSA) and medium particle size (D_{50}), are presented in Table 2. The [Mg-HA] powder presents the smallest medium particle size (D_{50} = 281 nm) and the highest SSA (27.4 $m^2 \cdot g^{-1}$). The D_{50} and SSA values measured for [HA] and [Sr-HA] powders are not much dissimilar, with the last one being slightly coarser and consequently presenting the lowest SSA. From the nanometre size of the primary particles observed by SEM (Fig. 1) one can easily conclude that the D_{50} values measured by DLS analysis (Table 2) respect to clusters of CaP particles.

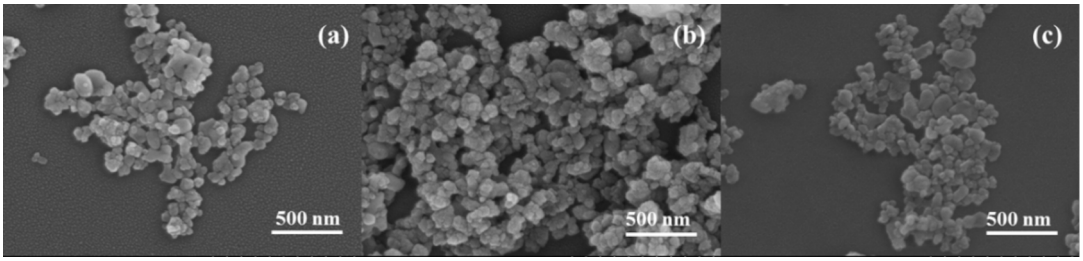

Fig. 1. SEM micrographs of CaP powders calcined at 800 ºC, (a) [HA], (b) [Mg-HA], (c) [Sr-HA].

Table 2. Physical properties, namely specific surface area and particle size, of [HA], [Mg-HA] and [Sr-HA]

CaP Powders	Specific Surface Area ($m^2 \cdot g^{-1}$)	Particle Size (D_{50}) (nm)
[HA]	20.4	320
[Mg-HA]	27.4	281
[Sr-HA]	19.7	325

Table 1 compares the planed compositions with the results of elemental ICP analysis performed to the synthesized powders. A fair agreement between the planned and the experimentally obtained values is observed.

The XRD patterns of the CaP powders calcined at 800 ºC (Fig. 2) reveal that they consist essentially of well-crystallized HA and β-TCP phases in different proportions. Pure HA phase (# 04-015-7245 [29]) was apparently formed in the stoichiometric [HA] composition, while the [Mg-HA] and [Sr-HA] compositions present both HA and β-TCP phases. The intensity of β-TCP peaks is higher in the case of [Mg-HA] in comparison to [Sr-HA] and appear slightly shifted to higher 2θ (smaller lattice parameters) relatively to the standard (# 04-006-9376) [30] card. The relative percentages of crystalline phases formed upon calcination were: 100% HA for [HA], 65% HA+ 35% β−TCP for [HA-Mg] and 92% HA+ 8% β−TCP for [HA-Sr]. Such crystalline phase assemblages can be understood considering that both doping elements are preferentially incorporated in the β−TCP lattice (especially Mg), enhancing its thermal stability [37].

Figure 3 compares the FTIR spectra of all the powders calcined at 800 ºC before and after LEV adsorption. The presence of vibrational modes of PO_4 groups at 475, 574, 609, 966 and 1020–1120 cm^{-1} and OH groups (630 and 3570 cm^{-1}) confirm the formation of an apatite phase in all the compositions [38], in good agreement with XRD results (Fig. 2). The intensity of the FTIR peaks relative to OH groups observed at 630 cm^{-1} (vibrational mode) and at 3570 cm^{-1} (stretching frequency) for the doped samples decreased in comparison to the stoichiometric HA (Fig. 3). The FTIR spectrum of LEV within 1100–1400 cm^{-1} exhibits some characteristic peaks, namely carbonyl C=O at 1724 cm^{-1}, aromatic C–H at 2935 cm^{-1}, O–H group of carboxyl group at 3265 cm^{-1}, C−N group at 1294 cm^{-1} due to stretching of amines and halogen group [39,40]. The presence of LEV in the LEV-adsorbed CaP powders is confirmed by the enhanced noisy appearance of the FTIR spectra between 1200 to 1600 cm^{-1}.

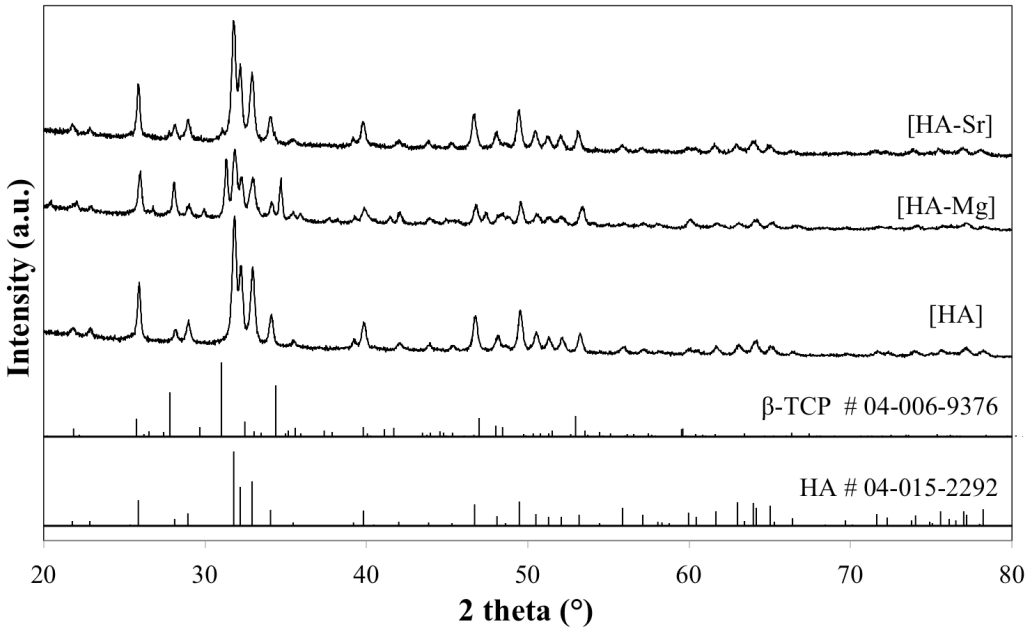

Fig. 2. XRD patterns of [HA], [Mg-HA] and [Sr-HA] calcined powders.

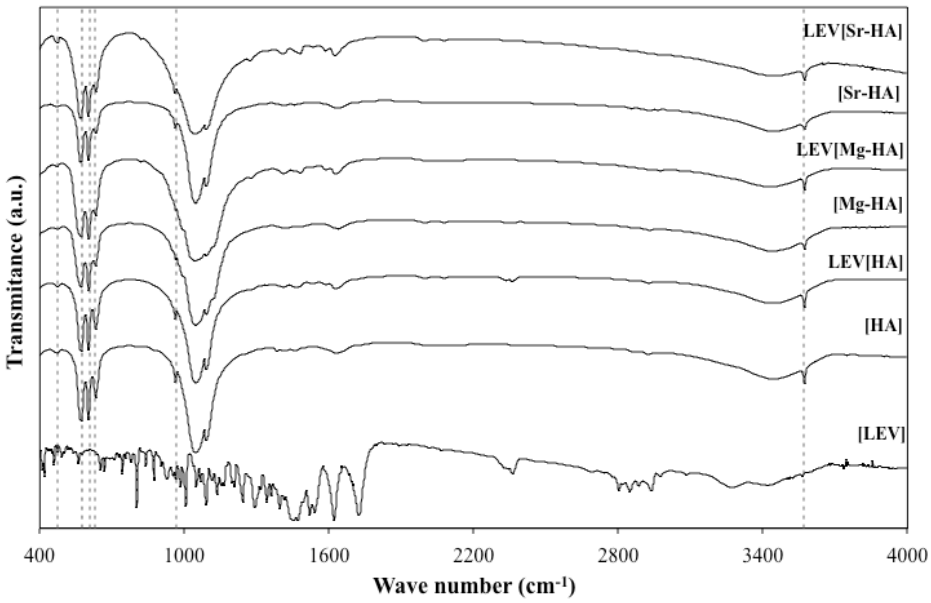

Fig. 3. FTIR spectra of [HA], [Mg-HA] and [Sr-HA] powders heat treated at 800 ºC before and after levofloxacin adsorption.

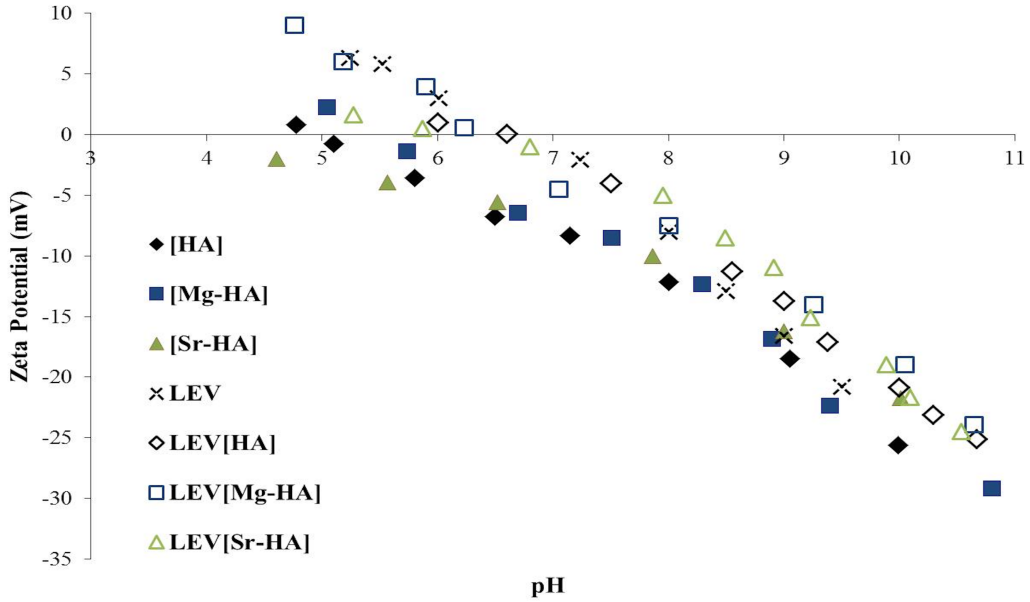

Fig. 4. Zeta potential of the [HA], [Mg-HA] and [Sr-HA] powders before (full bullets) and after levofloxacin adsorption (open bullets). The curve for LEV solid particles is also presented for comparison purposes.

The results of zeta potential (ZP) presented in Fig. 4 show that the apparent isoelectric points (IEPs) are roughly withing the pH gange of 4.8−6.8 and that the entire electrophoretic curves of LEV adsorbed samples appear slightly shifted towards the basic region and more positive ZP values. There is a good coincidence between the electrophoretic curves of LEV sample and LEV-loaded CaP powders. Significant diffferences among a given set of ZP curves (before, or after LEV adsorption) can hardly be noticed, but in both situations the pure and Mg-doped powders tend to exhibit slightly higher absolute ZP values at a given pH in comparison to Sr-doped one. The electrical conductivity ($\mu S \cdot m^{-1}$) values of the diluted suspensions used to measure ZP at pH ~7.4 were: 1.75, 2.34, 2.94, for [HA], [Sr-HA], and [Mg-HA], respectively.

3.2. *In vitro* levofloxacin release

The percentages of drug loading (*DL*) and corresponding adsorption efficiency (*AE*) of the different CaP powders are presented in Table 3. The *DL* for pure HA coincided well with the planned value of 2.5 wt.%. But the CaP-doped powders were able to retain higher doses, with the highest value being observed for LEV[Sr-HA].

Table 3. *DL* and *AE* values (%, $w/w_{particles}$) for CaP powders.

CaP Powders	$\%DL$ ($w_{LEV}/w_{particles}$)	$\%AE$ ($w_{LEV}/w_{initial\ LEV}$)
LEV[HA]	2.51 ± 0.33	18.9 ± 2.5
LEV[Mg-HA]	2.97 ± 0.33	22.3 ± 2.5
LEV[Sr-HA]	3.43 ± 0.22	25.8 ± 2.9

Concerning the release kinetics, there was a sudden burst at the first contact with the liquid medium in the case of LEV[HA] particles that hindered to establish any reliable time dependent relationship. The release data for LEV[Mg-HA] and LEV[Sr-HA] could be fitted to a first order model equation to determine the LEV release kinetics mechanism. The results presented in Table 4 reveal that the best fitting parameters were obtained for LEV[Mg-HA].

Table 4. Fitted parameter values and r^2 for the first order equation model used to fit the release mechanism of LEV from CaP powders.

		CaP powders	
Equation Models	**Models Parameters**	**LEV[Sr-HA]**	**LEV[Mg-HA]**
$M_t = 1 - e^{-kt}$	r^2	0.626	0.952
	k_{1st} (h^{-1})	0.644	0.771

The LEV release profiles for all CaP powders are displayed in Fig. 5. Fig. 5a highlights the changes occurring within the first hours of contact up to 6 h, while Fig. 5b shows the entire picture along the maximum testing period of 168 h. From

both plots, it is apparent that for LEV[HA] 100% release occurred immediately after the contact with the medium. Significant amounts (73-84%) of LEV were also released from doped CaP powders within the first 30 min. At the 6 h time point, complete release was achieved for LEV[Sr-HA], while a plateau at about 94% was reached in the case of LEV[Mg-HA], suggesting that about 6% remained adsorbed at the surface of the particles even after one week. This apparently enhanced affinity of LEV towards the surface of Mg-doped powder is consistent with its smaller particle size and consequently its higher specific surface area, as reported in Table 2. It is also noteworthy that some of the most significant differences between ZP curves (before, or after LEV adsorption) were observed for Mg-doped powder. The fast and complete release from LEV[HA] (100% HA) and the slowest kinetics observed for LEV[Mg-HA] (65% HA+ 35% β−TCP) also suggest a stronger adsorption of LEV at the surface of β−TCP particles in comparison to HA phase. This hypothesis needs to be further investigated in future works.

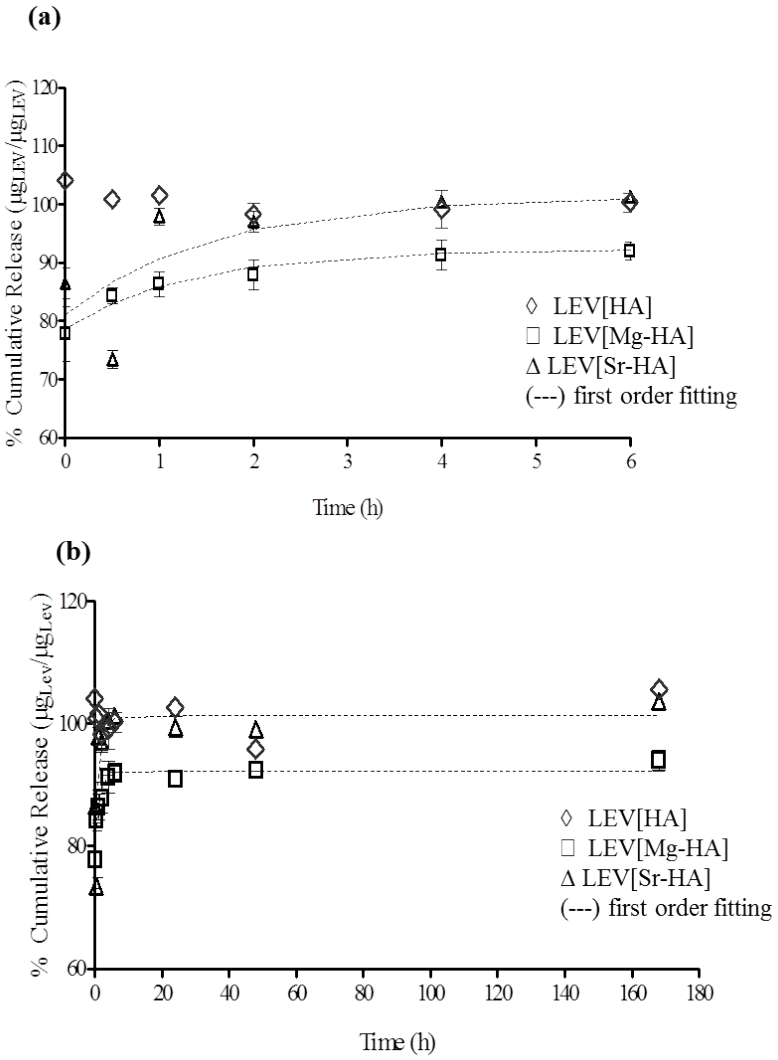

Fig. 5. Levofloxacin release profiles up to different time periods: (a) 6 h; (b) 168 h. Results are expressed as percentages of LEV released in relation to adsorbed antibiotic. Markers and error bars represent the means ± SD (n=3).

3.3. Biological properties

Safety issues must be always considered when developing materials for biomedical applications. Here, the antimicrobial susceptibility to LEV and the cytotoxicity of LEV-adsorbed CaP powders in L929 (mouse fibroblast cell line) and MG63 (human osteoblast cell line) cells were evaluated.

3.3.1. Antimicrobial susceptibility

The results of antimicrobial susceptibility to LEV released from CaP powders after 48 h are shown on Table 5. The results of antimicrobial susceptibility to LEV released from the powders are in agreement to the MIC values of a free LEV solution, meaning that powders formulation have not affected LEV antimicrobial effectiveness against the studied strains.

Table 5. Microbiological study related to LEV released from doped CaP powders after 48 h.

Microorganism Strain	**MIC ($\mu g \cdot mL^{-1}$)**			
	Levofloxacin	**LEV[HA]**	**LEV[Mg-HA]**	**LEV[Sr-HA]**
S. aureus	≥ 0.25	≥ 0.25	≥ 0.25	≥ 0.25
S. epidermidis	≥ 2	≥ 1	≥ 1	≥ 1
E. coli	≥ 0.03	≥ 0.03	≥ 0.03	≥ 0.03

3.3.2. Cytotoxicity evaluation of the CaP powders

The results of the *in vitro* biocompatibility of MG63 and L929 cells cultured for 24 h in the presence CaP powders with and without adsorbed LEV, and of the cell viability assessed by MTT assay, are presented in Fig. 6 and Fig. 7 respectively. No significant changes in cell viability were induced by the presence of LEV. Microscopic observations of cells in contact with LEV-loaded CaP powders before adding MTT showed no morphological changes in both osteoblasts and fibroblasts cells in comparison to those exhibited by the same cells in contact with culture medium (control) (Fig. 8). This is a clear evidence of the material biocompatibility.

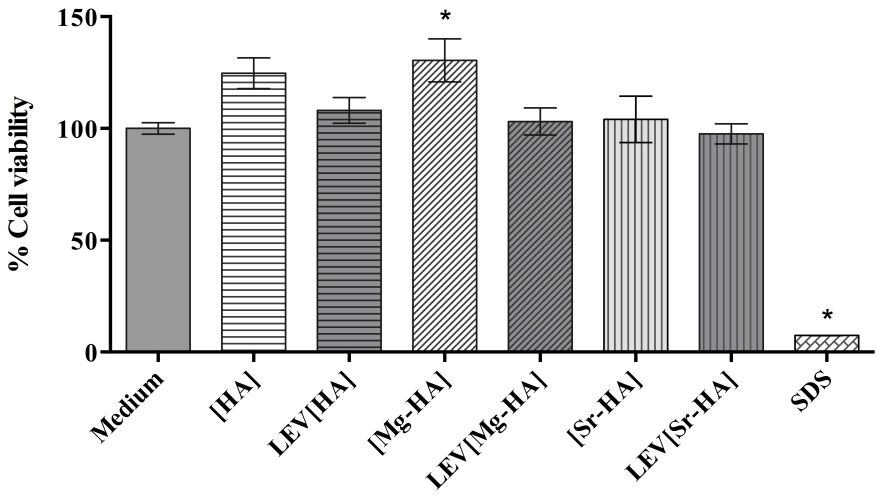

Fig. 6. Cell viability MTT assays of MG63 osteoblastic-like cells exposed to [HA], LEV[HA], [Mg-HA], LEV[Mg-HA], [Sr-HA], LEV[Sr-HA] powders, culture medium as negative control and sodium dodecyl sulphate (SDS) as positive control. Data are expressed as mean % of control ± SD of at least three independent experiments. Statistically significant difference are marked as * ($p < 0.05$).

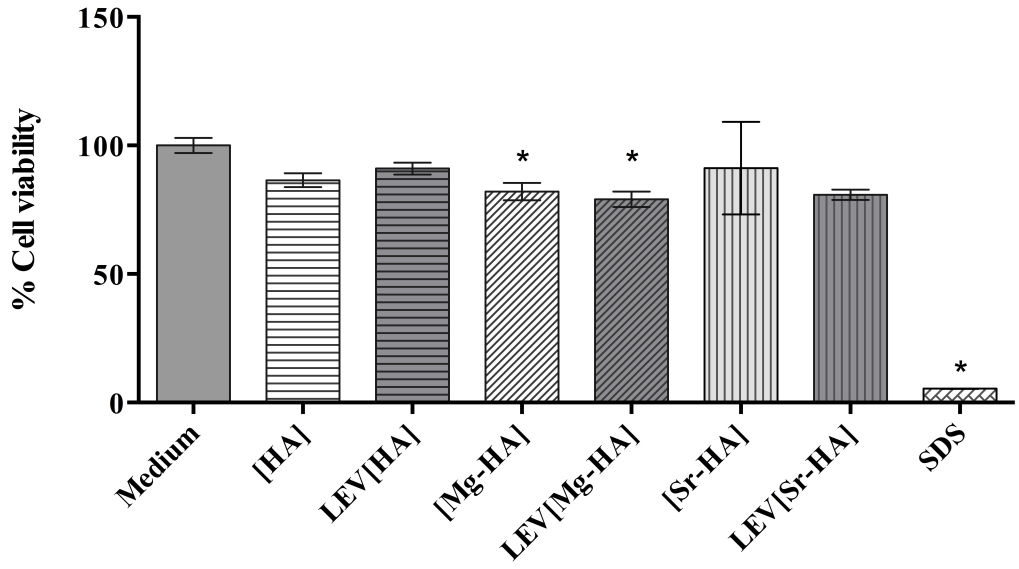

Fig. 7. Cell viability MTT assays of L929 mouse fibroblast cells exposed to [HA], LEV[HA], [Mg-HA], LEV[Mg-HA], [Sr-HA], LEV[Sr-HA] powders, culture medium as negative control and sodium dodecyl sulphate (SDS) as positive control. Data are expressed as mean % of control ± SD of at least three independent experiments. Statistically significant difference are marked as * ($p < 0.05$).

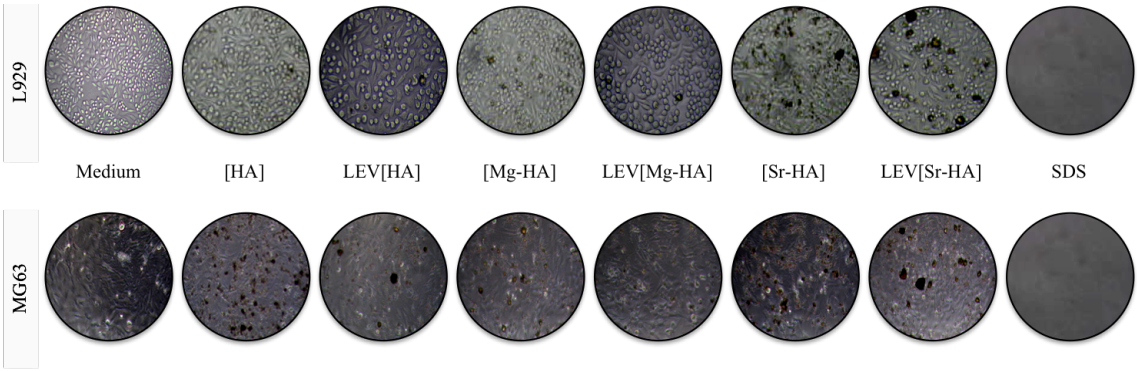

Fig. 8. Representative phase contrast microphotographs of MG63 and L929 cells exposed to [HA], LEV[HA], [Mg-HA], LEV[Mg-HA], [Sr-HA] and LEV[Sr-HA] powders after 24 h in culture.

4. Discussion

Being a well-known bioceramic, HA can be considered as a convenient drug delivery carrier. Doping HA with Mg and Sr ions is likely to further enhance the physico-chemical and especially the biological properties of the resulting materials [23-25]. While pure HA phase was obtained for the stoichiometric composition heat treated for 1 h at 800 ºC, doping with Mg and Sr ions resulted in the formation of β-TCP as secondary phase, which is more abundant in [Mg-HA], Fig. 2. This is not surprising considering the thermal stabilizing effect of Mg towards the β-TCP phase. Mg also influences the crystallinity, morphology, crystal size and thermal stability of biphasic CaP mixtures [25]. This is due to the preferential replacement of Ca in the β-TCP lattice [41,42]. This replacement causes a reduction in the lattice parameters of β-TCP induced by the smaller ionic radius of six-fold coordinated Mg^{2+} (0.65 Å) in comparison to that of Ca (0.99 Å) at Ca(5) site of β-TCP structure [43]. This explains why the XRD peaks of this phase appear shifted to higher 2θ angles relatively to the standard file (# 04-006-9376) in Fig. 2.

Despite having a larger ionic radius (1.13 Å), Sr can also replace Ca in both the HA and β-TCP structures over the whole range of compositions causing a linear expansion of lattice constants and a decreasing trend of crystallite size [44]. It was also concluded that Sr tends to preferentially occupy the Ca(1,2,3,4) sites of β-TCP

structure [45]. This stabilizing role of Sr towards β-TCP structure justifies the formation of trace amount of β−TCP in the [Sr-HA] powder as identified by XRD, and further confirmed by FTIR, namely, the decrease in intensity of peaks relative to OH groups observed at 630 cm^{-1} and at 3570 cm^{-1} for the Mg- and Sr-doped powders in comparison to the stoichiometric HA (Fig. 3) [44,46]. The formation of biphasic (HA + β−TCP) mixtures are usually preferred for bone graft applications because their resorption rate can be tuned to match the bone healing rate allowing to obtain a suitable balance between implant degradation and bone regeneration [47].

The different extents of LEV adsorption at the surface of CaP powders and of its *in vitro* release kinetics are likely to derive from the chemical changes and the lattice strains induced by doping. The adsorption capacity of a carrier is known to depend on several parameters such as its chemical composition, surface charge density [48], porosity [49,50] and specific surface area [51]. The results of XRD and FTIR gathered for the synthesized CaP powders did not reveal any changes in crystallinity and phase assemblage induced by LEV-loading. The FTIR spectra also confirmed the individual features of both powders and LEV, meaning the absence of any chemical interaction. These results suggest that LEV has been attached at the surface of CaP powder particles by physisorption.

The use of particles as drug carriers in drug delivery systems is usually driven by criteria that include bioavailability, predictable therapeutic response, greater efficacy, safety, and more controlled and prolonged release of drugs over time. HA powders as drug carriers aroused greater interest due to its biocompatibility and osteoconductive ability [52]. Doping HA with Mg and Sr noticeably affected *DL* and *AE*. The three different adsorption extents (Table 3) and release profiles (Fig. 5) observed for the [HA], [Mg-HA] and [Sr-HA] powders over 1-week period are probably related to variations in the contents of HA and β−TCP phases and to some lattice strains derived from the ionic substitutions. According to Sasikumar [53], the size and morphology of the particles are the most relevant parameters that control the adsorption and release kinetics of the drug, as they determine the exposed surface area, the packing efficiency and the diffusivity. A more extensive adsorption should be expected for the [Mg-HA] powder that presents the smallest particle size and the highest SSA (Table 2). But the adsorption data reported in Table 3 reveals that the highest LEV dose was

retained by LEV[Sr-HA], which exhibits the smallest SSA (close to that of [HA]). This means that besides size and morphology, the lattice strains induced doping and the variation in crystalline phase contents of the CaP powders also play some role. These would help explaining why doped powders were able to adsorb higher LEV doses. Moreover, electrostatic interactions constitute an important component of the driving forces that lead to adsorption. The small right shifting trend observed in ZP curves of CaP particles with adsorbed LEV means that drug species possess a slightly cationic character, fostering its electrostatic attraction to the surface. The extent of LEV adsorption at the surface of CaP powders is also likely to depend on the surface charge density and its distribution, which might vary with the polarity of doping ions. The field strength, defined as the charge of an ion divided by the square of its ionic radius, is a measure of the strength of the electrostatic field created by the ion. Accordingly, the electrical charge around Mg^{2+} is more locally concentrated than around larger alkaline earth cations, enabling a less localized and more uniform surface charge distribution in case of Sr-doped powder. This might help explaining why the extent of LEV adsorption was highest for LEV[Sr-HA] (Table 3).

The same ionic field strength considerations were recently suggested to govern the non-stoichiometric leaching of alkaline earth ions [54-56]. In those cases, the lower field strength associated to the larger size cation revealed a good consistency with the enhanced leaching easiness of larger Ba^{2+} ions to the solution. However, in the present case the electrical conductivity values ($\mu S \cdot m^{-1}$) of the diluted suspensions used to measure ZP (Fig. 4) at pH ~7.4 were: 1.75, 2.34, 2.94, for [HA], [Sr-HA], and [Mg-HA], respectively. These results indicate that the leaching easiness of alkaline earth ions in the present case could be ordered as follows: $Mg^{2+} > Sr^{2+} > Ca^{2+}$. This finding suggests that factors other than field strength (size of ionic cages in crystalline structure, and lattice strains associated to size fittingness) seem to prevail in dictating the dissolution behaviour and diffusivity of alkaline earth ions from pure and doped HA.

The same factors, together with the ionic polarity related issues, seem to play also important roles in determining the drug adsorption extent and release profiles. The non-distorted pure HA lattice adsorbed less and facilitated the LEV desorption through a burst type release. The lattice strains derived from the replacement of Ca^{2+}

(0.99 Å) in HA and β-TCP lattices by ions with smaller (Mg^{2+} = 0.65 Å) and larger (Sr^{2+} = 1.13 Å) sizes are expected to be higher in the case of [Mg-HA]. Forming a higher fraction of β-TCP and decreasing the lattice parameters was the thermodynamic response of the system to mitigate lattice distortions. The slowest release kinetics of LEV[Mg-HA] and the remnant of ~6% LEV in this powder after one week are likely related to a higher adsorption strength due to a more localised surface charge and the higher specific surface area of this powder. Oppositely, the lattice strains combined with a more uniform surface charge distribution seem to be the main factors determining the most extensive LEV adsorption by [Sr-HA] (Table 3), and its release profile from LEV[Sr-HA] (Fig. 5).

The relatively fast release rates mean that CaP powders alone do not exhibit the required features desired for controlled drug delivery systems. Indeed, the ultimate target of the present work was to prepare suitable drug carriers. The assessment of the drug release and *in vitro* behaviors aimed at gathering data to support the selection of the most promising CaP composition to further develop more complex biomedical devices cumulating the two functions: an antibiotic-loaded bone graft, and a drug carrier able to deliver it under controlled rates when incorporated into an adequate polymer matrix. This will hinder the burst release type profile [57]. The data gathered represent an important step towards this goal and to find out suitable solutions for chronic osteomyelitis, which is still very difficult to treat and presents a challenge to clinicians. For this reason, the bacteria strains that are major causative agents of orthopaedic infections (*S. aureus*, *S. epidermidis* and *E.coli*) were selected for the microbiological studies. The minimal inhibitory concentration (MIC) of the LEV was not affected for the presence of CaP powders. Additionally, the levels of drug released from LEV[Sr-HA] (89 $\mu g \cdot mL^{-1}$), LEV[Mg-HA] (69 $\mu g \cdot mL^{-1}$) and LEV[HA] (78 $\mu g \cdot mL^{-1}$), are well above for the LEV MIC values for these strains (Table 5). Furthermore, the systems reveal an initial burst release, which is one of the requirements for local antibiotic delivery systems (Fig. 5). After 48 h, the concentrations of LEV released increased to ~107 $\mu g \cdot mL^{-1}$, ~84 $\mu g \cdot mL^{-1}$ and ~80 $\mu g \cdot mL^{-1}$ for LEV[Sr-HA], LEV[Mg-HA] and LEV[HA] systems, respectively, discarding the possibility of sub-therapeutic or sub-inhibitory concentrations that could induce resistance in wound-site bacteria [58].

Biocompatibility is an important aspect to consider regarding the development of any antibiotic-loaded material as drug delivery systems. Cytotoxicity assay regarding the MG63 (osteoblasts) and L929 (fibroblasts) cells incubated in direct contact with the calcium phosphates powders, revealed no significant increase when compared with the correspondent plain calcium phosphates (Figs. 6 and 7). Considering the final values of LEV released, the biocompatibility evaluation was of utmost importance in spite of LEV being referred as a low-toxicity fluoroquinolone [28]. Moreover, all the obtained values for CaP powders cell viability where above 70%, when compared to medium, which reveals no cytotoxic potential [59].

5. Conclusions

The results presented and discussed along this work enable to draw the following conclusions:

1. Doping pure hydroxyapatite with elements having smaller (Mg^{2+} = 0.65 Å) and larger (Sr^{2+} = 1.13 Å) ionic radius than calcium (Ca^{2+} = 0.99 Å) while keeping constant the molar ratio (Ca+M/P = 1.67) favoured the formation of β-TCP as secondary phase, but with a contraction and an expansion of the lattice parameters, respectively. The greater the difference between the exchanged ionic radius the larger was the amount of β-TCP formed and the extent of lattice distortions.
2. The resulting lattice strains, the polarity and diffusivity of the alkaline earth ions dictate the extents of physical adsorption of Levofloxacin (LEV) at the surface of CaP powders and the easiness of its release through a complex interplay. All the CaP powders exhibited burst type release profile, but the non-distorted pure HA lattice adsorbed less and facilitated the release in comparison to the doped systems.
3. The *in vitro* antimicrobial activity of the antibiotic and the biocompatibility of all synthesized and LEV-loaded CaP powders were demonstrated. Considering the overall release results, the doped powders constitute promising candidate filler materials for biopolymer matrices for applications as controlled drug release systems.

4. The present results constitute a first step of a more extended research program aiming at developing an appropriate system for the controlled release of antibiotic in the treatment of chronic osteomyelitis.

REFERENCES

[1] D.P. Lew, F.A. Waldvogel, Osteomyelitis, Lancet 364 (2004) 79–369.

[2] A.L.L. Lima, P.R. Oliveira, V.C. Carvalho, S. Cimerman, E. Savio, Recommendations for the treatment of osteomyelitis, Braz J Infect Dis 18(5) (2014) 526–34.

[3] J.T. Mader, C.M. Stevens, J.H. Stevens, *et al.*, Treatment of experimental osteomyelitis with a fibrin sealant antibiotic implant, Clin Orthop Relat Res 403 (2002) 58–72.

[4] C. Soundrapandian, S. Datta, B. Sa, Drug-eluting implants for osteomyelitis, Crit Rev Ther Drug Carrier Syst 24(6) (2007) 493–545.

[5] C. Soundrapandian, B. Sa, S. Datta, Organic-inorganic composites for bone drug delivery, AAPS PharmSciTech 10(4) (2009) 1158–1171.

[6] L. Chen, H. Wang, J. Wang, *et al.*, Ofloxacin-delivery system of a polyanhydride and polylactide blend used in the treatment of bone infection, J Biomed Mater Res B Appl Biomater 83(2) (2007) 589–595.

[7] S. Gitelis, G.T. Brebach, The treatment of chronic osteomyelitis with a biodegradable antibiotic-impregnated implant, J Orthop Surg 10 (2002) 53–60.

[8] K.N. Samit, M. Prasenjit, R. Subhasis, *et al.*, Local antibiotic delivery systems for the treatment of osteomyelitis – A review, Mat Sci Eng C 29 (2009) 2478–2485.

[9] M.L. Azi, M.K. Junior, R. Martinez, *et al.*, Bone cement and gentamicin in the treatment of bone infection: background and in vitro study, Acta Ortop Bras 18(1) (2010) 31–34.

[10] K.W. Klemm, Antibiotic bead chains, Clin Orthop (1993) 63–76.

[11] G.Wei, Y. Kotoura, M. Oka, *et al.*, Bioabsorbable delivery system for antibiotic treatment of osteomyelitis, J Bone Jt Surg 73-B (1991) 246–252.

[12] J.K. Koort, T.J. Mäkinen, E. Suokas, *et al.*, Efficacy of ciprofloxacin-releasing bioabsorbable osteoconductive bone defect filler for treatment of experimental osteomyelitis due to *Staphylococcus aureus*, Antimicrob Agents Chemother 49 (2005) 1502–1508.

[13] Kanellakopoulou K and Giamarellos-Bourboulis EJ. Carrier systems for the local delivery of antibiotics in bone infections. Drugs 2000;59(6)1223–1232.

[14] A. El-Ghannam, K. Jahed, M. Omran, Nanoporous delivery system to treat osteomyelitis and regenerate bone: gentamicin release kinetics and bactericidal effect, J Biomed Mater Res B - Appl Biomater 73 (2005) 277–284.

[15] A. El-Ghannam, K. Jahed, M. Govindaswami, Resorbable bioactive ceramicfor treatment of bone infection, J Biomed Mater Res A 94 (2010) 308–316.

[16] V. Uskokovic´, T.A. Desai, Phase composition control of calcium phosphatenanoparticles for tunable drug delivery kinetics and treatment of osteomyelitis. I. Preparation and drug release, J Biomed Mater Res A 101 (2013) 1416–1426.

[17] H.W. Kim, J.C. Knowles, H.E. Kim, Hydroxyapatite/poly(epsilon-caprolactone) composite coatings on hydroxyapatite porous bone scaffold for drug delivery, Biomaterials 25(7-8) (2004) 1279–1287.

[18] S.K. Ghosh, S.K. Nandi SK, B. Kundu, *et al.*, In vivo response of porous hydroxyapatite and beta-tricalcium phosphate prepared by aqueous solution combustion method and comparison with bioglass scaffolds, J Biomed Mater Res B Appl Biomater 86(1) (2008) 217–227.

[19] I.R. de Lima, G.G. Alves, C.A. Soriano, *et al.*, Understanding the impact of divalent cation substitution on hydroxyapatite: an in vitro multiparametric study on biocompatibility, J Biomed Mater Res A 98(A) (2011) 351–358.

[20] C. Ergun, T.J. Webster, R. Bizios, *et al.*, Hydroxylapatite with substituted magnesium, zinc, cadmium, and yttrium. I. Structure and microstructure, J Biomed Mater Res 59 (2002) 305–311.

[21] E. Boanini, M. Gazzano, A. Bigi, Ionic substitutions in calcium phosphates synthesized at low temperature, Acta Biomater 6 (2010)1882–1894.

[22] S. Kannan, A.F. Lemos, J.M.F. Ferreira, Synthesis and Mechanical Performance of Biological-like Hydroxyapatites, Chem Mater 18(8) (2006) 2181–2186.

[23] S. Pina, S.I. Vieira, P. Rego, *et al.*, Biological responses of brushite-forming Zn- and ZnSr-substituted β-tricalcium phosphate bone cements, eCM 20 (2010)162–177.

[24] R.Z. LeGeros, Calcium Phosphates in Oral Biology and Medicine, Monogr Oral Sci 15 (1991) 1–201.

[25] F. Ren, Y. Leng, R. Xin, *et al.*, Synthesis, characterization and ab initio simulation of magnesium-substituted hydroxyapatite, Acta Biomater 6 (2010) 2787–2796.

[26] I.R. Gibson, W. Bonfield, Preparation and characterization of magnesium/carbonate co-substituted hydroxyapatites, J Mat Sci: Mater Med 13 (2002) 685–693.

[27] T. Rimmelé, E. Boselli, D. Breilh, *et al.*, Diffusion of levofloxacin into bone and synovial tissues, J Antimicrob Chemother 53 (2004) 533–535.

[28] P.D. Holtom, S.A. Pavkovic, P.D. Bravos, *et al.*, Inhibitory Effects of the Quinolone Antibiotics Trovafloxacin, Ciprofloxacin, and Levofloxacin on Osteoblastic Cells *In Vitro*, J Orthop Res 18(5) (2000) 721–727.

[29] D. Arcos, J. Rodriguez Carvajal, M. Vallet Regi, The effect of the silicon incorporation on the hydroxyapatite structure. A neutron diffraction study, Solid State Sci 6 (2004) 987– 994.

[30] S. Nicolopoulos, J.M. Gonzalez Calbet, M.P. Alonso, M.T. Gutierrez Rios, M.I. De Frutos, M. Vallet Regi, Characterization by TEM of Local Crystalline Changes during Irradiation Damage of Hydroxyapatite Compounds, J. Solid State Chem 116 (1995) 265– 274.

[31] E. Hart, K. Azzopardi, H. Taing, *et al.*, Efficacy of antimicrobial polymer coatings in an animal model of bacterial infection associated with foreign body implants, J Antimicrob Chemother 65 (2010) 974–980.

[32] Clinical and Laboratory Standards Institute (CLSI). Methods for Dilution Antimicrobial Susceptibility Tests for Bacteria That Grow Aerobically, Approved Standard. Ninth Edition, M07-A9, 2012, Wayne, PA, USA.

[33] Clinical and Laboratory Standards Institute (CLSI). Performance Standards for Antimicrobial. 560 Susceptibility Testing, Seventeenth Informational Supplement, M100-S17, 2007, Wayne, PA, USA.

[34] A. Cadete, L. Figueiredo, R. Lopes, *et al.*, Development and characterization of a new plasmid delivery system based on chitosan-sodium deoxycholate nanoparticles, Eur J Pharm Sci 45 (2012) 451–458.

[35] R. Lopes, C.V. Eleutério, L.M.D. Gonçalves, *et al.*, Lipid nanoparticles containing oryzalin for the treatment of leishmaniasis, Eur. J Pharm Sci 45 (2012) 442–450.

[36] A. Matos, L.M. Gonçalves, P. Rijo, *et al.*, A Novel Modified Acrylic Bone Cement Matrix. A Step Forward On Antibiotic Deliver Against Multiresistant Bacteria Responsible For Prosthetic Joint Infections, Mater Science and Eng: C 38 (2014) 218–226.

[37] P.M.C. Torres, J.C.C. Abrantes, A. Kaushal, S. Pina, N. Döbelin, M. Bohner, J.M.F. Ferreira, Influence of Mg-doping, calcium pyrophosphate impurities and cooling rate on the allotropic α↔ β-tricalcium phosphate phase transformations, J Eur Cer Soc 36 (3) (2016) 817– 827.

[38] S. Koutsopoulos, Synthesis and characterization of hydroxyapatite crystals: a review study on the analytical methods, J Biomed Mater Res 62(4) (2002) 600–612.

[39] V.K. Shahwal, B.K. Dubey, M. Bhoumick, Preformulation study of Levofloxacin, Int J of Adv in Pharmac 1 (2012) 1–8.

[40] H.B. Gevariya, S. Gami, N. Patel, Formulation and characterization of levofloxacin-loaded biodegradable nanoparticles, Asian J Pharm 5 (2011)114–9.

[41] S. Kannan, A.F. Lemos, J.H.G. Rocha, *et al.*, Synthesis and characterization of magnesium substituted biphasic mixtures of controlled hydroxyapatite/β -tricalcium phosphate ratio, J Solid State Chem 178 (2005) 3190–3196.

[42] S. Kannan, J.M. Ventura, J.M.F. Ferreira, Aqueous precipitation method for the formation of Mg-stabilized β-tricalcium phosphate: An X-ray diffraction study, Ceram Int 33(4) (2007) 637–641.

[43] S. Kannan, F. Goetz-Neunhoeffer, J. Neubauer, *et al.*, Rietveld structure and in vitro analysis on the influence of magnesium in biphasic (hydroxyapatite and β -tricalcium phosphate) mixtures, J Biomed Mater Res Part B: Appl Biomater 90B(1) (2009) 404–411.

[44] S. Kannan, S. Pina, J.M.F. Ferreira, Formation of Strontium-Stabilized β-Tricalcium Phosphate from Calcium-Deficient Apatite, J Am Ceram Soc 89(10) (2006) 3277–3280.

[45] S. Kannan, F. Goetz-Neunhoeffer, J. Neubauer, *et al.*, Synthesis and structural characterization of strontium- and magnesium-co-substituted beta-tricalcium phosphate, Acta Biomater 6(2) (2010) 571–576.

[46] I.R. Gibson, I. Rehman, S.M. Best, *et al.*, Characterization of the Transformation from Calcium-Deficient Apatite to β-Tricalcium Phosphate, J Mater Sci Mater Med 11(12) (2000) 799–804.

[47] T-W. Kim, Y.M. Park, D-H. Kim, *et al.*, In situ formation of biphasic calcium phosphates and their biological performance in vivo, Ceram Int 38(3) (2012) 1965–1974.

[48] A.C. Queiroz, J.D. Santos, F.J. Monteiro, *et al.*, Adsorption and release studies of sodium ampicillin from hydroxyapatite and glass-reinforced hydroxyapatite composites, Biomaterials 22 (2001) 1393–1400.

[49] B. Palazzo, M. Iafisco, M. Laforgia, *et al.*, Biomimetic hydroxyapatite-drug nanocrystals as potential bone substitutes with antitumor drug delivery properties, Adv Funct Mat 17 (2007) 2180–8.

[50] M. Hasegawa, A. Sudo, V.S. Komlev, *et al.*, High release of antibiotic from a novel hydroxyapatite with bimodal pore size distribution, J Biomed Mater Res Part B: Appl Biomater 70 (2004) 332–339.

[51] H. Seshima, M. Yoshinari, S. Takemoto, *et al.*, Control of bisphosphonate release using hydroxyapatite granules, J Biomed Mater Res Part B: Appl Biomater 78 (2006) 215–21.

[52] Y. Shinto, A. Uchida, F. Korkusuz, *et al.*, Calcium hydroxyapatite ceramic used as a delivery system for antibiotics, J Bone and Joint Surg 74-B (1992) 600–604.

[53] S. Sasikumar. Effect of particle size of calcium phosphate based bioceramic drug deliver y carrier on the release kinetics of ciprofloxacin hydrochloride: an in vitro study, Front Mater Sci 7(3) (2013) 261–268.

[54] J.M.F. Ferreira, S.M. Olhero, A. Kaushal, Is the ubiquitous presence of barium carbonate responsible for the poor aqueous processing ability of barium titanate?, J Eur Ceram Soc 33 (2013) 2509–2517.

[55] S.M. Olhero, A. Kaushal, J.M.F. Ferreira, Fabrication of barium strontium titanate ($Ba_{0.6}Sr_{0.4}TiO_3$) 3D microcomponents from aqueous suspensions, J Am Ceram Soc 97(3) (2014) 725–732.

[56] A. Kaushal, S.M. Olhero, B. Sing, *et al.*, Impedance analysis of $0.5Ba(Zr_{0.2}Ti_{0.8})O_3$–$0.5(Ba_{0.7}Ca_{0.3})TiO_3$ ceramics consolidated from micro-granules, Ceram Inter 40(7) (2014) 10593–10600.

[57] A.C. Matos, C.F. Marques, R.V. Pinto, I.A.C. Ribeiro, L.M. Gonçalves, M.A. Vaz, J.M.F Ferreira, A.J. Almeida, A.F. Bettencourt, Novel doped calcium phosphate-PMMA bone cement composites as levofloxacin delivery systems, Int J of Pharm 490 (2015) 200–208

[58] P. Wu, D.W. Grainger, Drug/device combinations for local drug therapies and infection prophylaxis, Biomaterials 27 (2006) 2450–2467.

[59] International Standard ISO Specification 10993(5): Biological evaluation of medical devices - Part 5: Tests for in vitro cytotoxicity. International Organization for Standardization, 3rd edition, 2009. (ISO, Geneva, Switzerland).

Chapter 3

BIOCOMPATIBILITY AND ANTIMICROBIAL ACTIVITY OF BIPHASIC CALCIUM PHOSPHATE POWDERS DOPED WITH METAL IONS FOR REGENERATIVE MEDICINE

Catarina F. Marques[a], Susana Olhero[a], J.C.C. Abrantes[a,b], Ana Marote[c], Sónia Ferreira[d], Sandra I. Vieira[c], José M.F. Ferreira[a]

[a] Department of Materials and Ceramics Engineering, University of Aveiro CICECO, 3810-193 Aveiro, Portugal

[b] UIDM, ESTG, Polytechnic Institute of Viana do Castelo, 4900 Viana do Castelo, Portugal

[c] Institute for Biomedicine (iBiMED), Department of Medical Sciences, University of Aveiro, 3810-193 Aveiro, Portugal

[d] Department of Health and Education, Institute of Education and Citizenship, 3770-033 Mamarrosa, Portugal

Journal Ceramics International 43(17) (2017) 15719-15728

Abstract

Biphasic [hydroxyapatite (HA) + β-tricalcium phosphate (β-TCP)] calcium phosphate powders with partial substitutions of Ca^{2+} by silver, copper, zinc and strontium ions were synthesized by precipitation. The aim was to improve the overall biological performance (antimicrobial effect and stimulated osteoblasts proliferation) of the bone graft materials made thereof. The prepared powders were calcined and characterized by different techniques including X-ray diffraction (XRD), elemental analysis, thermo gravimetric and differential thermal analysis (TG-DTA), Fourier Transform Infrared Spectroscopy (FT-IR) and Scanning Electron Microscopy (SEM). Rietveld refinement was used for quantitative phase analysis. The *in vitro* biocompatibility and the antibacterial activity of the powders were evaluated through the resazurin viability test with MG63 cells, and against *Escherichia coli* and *Staphylococcus aureus*, respectively. The quantitative elemental analysis revealed that only strontium ions have been fully incorporated into both HA and β-TCP phases. The *in vitro* biocompatibility with pre-osteoblasic cells was proved for all synthesized powders, while only the silver-doped powders exhibited antimicrobial activity against *S. aureus*. The information gathered is of high relevance for designing improved calcium phosphate bioceramics.

Keywords: Biphasic calcium phosphates, ionic substitution, antimicrobial, biocompatibility

1. Introduction

The use of synthetic bone substitutes for reconstructive surgery, orthopaedics, dentistry, spinal arthrodesis, oral, and maxillofacial surgery is increasing. This is particularly true for calcium phosphates (CaPs) due to their similar chemical composition to bone mineral [1], and their properties of biocompatibility and osteoconductivity [2,3]. These features make them suitable alternative materials to autologous bone grafts. The most widely used calcium phosphate-based materials are hydroxyapatite [HA, $Ca_{10}(PO_4)_6(OH)_2$] and β-tricalcium phosphate [β-TCP, $Ca_3(PO_4)_2$]. Both are bioactive but exhibit different biological resorption capacities, with HA being virtually non-resorbable, whereas β-TCP is a fully resorbable material [4]. Biphasic calcium phosphates (BCP) are mixtures of these phases that combine the biodegradability of β-TCP with the strong mechanical properties of HA [5], enabling the control of the resorption rate of CaP biomaterials [6] and leading to more complex biological and chemical events [7]. An optimal balance (β-TCP/HA) between the more stable phase of HA and more soluble TCP favours the gradual dissolution of calcium (Ca^{2+}) and phosphate (PO_4^{3-}) ions in the biological medium and seeding of new bone [8]. The superior properties of the BCP materials directly prepared [9] over those obtained by mixing two single phases have been also highlighted [10].

Bone is not a homogenous material, and besides Ca and P it also incorporates various trace elements that play vital roles in its formation, growth, and repair. In recent years, various studies demonstrated that adding trace elements to CaP materials can lead to controlled degradation, increase of the material's mechanical strength and positively influence the biological response [11,12]. This includes the promotion of bone apposition, improving the performance process after implantation [13,14]. Among the ionic groups within HA or TCP structure, Ca^{2+} can be replaced by various ions and, in the last decades, particular attention has been given to the strontium ion (Sr^{2+}) as it increases osteoclast apoptosis and enhances pre-osteoblast cell proliferation and collagen synthesis; consequently, it depresses bone resorption, while maintaining bone formation [15]. Ions that have antimicrobial properties, such as Ag^{+}, Cu^{2+} or Zn^{2+} [16,17], have also been widely studied, since one of the most common problems when using implants is the risk of developing post-operatory infections and/or rejection. Silver and silver ions are long known to have strong inhibitory and

bactericidal effects, as well as a broad spectrum of anti-microbial activities [18]. On the other hand, zinc and cooper are important trace elements in human development, essential for various metabolic processes: copper plays a role in the cross-linking of collagen and elastin of bone [19,20], whereas zinc stimulates the bone formation and mineralization [21,22], having a direct specific proliferative effect on osteoblastic cells *in vitro* and it is thought to possess a potent and selective inhibitory effect on osteoclastic bone resorption *in vivo* [23,24].

Different approaches have been reported in literature for doping CaP powders: hydrothermal synthesis [25], sol-gel process [26], neutralization method [17], wet-chemical method [16], ion exchange method [27] and microwave synthesis [28]. In this study, aqueous precipitation was adopted to synthesize ionic (silver, copper, zinc and strontium) substituted calcium phosphate powders in order to improve their overall biological performance. The effects of doping ions (Sr^{2+}, Ag^{+}, Zn^{2+} and Cu^{2+}) on the crystalline phase assemblage, and on the antimicrobial activity and biocompatibility of the powders, were investigated.

2. Materials and Methods

2.1. Powders preparation

Calcium nitrate tetrahydrate [$Ca(NO_3)_2 \cdot 4H_2O$, Panreac], diammonium hydrogen phosphate [$(NH_4)_2HPO_4$, Panreac], silver nitrate [$AgNO_3$, Alfa Saesar], copper (II) nitrate trihydratate [$Cu(NO_3)_2 \cdot 3H_2O$, Ridel-de Haën], zinc nitrate hexahydrate [$Zn(NO_3)_2 \cdot 6H_2O$, Sigma-Aldrich] and strontium nitrate [$Sr(NO_3)_2$, Sigma-Aldrich] were used as chemical precursors for Ca^{2+}, P^{5+}, Ag^{+}, Cu^{2+}, Zn^{2+} and Sr^{2+}, respectively. The planned doping levels were 3 mol% for Ag^{+}, Cu^{2+} and Zn^{2+} ions, and 7 and 10 mol% for Sr^{2+}. For all compositions, the concentration of Ca precursor was conveniently adjusted to keep a constant molar ratio of (Ca+M)/P = 1.62 (M=Ag, Cu or Sr), including a non-doped one used as control. For the Zn-doped composition, a total ratio (Ca+Zn)/P = 2.5 was required to grant the formation of a biphasic powder. Ionic zinc is described as one of the most effective HA crystal growth inhibitors, decreasing its crystallite size and thermal stability [29-32]. Doping with 3

mol% zinc and adopting the same conditions (pH, temperature, ripening time), a preliminary revealed that β-TCP was the single formed from a solution with a Ca/P ratio of 1.62, instead of phase (β-TCP+HA) composition as shown in the XRD pattern of the resulting powder (not shown in the manuscript).

The concentration of P precursor was maintained constant (1.2 M) for all synthises. Precipitation took place by slowly adding the P precursor solution to a mixed solution of cationic precursors under mechanical stirring (1000 rpm). The pH of the mixed solution/suspension was increased and maintained at 9 by adding 8 M NH_4OH solution (Sigma-Aldrich). The reaction was performed at 90ºC for 2 h under constant stirring conditions (1000 rpm). The slurries were poured out from the reactor and the precipitated particles were separated through vacuum filtration and dried at 80ºC overnight.

The powders were calcined at 1000ºC in a Thermolab furnace using a heating rate of 5ºC·min^{-1} followed by a dwelling time of 2 h and then cooled to room temperature (RT) at the rate of 5ºC·min^{-1}, being hereafter designated just as powders. The doped compositions were labelled as 3Ag, 3Cu, 3Zn, 7Sr, 10Sr, and the non-doped (control) as BCP.

2.2. Powders characterization

The thermal behaviour of the dried powders was assessed by thermal analysis (TG-DTA, (DTA, Netzsch STA 409 EP, Germany), using a heating rate of 10 ºC·min^{-1} between 30 and 1300 ºC in air atmosphere.

Qualitative crystalline phase analysis of calcined powders was performed using a high-resolution Bruker D8 Advance DaVinci diffractometer with Cu Kα radiation (λ = 1.5406 Å) produced at 40 kV and 40 mA. Data sets were recorded in the 2θ range of 20–80º with a step size of 0.015º 2θ s^{-1}. Collection of XRD pattern data for Rietveld refinement studies was performed using a conventional Bragg–Brentano diffractometer (Bruker D8 Advance DaVinci, Karlsruhe, Germany) with Ni-filtered Cu-Kα radiation, with a linear detector (Lynxeye 1-D) by recording X-ray diffraction data within the 2θ range = 20−80º (step size 0.015º and 0.5 s for each step). The software TOPAS version 4.2 (Bruker AXS, Karlsruhe, Germany) with the

fundamental parameter approach, and the ICDD card numbers of # 04-015-7245 for HA [33] and # 04-006-9376 for β-TCP [34] were used for Rietveld refinements.

The specific surface areas of the powders were obtained according to the Brunauer–Emmett–Teller method (BET) using a Micromeritics Gemini 2370 V5.00 (Norcross, USA) through the gas adsorption measurements, after degassing the powders in a Micromeritics Flow Prep 060 (Norcross, USA). Particle size distributions of the powders were determined using a light scattering instrument (Coulter LS 230, UK, Fraunhofer optical model). The morphology and microstructure of the particles was observed by scanning electron microscopy (SEM, Hitachi SU-70, Tokyo, Japan).

Elemental analyses of doped ions (Sr^{2+}, Ag^{+}, Cu^{2+} and Zn^{2+}) were determined for all powders using inductively coupled plasma (ICP) spectrometry (ICP-OES Jobin Yvon Activa M., USA). For this purpose, nitric acid with double-distilled water was used to dissolve the powders.

Infrared spectra were obtained by FT-IR spectroscopy (model MattsonGalaxy S-7000, USA). Each starting powder was mixed with KBr in the proportion of 1/150 (by weight) for 15 min and pressed into a pellet. Each infrared spectrum was the average of 32 scans collected at 2 cm^{-1} resolution at room temperature (RT).

2.3. Antimicrobial activity assay

An antimicrobial activity assay was carried out using pure culture colonies of two bacterial strains - *E. coli* (ATCC 25922) and *S. aureus* (ATCC 25923) – using an agar diffusion method on sterile Mueller-Hinton agar (MHA) plates (BioMerieux, France). The strains were grown overnight in PVX plates (BioMerieux, France), and a suspension of 0.5 MacFarland was achieved using 0.9% NaCl saline solution. The suspension was transferred to the surface of the plate using a sterile swab, and the entire surface was swabbed. The compacted powders (0.12 g of sample, 10 mm in diameter, pressed by 1200 kg for 20 s) (60 Pa·s) were placed on the agar surface and incubated for 24 h at 37 ºC. Antimicrobial activity was determined by measuring the width of the inhibition zone (mm).

2.4. Osteoblastic cytotoxicity and cell proliferation assay

2.4.1. MG-63 pre-osteoblasts cell culture

The human osteosarcoma-derived MG-63 cell line (ATCC CRL-1427) was maintained at 37ºC in a humidified atmosphere of 5% CO_2 in air, in Eagle's Minimum Medium in EBSS (Eagle's Balanced Salt Solution) supplemented with 1% non-essential amino acids (NEAA) and 2 mM L-Glutamine (Gibco BRL, Invitrogen), 10% (v/v) foetal bovine serum (FBS, Gibco BRL, Invitrogen), 1% (v/v) of a 100 $U \times mL^{-1}$ penicillin and 100 $mg \times mL^{-1}$ streptomycin solution (Gibco BRL, Invitrogen), and 2.2 $g \times L^{-1}$ $NaHCO_3$. Sub-confluent cultures (at 80-90% confluence) were split 1:5 using a 0.05% trypsin/EDTA solution (Gibco BRL, Invitrogen) at 5% CO_2, 37ºC.

2.4.2. Powders preparation and sterilization

Each powder formulation was weighted (≈800 μg) and sterilized by autoclave (121ºC, 20 min) before dissolution in 500 μL MG-63 cell culture medium. Solutions of cell culture media supplemented with powder at 1.6 $mg \times mL^{-1}$ were in this way prepared for each condition.

2.4.3. Cytotoxicity and cell proliferation assays

The resazurin metabolic and colorimetric assay was used to determine the powder's cytotoxicity and their effect on MG-63 pre-osteoblastic cells proliferation. Cells were seeded at $2x10^4$ $cells \times cm^{-2}$ in 24-well plates containing the medium with powders, and kept at 37ºC in a humidified 5% CO_2 and 95% air atmosphere for 14 days. At the indicated time points (days *in vitro*, DIV), cells were incubated for 4 h with fresh medium containing 10% of a resazurin solution [0.1 $mg \times mL^{-1}$ resazurin (Sigma Aldrich) in phosphate-buffered saline (PBS; Pierce, Perbio)]. Following, resazurin reduction to resofurin was spectrophotometrically measured (Infinite M200 PRO, Tecan) at 570 and 600 nm. For each time period, the resazurin conversion rate was calculated as the O.D. 570/O.D. 600 nm ratio minus the O.D. 570/O.D. 600 nm ratio of a negative control (resazurin media incubated for 4 h in the absence of cells). The resazurin/resofurin ratio was plotted against incubation time. The experiments were carried out in triplicate and data expressed as mean ± standard error.

2.4.4. Statistical analysis

The SPSS package v22 (IBM SPSS Statistics) was used to conduct all statistical analysis. All data is expressed as mean ± standard error of the mean. Mixed design factorial ANOVA was used to compare variability between and within (along 3DIV, 7DIV and 14DIV) groups in the metabolic activity assay. Post-hoc analysis (Bonferroni) was subsequently performed to compare differences between groups. All the requirements were previously verified using the following tests: Kolmogorov-Smirnov test and Shapiro-Wilk test for normal distribution assessment; Levene's test and Sphericity analysis to assess homogeneity of variances and/or covariances. Partial Eta squared (η^2_p) is described as a measure of size effect.

3. Results and Discussion

3.1. Powders thermal behaviour

The effectiveness of ions doping in biphasic calcium phosphate powders, namely ion amount incorporation in the lattice structure as well as ion preference for HA or β-TCP is the first studying step in order to go further for their biological performance.

FT-IR spectra of the as dried doped and non-doped powders are displayed in Fig. 1. All the powders exhibit similar spectra with the vibrational modes of $-PO_4$ groups appearing at 475, 574, 609, 966 and 1020–1120 cm^{-1} and those of –OH groups of apatite phase at 630 and 3570 cm^{-1}. The broad band extending from about 2500 cm^{-1} to about 3700 cm^{-1} corresponds to absorbed water. Other information from the FT-IR spectra is the presence of carbonate groups ($-CO_3$) at 1660 cm^{-1}, which are due to the adsorption of species remaining from the aqueous precipitation [35]. The bands in the 1320–1480 cm^{-1} region and at 875 cm^{-1} correspond to residual nitrates and ammonia (NO_3^-, NH_4^+) derived from the reagents used in the synthesis of powders [36].

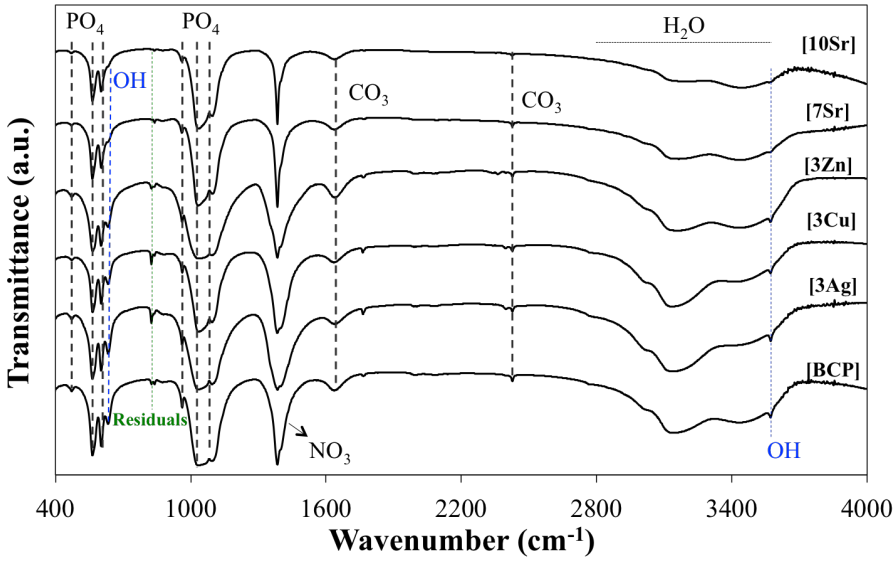

Fig. 1. FT-IR spectra obtained for as prepared all powders (BCP, 3Ag, 3Cu, 3Zn, 7Sr and 10Sr).

The thermal behaviour of the powders from 30ºC up to 1300ºC was studied by simultaneous thermogravimetric and differential thermal analysis to assess the influence of substituting ions on the phase transformation. The results displayed in Fig. 2 reveal that doping ions have a great impact on the thermal behaviour of the precipitated powders. The mass losses upon heating up to 1300ºC were 25%, 34%, 38% 23%, 24% and 19% for BCP, 3Ag, 3Cu, 3Zn, 7Sr and 10Sr, respectively. Despite these differences, the mass loss occurred in three different consecutive stages for all the powders. Within the first stage (30–250ºC), all samples experienced similar weight losses of about 5%, attributed to the removal of physically adsorbed water. As expected, the corresponding DTA curves reveal endothermic effects peaking at ~100–120ºC. The second step within the 250–300ºC range is due to the loss of chemisorbed residuals, accompanied by a structural reorganization as can be deduced from the exothermic peaks in DTA curves [37]. This exothermic effect can be attributed to the condensation of hydrogenophosphate ions (HPO_4^{-2}), resulting in the formation of pyrophosphates ($P_2O_7^{-4}$) [38] as given below in equation 1:

$$2Ca^{2+} + 2\,HPO_4^{2-} \rightarrow Ca_2P_2O_7 + H_2O \qquad (1).$$

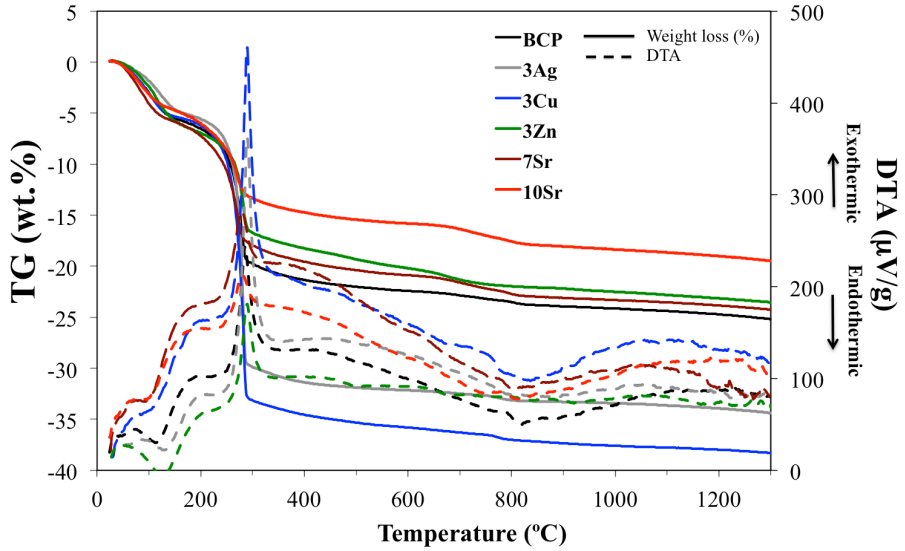

Fig. 2. TG (—) and DTA (- -) plots for different powders.

The release of water as described by Eq. (1) helps explaining the abrupt weight losses peaking at ~280–290ºC. These weight losses were higher for 3Ag and 3Cu powders. The FT-IR spectra of these two powders (Fig. 1) also confirm the presence of largest amounts of absorbed water together with residual species from the synthesis (carbonates and nitrates). The incorporation of these dopant ions (Ag^{+} and Cu^{2+}) in the crystalline lattice is more difficult as detailed below (Section 3.3), producing vacant positions in the Ca^{2+} lattice sites. Such structural defects are likely to foster water absorption, corroborating the higher weight losses determined by TG analysis (Fig. 2). Along the third step (temperatures >300ºC) all the powders experienced similar gradual weight losses of ~5%. The thermal curves present inflections centred at around 800ºC due to an endothermic event accompanied by a slight weigh loss. These effects can be attributed to the formation of β-$Ca_3(PO_4)_2$ [39] as described by equation (2):

$$Ca_2P_2O_7 + Ca(OH)_2 \rightarrow Ca_3(PO_4)_2 + H_2O \qquad (2).$$

These transformations within the temperature range of 700–800ºC gave raise to weight losses of about 1.2% in 7Sr and 10Sr powders, and to smaller variations in the other powders. The gradual formation of crystalline HA and β-TCP as temperature increases is translated by exothermic effects, which occur earlier in the case of doped

powders. The small differences observed are likely due to structural changes associated with the incorporation of the various doping ions in the biphasic mixtures. The small endothermic peaks appearing at ~1280ºC can be attributed to the α-TCP phase transformation. These results reveal that the ions have a great impact on the thermal behaviour of apatite powders.

The FT-IR spectra of doped and non-doped powders after calcination at 1000 ºC are displayed in Fig. 3. It can be seen that all the peaks powders corresponding to adsorbed water and residual nitrates and carbonates have disappeared and all the detected vibrations belong to calcium phosphates (HA and β-TCP). In addition to the typical $-PO_4$ and $-OH$ vibrations detected before calcination (Fig. 1), the absorption band at 475 cm^{-1} is assigned to doubly degenerate v_2 O–P–O bending moment, while bands at 575 cm^{-1} and 609 cm^{-1} are due to $-PO_4^{3-}$ vibration modes of HA. The absorbance bands at 940 cm^{-1} and 970 cm^{-1} are due to v_1 non-degenerate P–O symmetry stretching mode, 1041 cm^{-1} and 1160 cm^{-1} denote triply degenerate v_3 anti-symmetric vibration modes confirming the presence of β-TCP. The comparison of the FT-IR spectra from non-doped and doped compositions reveals an attenuation of the OH-related bands for doped powders. This intensity attenuation is consistent with the lower fraction of HA in doped powers, which is the phase responsible for the OH bands.

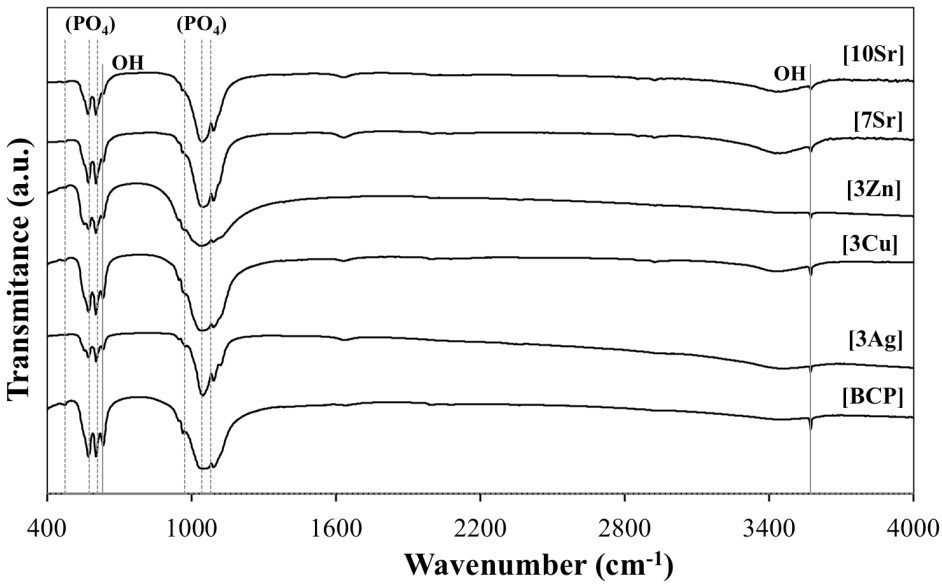

Fig. 3. FT-IR spectra obtained for all powders (BCP, 3Ag, 3Cu, 3Zn, 7Sr and 10Sr) after calcination at 1000ºC.

3.2. Physical characteristics

The values of specific surface area (SSA) measured for all powders, as prepared and after calcination at 1000ºC, are displayed in Fig. 4. Significant differences within the range of ~27–64 $m^2 \cdot g^{-1}$ can be observed among the as prepared powders doped with different ions. The lower SSA values were observed for 10Sr, followed by BCP, and the higher ones were registered for 3Cu and 3Zn. These differences suggest that the structural disturbances induced by the incorporation of dopant ions in the lattice are strongly dependent on the specific doping ion. On the other hand, calcination at 1000ºC induced drastic decreases in SSA for all tested powders to values within the range ~1–7 $m^2 \cdot g^{-1}$. Interestingly, the lowest value after calcination was measured for 3Zn powder that exhibited the highest SSA before calcination. This drastic decrease can be attributed to the role of zinc in enhancing mass bulk diffusion and densification. Mass diffusion upon calcination is expected to occur especially within agglomerates of fine particles as deduced from the relatively high values of SSA [40]. Less extensive decreases in SSA were observed for powders doped with other ions.

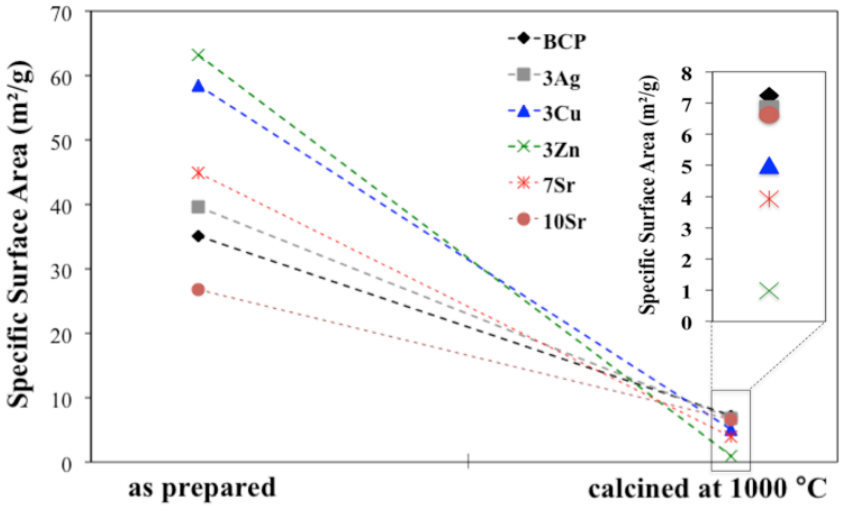

Fig. 4. Specific surface area of the as prepared and calcined at 1000ºC powders.

The SEM micrographs of as prepared powders are shown in Fig. 5, confirming that primary particles are sub micrometre and appear strongly agglomerated. This agglomeration most probably results from the strong capillary forces among fine primary particles upon drying.

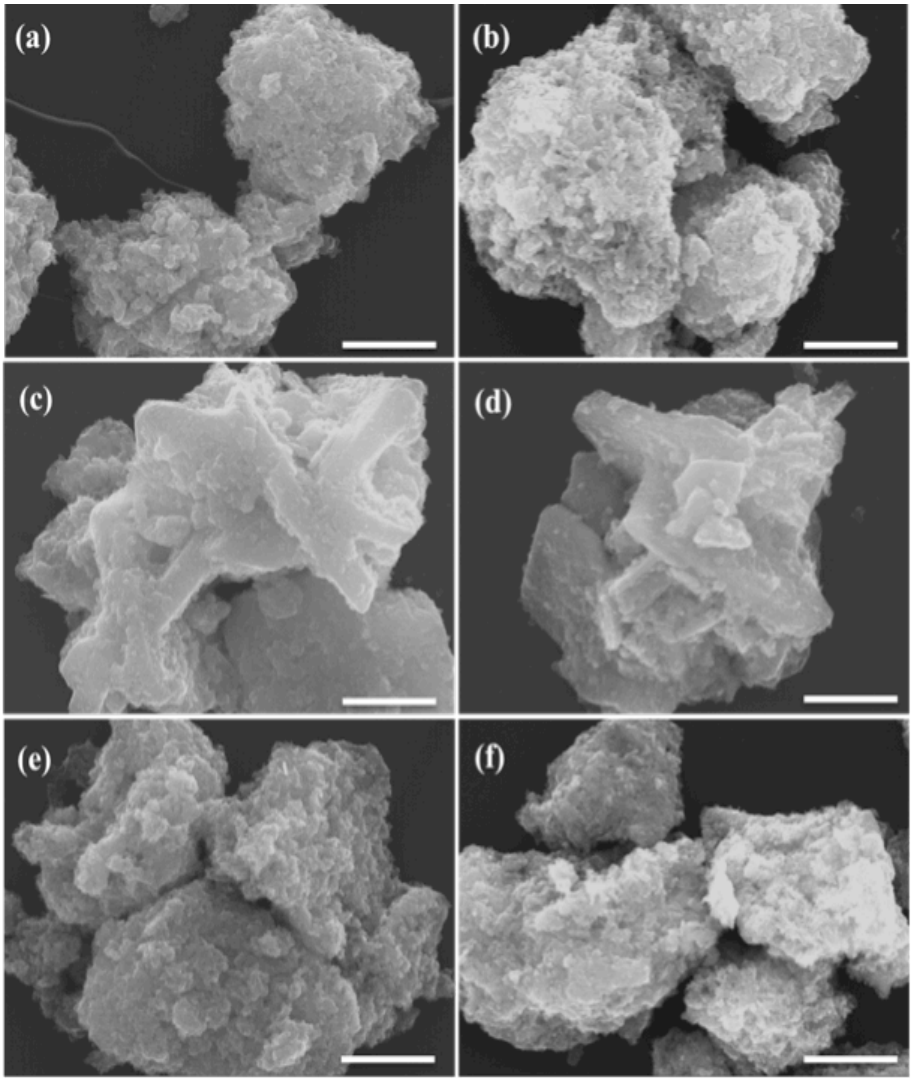

Fig. 5. SEM micrographs of the as prepared powders BCP (a), 3Ag (b), 3Zn c), 3Cu (d), 7Sr (e) and 10Sr (f) (bar: 5μm).

Particle/agglomerate size distributions (PSD) of calcined powders are presented in Table 1. All powder batches exhibit dissimilar size distributions, proving that particle agglomeration degree is strongly dependent on the dopant nature. The average

particle/agglomerate sizes measured were ~3.9 mm, 7.4 mm, 6.6 mm, 10.0 mm, 2.8 mm and 4.9 mm for BCP, 3Ag, 3Cu, 3Zn, 7Sr and 10Sr powders, respectively. These values confirm that particles are extensively agglomerated in good consistency with the morphological features of powders displayed in SEM photographs in Fig. 6.

Table 1. Particle size distributions of BCP, 3Ag, 3Cu, 3Zn, 7Sr and 10Sr powders, after calcination at 1000ºC.

	Particle size distribution			
		D_x[a] (µm) (±0.05 **µm**)		
Sample code	**Mean (µm)**	**D_{10}**	**D_{50}**	**D_{90}**
BCP	5.8	0.50	3.9	14.3
3Ag	8.7	0.73	7.4	18.3
3Cu	7.6	1.0	6.6	15.7
3Zn	10.2	1.4	10.0	18.7
7Sr	3.5	0.5	2.8	8.0
10Sr	4.8	0.6	4.9	9.0

[a] D_x is the particle diameter at or below which there is the amount x (vol.%) of particles in the cumulative (from 0 to 100%) particle size distribution curve.

It is also evident that morphological features of powders strongly depend on the specific doping element used, an effect that is likely associated to ion ability for bulk diffusion upon calcination, accentuating the neck formation among the primary particles. The agglomeration degree is apparently more severe in the case of the powder doped with zinc (3Zn), as expected, considering its lowest SSA value after calcination and the greater variation upon the heat treatment as referred above. This is the reason why zinc oxide is often used as sintering additive in diverse ceramic compositions. Silver seems to favour the formation of more elongated particle shapes, in contrast to the more rounded morphologies observed for the other compositions.

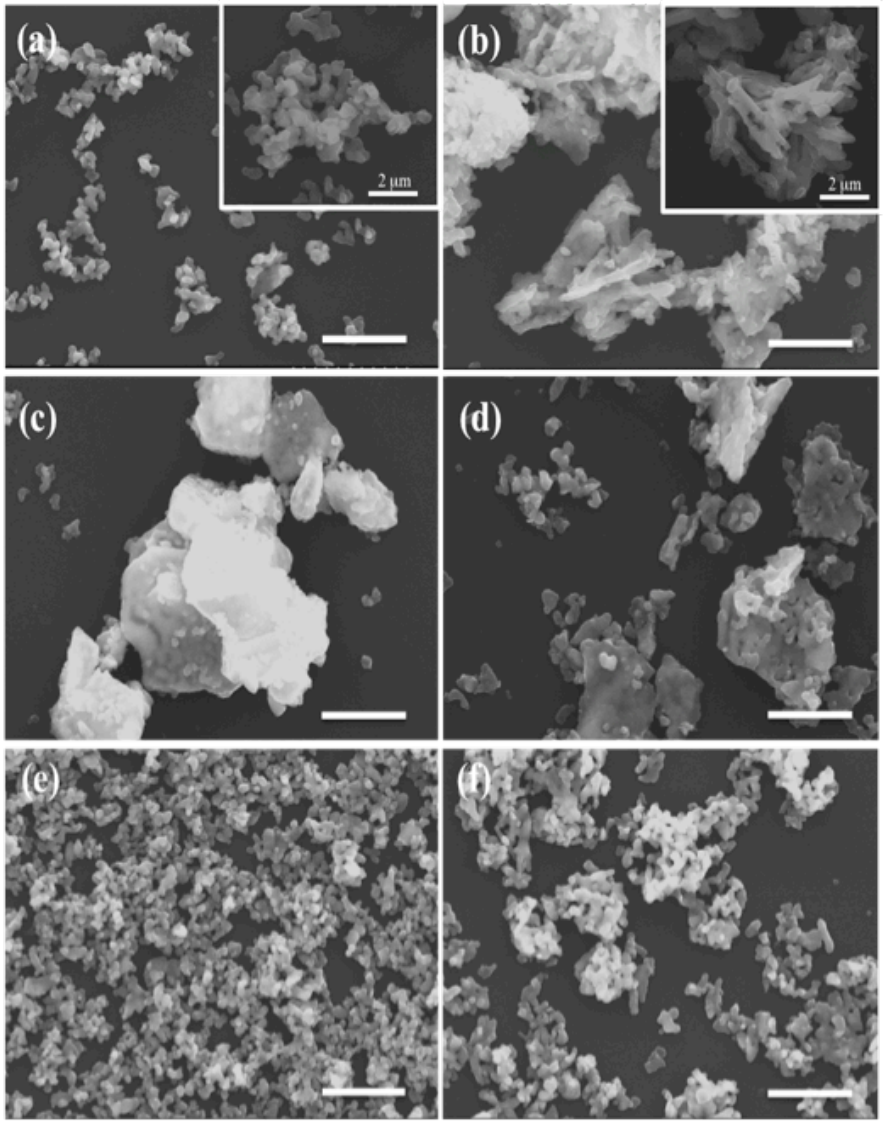

Fig. 6. SEM micrographs of the powders calcined, BCP (a), 3Ag (b), 3Zn c), 3Cu (d), 7Sr (e) and 10Sr (f) (bar: 5µm).

3.3. Phases identification and quantitative phases analysis

The effect of doping ions on crystalline phase assemblage was investigated after heat-treatment at 1000ºC. The XRD patterns of powders presented in Fig. 7 confirm the presence of two phases (HA and β-TCP) in all synthesised powders. The diffraction peaks are sharp and well defined. A detailed observation enables detecting slight shifts in the peak positions of the doped compositions in comparison to non-doped BCP. The shifts are towards the left or the right, when the ionic radius of dopant is

larger or smaller, respectively. The XRD data was refined assuming, for HA, the space group P63/m and the unit cell and structural parameters reported by Arcos *et al.* [33], and for β-TCP, the space group R3c and the parameters reported by S. Nicolopoulos *et al.* [34].

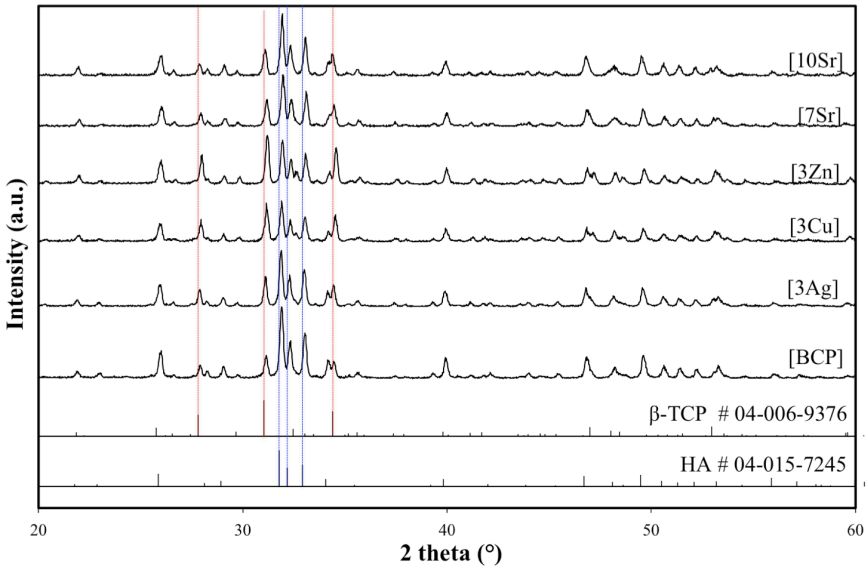

Fig. 7. XRD patterns of powders (BCP, 3Ag, 3Cu, 3Zn, 7Sr and 10Sr).

Fig. 8 presents the refined XRD for BCP powder as a representative example of all powders, being the refined lattice parameters for all compositions studied presented in Table 1. For BCP, the refined cell parameters were $a = b = 9.414432$ Å, $c = 6.876729$ Å, $\alpha = \beta = 90^{\circ}$, and $\gamma = 120^{\circ}$ in HA phase and $a = b = 10.43256$ Å, $c = 37.35914$ Å, $\alpha = \beta = 90^{\circ}$, and $\gamma = 120^{\circ}$ in β-TCP phase.

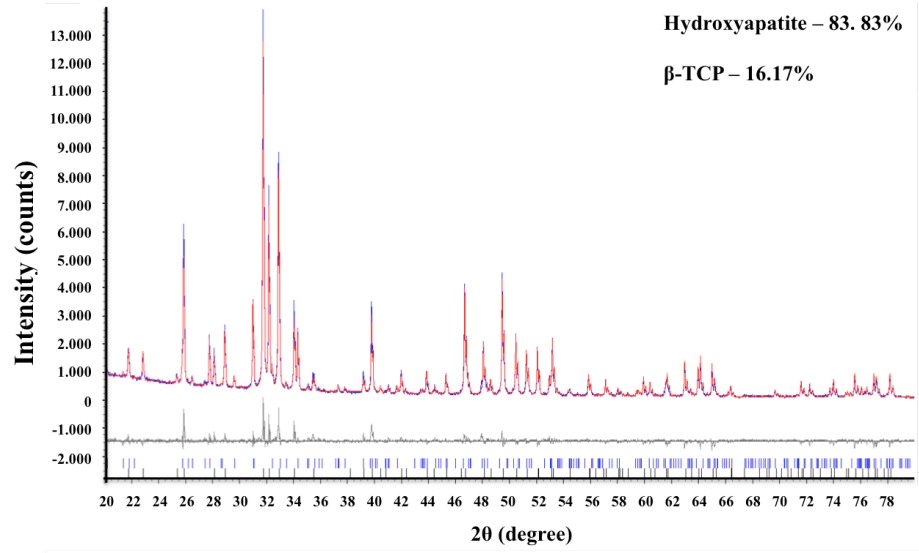

Fig. 8. Rietveld analysis patterns of powder diffraction data of non-doped powder (BCP). Blue line: calculated intensities; Red line: observed intensities. The difference between the observed and calculated intensities is plotted below the profile.

The refined lattice data for all doped (3Ag, 3Cu, 3Zn, 7Sr, 10Sr) and non-doped (BCP) powders are plotted in Fig. 9. As it can be seen, all doped compositions present slight changes in lattice parameters in comparison to BCP. The lattice parameters are higher for powders containing Ag^{+} and Sr^{2+}, meaning that the substitution of Ca^{2+} (0.099 nm) in the HA and β–TCP lattices by ions with larger radii, Sr^{2+} (0.12 nm) and Ag^{+} (0.126 nm) makes the lattices to expand. The effect becomes even more evident for the higher strontium content (10Sr). Oppositely, the lattices of powders doped with elements of smaller ionic radii, Cu^{2+} (0.072 nm) and Zn^{2+} (0.075 nm) underwent slight decreases in their cell parameters. These results are in good agreement with previous reports, where the authors shown that Zn^{2+} and Cu^{2+} substitute Ca^{2+} sites in HA or β–TCP lattice, resulting in a shrinkage of the unit cell parameters due to the smaller size of dopant cations when compared to calcium ion [17,41]. Increases in cell parameters were observed for HA and β–TCP doped with larger sized ions than calcium [41,42]. Moreover, from the results presented in Fig. 9, there seems to be a tendency for these doping elements to enter preferentially in the β–TCP lattice rather than HA.

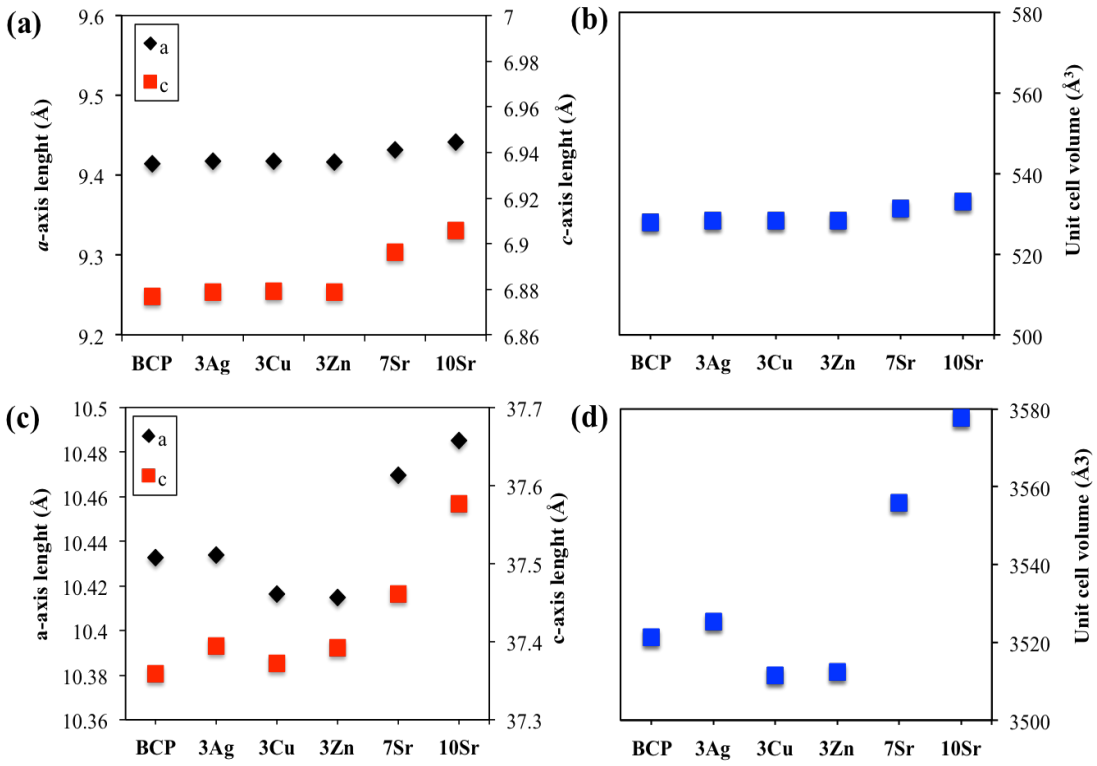

Fig. 9. Influence of doping ions (Ag, Cu, Zn and Sr) on the lattice *a*- and *c*-axis parameters and the unit cell volumes of HA (a, b) and β-TCP (c, d). Lattice parameters measured for BCP (biphasic calcium phosphate): a = 9.414432 Å, c = 6.876729 Å for HA; a = 10.43256 Å, c = 37.35914 Å for β-TCP.

Table 2 compares the planned and experimentally determined ions content (by ICP analysis) in the different powder compositions, which together with changes in the unit cell parameters (Fig. 9) confirm the incorporation of dopant ions into the HA and β-TCP lattices. The quantitative phase analysis data from Rietveld refinement is also reported, confirming the presence of both HA and β-TCP phases in all compositions. The amount of HA is highest for the control BCP sample, thus, the amounts of β-TCP increase in detriment of HA in doped compositions, but not in the same extent.

Table 2. Compositions planned and experimentally obtained from ICP analysis. The amounts of HA and β-TCP were determined by Rietveld refinement. 95% repeatability limits of the phase quantification should be considered to be close to ±1% [43].

Sample Code	(Ca+M)/P molar ratio	Ca/P molar ratio	Compositions (mol%)								Wt. % of phase composition (±1)	
			Planned				Experimental (± 0.03)					
			M				M				HA	β–TCP
			Ag	Cu	Zn	Sr	Ag	Cu	Zn	Sr		
BCP	1.62	1.62	0	0	0	0	0	0	0	0	83.8	16.2
3Ag	1.62	1.57	3	0	0	0	0.8	0	0	0	66.1	33.9
3Cu	1.62	1.57	0	3	0	0	0	2.6	0	0	50.0	50.0
3Zn	2.50	2.42	0	0	3	0	0	0	2.9	0	46.7	53.3
7Sr	1.62	1.50	0	0	0	7	0	0	0	7.0	64.1	35.9
10Sr	1.62	1.45	0	0	0	10	0	0	0	10.1	66.9	33.1

The unit cell of HA, $Ca_{10}(PO_4)_6(OH)_2$, contains 10 Ca^{2+} in two different positions: the Ca(1) site, where four cations are connected with nine oxygen atoms (mean Ca(1)–O distances 0.255 nm), and the Ca(2) site, where six cations are connected with seven oxygen atoms (mean Ca(2)–O distance 0.245 nm) [44-46]. When doping ions are added to the structure, Ca(1) atoms (aligned in columns within the HA) are preferably substituted by the smaller or slightly larger ones in low concentrations. As stronger interactions are present in these sites, any small change in the metal–oxygen interactions affects the entire lattice [46]. The Ca(2) atoms, displayed in consecutive staggered layers, allow random local substitutions without compromising the whole structure, consequently, larger cation, even at high concentrations, tend to substitute Ca(2) [46].

On the other hand, the crystal structure of β-TCP possesses five different Ca sites in its structure. According to Ananth *et al.* [47], Ca(4) and Ca(5) in β-TCP structure are distinct from the other three sites and are prone for substitution with smaller cations. Ca(4)–O(9) bond length is 0.304 nm, longer than the normal Ca–O bonds length of 0.240 nm, with Ca(5) sites surrounded by O in six fold distorted octahedral coordination. All these structural characteristics make small ionic substitutions possible.

In the present case, not only dopant amounts are varied as well as their size is different. So, the substitution level of Ca^{2+} in the Ca(I) or Ca(II) position was responsible for the difference in the percentage transformation of HA to β-TCP phase. Doping elements with ionic radii smaller than Ca tend to preferentially occupy Ca lattice places in the structure of β-TCP, stabilizing it and favouring the formation of higher percentages of this phase. Oppositely, the substitution of Ca^{2+} by larger size Sr^{2+} or Ag^{+} ions leads to denser atomic packings, causing retardation of crystal growth. This tends to hinder the formation of β-TCP [48] as confirmed by Rietveld refinement results, where higher HA contents were observed in powders doped with Sr^{2+} or Ag^{+} (Table 2).

The amounts of reagents were planned by assuming that doping ions (silver, copper, zinc and strontium) would substitute equivalent amounts of calcium ions. A good matching between planned and experimentally measured values is observed for strontium that has an ionic radius ~21% larger in comparison to Ca^{2+}. However, when the ionic size mismatch increases to ~27% (Ag^{+}) the degree of substitution becomes more difficult. The data reported in Table 2 reveals that only about 27% of the planned Ag^{+} has entered the crystalline lattices. This discrepancy in the incorporation hindrance can be caused by silver´s ionic size and its fusion temperature (T_{fus} = 961.8 ºC), that can lead the ions to leave the structure during the calcination process [49]. The measured concentrations are close than the planned ones for cooper (~87%) and zinc (~97%), even though in this last case a total ratio (Ca+Zn)/P = 2.5 had to be used to grant the formation of a biphasic powder, as stated in the experimental section (2.1.1. Powders preparation). As mentioned in the existing literature, zinc tends to inhibit the formation of HA phase, reducing the crystallite size and decreasing thermal stability [29,30].

3.4. Biological Properties

The antimicrobial activity of powders against the two most common bacterial strains that frequently cause infection in humans, Gram-negative *E. coli* (ATCC 25922) and Gram-positive *S. aureus* (ATCC 25923), were qualitatively evaluated. The results of the disk diffusion tests showed that only 3Ag powders affect the *S. aureus* (Fig. 10a), being the average inhibition zone around 2 mm. The fact that the antimicrobial activity has only been verified against one of the bacterial strains can be explained by differences in their cell envelope structures, since *S. aureus* is Gram-positive and *E. coli* is Gram-negative bacteria. It was difficult to establish any bactericidal effect for the powders doped with zinc and copper (results not shown). There are three main mechanisms to explain the antimicrobial activity of these ions [50-53]. First, metal ions could bind to specific groups of the protein chains deactivating them. Second, metal ions can interact with microbial membrane and induce structural and permeability changes. Finally, metal ions could interact with microbial nucleic acids, preventing microbial replication.

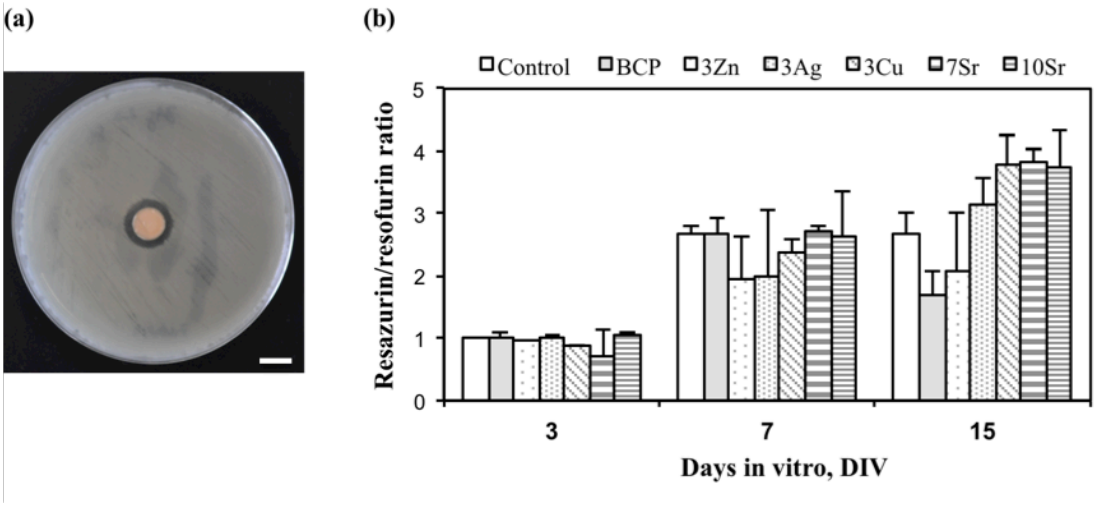

Fig. 10. Biological activities of the sintered powders. (a) Photographs of antimicrobial test for 3Ag against S. aureus (ATCC 29213). Bar: 1 cm. (b) Influence of BCP, 3Zn, 3Ag, 3Cu, 7Sr and 10Sr on the metabolic activity of MG-63 pre-osteoblastic cells. Results are depicted as mean final optical density (O.D.f) ± SE (n = 3-4). Statistically significant differences of metabolic activity were found throughout cell culture ($F(2,18) = 103.097$; $p = <0.001$ $\eta^2p = 0.920$; Bonferroni post-hoc analysis: 3 DIV *vs* 7 DIV and 14 DIV $p = <0.001$; 7DIV *vs* 14DIV $p = 0.003$). No statistically significant differences between groups ($F(6,9) = 3.019$; $p = 0.067$ $\eta^2p = 0.668$).

The alterations in the metabolic activity of pre-osteoblastic cells, assessed through the reversible resazurin assay that indirectly measures the number of live cells, is displayed in Fig. 10b. Results indicate that doping ions (Ag^{+}, Zn^{2+}, Cu^{2+} and Sr^{2+}) do not exert any cytotoxic effects on MG-63 pre-osteoblastic cells. Similar levels of resazurin reduction by cells exposed to the powders or not (control cells) were registered on day 3. Differences began to be noticed from day 7 in culture. The most severe decrease in the proliferative response occurred for cells grown with the BCP and 3Zn at both time points (7 and 14 DIV). In opposition, the 3Ag, 3Cu, 7Sr and 10Sr present the highest levels of resazurin conversion on day 14. These findings demonstrated that doping biphasic calcium phosphate powders with these ions stimulate cell growth. Strontium is already known to increase osteoblastic proliferation [15,42,54]. According to Caverzasio [55], Sr^{2+} may directly interact with the calcium sensing receptor in osteoblast cells to trigger mitogenic signals, via activation of the protein kinases ERK, PKC and PKD signaling pathways, resulting in increased cell division. Nevertheless, the mechanisms by which Ag^{+} and Cu^{2+} ions affect the biological response are still unclear and require further investigation.

4. Conclusions

Biphasic calcium phosphates doped with different ions were successfully synthesized by precipitation from all compositions, with the crystalline phase assemblages and the biological performances were strongly depending on the specific dopant ions. Sr^{2+} was the only one capable to enter totally in the lattice structures of both HA and β-TCP phases replacing calcium ions. The results indicate that the ability to substitute Ca^{2+} by other ions in the HA or β–TCP lattice structures is greatly dependent on the ionic size, with larger ionic radii mismatches resulting in less extensive substitution degrees. Only silver-doped powder exhibited antimicrobial activity against *S. aureus*, while powders doped with copper and zinc did not show any antimicrobial effects. Good osteoblastic biocompatibility was demonstrated for Ag, Cu and Sr-substituted powders. These findings are important tips for designing better synthetic bone graft substitute materials and constitute a first step of a more extended research program aiming to develop appropriate powders for biomedical applications including osteoregeneration, providing a good environment for osteoblasts.

REFERENCES

[1] A. Oryan, S. Alidadi, A. Moshiri, N. Maffulli, Bone regenerative medicine: classic options, novel strategies, and future directions, J. Orthop. Surg. Res. 9 (2014) 1–27.

[2] L.L. Hench, Bioceramics, J. Am. Ceram. Soc. 81 (1998) 1705–1728.

[3] D.C. Greenspan, Bioactive ceramic implant materials, Curr. Opin. Solid State Mater. Sci. 4 (1999) 389–393.

[4] G. Daculsi, R.Z. LeGeros, D. Mitre, Crystal dissolution of biological and ceramic apatites, Calcif. Tissue Int. 45 (1989) 95–103.

[5] J. Franco, P. Hunger, M.E. Launey, A.P. Tomsia, E. Saiz, Direct write assembly of calcium phosphate scaffolds using a water-based hydrogel, Acta Biomater. 6 (2010) 218–228.

[6] S. Kannan, J.M.G. Ventura, A.F. Lemos, A. Barba, J.M.F. Ferreira, Effects of sodium addition on the precipitation of hydroxyapatites and biphasic ceramics, Ceram. Int. 34 (2008) 7–13.

[7] M. Kamitakahara, C. Ohtsuki, T. Miyazaki, Review paper: behaviour of ceramic biomaterials derived from tricalcium phosphate in physiological condition, J. Biomater. Appl. 23 (2008) 197–212.

[8] G. Daculsi, Biphasic calcium phosphate concept applied to artificial bone, implant coating and injectable bone substitute, Biomaterials 19 (1998) 1473-1478.

[9] R.Z. LeGeros, S. Lin, R. Rohanizadeh, D. Mijares, J.P. LeGeros, Biphasic calcium phosphate bioceramics: Preparation, properties and applications, J. Mater. Sci. Mater. Med. 14 (2003) 201–209.

[10] O. Gauthier, J.M. Bouler, E. Aguado, R.Z. LeGeros, P. Pilet, G. Daculsi, Elaboration conditions influence physicochemical properties and in vivo bioactivity of macroporous biphasic calcium phosphate ceramics, J. Mater. Sci. Mater. Med. 10(4) (1999) 199–204.

[11] M. Bohner, Silicon-substituted calcium phosphates–a critical view, Biomaterials 30 (2009) 6403–6406.

[12] S. Kannan, F. Goetz-Neunhoeffer, J. Neubauer, A.H.S. Rebelo, P. Valério, J.M.F. Ferreira, Rietveld structure and in vitro analysis on the influence of

magnesium in biphasic (hydroxyapatite and β -tricalcium phosphate) mixtures, J. Biomed. Mater. Res. Part B: Appl. Biomater. 90B (2009) 404–411.

[13] P.M.C. Torres, S.I. Vieira, A.R. Cerqueira, S. Pina, O.A.B. da Cruz Silva, J.C.C. Abrantes, J.M.F. Ferreira, Effects of Mn-doping on the structure and biological properties of β-tricalcium phosphate, J. Inorg. Biochem. 136 (2014) 57–66.

[14] G.A. Fielding, A. Bandyopadhyay, S. Bose, Effects of SiO_2 and ZnO doping on mechanical and biological properties of 3D printed TCP scaffolds, Dent. Mater. 28 (2012) 113–122.

[15] S. Pina, S.I. Vieira P. Rego, P.M.C. Torres, O.A.B. da Cruz e Silva, E.F. Cruz e Silva, J.M.F. Ferreira, Biological responses of brushite-forming Zn- and ZnSr-substituted β-tricalcium phosphate bone cements, Eur Cell Mater 20 (2010) 162–177.

[16] T.N. Kim, Q.L. Feng, J.O. Kim, J. Wu, H. Wang, G.C. Chen, F.Z. Cui, Antimicrobial effects of metal ions (Ag^{+}, Cu^{2+}, Zn^{2+}) in hydroxyapatite, J. Mater. Sci. Mater. Med. 9(3) (1998) 129–34.

[17] V. Stanić, S. Dimitrijević, J. Antić-Stanković, M. Mitrić, B. Jokić, I. B. Plećaš, S. Raičević, Synthesis, characterization and antimicrobial activity of copper and zinc-doped hydroxyapatite nanopowders, Appl. Surf. Sci. 256 (2010) 6083–6089.

[18] Y. Chen, X. Zheng, Y. Xie, Ch. Ding, H. Ruan, C. Fan, Anti-bacterial and cytotoxic properties of plasma sprayed silver-containing HA coatings, J. Mater. Sci. Mater. Med. 19 (2008) 3603–3609.

[19] W. Opsahl, H. Zeronian, M. Ellison, D. Lewis, R.B. Rucker, R.S. Riggins, Role of copper in collagen cross-linking and its influence on selected mechanical properties of chick bone and tendon, J. Nutr. 112 (1982) 708–716.

[20] N.M. Lowe, W.D. Fraser, M.J. Jackson, Is there a potential therapeutic value of copper and zinc for osteoporosis?, Proc. Nutr. Soc. 61 (2002) 181–185.

[21] M. Yamaguchi, H. Oishi, Y. Suketa, Stimulatory effect of zinc on bone-formation in tissue-culture, Biochem. Pharmacol. 36 (1987) 4007–4012.

[22] M. Yamaguchi, R. Yamaguchi, Action of zinc on bone metabolism in rats – increases in alkaline-phosphatase activity and DNA content, Biochem. Pharmacol. 35 (1986) 773–777.

[23] X. Li, Y. Sogo, A. Ito, H. Mutsuzaki, N. Ochiai, T. Kobayashi, S. Nakamura, K. Yamashita, R.Z. LeGeros, The optimum zinc content in set calcium phosphate cement for promoting bone formation in vivo, Mater. Sci. Eng. C 29 (2009) 969–975.

[24] M. Otsuka, S. Marunaka, Y. Matsuda, A. Ito, P. Layrolle, H. Naito, N. Ichinose, Calcium level-responsive in vitro zinc release from zinc containing tricalcium phosphate (ZnTCP), J. Biomed. Mater. Res. 52 (2000) 819–824.

[25] Z. Radovanović, B. Jokić, D. Veljović, S. Dimitrijević, V. Kojić, R. Petrović, D. Janaćković, Antimicrobial activity and biocompatibility of Ag^{+}- and Cu^{2+}-doped biphasic hydroxyapatite/α-tricalcium phosphate obtained from hydrothermally synthesized Ag^{+}- and Cu^{2+}-doped hydroxyapatite, Appl. Surf. Sci. 307 (2014) 513–519.

[26] W. Chen, S. Oh, A.P. Ong, N. Oh, Y. Liu, H.S. Courtney, M. Appleford, J.L. Ong, Antibacterial and osteogenic properties of silver-containing hydroxyapatite coatings produced using a sol–gel process, J. Biomed. Mater. Res. A, 82 (2007) 899–906.

[27] Y. Li, J. Ho, C.P. Ooi. Antibacterial efficacy and cytotoxicity studies of copper(II) and titanium(IV) substituted hydroxyapatite nanoparticles. Mater. Sci. Eng. C 30 (2010) 1137–1144.

[28] N. Iqbal, M.R.A. Kadir, N.H. Mahmood, N. Salim, G.R.A. Froemming, H.R. Balaji, T. Kamarul, Characterization, antibacterial and in vitro compatibility of zinc–silver doped hydroxyapatite nanoparticles prepared through microwave synthesis, Ceram. Inter. 40 (2014) 4507–4513.

[29] A. Bigi, E. Foresti, M. Gandolfi, M. Gazzano, N. Roveri, Inhibiting effect of zinc on hydroxylapatite crystallization, J Inorg Biochem 58 (1995) 49–58.

[30] F. Miyaji, Y. Kono, Y. Suyama, Formation and structure of zinc-substituted calcium hydroxyapatite, Mater. Res. Bull. 40 (2005) 209–220.

[31] N. Kanzaki, K. Onuma, G. Treboux, S. Tsutsumi, A. Ito, Inhibitory effect of magnesium and zinc on crystallization kinetics of hydroxyapatite (0 0 0 1) face, J Phys Chem B 104 (2000) 4189–4194.

[32] T.A. Fuierer, M. LoRe, S.A. Puckett, G.H. Nancollas, A mineralization adsorption and mobility study of hydroxyapatite surfaces in the presence of zinc and magnesium ions, Langmuir 10 (1994) 4721–4725.

[33] S. Nicolopoulos, J.M. Gonzalez Calbet, M.P. Alonso, M.T. Gutierrez Rios, M.I. De Frutos, M. Vallet Regi, Characterization by TEM of Local Crystalline Changes during Irradiation Damage of Hydroxyapatite Compounds, J. Solid State Chem. 116 (1995) 265–274.

[34] D. Arcos, J. Rodriguez-Carvajal, M. Vallet-Regi, The effect of the silicon incorporation on the hydroxylapatite structure. A neutron diffraction study, Solid State Sci. 6 (2004) 987–994.

[35] I.R. Gibson, S.M. Best, W. Bonfield, Chemical characterization of silicon substituted hydroxyapatite, J. Biomed. Mater. Res. 44 (1999) 422 – 428.

[36] S. Raynaud, E. Champion, D. Bernache-Assollant, P. Thomas, Calcium phosphate apatites with variable Ca/P atomic ratio I. Synthesis, characterisation and thermal stability of powders, Biomaterials 23 (2002) 1065–1072.

[37] S. Kannan, A. Rebelo, A.F. Lemos, A. Barba, J.M.F. Ferreira, Synthesis and mechanical behaviour of chlorapatite and chlorapatite/β-TCP, J. Eur. Ceram. Soc. 27(5) (2007) 2287–2294.

[38] S. Kannan, F. Goetz-Neunhoeffer, J. Neubauer, S. Pina, P.M.C. Torres, J.M.F. Ferreira, Synthesis and structural characterization of strontium- and magnesium-co-substituted β-tricalcium phosphate, Acta Biomaterialia 6 (2) (2010) 571-576.

[39] A. Mortier, J. Lemaître, P.G. Rouxhet, Temperature-programmed characterization of synthetic calcium-deficient phosphate apatites, Thermochim. Acta 143 (1989) 265–282.

[40] R.Z. LeGeros, N. Balmain, G. Nonel, Age-related changes in mineral of rat and bovine cortical bone, Calcif. Tissue Int. 41(3) (1987) 137–144.

[41] K. Sanjeevi, F. Goetz-Neunhoeffer, J. Neubauer, J.M.F. Ferreira, Cosubstitution of Zinc and Strontium in β-Tricalcium Phosphate: Synthesis and Characterization, J. Am. Ceram. Soc. 94(1) (2010) 230–235.

[42] G.A. Fielding, M. Roy, A. Bandyopadhyay, S. Bose, Antibacterial and biological characteristics of silver containing and strontium doped plasma sprayed hydroxyapatite coatings, Acta Biomater. 8 (2012) 3144–3152.

[43] N. Döbelin, Interlaboratory study on the quantification of calcium phosphatephases by Rietveld refinement, Powder Diffr. 30 (3) (2015) 231–241.

[44] J.C. Elliott, Structure and Chemistry of the Apatites and Other Calcium Orthophosphates, Elsevier, Amsterdam, 1994.

[45] D.E. Ellis, J. Terra, O. Warschkow, M. Jiang, G.B. González, J.S. Okasinski, M.J. Bedzyk, A.M. Rossi, J.G. Eon, A theoretical and experimental study of lead substitution in calcium hydroxyapatite, Phys. Chem. Phys. 28 (2006) 967–976.

[46] E. Boanini, M. Gazzano, A. Bigi, Ionic substitutions in calcium phosphates synthesized at low temperature, Acta Biomater. 6 (2010) 1882–1894.

[47] K. P. Anantha, S. Shanmugam, S.P. Jose, A.J. Nathanael, T.H. Oh, D. Mangalaraj, A.M. Ballamurugan, Structural and chemical analysis of silica-doped β-TCP ceramiccoatings on surgical grade 316L SS for possible biomedical application, J. Asian Ceram Soc 3 (2015) 317–324.

[48] C.M. Mardziah, I. Sopyan, S. Ramesh, Strontium-Doped Hydroxyapatite Nanopowder via Sol-Gel Method: Effect of Strontium Concentration and Calcination Temperature on Phase Behavior, Organs 23 (2009) 105 –113.

[49] S. Range, D. Hagmeyer, O. Rotan, V. Sokolova, J. Verheyen, B. Siebersb, M. Epple, A continuous method to prepare poorly crystalline silver-doped calcium phosphate ceramics with antibacterial properties, RSC Adv. 5 (2015) 43172–43177.

[50] G. Borkow, J. Gabbay, Copper as a biocidal tool, Curr. Med. Chem. 12 (2005) 2163–2175.

[51] B. Sugarman, Zinc and infection, Rev. Infect. Dis. 5 (1983) 137–147.

[52] S. Atmaca, K. Gül, R. Çiçek, The effect of zinc on microbial growth, Turk. J. Med. Sci. 28 (1998) 595–597.

[53] T.N. Phan, T. Bucker, J. Sheng, J.D. Baldeck, R.E. Marquis, Physiologic actions of zinc related to inhibition of acid and alkali production by oral streptococci in suspensions and biofilms, Oral Microbiol. Immun. 19 (2004) 31–38.

[54] C.F. Marques, A. Lemos, S.I. Vieira, O.A.B. da Cruz e Silva, A. Bettencourt, J.M.F. Ferreira, Antibiotic-loaded Sr-doped porous calcium phosphate granules as multifunctional bone grafts, Ceramic International 42(2) (2016) 2706–2716.

[55] J. Caverzasio, Strontium ranelate promotes osteoblastic cell replication through at least two different mechanisms, Bone 42 (2008) 1131–1136.

Chapter 4

BIPHASIC CALCIUM PHOSPHATE SCAFFOLDS FABRICATED BY DIRECT WRITE ASSEMBLY: MECHANICAL, ANTI-MICROBIAL AND OSTEOBLASTIC PROPERTIES

Catarina F. Marques[1], Fidel Hugo Perera[2], Ana Marote[3], Sónia Ferreira[4], Sandra I. Vieira[3], Susana Olhero[1], Pedro Miranda[2], José M.F. Ferreira[1]

[1] Department of Materials and Ceramics Engineering, University of Aveiro CICECO, 3810-193 Aveiro, Portugal

[2] Departamento de Ingeniería Mecánica, Energética y de los Materiales, Universidad de Extremadura, 06006 Badajoz, Spain

[3] Institute for Biomedicine (iBiMED), Department of Medical Sciences, University of Aveiro, 3810-193 Aveiro, Portugal

[4] Department of Health and Education, Institute of Education and Citizenship, 3770-033 Mamarrosa, Portugal

Journal of the European Ceramic Society 37 (2017) 359-368

Abstract

The present work reports on the fabrication of 3-D porous calcium phosphate scaffolds by robocasting from biphasic (HA/β-TCP ≈ 1.5) powders, undoped and co-doped with Sr and Ag. Scaffolds with different pore sizes and rod diameter of 410 μm were fabricated and sintered at 1100 ºC. The size and morphology of the powder particles, and the concentrations of the processing additives, were shown to play major roles in the robocasting process. For all pore sizes tested, the compressive strength of scaffolds was comparable to or even higher than that of cancellous bone, and mechanical data could be systematically correlated with the porosity fraction. Co-doping the starting powders with Sr and Ag enhanced the mechanical strength of scaffolds, conferred good antimicrobial activity against *Staphylococcus aureus* and *Escherichia coli*, and did not induce any cytotoxic effects on human MG-63 cells. Furthermore, the co-doped powder was more effective in inducing pre-osteoblastic proliferation.

Keywords: Robocasting, Biphasic calcium phosphate, Bone scaffolds, Mechanical properties.

1. Introduction

Calcium phosphate (CaP) bioceramics, both of natural and synthetic origin, are among the biomaterials with higher bone replacement potential [1,2]. In this regard, hydroxyapatite (HA) has received particular attention due to its biocompatibility, bioactivity, osteoconductivity and osteophilic nature [3,4]. The HA inability to resorb is however a weak point [5], and hence, biodegradable systems that do not require surgical removal have been emphasized [6-8]. Biphasic calcium phosphates (HA + β−TCP) possess a set of attractive characteristics, including: (a) different dissolution rates (HA, non-resorbable and β−TCP, resorbable); (b) rapid bone formation around the implant site; and (c) similarity to the inorganic component of bones [9-11].

In recent years, ionic substitutions in calcium phosphates (CaP) ceramics have been subject of massive interest owing to the critical roles these ions play in the biological process after implantation. For example, strontium (Sr^{2+}) increases osteoclast apoptosis and enhances pre-osteoblastic cell proliferation and collagen synthesis, and consequently depresses bone resorption, while maintaining bone formation [12]. Therefore, Sr-substituted CaPs are expected to produce enhanced biological and chemical responses in the body [13,14]. Since one of the most common problems when using implants is the risk of developing post-operatory infections and/or rejection, some attention has been turned to silver (Ag^{+}), an element with a long history in medicine as an antibacterial agent [15,16]. Accordingly, silver and silver ions are known to have strong inhibitory and bactericidal effects, as well as a broad spectrum of anti-microbial activities [17].

The strategies to regenerate bone tissues include the use of scaffolds with suitable 3D porous structures to act as temporary templates for migration, proliferation and differentiation of osteoblasts, which are the cells responsible for new bone formation [18–20]. Porosity and pore size of biomaterial scaffolds play a critical role in bone formation *in vitro* and *in vivo*. Porosity is necessary for bone tissue formation since it allows migration and proliferation of osteoblasts and mesenchymal stem cells, matrix deposition in the empty spaces, as well as vascularization. Several studies investigated the effects of pore size on the regeneration efficacy of mineralized bone. Altogether, results indicate that a minimum pore size of about 100 μm is required for cell migration and transport [21].

Current bone regeneration strategies are mainly based on the development of scaffolds, but the difficulties of manufacturing porous structures with suitable characteristics (geometry and size of pores, their spatial distribution, etc.) have been the major obstacles and constitute some of the greatest challenges in this area. Solid-freeform fabrication (SFF) techniques can overcome these obstacles, producing scaffolds with customized shape and predefined internal morphology, by building the structure layer-by-layer following a computer design, without the need for subsequent machining. Among these, robocasting, also referred to as direct-write assembly (DWA), is an additive manufacturing technique based on the extrusion of a concentrated colloidal suspension (ink/paste) [22,23]. The extruded continuous filament has pseudo-solid behaviour and is able to support its own weight during the assembly of the 3-D structures layer-by-layer. This technique has been successfully applied to the fabrication of bone tissue engineering scaffolds from both calcium phosphates and bioglasses [23-28]. Porosity in robocast scaffolds can be tailored on three length scales: macro- (greater than 100 μm), micro- (1–30 μm), and submicron (less than 1 μm). Macroscale porosity is introduced directly by the robocasting process as it draws successive layers. Robocast rods arranged in latticed patterns create macroporous pathways in three dimensions. By varying the rod spacing and size, these pathways can be precisely constructed to produce highly uniform macropores [29].

The main aims of the present study are: (i) the synthesis of CaP powders with antimicrobial and osteoblastic stimulation properties; (ii) developing high concentrated colloidal paste-like systems from these powders with the appropriate viscoelastic properties for scaffolds fabrication by robocasting, with controlled pore size (macroporosity) for bone regeneration and tissue engineering applications; (iii) correlate the porosity with the mechanical performance of the scaffolds.

2. Experimental procedure

2.1. Synthesis and characterisation of the starting powders

Calcium nitrate tetrahydrate [$Ca(NO_3)_2 \cdot 4H_2O$, Quality Chemicals, Spain], strontium nitrate [$Sr(NO_3)_2$, Sigma-Aldrich, Germany] and silver nitrate [$AgNO_3$, Alfa Aesar, Germany] were used as cationic precursors for Ca, Sr and Ag. Diammonium hydrogen phosphate solution [$(NH_4)_2HPO_4$, Quality Chemicals, Spain], was used as the source of phosphate.

The synthesis of the starting biphasic calcium phosphate powders with a planned total cationic/anionic molar ratio of 1.62 was envisaged in this work, one undoped (BCP) and the other a co-doped with 7 mol% Sr^{2+} and 3 mol% Ag^{+} (BCP-7Sr3Ag). For this, solutions of P and cationic species were firstly prepared with molar concentrations of 1.2 M and 1.94 M, respectively. The precipitation was carried out by slowly adding the required volume of P solution to a given volume of each continuously stirred (1000 rpm) cationic solution. The pH of the mixed system was increased to 9 and maintained at this value by adding the required amounts of 8 M ammonium hydroxide [NH_4OH, Sigma-Aldrich, Germany] solution. The reaction was performed at 90ºC for 2 h under constant stirring conditions (1000 rpm).

The suspensions were poured out from the reactor and the precipitates separated through vacuum filtration and dried at 100 ºC overnight. The prepared powders were calcined at 1100 ºC in a Thermolab furnace (Pt30%Rh/Pt6%Rh thermocouple) using a heating rate of 5 $ºC \times min^{-1}$ followed by a dwelling time of 2 h at that temperature, and then cooled to room temperature (RT). The calcined powders were then dry milled for 45 min in a high energetic ball milling up to achieving mean particle sizes of ~1 μm.

The phase assemblage of calcined powders was studied using a High Resolution X-ray Diffractometer (PANalytical X'Pert PRO) with Cu Kα radiation (k = 1.5406 Å) produced at 45 kV and 40 mA, which scanned the diffraction angles (2θ) between 20º and 80º with a step size of 0.01º, time per step 198,6450 s. A spectra-fitting software called HighScorePlus was utilised to quantify the percentages of crystalline phases for the calcined powders. This software requires crystallographic information files to fit

and quantify each specific phase within a XRD spectrum. The database utilized was PDF-47 2015 RDB, and the files utilised in the evaluation of the powders were; HA (# 01-079-5683) [30], β–TCP (# 04-014-2292) [31].

Particle size and particle size distributions of all powders were evaluated using a particle size analyser (COULTER LS230, UK) with Fraunhofer optical model.

2.2. Preparation and rheological characterization of the inks

The CaP inks for robocasting were prepared by dispersing the starting powders in aqueous media in the presence of some processing additives (dispersant, viscosifier agent and jellifying agent). Initially, high concentrated aqueous suspensions (55 vol.% and 60 vol.%, from BCP and BCP-7Sr3Ag powders, respectively) were prepared by adding 0.4 wt.% (relative to the dry mass of solids) of ammonium polycarbonate dispersant (Targon 1128, BK Ladenburg, Germany). Different amounts (1–2 % based on mass of solids) of hydroxypropyl methylcellulose (HPMC, average Mn~10,000, Sigma-Aldrich) were also added to increase the intrinsic viscosity of the liquid. The subsequent addition of varied amounts (0.1–1 %, based on mass of solids) of polyethylenimine (PEI, 50% w/v in water, Sigma-Aldrich) as cationic jellifying agent enabled adjusting the viscoelastic behaviour of the suspensions. The most drastic changes on the rheological properties occurred in the presence of 0.3 wt.% PEI. The resulting inks were suitable for robocasting. Since both HPMC and PEI were added as aqueous solutions, the final solid loadings of the inks decreased to 48 vol.% and 53 vol.% for BCP and BCP-7Sr3Ag, respectively. After each component addition, the system was placed in a planetary centrifugal mixer (ARE-250, Thinky Corp., Tokyo, Japan) for a few minutes to improve the homogeneity of the mixture.

Rheological measurements at different steps of ink preparation (after each incremental amount of the processing additives), were made using a Kinexus Pro^{+} Rheometer (Malvern, USA). The apparent viscosity of the ink was measured in viscometry mode using a cone and plate sensor system (4º/40 mm) and 150 μm gap size. The visco-elastic properties were assessed using the same rheometer equipped with plate and plate sensor (20 mm), with 1 mm gap size, in the oscillatory mode

using a solvent trap (a metal ring with di-ionized water) to prevent water evaporation from the samples during the tests.

In order to understand the specific interactions between the processing additives and the surface of calcium phosphate powder particles, zeta-potential measurements were evaluated (Malvern Zeta sizer, Nano ZS, Malvern, Worcestershire, UK) at several pH values. A dilute suspension was firstly prepared by ultrasonically dispersing the testing powder for 10 min, followed by 30 min rest for allowing the larger particles to settle. An aliquot taken from the supernatant was then used to measure the zeta potentials at different pH values. The pH of the suspensions was adjusted with 0.1 M HCl and 0.1 M NaOH, for decreasing and increasing pH runs, respectively.

2.3. Scaffolds printing by robocasting

3D BCP scaffolds consisting of a mesh of ceramic rods were constructed layer-by-layer via direct write assembly of the ink using a robotic deposition device (3-D Inks, Stillwater, OK) as illustrated in Fig. 1. The ink was deposited through cylindrical metallic deposition nozzles (EFD Inc., East Providence, RI) with a diameter d = 410 μm, at a printing speed of 10 $mm \cdot s^{-1}$ (Fig. 1a). The external dimensions of the scaffolds were about 9×9×3 (Fig. 1b) in a total of 12 layers. Each structure consisted of 9 individual scaffolds of 3×3×3 mm (Fig. 1c-d), which were produced with six different pore sizes of 120, 180, 220, 300, 350 and 500 μm. The deposition was performed into a paraffin oil bath to ensure uniform drying during assembly. The samples were removed from the bath and dried in air at RT for 24 h, heat treated at the heating rate of $1ºC \cdot min^{-1}$ up to 400ºC, and held at this temperature for 1 h to burnout the organics. The samples were subsequently sintered at 1100 ºC for 2 h using a heating rate of $5\ ºC \cdot min^{-1}$.

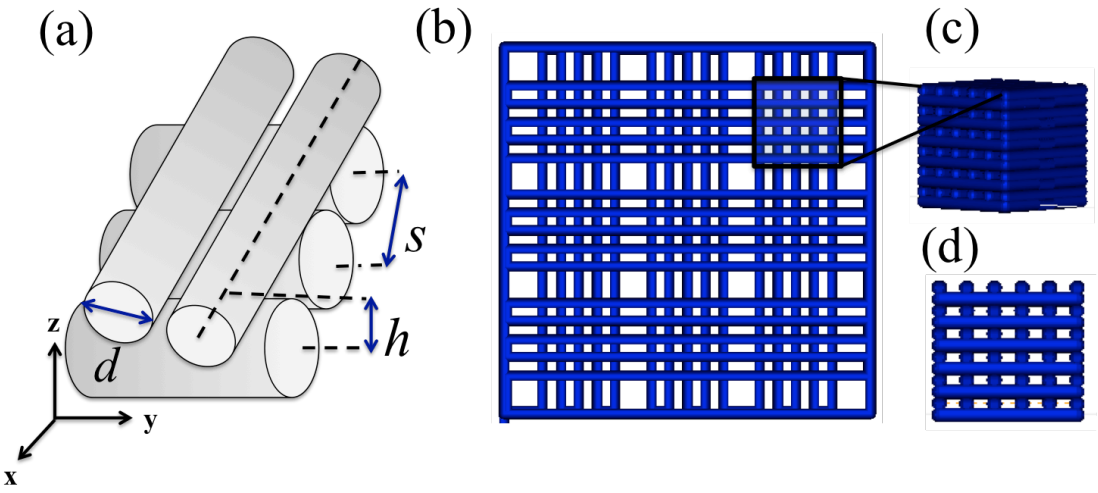

Fig. 1. Robocasting fabrication process: the ceramic scaffold is built layer-by-layer from a computer design (a). The external dimensions of the scaffolds were about 15×15×3 (b) in a total of 12 layers being 9 individual scaffolds of 3×3×3 mm (c) and (d).

2.4. Microstructural and mechanical characterization

The density of the scaffolds, ρ_s, was determined from the mass and external dimensions of the structures of at least 25 samples with regular shape. The porosity, P, was then calculated according to equation 1:

$$P = 1 - (\rho_s / \rho_{th}) = 1 - \rho_{rel} \quad (1)$$

where ρ_{th} is the theoretical density, calculated taking into account the percentage of each phase (HA and β−TCP) in each composition, and considering 3.13 $g \cdot cm^{-3}$ and 3.12 $g \cdot cm^{-3}$ the theoretical density values for pure BCP and BCP-7Sr3Ag, respectively.

The morphological features and the microstructure of the sintered scaffolds were analysed by scanning electron microscopy (SEM, Hitachi SU-70, Hitachi High-Technologies Europe, GmbH, Germany), under an acceleration voltage of 25 kV and a beam current of 10 μA. Internal dimensions of the different scaffolds fabricated (rod diameter, spacing between rods, etc.) were determined as the average of minimum 25 direct measurements performed on SEM images, using the ImageJ Software. These dimensions were then used to estimate the macroscopic, pre-designed porosity from

geometrical considerations assuming an ideal network of interpenetrating cylinders [32]:

$$P = 1 - \frac{2\pi\left(\frac{d}{2}\right)^2 s - v_i}{2d(h/d)s^2} \cong 1 - \frac{\pi}{4(h/d)}\frac{d}{s} \quad \textbf{(2)}$$

where *d, h*, and *s* are the scaffold dimensions as defined in Fig. 1a and v_i is the volume of the cylinders' intersection that can be neglected for small (≤ 20%) layer overlaps since it is well below 1% of the total volume of the scaffold.

The compressive strength of the sintered scaffolds was determined by performing uniaxial tests on approximately cubic blocks of 3 mm side (Fig. 1c). The tests were carried out in air on a universal testing machine (AG-IS10kN, Shimadzu, Kyoto, Japan) at a constant crosshead speed of 0.6 mm·min^{-1}. Tests were performed in the direction perpendicular to the printing plane. The load–displacement curves were registered during the tests. The compressive strength of the structure was calculated as the maximum applied load divided by the measured square section of the sample. A minimum of 25 samples were tested in each testing condition in order to get statistically reliable values. Weibull statistics [33] was used for the analysis of the resulting strength data, where failure probability, P, is given by

$$\mathbf{P = 1 - \exp\left[-\left(\sigma/\sigma_0\right)^m\right]} \quad \textbf{(3)}$$

where *m* is the Weibull modulus, which is a measure of sample reliability, and σ_0 is the central value of the strength distribution.

2.5. Antimicrobial activity assay of powders

An antimicrobial activity assay was carried out using pure culture colonies of two bacterial strains - *E. coli* (ATCC 25922) and *S. aureus* (ATCC 25923) – using an agar diffusion method on sterile Mueller-Hinton agar (MHA) plates (BioMerieux, France). The strains were grown overnight in PVX plates (BioMerieux, France), and a suspension of 0.5 MacFarland was achieved using 0.9% NaCl saline solution. The suspension was transferred to the surface of the plate using a sterile swab, and all the surface was swabbed. The compacted powders (0.12 g of sample, 10 mm in diameter,

pressed by 1200 kg for 20 s) (60Pa.s) were placed on the agar surface and incubated for 24 h at 37 ºC. Antimicrobial activity was determined by measuring the width of the zone of inhibition (mm).

2.6. Osteoblast-like cytotoxicity and cell proliferation assay

2.6.1. MG-63 cell culture

The human osteosarcoma derived MG-63 cell line (ATCC CRL-1427) was maintained at 37ºC in a humidified atmosphere of 5% CO_2 in air, in Eagle's Minimum Medium in EBSS (Eagle's Balanced Salt Solution) supplemented with 1% NEAA and 2 mM L-Glutamine (Gibco BRL, Invitrogen), 10% (v/v) fetal bovine serum (FBS, Gibco BRL, Invitrogen), 1% (v/v) of a 100 $U \cdot mL^{-1}$ penicillin and 100 $mg \cdot mL^{-1}$ streptomycin solution (Gibco BRL, Invitrogen), and 2.2 $g \cdot L^{-1}$ $NaHCO_3$. Sub-confluent cultures (at 80–90% confluency) were split 1:5 using a 0.05% trypsin/EDTA solution (Gibco BRL, Invitrogen) at 5% CO_2, 37ºC.

2.6.2. Powders preparation and sterilization

Each powder formulation (BCP and BCP-7Sr3Ag) was weighted (≈800 μg) and sterilized by autoclave before dissolution in 500 μL MG-63 cell culture medium. Solutions of cell culture media supplemented with powder at 1.6 $mg \cdot mL^{-1}$ were in this way prepared for each condition.

2.6.3. Cytotoxicity and cell proliferation assays

The resazurin metabolic and colorimetric assay was used to determine the powder's cytotoxicity and their effect on MG-63 osteoblast-like cells proliferation. Cells were seeded at $2x10^4$ $cells \cdot cm^{-2}$ in 24-well plates containing the medium with powders, and kept at 37ºC in a humidified 5% CO_2 and 95% air atmosphere for 14 days. At the indicated time points (days *in vitro*, DIV), cells were incubated for 4 h with fresh

medium containing 10% of a resazurin solution [0.1 mg·mL^{-1} resazurin (Sigma Aldrich) in phosphate-buffered saline (PBS; Pierce, Perbio)]. Following, resazurin reduction to resofurin was spectrophotometrically measured (Infinite M200 PRO, Tecan) at 570 and 600 nm. For each time period, the resazurin conversion rate was calculated as the O.D. 570/O.D. 600 nm ratio minus the O.D. 570/O.D. 600 nm ratio of a negative control (resazurin media incubated for 4 h in the absence of cells). The resazurin/resofurin ratio was plotted against time of incubation. The experiments were carried out in triplicate and data expressed as mean ± standard error.

2.6.4. Statistical analysis

The SPSS package v22 (IBM SPSS Statistics) was used to conduct all statistical analyses. All data is expressed as mean ± standard error of the mean (SEM). Mixed design factorial ANOVA was used to compare variability between and within (along 3DIV, 7DIV and 14DIV) groups in the metabolic activity assay. Post-hoc analysis (Bonferroni) was subsequently performed to compare differences between groups. All the requirements were previously verified using the following tests: Kolmogorov-Smirnov (KS) test and Shapiro-Wilk (SW) test for normal distribution assessment; Levene's test and Sphericity analysis to assess homogeneity of variances and/or covariances. Partial Eta squared (η^2_p) is described as a measure of effect size.

2.6.5. Morphological analysis of MG-63 cells cultured in the presence of powders

At the end of the viability assay (14th day), cells were washed with PBS, fixed in a 4% paraformaldehyde PBS solution and further washed three times with PBS. Afterwards, cells morphology was evaluated by phase contrast (PhC) microscopy in an inverted Olympus (Hamburg, Germany) IX81 epifluorescence microscope, as before [34].

3. Results and discussion

3.1. Powders characterization

Ceramics scaffolds based on biphasic calcium phosphate have a greater potential for bone tissue since they have the ability to improve the formation of new bone inside the implanted scaffolds. Doping biphasic calcium phosphate with Sr and Ag ions is expected to further enhance the physico-chemical and particularly the biological properties of the resulting materials [35-37].

The crystalline phase assemblages of powders calcined at 1100ºC are presented in Fig. 2. The X-ray diffraction patterns confirm the formation of the HA phase (ICDD # 01-079-5683) [30] with the most intense XRD peaks in the diffraction planes (211), (112) and (300), and of the β-TCP phase (ICDD # 04-014-2292) [31] with the most intense XRD peaks in the diffraction planes (217), (214) and (220). Both powder compositions exhibit similar XRD patterns, but the peaks of the BCP-7Sr3Ag composition appear slightly shifted to lower 2θ angles in comparison to the control sample (BCP) ones. This is a clear indication that the larger size dopant ions (Sr^{2+} 1.20 Å, Ag^{+} 1.26 Å, in comparison to Ca^{2+} 0.99 Å) have been incorporated into the Ca^{2+} sites of the HA and β-TCP lattice structures replacing calcium. The relative percentages of crystalline phases presented in each composition after calcination at 1100ºC, as estimated by HighScorePlus software for the both BCP and BCP-7Sr3Ag compositions, were: 80% HA + 20% β−TCP and 60% HA+ 40% β−TCP, respectively.

The results of the particle/agglomerate size (PS) and size distributions (PSD) of BCP and BCP-7Sr3Ag compositions calcined at 1100ºC, used for inks preparation are shown in Fig. 3. Both samples presented similar size distribution curves, with main populations centred at sizes <1 μm and a coarser population corresponding to particle agglomerates. The measured average particle/agglomerate sizes are ~0.9 μm and ~1.03 μm for BCP and BCP-7Sr3Ag powders, respectively. PS and PSD are parameters of crucial importance for the preparation of robocasting inks. Small size particles expose higher surface areas and are more prone to form agglomerates that might obstruct the extrusion nozzle during printing. On the other hand, a PSD with a suitable packing behaviour is likely to allow the preparation of suspensions with high

solid loading [38], with the finer ones occupying the interstitial spaces left by the coarser ones [39].

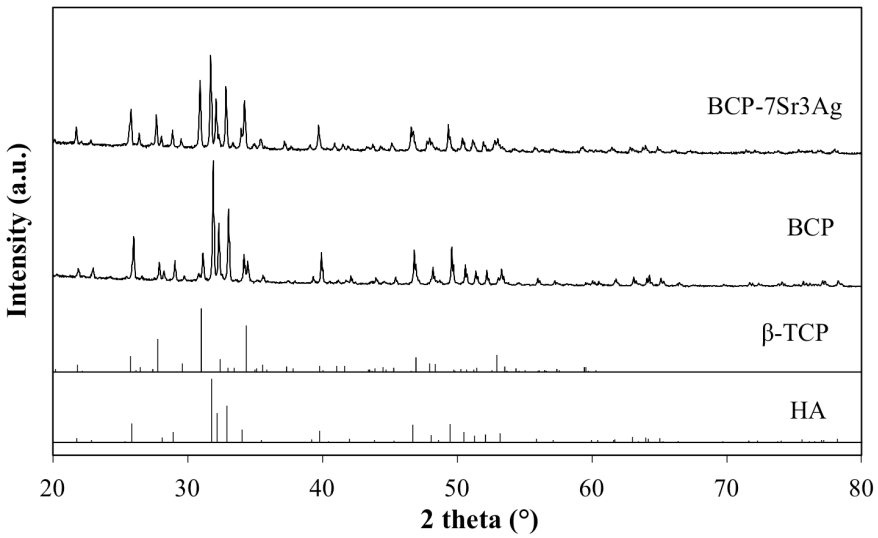

Fig. 2. XRD patterns of the BCP and BCP-7Sr3Ag powders calcined at 1100 ºC. The standard ICDD PDF # 01-079-5683 and # 04-014-2292 of pure HA and β-TCP, respectively, are also presented for comparison.

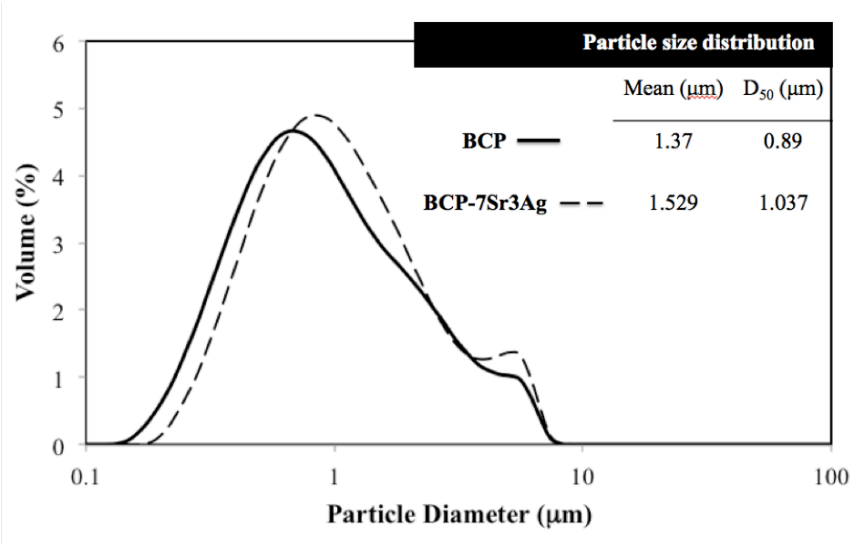

Fig. 3. Particle size distributions of the BCP and BCP-7Sr3Ag powders calcined at 1100 ºC and dry milled for 30 min. D_{50} is the diameter where half of the population lies below this value.

3.2. Optimization of robocasting ink formulation

Starting from suspensions with maximized solids loading in the presence of the dispersant is of paramount importance when preparing extrudable pastes for robocasting, as a certain degree of dilution occurs upon adding the other processing additives as aqueous solutions. From the non-doped BCP powder, a suspension with solid loadings up to 55 vol.% could be prepared in the presence of Targon 1128 as dispersant. Fig. 4a compares the apparent viscosity *versus* shear rate curves for BCP suspensions containing: (i) 55 vol.% and 50% vol.% solids without any processing additive other than Targon 1128; (ii) 50% vol.% solids with further added different amounts of HPMC (1 and 2 wt.% relative to the dry mass of solids) to the most concentrated suspension; (iii) the final ink containing 2 wt.% of HPMC and the gelling agent (PEI). In this last case, the solids loading was decreased to 48 vol.% due to the diluting effect of adding PEI solution. It can be seen that all these suspensions exhibit a shear-thinning behaviour, characteristic of homogeneous and well dispersed suspensions. As expected, for suspensions with only added dispersant, the apparent viscosity curve of the most concentrated one (55% vol.%) is above that of 50% vol.% one. The addition of increasing amounts of HPMC to this last suspension caused noticeable gradual upshifts of the apparent viscosity curves in good agreement with the expected thickening role for this additive. With further addition of flocculating agent (PEI), the suspension viscosity increased significantly while the solids loading was consequently decreased to 48 vol.%. The BCP-7Sr3Ag composition allowed the preparation of a higher initial solids loading (60 vol.%) suspension (Fig. 4b). Even though, the apparent viscosity was somewhat lower in comparison to that of BCP suspension containing 55 vol.% solids.

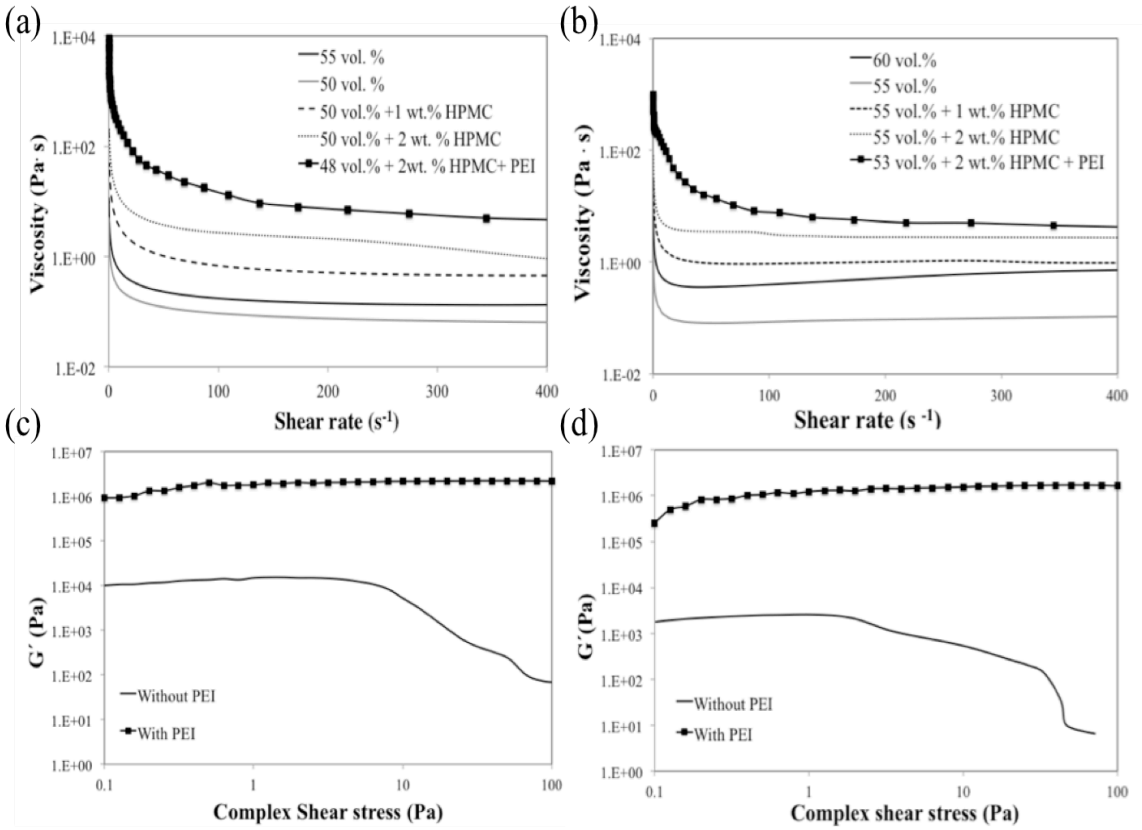

Fig. 4. Rheological behaviour of BCP (a) and BCP-7Sr3Ag (b) composition viscosity as a function of shear rate for suspension with different loading percentage of solids, with increasing amounts of HPMC (1 and 2 wt.% for solids), and with 0.3 wt.% PEI. Effects of the PEI in inks were measurement in oscillatory amplitude sweep BCP (c) and BCP-7Sr3Ag (d).

The suspensions exhibit overall shear-thinning behaviours, especially when derived from the BCP powder. This trend is less clear for suspensions prepared from the BCP-7Sr3Ag powder, especially within the higher shear rate range. The main reasons may relay on their higher solids loading, an efficient destruction of particle agglomerates, and a suitable particle/agglomerate size distribution, as all these factors play a role here. Starting from high concentrated suspensions is always desirable in order to easily accommodate the unavoidable dilution effect upon adding the aqueous solutions of the other processing additives (HPMC, PEI). Accordingly, the highest solids loading suspension for each powder system was used as the starting point to prepare the inks. This enabled obtaining extrudable pastes from BCP and BCP-7Sr3Ag powders with final solid loadings of 48 vol.% and 53 vol.%, respectively.

The shape stability of the extruded filaments can be inferred from the results of the stress sweep tests. The dynamic mechanical spectra and limit of linear viscoelasticity of the BCP and BCP-7Sr3Ag inks are presented in Fig. 4c-d, respectively. As can be observed, the addition of PEI significantly increased the elastic modulus (G´) and enlarged the limit of linear viscoelasticity region (LVR) for both ink compositions tested, in comparison to the systems in the previous condition (only with Targon 1128 and HPMC). Final inks stay stable along all the shear stress range tested, suggesting that the deposited filaments will be mechanically stable and capable of fully supporting their own weight during the assembly. These results confirm that the powders and the processing additives have been suitably combined to obtain network structures with predicted good extrusion behaviours during printing in robocasting.

In order to obtain information about the specific effects exerted by the processing additives [dispersant (Targon 1128), thickening agent (HPMC) and jellifying agent (PEI)] at the solid/liquid interface, zeta potential (ZP) measurements were performed for both powder particles (BCP and BCP-7Sr3Ag) as a function of pH in the presence and absence of each processing additive tested. The results are presented in Fig. 5a and Fig. 5b, for BCP and BCP-7Sr3Ag, respectively. In the absence of any additive the zeta potential curves of both powders particles show a continuous decreasing trend with increasing pH, with apparent isolectric points (IPE) around 5 (Fig. 5a) and 4 (Fig. 5b). Accordingly, the addition of the processing additives also caused similar effects at the solid/liquid interface of both powders. The dispersing agent caused significant shifts of the entire electrophoresis curves towards the acidic region and more negative ZP values in good agreement with the anionic nature of this polyelectrolyte, confirming the occurrence of specific adsorption at the surface of calcium phosphate powders. These data confirm that Targon 1128 has a strong ability to act as a surface charge modifier of the dispersed calcium phosphate powders, explaining its ability to promote the dispersion of high concentrated suspensions. The addition of HPMC did not cause any noticeable shift in the IEP, but the ZP values became less negative. This effect can be attributed to a reduction of the electrophoretic mobility caused by the adsorbed HPMC chains protruding to the solution. On the other hand, adding PEI caused noticeable shifts of the entire electrophoresis curves upwards and towards the basic region, with IEPs within the range of 9.4–9.7. Such shifts are in good agreement with the cationic nature of PEI

and prove that the resulting cationic species specifically adsorb at the surface of the calcium phosphate powders.

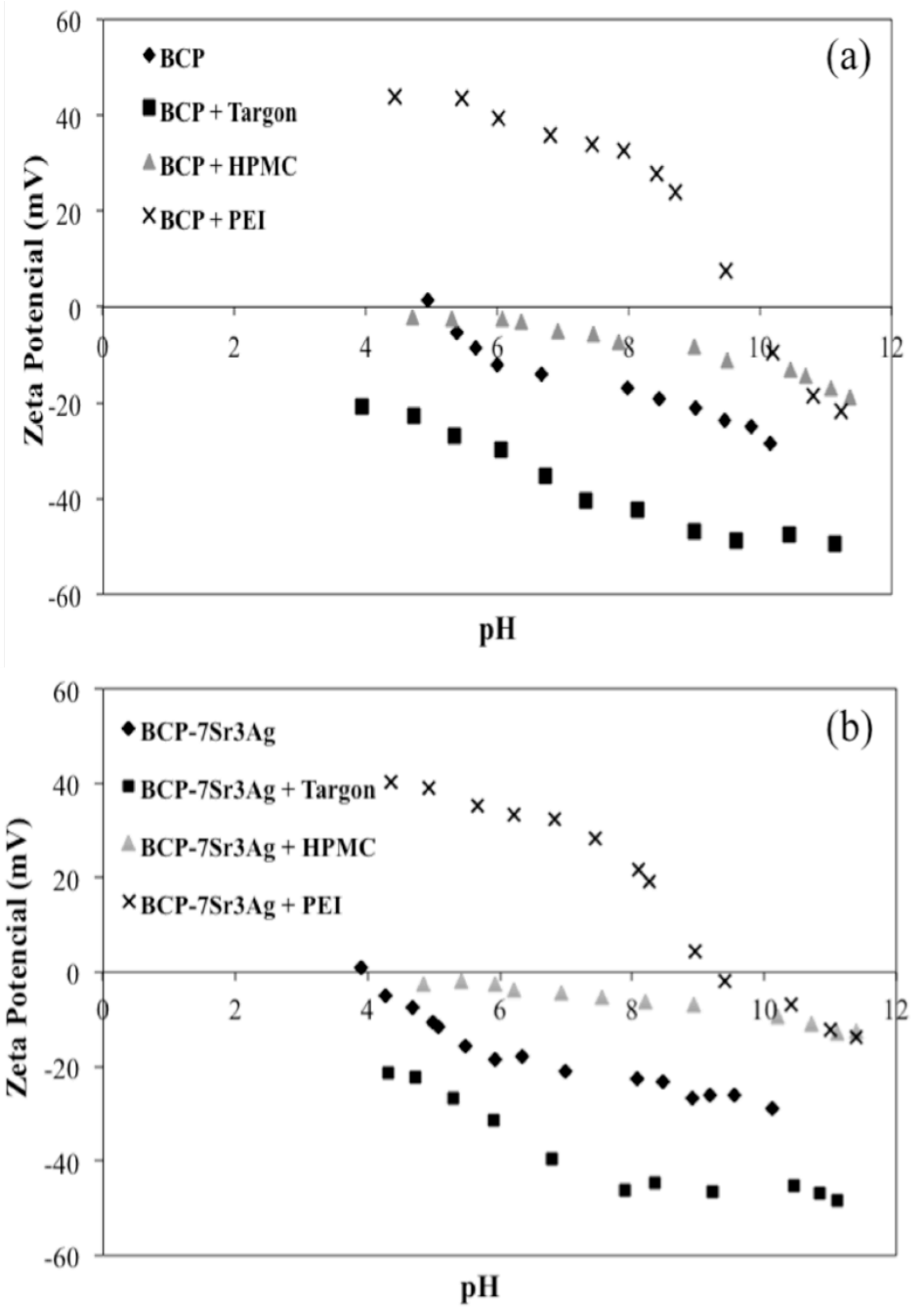

Fig. 5. Zeta-potential *versus* pH of BCP (a) and BCP-7Sr3Ag (b) powders in the absence and in the presence of the optimal amounts of processing additives for robocasting.

3.3. Scaffolds microstructural characterization

Scaffolds with different pore sizes were prepared using the previously optimized inks. The porosity fraction was controlled by varying the gap between the rods in the x-y plane during the printing process (initial gap from 120 to 500 μm). The macroporosity of the scaffolds was assessed through SEM observations. The images of BCP and BCP-7Sr3Ag scaffolds are shown in Fig. 6a-g. The salient features include a good regularity of the structure, the straight geometry of the rods and their mutual extensive adhesion, predicting a reasonable mechanical strength for tissue engineering applications. All these features confirm the quality of the inks derived from both powder compositions. Only for the scaffolds with 500 μm pore size, (Fig. 6f) it is possible to observe slight deformations of the rods caused by the gravity during printing. The SEM micrographs presented in Fig. 6g1-g2 show high resolution images of the microstructure of the sintered rods of BCP and BCP-7Sr3Ag scaffolds, respectively. They confirm that both compositions sintered well, but the BCP-7Sr3Ag sample exhibits somewhat lower in-rod microporosity.

Comparing the pore sizes designed on the CAD software, ranged from 120 to 500 μm to the real scaffolds after sintering, is possible to verify that pores in sintered scaffolds are slightly smaller for the BCP composition due to the different shrinkage extents, being ~11% and ~7% for BCP and BCP-7Sr3Ag, respectively. The smaller shrinkage of BCP-7Sr3Ag scaffolds can be attributed to the higher solids loading achieved for the starting suspension, resulting in better particle packing in green state. The obtained pore dimensions may promote cell seeding, proliferation, and vascularization, and bone formation inside the scaffold as literature indicates that pores in the range of 100–400 μm are optimal for the bone ingrowth [40-44]. This macroporosity must also provide transport pathways for nutrients, oxygen, and wastes necessary to maintain living cells within the scaffold.

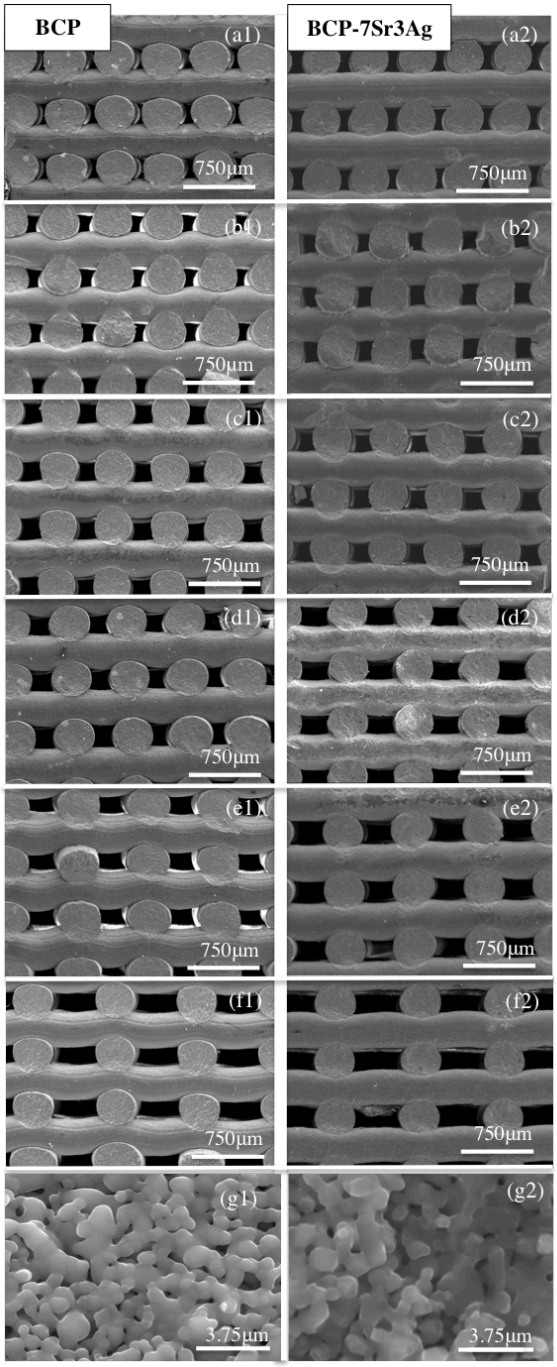

Fig. 6. SEM micrographs comparing the internal microstructure of the BCP (left side) and BCP-7Sr3Ag (right side) scaffolds fabricated by robocasting and sintered at 1100 ºC with different pore size, (a) 120; (b) 180; (c) 220; (d) 300; (e) 350; (f) 500 µm (g) rods microstructure.

The evolution of total porosity, microporosity and macroporosity for sintered scaffolds of both compositions with initial macropore/gap size is shown in Fig. 7. As expected, the macroporosity, and thus the total porosity, increases with the gap between the rods (pore size). The aforementioned slightly smaller shrinkage observed in BCP-7Sr3Ag is evidenced here as a slightly increased macroporosity at each initial gap size. Also included in this figure are the evaluated in-rod microporosity, which is intrinsic to each material and independent of the distance between rods, and results from both the burnout of the organics present in the initial inks and sintering conditions, as well as from the particle packing achieved in the green structures. Averaging the experimental data for all gap sizes it is found that microporosity in BCP-7Sr3Ag is substantially lower than in BCP (27.7 ± 0.5 % *vs*. 39.6 ± 0.4 %). This difference is consistent with the higher particle packing achieved in the former system, which enabled starting solid loadings as high as 60 vol.% and with the lower extent of shrinkage during the drying and sintering steps.

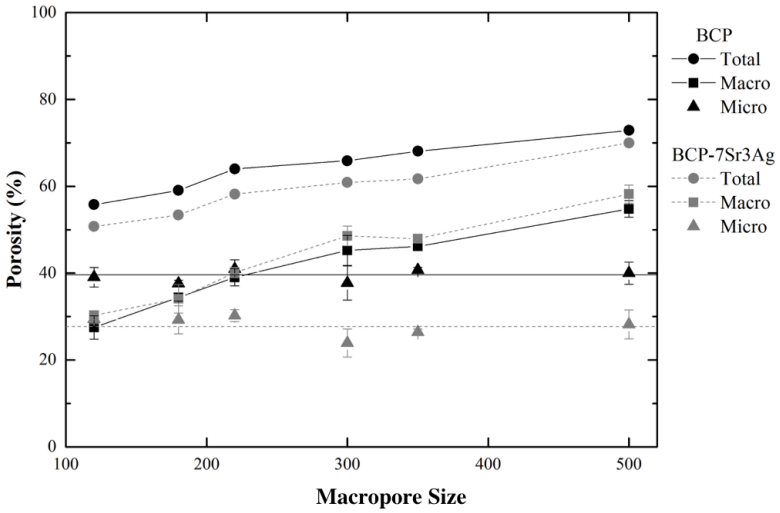

Fig. 7. Evolution of porosity (total, macroporosity and microporosity) for scaffolds fabricated by robocasting and sintered at 1100 ºC as a function of the macropore size, solid black lines correspond to BCP and dashed grey lines to BCP-7Sr3Ag. Data represent mean values with standard derivations as error bars.

3.4. Mechanical response of sintered scaffolds

The size and fraction of macroporosity are important factors for bone ingrowth into the scaffolds [40-44], but has also obvious implications in their mechanical performance. Because of that, it is important knowing the interdependence of compressive strength and density of sintered scaffolds fabricated by robocasting as a function of macroporosity. Gibson and Ashby describe the interdependence of compressive strength, $\boldsymbol{\sigma}$, and macroporosity (represented by ratio *d*/*s*) for porous structures by the equation [46]

$$\boldsymbol{\sigma} = \mathbf{C}\boldsymbol{\sigma_0} \cdot \left(\boldsymbol{d}/\boldsymbol{s}\right)^{\mathbf{3}} \qquad (4)$$

where $\boldsymbol{\sigma_0}$ is the intrinsic compressive strength.

The compressive strength results obtained for robocast scaffolds of BCP and BCP-7Sr3Ag compositions are displayed in Fig. 8. For both compositions, the compressive strength gradually increases as ratio *d*/*s* increases, and macroporosity reduces, as expected. The best-fits of Eq. (4) to the experimental data are shown as solid lines within the plot, exhibiting a very good agreement for both materials. From the analysis of the fitting parameters it can be easily calculated that the intrinsic compressive strength is 22 % higher for the BCP-7Sr3Ag samples, in comparison to BCP ones, in good agreement with their lower in-rod microporosity (Fig. 8). Consequently, the better mechanical performance of BCP-7Sr3Ag samples can again be attributed to the higher solids loading in the final ink (53 vol.%), thanks to the enhanced packing efficiency of the respective powder particles in suspension and in green bodies, which, in turn, led to a higher final density of the rods. For both powder compositions, the compressive strength of scaffolds with macroporosity values below ~48% are higher than that of cancellous bone (2 – 12 MPa [45]), falling within that range for larger fractions of macroporosity. Moreover, even the compressive strength values measured for the scaffolds made from the weaker composition (BCP) are similar to those reported in the literature for calcium phosphates with similar levels of porosity [47-49]. These results make the scaffolds interesting candidate materials for *in vitro* or *in vivo* experiments.

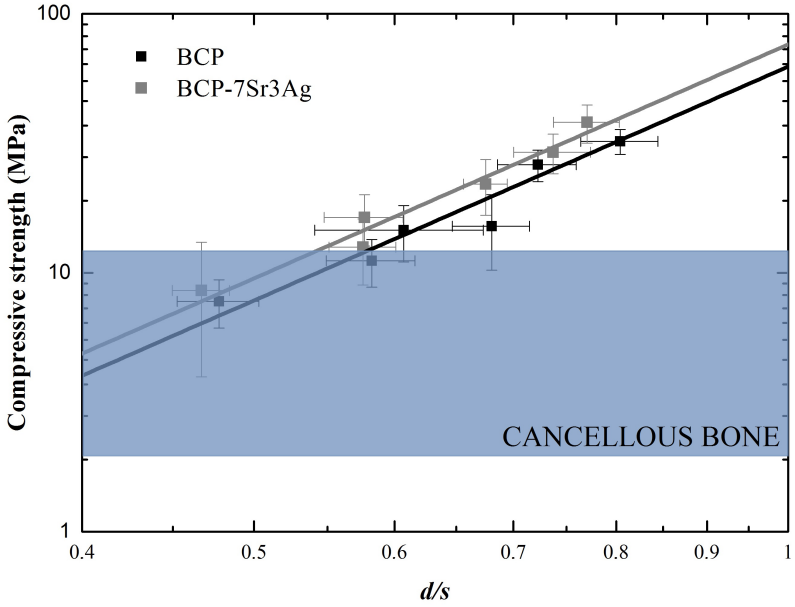

Fig. 8. Evolution of the compressive strength of BCP and BCP-7Sr3Ag robocast scaffolds sintered at 1100 ºC with the d/s. Cancellous bone strength (shaded band) is included for comparison [45]. Data represent mean values with standard derivations as error bars.

Besides the average compressive strength values, evaluating their scattering is also essential to predict the mechanical reliability. The probability of failure as a function of applied compressive stress was evaluated using the Weibull statistics. Fig. 9 presents the Weibull plots of the compressive strength data obtained for BCP and BCP-7Sr3Ag for all planned pore sizes. Each point corresponds to a single test and the straight lines are the best data fits using the Weibull probability function. Obviously, for both compositions, strength gradually decreases with increasing pore size, in good agreement with the results discussed above (Fig. 8). The Weibull modulus data for BCP and BCP-7Sr3Ag scaffolds are also reported in the table included as Fig. 9c. From these data it can be concluded that samples of both compositions exhibit high Weibull modulus, which tend to decline with increasing pore size. This must be related to the decreasing volume of material in samples of constant size and to the increasing number of printing defects as the gap to span by the filaments increases, with BCP scaffolds being more reliable in comparison to the BCP-7Sr3Ag ones. This might be attributed to the higher fraction of microporosity in

BCP scaffolds and its uniform distribution in the structure, with micropores acting as structural defects of similar size. The distribution of micropores is expected to be less uniform in the denser BCP-7Sr3Ag samples, being the source of the slightly higher variability of the measured compressive strength.

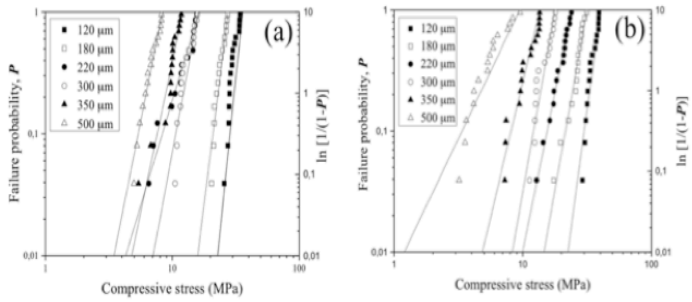

(c)

Pore size (µm)	Weibull modulus	
	BCP	BCP-7Sr3Ag
120	36.33 ± 0.011	20.04 ± 0.014
180	27.79 ± 0.015	20.70 ± 0.012
220	9.64 ± 0.024	16.66 ± 0.077
300	15.48 ± 0.023	17.36 ± 0.019
350	12.36 ± 0.025	11.60 ± 0.021
500	11.09 ± 0.013	5.01 ± 0.055

Fig. 9. Weibull plots of the compressive strength stress data for (a) BCP and (b) BCP-7Sr3Ag with different pore sizes. Straight lines are best fits to data using the Weibull probability function. Weibull modulus of the BCP and BCP-7Sr3Ag with different pore sizes (c).

3.5. *In vitro* prokaryotic and eukaryotic cells-powders interactions

The prokaryotic antimicrobial inhibitory effect of the powder compositions was manifested by the formation of circular clear zones of inhibition around the disks, as shown in Fig. 10. The sample co-doped with strontium and silver (BCP-7Sr3Ag) showed inhibitory effects on *S. aureus* (ATCC 29213) and *E. coli* (ATCC 25922). The diameters of the inhibition zones were measured, being 1.5 mm for *S. aureus* and 1 mm for *E. coli*. These results suggest that this composition can be considered an antibacterial material to be used in implants for bone tissue engineering. The mechanisms of action of silver ions on microorganisms' cells are very complex, but several hypotheses have been advanced to explain their antimicrobial effects. Firstly, silver ions bind to the prokaryotic cell envelope, thereby causing a change in their structure and permeability, and inactivate proteins [50,51]. Finally, the silver ions penetrate into the cell and inhibit various proteins in the cytoplasm and ribosome; inside cells, silver ions can interact with nucleic acids preventing replication and translation processes, ultimately causing cell death [52,53].

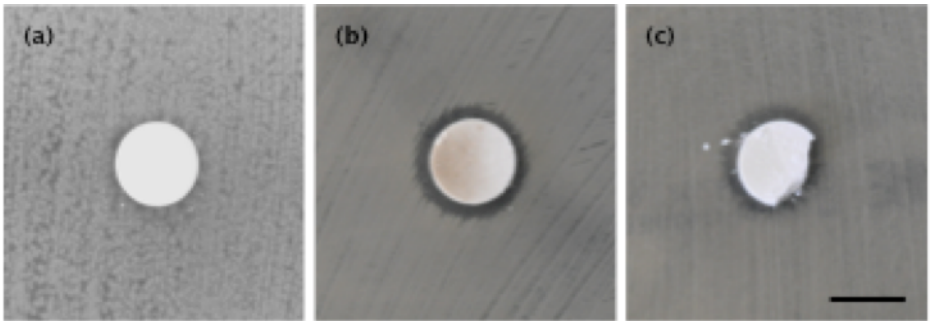

Fig. 10. Photographs of antimicrobial test results of BCP-7Sr3Ag samples against (a) *S. aureus* (ATCC 29213) and (b) *E. coli* (ATCC 25922).

An ideal material for bone tissue engineering should promote an osteoblastic phenotype. The human osteoblast-like MG-63 cells adopted in this study are typically used to assess biomaterials' effects on bone growth metabolism and cell-biomaterial interactions in bone tissue engineering [54-57]. Although Ag^{+} has been extensively used as an antimicrobial agent in clinical setting, there are still concerns about its cytocompatibility with eukaryotic cells. MG-63 cells typically display rapid cell growth and comprise an "immature" phenotype of primary osteoblasts [58]. Fig. 11 'control' depicts the normal exponential growth of MG-63 cells during 14 days. Regarding the BCP-7Sr3Ag sample, this did not exhibit any significant negative effect on cellular proliferation after 3 and 7 DIV, in comparison to control cells (grown in the absence of any powder) or to undoped BCP. Oppositely, over time in culture, the BCP-7Sr3Ag powder was more efficient in inducing pre-osteoblastic proliferation (Fig. 11, 14 DIV). Phase contrast morphological analysis at this time point (14 DIV) also reveal the typical oval to spindle-shape of MG-63 cells in all groups (Fig. 12) [59]. Hence, cells cultured with BCP-7Sr3Ag doped-culture medium are able to proliferate and maintain their normal morphology. These results point to a non-toxic effect of silver ions on osteoblastic cells, and to a proliferative effect induced by Sr that is well reported in the literature [54, 57, 58].

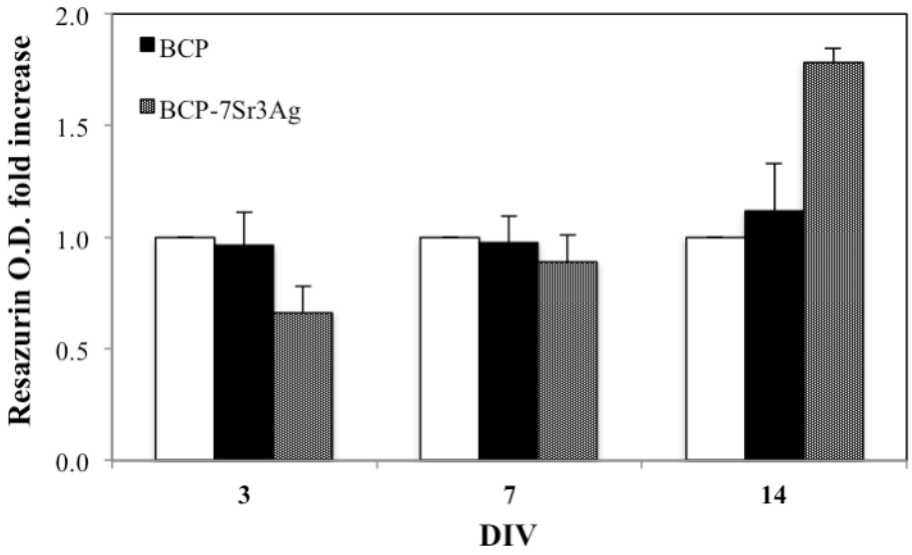

Fig. 11. Influence of BCP and BCP-7Sr3Ag on the viability of osteoblastic-like cells. MG-63 osteoblastic-like cells were seeded at $2x10^4$ cells.cm^{-2} and exposed to both powders composition (BCP and BCP-7Sr3Ag) for 14 days. The number of viable cells was indirectly accessed by the metabolic reversible resazurin assays at the indicated days *in vitro* (DIV). Results are depicted as fold increase of mean final optical density (O.D.f) over control ± SE (n=4-8). Statistically significant differences of metabolic activity were found between groups throughout cell culture (mixed design factorial ANOVA) ($F_{GreenhouseGeisser}(2.036, 5.089)=6.442$; $p=0.04$ $\eta^2p=0.720$; Bonferroni post-hoc analysis (14DIV: Control vs SrAg $p=0.025$; BCP vs SrAg $p=0.006$).

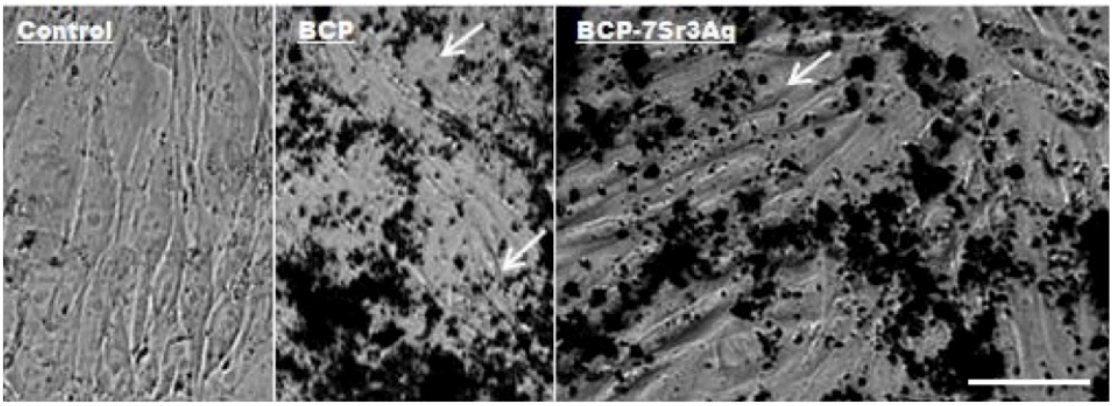

Fig. 12. Microphotographs of MG-63 cells cultured for 14 days on BCP and BCP-7Sr3Ag powders doped- culture medium. Full arrows highlight the presence of MG-63 cells on the presence of doped culture medium.

4. Conclusions

The results presented and discussed along this report demonstrate the successful production of 3-D structures by robocasting from BCP and BCP-7Sr3Ag powders, suitable for bone tissue engineering. This additive manufacturing technique provides great design flexibility and offers the possibility of manipulating the interconnected macroporosity of the scaffolds. The powders of two compositions exhibited different packing efficiencies in the slurry state, determining distinct maximum achievable solids loadings either in suspensions and in the inks prepared thereof, with impacts on the shrinkage, porosity fraction and distribution, and mechanical performance. Denser BCP-7Sr3Ag scaffolds exhibited higher mechanical strength ranging from ~7 to ~40 MPa with total porosity varying from ~70 to ~50%, respectively, although being slightly less reliable. In terms of mechanical behaviour, the scaffolds derived from both compositions present compressive strength values equal or even higher than the human cancellous bone, qualifying them for potential tissue engineering applications. Preliminary in vitro data indicates that BCP-7Sr3Ag powders can be cytotoxic to prokaryotes while stimulating osteoblasts. Future *in vivo* studies will hopefully confirm the good osteocompatibility of the BCP-7Sr3Ag scaffolds.

REFERENCES

[1] S. Sanchez-Salcedo, F. Balas, I. Izquierdo-Barba, M. Vallet-Regi, In vitro structural changes in porous HA/β -TCP scaffolds in simulated body fluid, Acta Biomater. 5 (2009) 2738–2751.

[2] T.-W. Kim, Y.M. Park, D.-H. Kim, H.-H. Jin, K.-K. Shin, J.S. Jung, H.-C. Park, S.-Y.Yoon, In situ formation of biphasic calcium phosphates and their biological performance in vivo, Ceramics International 38(3) (2012) 1965–1974.

[3] S.K. Ghosh, S.K. Nandi, B. Kundu, S. Datta, D.K. De, S.K. Roy, D. Basu, In vivo response of porous hydroxyapatite and β-tricalcium phosphate prepared by aqueous solution combustion method and comparison with bioglass scaffolds, J Biomed Mater Res B Appl Biomater 86 (1) (2008) 217–227.

[4] Y. Wu, S. Bose, Nanocrystalline Hydroxyapatite: Micelle Templated Synthesis and Characterization, Langmuir 21(8) (2005) 3232–3234.

[5] R. Bhattacharya, B. Kundu, S.K. Nandi, D. Basu, Systematic approach to treat chronic osteomyelitis through localized drug delivery system: Bench to bed side, Materials Science and Engineering C 33 (2013) 3986–3993.

[6] J.M. Ramchandani. In: Ph.D. dissertation, Department of Pharmaceutical Sciences, University of Nebraska Medical Center. Biodegradable antibiotic delivery systems for the localized treatment of osteomyelitis. Omaha, Nebraska, 1994.

[7] K.L. Garvin, B.G. Evans, E.A. Salvati, B.D. Brause, Palacos gentamicin for the treatment of deep periprosthetic hip infections, Clin Orthop Relat Res 298 (1994) 97–105.

[8] I. Gürsel, F. Korkusuz, F. Türesin, N. Gürdal Alaeddinoğlu, V. Hasirci, In vivo application of biodegradable controlled antibiotic release systems for the treatment of implant-related osteomyelitis, Biomaterials 22(1) (2001) 73–80.

[9] R.Z. Le Geros, S. Lin, R. Rohanizadeh, D. Mijares, J.P. LeGeros, Preparation, properties and application, J Mater Sci Mater Med 14 (2003) 201–209.

[10] A.T. Livingston, T. Tran, J. Mcalary, G. Daculsi, A comparative study of biphasic calcium phosphate ceramics for human mesenchymal stem-cell-induced bone formation, Biomaterials 26(17) (2005) 3631–3638.

[11] J.M. Bouler, M. Trecant, J. Delecrin, J. Royer, N. Passuti, G. Daculsi, Macroporous biphasic calcium phosphate ceramics: influence of five synthesis parameters on compressive strength, J Biomed Mater Res 32 (4): (1996) 603–609.

[12] S. Pina, S.I. Vieira, P. Rego, P.M.C. Torres, O.A.B. da Cruz e Silva, Cruz e Silva EF, J.M.F. Ferreira, Biological responses of brushite-forming Zn- and ZnSr-substituted β-tricalcium phosphate bone cements, eCM 20 (2010) 162–177.

[13] P.J. Marie, P. Ammann, G. Boivin, C. Rey, Mechanisms of action and therapeutic potential of strontium in bone, Calcif Tissue Int 69 (2001) 121–129.

[14] C.T. Wong, W.W. Lu, W.K. Chan, K.M.C. Cheung, D.K. Luk, D.S. Lu, A.B. Rabie, L.F. Deng, J.C. Leong, In vivo cancellous bone remodeling on a strontium containing hydroxyapatite (Sr-HA) bioactive cement, J Biomed Mater Res 68(A) (2003) 513–521.

[15] S. Galdiero, A. Falanga, M. Vitiello, M. Cantisani, V. Marra, M. Galdiero, Silver nanoparticles as potential antiviral agents, Molecules 16 (2011) 8894–8918.

[16] K. Chaloupka, Y. Malam, A.M. Seifalian, Nanosilver as a new generation of nanoproduct in biomedical applications, Trends Biotechnol. 28 (2010) 580–588.

[17] Y. Chen, X. Zheng, Y. Xie, Ch. Ding, H. Ruan, C. Fan, Anti-bacterial and cytotoxic properties of plasma sprayed silver-containing HA coatings, J. Mater. Sci. Mater. Med. 19 (2008) 3603–3609.

[18] S.J. Hollister, Scaffold design and manufacturing: from concept to clinic, Adv. Mater. 21 (2009) 3330–3342.

[19] R. Langer, J.P. Vacanti, Tissue engineering, Science 260 (5110) (1993) 920–926.

[20] T.G. Kim, H. Shin, D.W. Lim, Biomimetic scaffolds for tissue engineering, Adv. Funct. Mater. 22 (2012) 2446–2468.

[21] V. Karageorgiou, D. Kaplan, Porosity of 3D biomaterial scaffolds and osteogenesis, Biomaterials 26 (27) (2005) 5474–5491.

[22] J.E. Smay, J. Cesarano III, J.A. Lewis, Colloidal Inks for Directed Assembly of 3-D Periodic Structures, Langmuir 18 (2002) 5429–5437.

[23] P. Miranda, E. Saiz, K. Gryn, A.P. Tomsia, Sintering and robocasting of beta-tricalcium phosphate scaffolds for orthopaedic applications, Acta Biomater. 2 (4) (2006) 457–66.

[24] S. Michna, W. Wu, J.A. Lewis, Concentrated hydroxyapatite inks for direct-write assembly of 3-D periodic scaffolds, Biomaterials. 26 (2005) 5632–-5639.

[25] S. Eqtesadi, A. Motealleh, P. Miranda, A. Lemos, A. Rebelo, J.M.F. Ferreira, A simple recipe for direct writing complex 45S5 Bioglass® 3D scaffolds, Mater Lett. 93 (2013) 68–71.

[26] S. Eqtesadi, A. Motealleh, P. Miranda, A. Pajares, A. Lemos, J.M.F. Ferreira, Robocasting of 45S5 bioactive glass scaffolds for bone tissue engineering, Journal of the European Ceramic Society 34 (2014) 113–124.

[27] Q. Fu, E. Saiz, A.P. Tomsia, Direct ink writing of highly porous and strong glass scaffolds for load-bearing bone defects repair and regeneration, Acta Biomater. 7 (2011) 3547–3554.

[28] S. Eqtesadi, A. Motealleh, A. Pajares, P. Miranda, Effect of milling media on processing and performance of 13-93 bioactive glass scaffolds fabricated by robocasting, Ceram. Int. 41 (2015) 1379–1389

[29] J.G. Dellinger, J. Cesarano III, R.D. Jamison. Robotic deposition of model hydroxyapatite scaffolds with multiple architectures and multiscale porosity for bone tissue engineering, Journal of Biomedical Materials Research Part A (2007) 383–394.

[30] N.Y. Mostafa, P.W. Brown, Computer simulation of stoichiometric hydroxyapatite: structure and substitutions, J. Phys. Chem. Solids 68 (2007) 431–437.

[31] M. Yashima, A. Sakai, T. Kamiyama, A. Hoshikawa, Crystal structure analysis of β-tricalcium phosphate Ca3(PO4)2 by neutron powder diffraction, J. Solid State Chem. 175 (2003) 272–277.

[32] J.A. Norato, A.J. Wagoner Johnson, A Computational and Cellular Solids Approach to the Stiffness-Based Design of Bone Scaffolds, Journal of Biomechanical Engineering, 133(9) (2011) 091003.

[33] W. Weibull, A statistical distribution function of wide applicability, J. Appl. Mech. Trans. 18(1951) 293–297.

[34] V.V. Serra, F. Camoes, S.I. Vieira, M. Faustino, J.P.C. Tomé, D.C. Pinto, M.G. A.C. Tomé, A.M. Silva, E.S. Da Cruz, J.A.S Cavaleiro, Synthesis and biological evaluation of novel chalcone-porphyrin conjugates, Acta Chimica Slovenica 56(3) (2009)603–611.

[35] A. Peetscha, C. Greulichb, D. Braunc, C. Stroetgesd, H. Rehaged, B. Siebersc, M. Köllerb, M. Epplea, Silver-doped calcium phosphate nanoparticles: Synthesis, characterization, and toxic effects toward mammalian and prokaryotic cells, Colloids and Surfaces B: Biointerfaces 102 (2013) 724–729.

[36] M. Díaz, F. Barba, M. Miranda, F. Guitián, R. Torrecillas, J.S. Moya, Synthesis antimicrobial activity of a silver-hydroxyapatite nanocomposite, J. Nanomater. 2009 (2009) 1–6.

[37] S. Wu, X. Liu, K.W.K. Yeung, C. Liu, X. Yang, Biomimetic porous scaffolds for bone tissue engineering, Materials Science and Engineering: R: Reports 80 (2014) 1–36.

[38] A.F. Lemos, J.D. Santos, J.M.F. Ferreira, Influence of characteristics of starting hydroxyapatite powders and of deagglomeration procedure, on rheological behaviour of HA suspensions, Mater. Sci. Forum 455–456 (2004) 361–365.

[39] J. Franco, P. Hunger, M.E. Launey, P. Tomsia, E. Saiz, Direct write assembly of calcium phosphate scaffolds using a water-based hydrogel, Acta Biomater. 6(1)(2010) 218–228.

[40] C.M. Murphy, M.G. Haugh, F.J. O'Brien, The effect of mean pore size on cell attachment, proliferation and migration in collagen–glycosaminoglycan scaffolds for bone tissue engineering, Biomaterials 31(3) (2010) 461–466 .

[41] S.H. Oh, I.K. Park, J.M. Kim, J.H. Lee, In vitro and in vivo characteristics of PCL scaffolds with pore size gradient fabricated by a centrifugation method, Biomaterials 28(9) (2007) 1664–1671.

[42] V. Karageorgiou, D. Kaplan, Porosity of 3D biomaterial scaffolds and osteogenesis, Biomaterials 26(27) (2005) 5474–5491.

[43] H. Petite, V. Viateau, W. Bensaıd, A. Meunier, C. De Pollak, M. Bourguignon, K. Oudina, L. Sedel, G. Guillemin, Tissue-engineered bone regeneration, Nat Biotechnol 18(9) (2000) 959–963.

[44] L.M. Pineda, M. Busing, R.P. Meinig, S. Gogolewski, Bone regeneration with resorbable polymeric membranes. III. Effect of poly(L-lactide) membrane pore size on the bone healing process in large defects, J Biomed Mater Res 31(3) (1996) 385–394.

[45] Dennis R. Carter, Greg H. Schwab & Dan M. Spengler (1980) Tensile Fracture of Cancellous Bone, Acta Orthopaedica Scandinavica, 51:1-6, 733–741

[46] L.J. Gibson, M.F. Ashby. Cellular Solids Structure and Properties. 2nd Edition. Cambridge Solid State Science Series, Cambridge University Press. 1999, p. 211.

[47] A.J. Wagoner Johnson, B.A. Herschler, A review of the mechanical behavior of CaP and CaP/polymer composites for applications in bone replacement and repair, Acta Biomater 7(1) (2011) 16–30.

[48] J.M. Cordell, M.L. Vogl, A.J. Wagoner Johnson, The influence of micropore size on the mechanical properties of bulk hydroxyapatite and hydroxyapatite scaffolds, J Mech Behav Biomed Mater 2(5) (2009) 560–570.

[49] A. Bignon, J. Chouteau, J. Chevalier, G. Fantozzi, J. Carret, P. Chavassieux, G. Boivin, M. Melin, D. Hartmann, Effect of micro- and macroporosity of bone substitutes on their mechanical properties and cellular response, J Mater Sci Mater Med 14(12) (2003) 1089–1097.

[50] A.D. Russell, W.B. Hugo, Antimicrobial activity and action of silver, Prog Med Chem 31 (1994) 351–370.

[51] W.K. Jung, H.C. Koo, K.W. Kim, S. Shin, S.H. Kim, Y.H. Park, Antibacterial activity and mechanism of action of the silver ion in *Staphylococcus aureus* and *Escherichia coli*, Appl Environ Microbiol 74 (2008) 2171–2178.

[52] H.J. Klasen, A historical review of the use of silver in the treatment of burns. II. Renewed interest for silver, Burns 26 (2000) 131–138.

[53] Q.L. Feng, J. Wu, G.Q. Chen, F.Z. Cui, T.N. Kim, J.O. Kim, A mechanistic study of the antibacterial effect of silver ions on *Escherichia coli* and *Staphylococcus aureus*, J Biomed Mater Res 52 (2000) 662–668.

[54] S. Pina, S.I. Vieira, P.M.C. Torres, F. Goetz-Neunhoeffer, J. Neubauer, O.A.B. da Cruz e Silva, E.F. Cruz e Silva, J.M.F. Ferreira, In Vitro performance assessment

of new brushite-forming Zn- and ZnSr-substituted beta-TCP bone cements, J Biomed Mater Res B Appl Biomater. 94(2) (2010) 414–420.

[55] C. Wirth, B Grosgogeat, C. Lagneau, N. Jaffrezic-Renault, L. Ponsonnet, Biomaterial surface properties modulate in vitro rat calvaria osteoblasts response: Roughness and or chemistry?, Mater. Sci. Eng. C 28 (2008) 990–1001.

[56]W. Qian, S. Zhong, J. Ouyang, L. Jiang, Z. Zhang, Y. Xie, S. Luo, Osteogenesis of electrically stimulated bone cells mediated in part by calcium ions, Clin. Orthop. Rel. Res. 348 (1998) 259–268.

[57] C.F. Marques, A. Lemos, S.I. Vieira, O.A.B. da Cruz e Silva, A. Bettencourt, J.M.F. Ferreira. Antibiotic-loaded Sr-doped porous calcium phosphate granules as multifunctional bone grafts. Ceramics International 42 (2) Part A (2016) 2706–2716.

[58] E.M. Czekanska, M.J. Stoddart, R.G. Richards, J.S. Hayes, In search of an osteoblast cell model for in vitro research, Eur Cell Mater 24 (2012) 1–17.

[59] C. Pautke, M. Schieker, T. Tischer, A. Kolk, P. Neth, W. Mutschler W, S. Milz, Characterization of osteosarcoma cell lines MG-63, Saos-2 and U-2 OS in comparison to human osteoblasts, Anticancer Res. 24(6) (2004) 3743–3748.

Chapter 5

THE EFFECT OF POROSITY OF BIPHASIC CALCIUM PHOSPHATE SCAFFOLDS FABRICATED BY ROBOCASTING ON OSTEOGENIC DIFFERENTIATION OF hMSCs

Catarina F. Marques[1,2], Aureliana Sousa[2,3], Susana Olhero[1], Fidel Hugo Perera[4], Pedro Miranda[4], Pedro Granja[2,3,5,6], José M.F. Ferreira[1]

1 Department of Materials and Ceramics Engineering, CICECO University of Aveiro, 3810-193 Aveiro, Portugal

2 i3S – Instituto de Investigação e Inovação em Saúde

3 INEB – Instituto Nacional de Engenharia Biomédica, 4200-135, Portugal

4 Departamento de Electrónica e Ingeniería Electromecánica, Universidad de Extremadura, 06071 Badajoz, Spain

5 FEUP – Faculdade de Engenharia da Universidade do Porto, 4200-464, Portugal

6 ICBAS - Instituto de Ciências Biomédicas Abel Salazar, Porto, Portugal

Abstract

One strategy to induce bone regeneration includes the use of gridded structures able to allow migration and proliferation of osteoblasts and mesenchymal stem cells, matrix deposition in the empty spaces, as well as neo-vascularization. In the present study, several macroporous scaffolds were prepared by robocasting to evaluate the impact of the macropore size on the *in vitro* osteogenic differentiation of human mesenchymal stem cells (hMSCs) *in vitro*. Many ions have been described as adjuvants on hMSCs differentiation onto the osteogenic lineage and in this work we used biphasic calcium phosphate (HA/β-TCP) powders doped with strontium and zinc ions to produce the scaffolds.

After ink parameters optimization we were able to successfully print scaffolds with a range of lattice pores size's (120 - 500 μm) by robocasting. Doped biphasic calcium phosphate based scaffolds revealed to be appropriate matrices for long term *in vitro* cell culture. The obtained results demonstrate that hMSCs are able, not only to survive, proliferate and produce extracellular matrix components but also to differentiate onto the osteogenic lineage upon induction, in fact the ion-doped scaffolds displayed higher increased levels of ALP after 14 days even without the addition of external differentiation inductive factor (basal conditions) thus indicating that these scaffolds are able to induce osteogenic differentiation *per se.* For all scaffolds the mechanical properties (compressive strength) were comparable to or even higher than that of cancellous bone. The results suggest that these newly developed scaffolds can be used as matrices for bone regeneration with a potential for promoting the differentiation of hMSCs into osteoblasts.

Keywords: calcium phosphate, porosity, mesenchymal stem cells, osteogenic differentiation.

1. Introduction

Bone is the second most common transplanted tissue and although natural bone substitutes such as autografts and allografts have been used in the regeneration of damaged bone, they exhibit limitations such as donor-to-recipient infection, disease transmission, and induction of host immune responses [1]. Calcium phosphates (CaPs) have been widely studied as bioactive synthetic bone grafts mainly because their chemical composition resembles that of bone mineral and they exhibit excellent biocompatibility and bioactivity [2,3]. The most commonly employed CaPs are hydroxyapatite (HA) [$Ca_{10}(PO_4)_6(OH)_2$] and tricalcium phosphate in both of its polymorphs (α- and β-TCP) [$Ca_3(PO_4)_2$] [4]. The solubilities and *in vivo* behaviours of HA and TCP are very different, and several studies suggest that an ideal CaP scaffold should be a mixture of both phases (biphasic calcium phosphates) [5,6]. In recent years, ionic substitutions have been broadly explored as a way for improving the physicochemical properties of CaPs. Ionic substitutions may enhance the biocompatibility of CaP based scaffolds, playing critical roles in the biological process after implantation. For instance, strontium (Sr^{2+}) has demonstrated the capability to support osteoblastic differentiation while simultaneously inhibiting osteoclastogenesis [7]; consequently, it decreases bone resorption, while maintaining bone formation. Yang *et al.* showed that *in vitro* osteogenic differentiation enhancement was observed in human mesenchymal stem cells (hMSCs) cultured in presence of increased Sr^{2+} concentrations through Wnt/β-catenin signaling [8]. In addition of Sr^{2+}, it has been shown that zinc can influence the behaviour of (pre)osteoblast and osteoclast and influence the differentiation of osteogenic cells [9]. Zinc also exerts a stimulatory effect on bone formation and mineralization *in vivo* and *in vitro*. Implants incorporating Zn promote bone formation around the material, improve biological properties, decrease the inflammatory response, and exhibit bactericidal properties [10-12].

The strategies to regenerate bone include the use of scaffolds with suitable 3D porous structures to act as temporary templates for the biological processes leading to new bone formation, which should exhibit mechanical properties comparable to the host tissue [13-15]. The porosity of such scaffolds plays a significant role in tissue regeneration and should allow migration and proliferation of osteoblasts and mesenchymal stem cells, matrix deposition in the empty spaces, as well as

vascularization, promoting the bone tissue ingrowth and remodelling. Hierarchical 3D porous architectures at scales ranging from 10 to 1000 μm are essential, and each pore size plays a different role [16]. The macro pores (greater than 100 μm) allow cell ingrowth. The micro- (1–30 μm), and submicron (less than 1 μm) pores enable to establish a sufficiently high specific surface area for efficient binding of a critical number of cells to the scaffolds [17].

Attempting to overcome the difficulties of conventional manufacturing techniques, porous structures with suitable characteristics for bone tissue engineering (geometry and size of pores, their spatial distribution, etc.), direct write assembly, also frequently called robocasting, has been often used for the fabrication of scaffolds. This layer-by-layer additive manufacturing technique involves the extrusion of a ink/paste through fine nozzles and the deposition of filaments according to a computer-aid design (CAD) model to create complex 3D porous structures [18-21]. Highly uniform macropores can be obtained by varying the rod spacing and size to build the 3D lattice patterns [22]. This ability of robocasting to provide by a fully controlled reproducible and customizable architecture has been recently combined with the excellent biological properties of bioceramics [21,23-26]. However, the extensive materials characterization performed so far has been mostly intended to elucidate the dependence of mechanical properties of robocast scaffolds on the processing variables. There is few biological information available supporting the expected applicability of these architecturally well-defined porous ceramics on the *in vitro* behaviour to help predicting the new bone tissue formation after implantation. In this study, macroporous scaffolds with different macropore sizes were prepared by robocasting from biphasic calcium phosphate doped with strontium and zinc. The aim was to correlate pore size with *in vitro* osteogenic potential of human mesenchymal stem cells (hMSCs) by evaluating different cell parameters such as morphology, viability, adhesion and proliferation.

2. Materials and Methods

2.1. Synthesis and characterization of calcium phosphate powder

Calcium nitrate tetrahydrate [$Ca(NO_3)_2.4H_2O$, Panreac], strontium nitrate [$Sr(NO_3)_2$, Sigma-Aldrich] and zinc nitrate hexahydrate [$Zn(NO_3)_2.6H_2O$, Sigma-Aldrich] were used as cationic precursors for Ca, Sr and Zn, respectively. Diammonium hydrogen phosphate solution [$(NH_4)_2HPO_4$, Panreac] was used as phosphate source.

Biphasic calcium phosphate powders with a planned total cationic/anionic molar ratio of 1.62 were envisaged in this work. The precursor of calcium was partially replaced by co-doping with 7 mol% Sr^{2+} and 3 mol% Zn^{+}. The nomenclature used for this powder was BCP-7Sr3Zn. Two stock solutions of P and cationic precursors were firstly prepared with molar concentrations of 1.2 M and 1.94 M, respectively. The precipitation was carried out by slowly adding the required volume of P solution to a given volume of each continuously stirred (1000 rpm) cationic solution. The pH of the mixed system was increased to 9 and maintained at this value by adding the required amounts of 8 M ammonium hydroxide [NH_4OH, Sigma-Aldrich, Germany] solution. The reaction was performed at 90 ºC for 2 h under constant stirring conditions (1000 rpm).

The suspensions were poured out from the reactor and the precipitates separated through vacuum filtration and dried at 100 ºC overnight. The prepared powders were calcined at 1100 ºC in a Thermolab furnace (Pt30%Rh/Pt6%Rh thermocouple) using a heating rate of 5 ºC min^{-1} followed by a dwelling time of 2 h at that temperature, and then cooled to room temperature (RT). The calcined powders were then dry milled for 45 min in a high energetic ball milling up to achieving mean particle sizes of ~1 μm.

Particle size distributions of the powders were determined using a light scattering instrument (Coulter LS 230, UK, Fraunhofer optical model). The morphology and microstructure of the particles was observed by scanning electron microscopy (SEM, Hitachi S4100, Tokyo, Japan). The specific surface areas of the powders were measured by the Brunauer–Emmett–Teller method (BET) using a Micromeritics

Gemini 2370 V5.00 (Norcross, USA) through the gas adsorption after degassing the powders in a Micromeritics Flow Prep 060 (Norcross, USA).

Qualitative crystalline phase analysis of calcined powders was performed using a high-resolution Bruker D8 Advance DaVinci diffractometer with Cu Kα radiation (λ = 1.5406 Å) produced at 40 kV and 40 mA. Data sets were recorded in the 2θ range of 20–80º with a step size of 0.015º 2θ s^{-1}. Collection of XRD pattern data for Rietveld refinement studies was performed using a conventional Bragg–Brentano diffractometer (Bruker D8 Advance DaVinci, Karlsruhe, Germany) with Ni-filtered Cu-Kα radiation by recording X-ray diffraction data within the 2θ range = 20−80º (step size 0.015º and 0.5 s for each step). The software TOPAS version 4.2 (Bruker AXS, Karlsruhe, Germany) with the fundamental parameter approach, and the ICDD card numbers of # 04-015-7245 for HA [27] and # 04-006-9376 for β-TCP [28] were used for Rietveld refinements.

2.2. Printing 3D porous scaffolds by robocasting

A BCP-7Sr3Zn ceramic ink for robocasting with a final solid content of 53 vol.% was prepared following a previous work [23]. Briefly, a stable suspension was initially prepared by adding 0.4 wt.% (relative to the dry mass of solids) of ammonium polycarbonate dispersant (Targon 1128, BK Laden-burg, Germany) in distilled water, with a gradual addition of powders to reach up to 60 vol.% solids. Different amounts (1–2 wt.% based on mass of solids) of hydroxypropyl methylcellulose (HPMC, average M_n <10,000, Sigma-Aldrich) were also added to increase the intrinsic viscosity of the liquid. The as obtained suspension was subsequently turned into a jellylike ink by adding 0.3 wt.% (based on mass of solids) of polyethylenimine (PEI, 50% w/v in water, Sigma-Aldrich) as flocculant. After each component addition, the system was placed in a planetary centrifugal mixer (ARE-250, ThinkyCorp., Tokyo, Japan) for a few minutes to improve the homogeneity of the mixture.

Rheological measurements were made after each incremental amount of the processing additives using a Kinexus Pro^{+}Rheometer (Malvern, USA). The apparent viscosity of the ink was measured in viscometry mode using a cone and plate sensor

system (4º/40 mm) and 150 µm gap size. The viscoelastic properties were assessed using the same rheometer equipped with plate and plate sensor (20 mm) with 1 mm gap size in the oscillatory mode. A solvent trap (a metal ring with di-ionized water) was used in all the rheological measurements to prevent water evaporation from the samples during the tests.

3D scaffolds were constructed via direct-write assembly the extruded ink filaments layer-by-layer, using a robotic deposition device (3-D Inks, Stillwater, OK) as illustrated in Fig. 1. Cylindrical metallic deposition nozzles (EFD Inc., East Providence, RI) with a diameter d = 410 µm and a printing speed of 10 mm s^{-1} were adopted (Fig. 1a-c). The external dimensions of the scaffolds were about 9×9×3 in a total of 12 layers. Each structure consisted of 9 individual scaffolds of 3×3×3 mm (Fig. 1d-e), which were produced with six different pore sizes of 120, 180, 220, 300, 350 and 500 µm. The deposition was performed into a paraffin oil bath to ensure uniform drying during assembly. The samples were removed from the bath and dried in air at RT for 24 h, heat treated at the heating rate of 1 ºC min^{-1} up to 400 ºC, and held at this temperature for 1 h to burnout the organics. The samples were subsequently sintered at 1100 ºC for 2 h using a heating rate of 5 ºC min^{-1}.

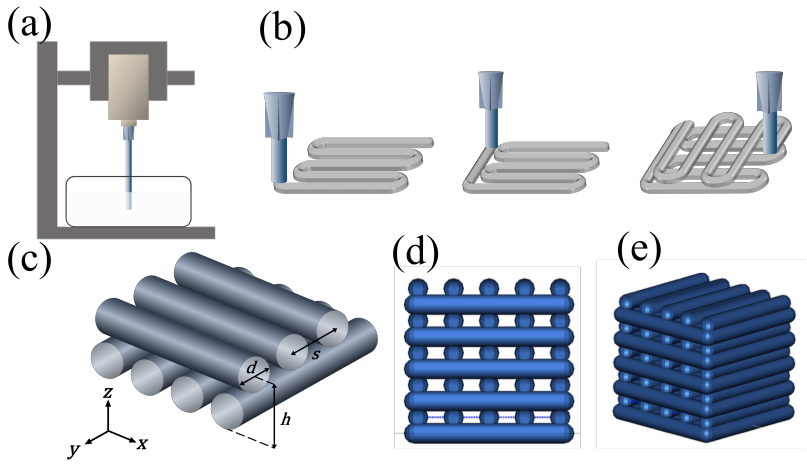

Fig. 1. The robocasting fabrication process: the ceramic scaffold is built layer-by-layer from a computer design (a-c). The dimensions of individual scaffolds were 3 × 3 × 3 mm (d) and (e) with a total of 12 layers.

2.3. Microstructural and mechanical characterization

The density of the scaffolds, ρ_s, was determined from the mass and external dimensions of the structures of at least 25 samples with regular shape. The porosity, P, was then calculated according to equation 1:

$$P = 1 - (\rho_s / \rho_{th}) = 1 - \rho_{rel} \quad (1)$$

where ρ_{th} is the theoretical density (3.1 $g \cdot cm^{-3}$) given by the Rietveld refinement taking into account the percentage of each phase (HA and β−TCP) in the doped powder.

The morphological features and the microstructure of the sintered scaffolds were analysed by scanning electron microscopy (SEM, Hitachi SU-70, Hitachi High-Technologies Europe, GmbH, Germany), under an acceleration voltage of 25 kV and a beam current of 10 μA. Internal dimensions of the different scaffolds (rod diameter, spacing between rods, etc.) were determined as the average of minimum 25 direct measurements performed on SEM images, using the ImageJ Software. These dimensions were then used to estimate the macroscopic, pre-designed porosity from geometrical considerations assuming an ideal network of interpenetrating cylinders [29]:

$$P = 1 - \frac{2\pi\left(\frac{d}{2}\right)^2 s - v_i}{2d(h/d)s^2} \cong 1 - \frac{\pi}{4(h/d)}\frac{d}{s} \quad (2)$$

where *d, h*, and *s* are the scaffold dimensions as defined in Fig. 1c and v_i is the volume of the cylinders' intersection that can be neglected for small (≤ 20%) layer overlaps since it is below 1% of the total volume of the scaffold.

The compressive strength of the sintered scaffolds was determined by performing uniaxial tests on approximately cubic blocks of 3 mm side (Fig. 1d-e). The tests were carried out in air on a universal testing machine (AG-IS10kN, Shimadzu, Kyoto, Japan) at a constant crosshead speed of 0.6 mm min^{-1}. Tests were performed in the direction perpendicular to the printing plane. The load–displacement curves were registered during the tests. The compressive strength of the structure was calculated as the maximum applied load divided by the measured square section of the sample, and a minimum of 25 samples were tested.

2.4. *In vitro* studies

2.4.1. hMSCs culture and seeding on the scaffolds

Human mesenchymal stem cells (hMSCs, Lonza) were cultured, expanded, and maintained at 37 ºC in a humidified atmosphere of 5% CO_2 in α-MEM (α-MEM, Gibco), supplemented with 10% v/v inactivated foetal bovine serum (FBS, Gibco), and 1% v/v penicillin/streptomycin (P/S, Biowest). The culture medium was refreshed every 2–3 days. hMSCs were harvested at pre-confluence using TrypLE™ (TrypLE™) solution. Cells were used between 6 and 8 passages.

The calcium phosphate scaffolds were sterilized by autoclave (121 ºC, 20 min) and placed in uncoated 48-well cell culture plates (Cellstar®) to avoid cell adhesion to the bottom of the wells. Non-doped biphasic calcium phosphate (BCP) scaffolds, containing approximately 50% of HA and 50% of β-TCP were also studied for comparison. Before cell seeding the scaffolds were pre-incubated in medium for 1 h, followed by seeding with cells at a density of $3x10^4$ cells per scaffold. hMSCs were allowed to adhere for 20 min and 500 μl of the fresh medium was added to each well. hMSCs were cultured on calcium phosphate scaffolds for 14 days. After 1, 7 and 14 days of culture, samples were evaluated for cell metabolic activity and morphology.

One day after seeding, and in order to induce the hMSCs differentiation into the osteoblastic lineage, cells were also cultured with osteogenic medium: basal medium supplemented with 10 mM glycerophosphate (Sigma–Aldrich), 100 nM dexamethasone (Sigma–Aldrich), and 0.05 mM ascorbic acid (Fluka). At time-points 7 and 14 days of culture osteogenic differentiation was evaluated.

2.4.2. Cell metabolic activity

Metabolic activity was measured using a resazurin assay at days 1, 7 and 14. Resazurin (Sigma) was added to fresh medium at a final concentration of 20% (v/v). The scaffolds with cells were incubated in this solution at 37 ºC for 3 h, after which 100 μL per well was transferred to a 96-well black plate and fluorescence was

measured (Ex 530 nm/Em 590 nm) using a micro plate reader spectrophotometer (Bioteck Plate Reader, Synergy MX).

The dsDNA quantification was performed using the Quant-iT PicoGreen dsDNA kit (Molecular Probes, Invitrogen), according to the manufacturer's instructions. Briefly, the frozen samples were thawed and lysed in 1% v/v Triton X-100 (in PBS) for 1 h at 250 rpm and 4 ºC. Then, they were transferred to a black 96-well plate with clear bottom (Greiner) and diluted in TE buffer (200 mM Tris–HCl, 20 mM EDTA, pH 7.5). After adding the Quant-iT PicoGreen dsDNA reagent, samples were incubated for 5 min at RT in the dark, and fluorescence was measured using a microplate reader (Ex 480/ Em 520 nm) (Bioteck Plate Reader, Synergy MX).

2.4.3. Cell Morphology

At different time points (1, 7 and 14 days after *in vitro* culture initiation), samples of each pore size were processed for cell morphology and cell distribution analysis by scanning electron microscopy (SEM). The scaffolds were washed in PBS and fixed in 4% w/v paraformaldehyde in PBS for 20 min at room temperature, followed by dehydration with graded ethanol series (60%, 70%, 80%, 90%, and 99%) for 10 min in each solution and overnight in hexamethyldisilazane (Sigma-Aldrich). They were sputter-coated with carbon and observed using a Hitachi S-4100.

At days 7 and 14 an immunocytochemical staining of actin filaments (F-actin) and nuclei was used to assess cytoskeleton organization of hMSCs. In order to evaluate the differentiation of the hMSCs the ALP was also stained. Briefly, cultured scaffolds were rinsed with PBS and fixed in 4% w/v paraformaldehyde in PBS and permeabilization with 0.1% v/v Triton X-100 for 5 min, then samples were incubated for 30 min with 1 wt.% bovine serum albumin (BSA, Merck) in PBS to block any non-specific staining.

For alkaline phosphatase (ALP) staining, scaffolds were incubated overnight at 4 ºC with ALP antibody, monoclonal mousse IgG_1 (Bio-Techne 3:100) and then with the goat anti-mousse secondary antibody Alexa Fluor® 594 (Molecular Probes-Invitrogen, 1:1000, 45 min at RT). For F-action staining samples were incubated with the conjugated probe phalloidin/Alexa Fluor® 488 (Molecular Probes-Invitrogen,

1:40 in 1% BSA, 45 min at RT). Finally, samples were washed three times with PBS, and just before confocal visualization the nuclei were counterstained with 4',6-diamidino-2-phenylindole dihydrochloride (DAPI, H-1200, Vector). Samples were immunostained immediately before confocal visualization as described in the section above (CLSM, Leica SP5AOBS, Leica Microsystems) and acquired using LCS software (Leica Microsystems). The scanned Z-series were projected onto a single plane and pseudo-coloured using ImageJ and final panels were obtained using Photoshop CC 2017 vs 2017.1.1.

2.4.4. ALP mean pixel intensity quantification

Samples were imaged on MatTek glass bottom dishes (MatTek Corporation) using Vectashield containing DAPI (Vector Laboratories) for observation in a Leica SP5AOBS SE scanning confocal microscope (Leica Microsystems). Fluorescence intensity profiles were traced using an RGB profiler plugin of ImageJ1.45h Software (NIH). The relative intensities of ALP fluorescence were determined on maximum projected images acquired with fixed exposure acquisition settings; DAPI staining was used to define a selected area, and mean pixel intensities were determined (ImageJ).

2.5. Statistical analyses

Statistical analyses were performed using GraphPad Prism 7.0 software (version 7.0a). For both the metabolic activity measurements normalized for the DNA content and ALP mean pixel intensity data comparison the non-parametric Mann-Whitney test was used. All tests were performed using a 95% confidence interval and statistically significant differences are marked with * ($p < 0.05$), ** ($p < 0.01$) , *** ($p < 0.001$) or **** ($p < 0.0001$). For the sake of graph clarity, specific p values are depicted in the supplementary table (Table 1) for Fig. 7.

3. Results and Discussion

3.1. Characterization of BCP-7Sr3Zn powders

CaP based biomaterials are well known for their bioactivity and similarity to the mineral phase of bone in terms of composition and structure. Biphasic calcium phosphate ceramics consisting of β-TCP and HA blends present excellent bioresorbability and bioactivity and proper osteoconductive properties resultant from the different performance of both phases [30,31]. The dissociation of β-TCP from BCP induces local super-saturation of calcium and phosphate ions, increasing the degradability and the nucleation of biological apatite. In addition, HA provides a bone-like environment with good osteoconductive and/or osteoinductive properties [32].

Strontium and zinc ions are presented in trace concentrations in natural bone [33] and have been demonstrated to significantly improve osteoblastic response on calcium phosphate bioceramics when added individually [34,35]. In the present study, the behaviour of BCP powders doped with both ions has been evaluated.

Fig. 1 shows the physical-chemical characterization of BCP-7Sr3Zn powders after calcination at 1100 ºC. The XRD patterns present sharp and well defined diffraction peaks of the two phases, HA and β-TCP, as expected. The XRD data was refined assuming, for HA, the space group P63/m and the unit cell and structural parameters reported by Arcos *et al.* [27], and for β-TCP, the space group R3c and the parameters reported by Nicolopoulos *et al.* [28]. The quantitative phase analysis obtained by Rietveld refinement (wt.%) indicate the presence of 45.77% of HA and 54.23% of β−TCP. The refined cell parameters were a = b = 9.430664 Å, c = 6.907843, α = β = 90º and γ = 120º in HA phase and a= b = 10.44789, c = 37.49057, α = β = 90º, and γ = 120º in β-TCP phase.

Morphological features of calcined powders observed by SEM show small and tightly agglomerated particles with regular shape and non-uniform size. Particle size distribution parameters including D_{50}, average, as well as BET specific surface area are also detailed in Fig. 2 (b). BCP-7Sr3Zn powders present a bimodal distribution

with a measured average particle/agglomerates size of 1.02 μm.

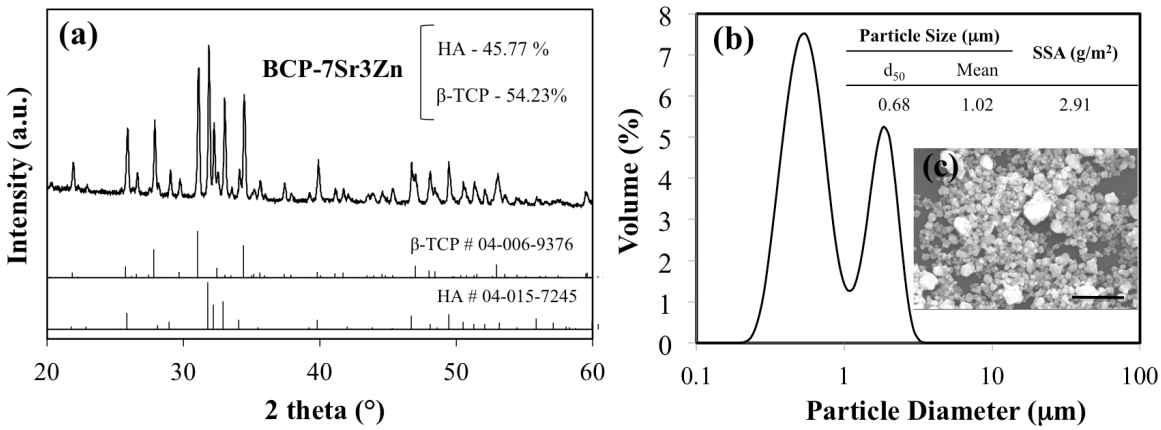

Fig. 2. Physical-chemical characterization of BCP-7Sr3Zn powder after calcination at 1100 ºC: (a) X-ray diffraction pattern showing two phases, HA and β-TCP; (b) particle size distribution and specific surface area after dry milling for 30 min (D_{50} is the diameter where half of the population lies below this value); (c) SEM micrographs (bar: 6 μm).

These particles size distributions are likely to allow the preparation of suspensions with high solid loading [36], important factor to avoid high shrinkage levels and improve the mechanical integrity of the final scaffolds.

3.2. Optimization of scaffolds processing

Specific effects exerted by the processing additives [dispersant (Targon 1128), thickening agent (HPMC) and jellifying agent (PEI)] at the solid/liquid interface of BCP-7Sr3Zn particles were evaluated by zeta potential (ZP) measurements in presence and absence of each processing additive, which results are presented in Fig. 3.

In the absence of processing additives, zeta potential curve for BCP-7Sr3Zn powder shows a continuous decreasing trend as pH increases and an isolectric point (IEP) around pH 4. Measurements below ~pH 4 are not reliable for CaPs due to their enhanced solubility and the consequent increase in ionic strength under stronger acidic conditions. The dispersing agent promoted a significant shift of the

electrophoretic curve towards more negative ZP values, confirming its anionic nature and specific adsorption at the surface of BCP-7SrZn powder. This is in good agreement with previous findings that pointing out Targon 1128 as a very efficient surface charge modifier for calcium phosphate powders, enabling the preparation of high concentrated suspensions [23,37]. The IEP did not change with the further addition of HPMC, but ZP values became noticeably less negative. However, such noticeably decrease of absolute ZP values occurred without negatively affecting the apparent colloidal stability of the system. This can be explained either by an airy-like configuration adopted by the HPMC molecules adsorbed at the surface of BCP particles, slowdown their electrophoretic mobility, or by shifting of the shear plan to larger distances from the particle surface, or both. Adding PEI shifted the entire electrophoresis curve upwards and towards the basic region, with IEP at pH 10. Such shift is in good agreement with the cationic nature of PEI, attesting the specific adsorption of cationic species at the surface of the calcium phosphate based powders.

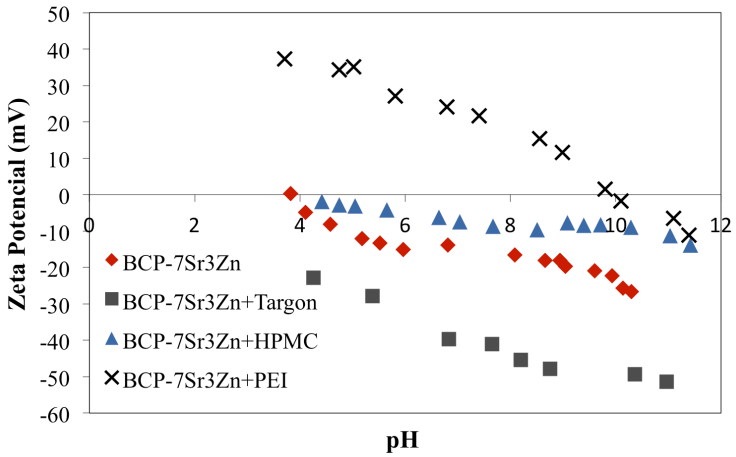

Fig. 3. Zeta-potential *versus* pH of BCP-7Sr3Zn powders in absence and in presence of the optimal amounts of processing additives for robocasting ink.

Colloidal inks for printing by robocasting process should have a high solid volume concentration to minimize shrinkage during drying and sintering. Exhibiting proper viscoelastic properties to flow through the fine deposition nozzle and then set to keep filament shape and support their own weigh layer by layer is another important requirement. A suspension with solid loadings up to 60 vol.% could be prepared from the BCP-7Sr3Zn powder in presence of Targon 1128 as dispersant. It is worthy to

underline that the addition of processing additives as aqueous solutions imply a certain diluting effect. Fig. 4(a) compares the apparent viscosity *versus* shear rate curves for suspensions containing: (i) 60 vol.% and 55% vol.% solids with added Targon 1128 as the only processing additive; (ii) 55% vol.% solids with further added different amounts of HPMC (1 and 2 wt.% relative to the dry mass of solids) to the most concentrated suspension; (iii) the final ink containing 2 wt.% of HPMC and the gelling agent (PEI), the addition of which justified a further decrease in solids loading to 53 vol.%.

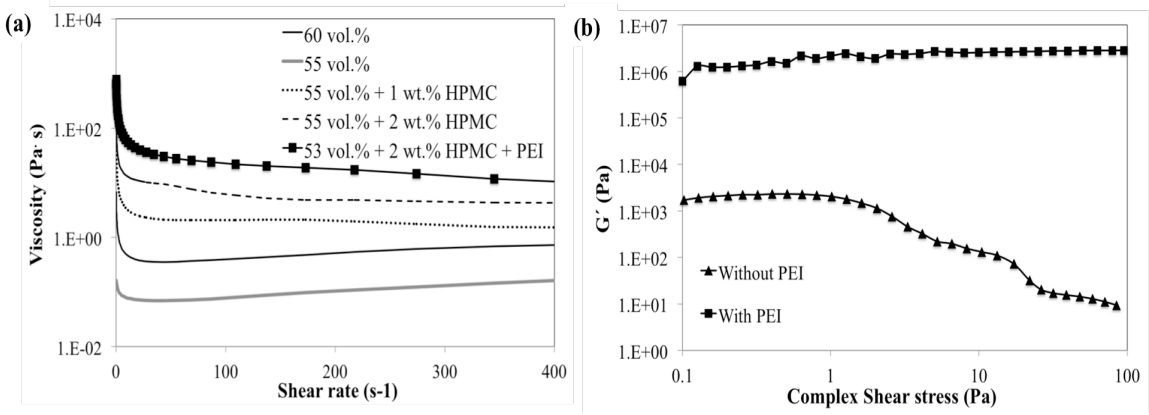

Fig. 4. Rheological behaviour of BCP-7Sr3Zn suspension/ink: (a) viscosity *versus* shear rate for suspensions with different solids loading in the absence (55 and 60 vol.%) or in the presence of HPMC (55 vol.% + 1 and 2 wt.% for solids), and with 53 vol.% in the presence of all processing additives (53 vol.% + 2 wt.% HPMC + 0.3 wt.% PEI). (b) Oscillatory amplitude sweep of final inks in the absence (55 vol.% + 2 wt.% HMPC) and in the presence of PEI (53 vol.% + 2 wt.% HPMC + PEI).

The apparent viscosity of the most concentrated suspension (60% vol.%) is above that of 55% vol.%, as expected. In the presence of dispersant only, both systems exhibit slightly shear thickening behaviour. This can be attributed to the high solids loading and to the low intrinsic viscosity of the dispersing solution. But all the other suspensions with added HPMC exhibit shear-thinning behaviours, more accentuated with increasing the content of this processing additive, in good agreement with its thickening role. HPMC enhances the intrinsic viscosity of the dispersing liquid and

smooths the collisions between particles under flow, while confers a certain internal structure to the system that is gradually broken down as shear rate increases. The further addition of flocculating agent (PEI) has significantly increased the viscosity of the system, turning it into an extrudable ink in good agreement with ZP results (Fig. 3).

The viscoelastic properties of the inks can be inferred from the results of the stress sweep tests. The dynamic mechanical spectra and limit of linear viscoelasticity of the BCP-7Sr3Zn inks are presented in Fig. 4(b). As can be observed, the addition of PEI significantly increased the elastic modulus (G´) and enlarged the limit of linear viscoelasticity region (LVR) in comparison to the systems without PEI (with only with Targon 1128 and HPMC). The final ink with all the ingredients remained stable along all the shear stress range tested. Such viscoelastic behaviour suggests that the extruded filaments will be mechanically stable and capable of keep their shape after the printing step. These results confirm that the powders and the processing additives have been suitably combined to obtain pastes with predicted good extrusion behaviours during printing in robocasting.

3.3. 3D porous scaffolds characterization

It has been shown that pore size in scaffolds with approximately 100 μm diameter is required for ingrowth of bone cells, and that sizes in the range of 100–600 μm facilitates osteoconductivity [38]. Although several strategies can be used to obtain a scaffold with different porosity, the control of pore size, geometry and interconnectivity of pores, essential to nutrients diffusion, is difficult in most of the common techniques (as for example polymeric sponge replication). Robocasting emerges as a 3D printing technique capable to fabricate scaffolds with a precise macroporosity and controlled geometry.

Scaffolds with different pore sizes were prepared using the previously optimized inks. The macroporosity of the scaffolds was assessed through SEM observations and the images are presented in Fig. 5A (a-f). The porosity fraction was controlled by varying the gap between the rods in the x-y plane during the printing process (initial gap from

120 to 500 μm). The prominent features include a good regularity of the structure, the straight geometry of the rods and their mutual extensive adhesion, predicting a reasonable mechanical strength for tissue engineering applications. Fig. 5B shows the geometrical parameters of scaffolds measured from the SEM images. All these features confirm the suitable viscoelastic properties of the inks (Fig. 4). Comparing the distance d_{xy} to the original CAD model, a slightly shrinkage (5%) in the scaffolds after sintering can be detected, thanks to the high percentage of solids in the ink. Concerning the distance d_z, the scaffolds with larger pore size (500 μm) present higher deformation due to gravity phenomenon, as expected.

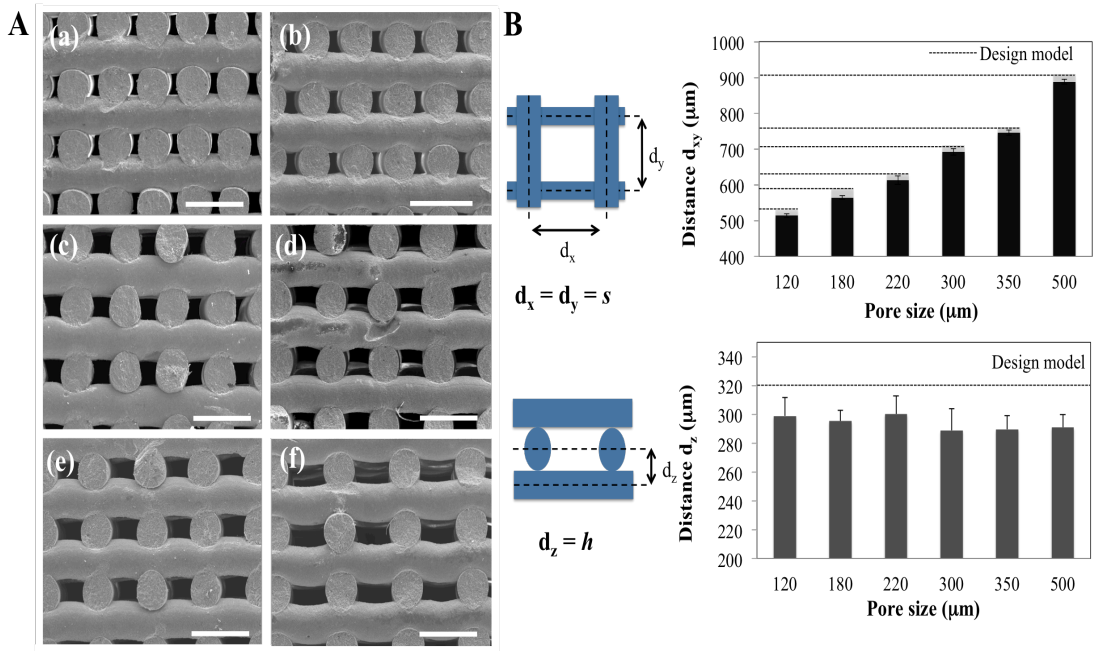

Fig. 5. 3D porous scaffolds characterization. (A) SEM micrographs of the cross-sections of the BCP-7Sr3Zn scaffolds with different pore sizes [(a) 120; (b) 180; (c) 220; (d) 300; (e) 350; (f) 500 μm, (bar: 750 μm)], fabricated by robocasting and sintered at 1100 ºC. (B) Measurements of the rod distances in the scaffolds. The dashed lines on graphs refer to the CAD design model.

Fig. 6 (a) shows the evolution of total porosity, microporosity and macroporosity for sintered scaffolds with initial macropore/gap size. The geometrical properties of the scaffolds were measured from SEM images and used for the calculation of the total porosity, which ranged from ~50% and ~70%. The macroporosity, increases as gap between rods increases, as expected, varying between 26.6% and 50.8% for pore size of 120 μm and 500 μm, respectively. Concerning the microporosity, which is intrinsic to each material and result from both the burnout of the organics presented in the initial ink and sintering conditions, was around 26%. The compressive strength results obtained for robocast scaffolds are displayed in Fig. 6 (b). As expected, the compressive strength gradually decreases as pore size increases. Nevertheless, even the lower compressive strength values obtained for scaffolds with 500 μm pore size, are in the range of the cancellous bone (2–12 MPa [39]).

From the mechanical view point, it can be concluded that all the scaffolds present satisfactory mechanical properties for being used as bone substitutes, justifying their further use in *in vitro* studies aiming at evaluating their biological performance.

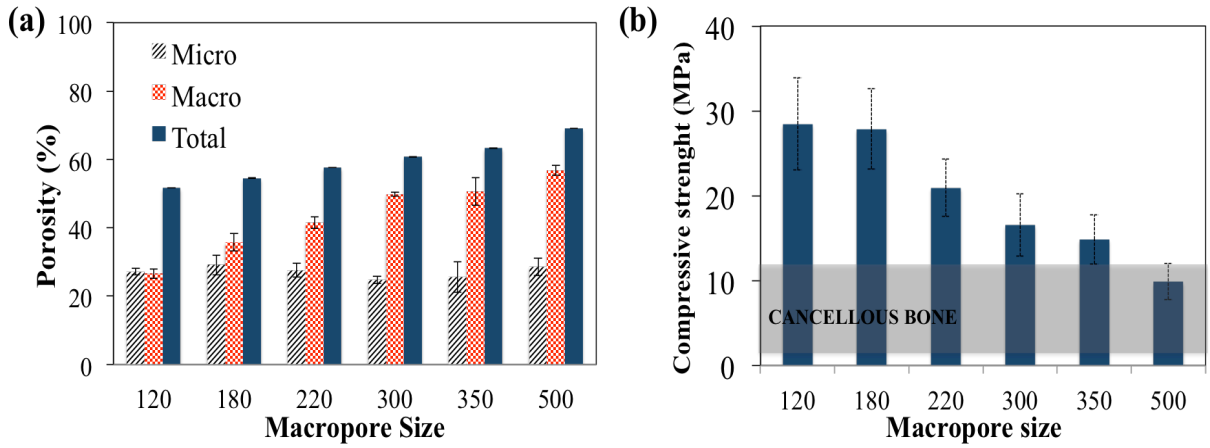

Fig. 6. Evolution of structural and mechanical features of robocast scaffolds sintered at 1100 ºC with macropore size: (a) porosity (total, macroporosity and microporosity); and (b) compressive strength. For comparison, a shaded band representing the cancellous bone strength is also included [39]. Data represent mean values with standard derivations as error bars.

3.4. hMSCs activity on the scaffolds

The metabolic activity of hMSCs culture on scaffolds with different pore size (lowest (120 μm), intermediate (300 μm) and highest (500 μm)) was measured using the resazurin-based method after 1, 7 and 14 days and normalized with DNA content for each time point (Fig. 7A). The hMSCs remained viable and metabolically active throughout the 14 days of culture in all scaffolds, with a continuous increase in cells metabolic activity for all macropore sizes. Comparing the BCP-7Sr3Zn with the non-doped scaffolds (used as control), the doped composition scaffolds showed higher metabolic activity values for all pore sizes. Analysing the values normalized with DNA content, an increase in the values displayed in the Fig. 7A indicates an increase on the metabolic activity of the individual cell, showing that the doped scaffolds could enhance cell metabolism. Studies of Pina *et al.* [40] have shown that β-TCP bone cement doped with strontium and zinc ions improved the metabolic activity *in vitro* of MC3T3- E1 cells. Furthermore, J. Caverzasio showed that Sr may directly interact with the calcium sensing receptor in osteoblast cells (MC3T3- E1) to trigger mitogenic signals in the protein kinase c/d signalling pathways, resulting in increased cell division [41]. Though no proliferation marker was used in this study, it can clearly be observed the difference on the number of cells throughout time in culture (Figs. 7, 8 and 9) justifying the increase of the scaffold occupancy by the hMSCs.

Cells attach and spread when in contact with an adequate surface through adhesion proteins-dependent processes. The quality of cell attachment affects the cell morphology as well as their proliferation and differentiation ability [42]. Microscopic analyses were used to evaluate the distribution of hMSCs on the BCP-7Sr3Zn scaffolds after 1, 7 and 14 days in culture (Fig. 7B) and revealed that cells were well were able to adhere to the scaffold surfaces. An increase on cell density from day 1 to day 14 can be observed since After 14 days the side of scaffolds was completely covered with cells, indicating their survival, regardless of pore size. Moreover, seeing in detail the morphology of the cells 24 h after the seeding, it is possible to observe that cells exhibit a nearly polygonal shape with a multiple filopodia attached to the scaffolds (Fig. 7C (a)). The absorption of proteins integrins (major cell receptors involved in the cell-binding-to-matrix) from culture mediums determines the early non-specific stage of cell adhesion, enabling cell spreading on the scaffolds through

the formation of a conditioning protein layer that promotes this adhesion [43, 44]. Moreover, the surface area (total of porosity in range of ~50% and ~70%) and microporosity (Fig. 6) facilitate the wettability of the scaffolds and provide much more contact points for protein anchorage. By day 7, in some areas of the scaffolds, cells were already disposed in a monolayer with cell-to-cell contact, partially coating the materials surface (Fig. 7C (b)). After 14 days in culture, hMSCs were visible on the top surface of the 500μm pore size scaffold, linking the structure´s filaments (Fig. 7C (c)).

The morphology of the hMSCs on the scaffolds is shown in CLSM images of Figs. 8 and 9 for BCP and BCP-7Sr3Zn, respectively, assessed by labelling f-actin filaments (green) and nuclei (blue), in basal and osteogenic medium (where no osteoinductive agents were provided to the cells), after 7 and 14 days in culture. The cells were well spread under all pore size in both compositions (BCP and BCP-7Sr3Zn) but when comparing basal and osteogenic conditions, it seems obvious, that the cells occupied the surface of the scaffold filaments differently. After 7days in culture, the cell number was higher in the basal medium. In the presence of differentiation inductors, there is a metabolism-shift on hMSCs and it is already reported that cells proliferate less on osteogenic inductive medium when compared with basal medium [45].

hMSCs are promising cell sources for bone engineering because of its osteogenic capacity under certain conditions [46]. Previous studies demonstrate the osteogenic capability of MSCs cultured on calcium phosphate ceramics (CaPs), as well as showing that adhesion, localization, ECM deposition and cell differentiation is affected by design and pore geometry of the scaffolds [47].

ALP is a functional enzyme, which plays a key role in bone formation and mineralization and has always been related to osteoblast differentiation [48]. In order to evaluate the effect of macropore size on osteogenic differentiation we quantified the signal intensity of ALP (a marker of early osteogenesis) produced from hMSCs on culture after 7 and 14 days (Fig. 10).

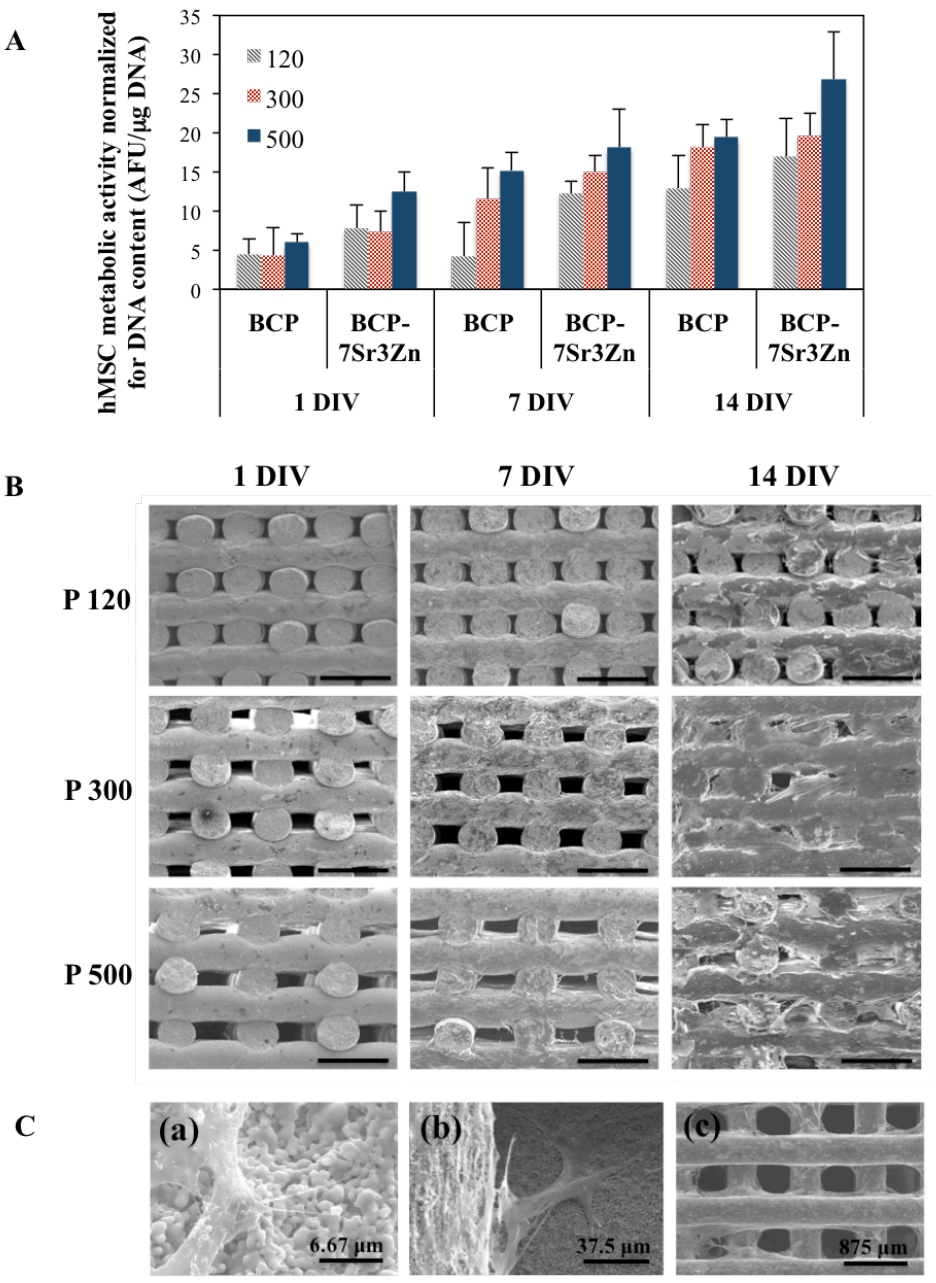

Fig. 7. (A) Metabolic activity normalized for DNA content of hMSCs on BCP and BCP-7Sr3Zn, with different pore size (120, 300 500 µm), after 1, 7 and 14 days of culture. Statistical analysis results can be found on supplementary Table 1. (B) SEM images of hMSCs on BCP-7Sr3Zn after 1, 7 and 14 days in culture in basal medium (bar: 750 µm); (C) seeded hMSCs adhered on the 500 µm pore size scaffolds after 24h (a) and 7 days (b); (c) Top-view of the 500 µm pore size scaffold after 14 days in culture.

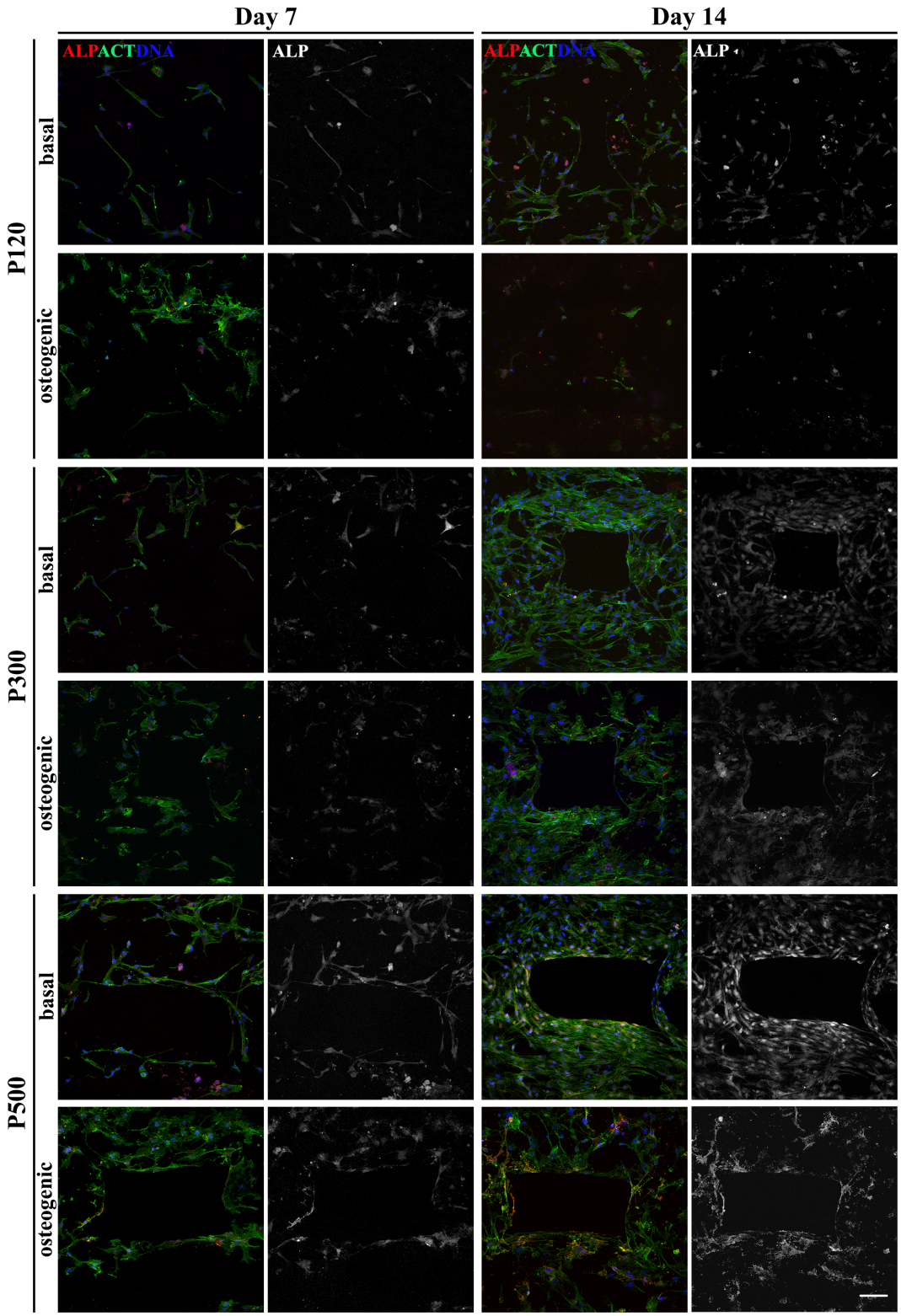

Fig. 8. Immunocytochemistry of ALP protein (red), nuclei (blue) and actin filaments (green) of hMSCs on BCP scaffolds, with different porosity, after 7 and 14 days in basal and osteogenic medium (scale bar = 100 μm)

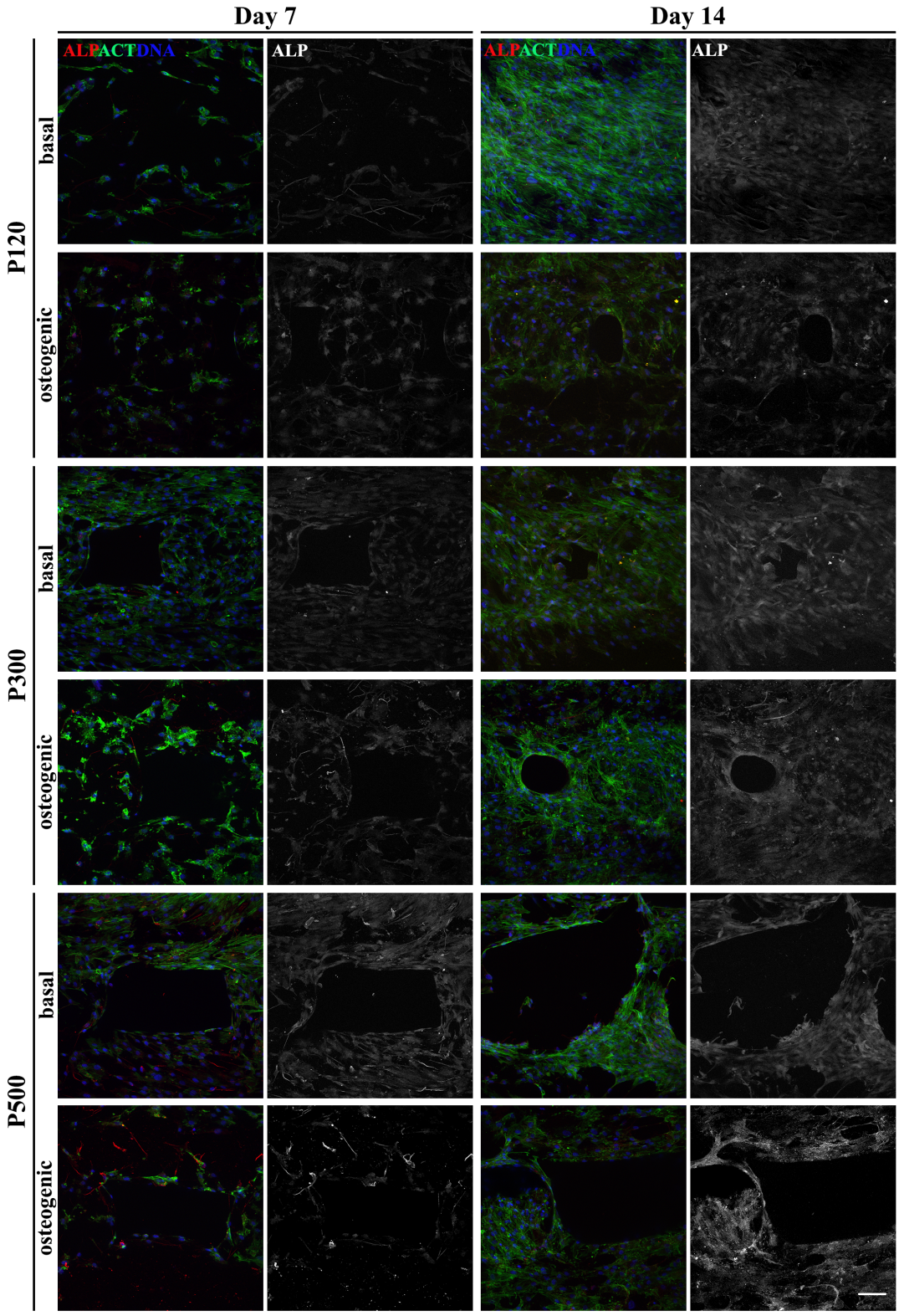

Fig. 9. Immunocytochemistry of ALP protein (red), nuclei (blue) and actin filaments (green) of hMSCs on BCP-7Sr3Zn scaffolds, with different porosity, after 7 and 14 days in basal and osteogenic medium (scale bar = 100 μm).

In order to evaluate the macropore size effect on the osteogenic differentiation we quantified the mean pixel intensity of ALP by standard procedures (described in section 2.4.4). Fig. 10A and Fig. 10B show that when comparing the range of pore size in basal conditions, higher levels of ALP (in the individual cells) were detected in the higher pore sized scaffolds (500 μm), proving higher osteogenic differentiation of hMSCs on these scaffolds, when compared with smaller pore sized ones. For BCP scaffolds, when comparing 7 days data with 14 days data under basal conditions, the highest statistical significance detected was in the 500 μm pore size with a $p < 0.0001$ thus indicating that this increase in ALP staining is proof of osteoinduction without the addition of osteoinductive exogenous factors, thus representing a key advantage on the future application of these biofabricated scaffolds. A possible explanation could be related to the small pore size closing faster, causing a deficiency of nutrient and oxygen for the cells located in that zone in comparison to the cells in the larger pores. The same tendency is observed on the basal medium cultured ion-doped scaffolds with the higher ALP intensity values being detected on the bigger pore sized scaffolds.

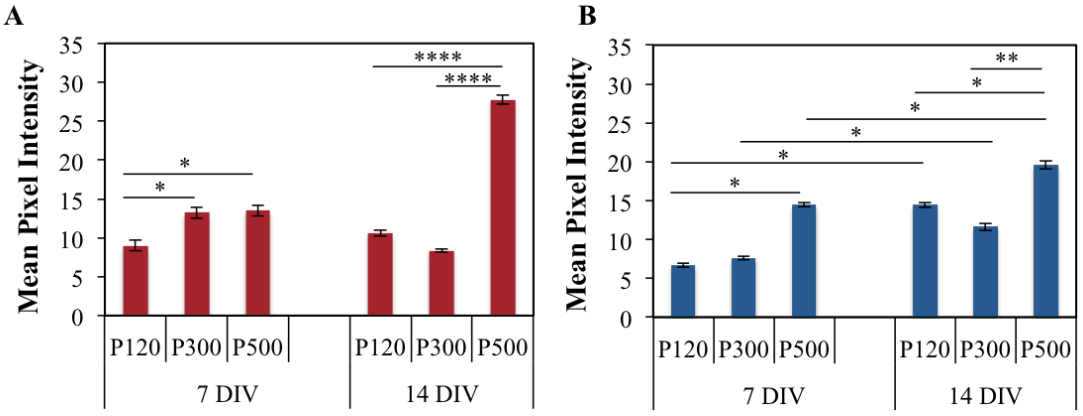

Fig. 10. Quantification of immunostained ALP using the a confocal images of hMSCs in culture in basal medium in BCP (A) and BCP-7Sr3Zn (B) scaffolds with different pore sizes, after 7 and 14 days. Statistically significant difference are marked as * ($p < 0.05$), ** ($p < 0.01$) and **** ($p < 0.0001$).

ALP staining was also quantified for both BCP and BCP-7Sr3Zn 500 μm pore scaffolds and the results shown in Fig. 11 display the same tendency on osteogenic differentiation for both scaffold formulations. Upon exposure to the osteoinductive factors added to the basal culture media, hMSCs undergo a rapid differentiation event onto the osteogenic lineage as assessed by ALP mean pixel intensity. After 7 days, the highest values for ALP can be detected for both types of scaffolds but the continuous supply of such factors seems to traduce in the stabilization of such levels since no significant differences are observed when comparing 7 days post-induction with 14 days for both scaffolds.

When we analyse the difference between the BCP and the ion-doped scaffolds, higher absolute levels of ALP are quantified for the ion-doped formulation indicating a beneficial effect of the presence of Sr and Zn regarding the osteogenic differentiation. These findings are in line with the results describing the influence of such ions in osteoinduction [49,50].

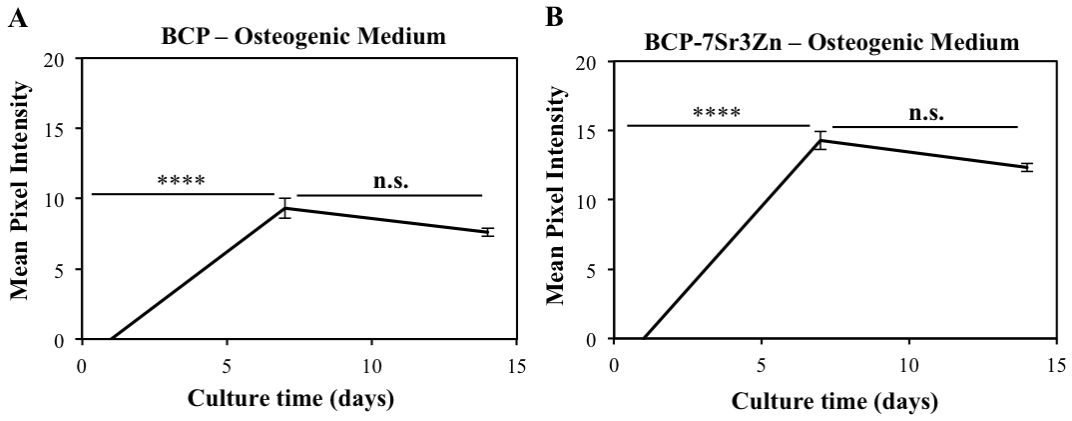

Fig. 11. Quantification of immunostained ALP using the a confocal images of hMSCs in culture in osteogenic medium in BCP (A) and BCP-7Sr3Zn (B) scaffolds with 500 μm after 7 and 14 days Statistically significant difference are marked as **** ($p < 0.0001$), n.s. means not statistically significant.

4. Conclusions

Biphasic calcium phosphate scaffolds doped with strontium and zinc ions with pore sizes in the range of 120-500 μm were successfully printed by robocasting. Inks with suitable viscoelastic behaviour for printing process were obtained from aqueous starting suspensions containing 60 vol.% of solids with subsequent addition of 2 wt.% of thickening agent (HPMC) and 0.3 wt.% of flocculating agent (PEI). All porous scaffolds presented compressive strength values equal or even higher than the human cancellous bone. *In vitro* studies performed in hMSCs culture presented a positive response towards the investigated compositions. hMSCs differentiation analysed by the ALP activity showed that the BCP-7Sr3Zn induce osteogenic differentiation *per se* with better results for the scaffolds with 500 μm pore size. These results suggest a better tissue response for this last pore size scaffolds, predicting an enhanced bone formation after *in vivo* implantation.

REFERENCES

[1] Paulius Danilevicius, Leoni Georgiadi, Christopher J. Pateman, Frederik Claeyssens, Maria Chatzinikolaidou, Maria Farsari. The effect of porosity on cell ingrowth into accurately defined, laser-made, polylactide-based 3D scaffolds. Applied Surface Science 336(2015):2-10

[2] R.Z. LeGeros, Calcium phosphate-based osteoinductive materials, Chem Rev 108 (2008) 4742–4753.

[3] Z. Yang, H.Yuan, W. Tong, P. Zou, W. Chen, X. Zhang, Osteogenesis in extraskeletally implanted porous calcium phosphate ceramics: variability among different kinds of animals, Biomaterials 17 (1996) 2131–2137.

[4] S. Bose M. Roy, A. Bandyopadhyay, Recent advances in bone tissue engineering scaffolds, Trends in Biotechnology, 30 (10) (2012) 546–554.

[5] J. Franco, P. Hunger, M.E. Launey, A.P. Tomsia, E. Saiz, Direct-Write Assembly of Calcium Phosphate Scaffolds Using a Water-Based Hydrogel, Acta Biomaterialia 6 (2010) 218–228.

[6] S.A. Kuznetsov, K.E. Huang, G.W. Marshall, P.G. Robey, M.H. Mankani, Long-term stable canine mandibular augmentation using autologous bone marrow stromal cells and hydroxyapatite/tricalcium phosphate, Biomaterials 29 (2008) 4211–4216.

[7] W. Zhang, Y. Shen, H. Pan, K. Lin, X. Liu, B.W. Darvell, W.W. Lu, J. Chang, L. Deng, D. Wang, W. Huang, Effects of strontium in modified biomaterials, Acta Biomater 7 (2011) 800–808.

[8] F. Yang, D. Yang, J. Tu, Q. Zheng, L. Cai, L. Wang, Strontium enhances osteogenic differentiation of mesenchymal stem cells and in vivo bone formation by activating Wnt/catenin signalling, Stem Cells 29 (2011) 981–991.

[9] Xiaoman Luo, Davide Barbieri, Noel Davison, Yonggang Yan, Joost D. de Bruijn, Huipin Yuana, Zinc in calcium phosphate mediates bone induction: In vitro and in vivo model, Acta Biomaterialia 10(1) (2014) 477–485.

[10] E.S. Thian, T. Konishi, Y. Kawanobe, P.N. Lim, C. Choong, B. Ho, M. Aizawa, Zinc-substituted hydroxyapatite: a biomaterial with enhanced bioactivity and antibacterial properties, J Mater Sci Mater Med 24(2) (2013) 437–445.

[11] M. Yamaguchi, H. Oishi, Y. Suketa, Stimulatory effect of zinc on bone formation in tissue culture, Biochem Pharmacol, 36 (22) (1987) 4007–4012.

[12] X. Li, Y. Sogo, A. Ito, H. Mutsuzaki, N. Ochiai, T. Kobayashi, S. Nakamura, K. Yamashita, R.Z. Legeros, The optimum zinc content in set calcium phosphate cement for promoting bone formation in vivo, Mater Sci and Eng C, 29(2009) 969–975.

[13] S.J. Hollister, Scaffold design and manufacturing: from concept to clinic, Adv Mater 21 (2009) 3330–3342.

[14] R. Langer, J.P. Vacanti, Tissue engineering, Science 260 (1993) 920–926.

[15] T.G. Kim, H. Shin, D.W. Lim, Biomimetic Scaffolds for Tissue Engineering, Adv Funct Mater 22 (2012) 2446–2468.

[16] S.J. Hollister, Porous scaffold design for tissue engineering, Nat Mater 4(7) (2005) 518–524.

[17] F.J. O'Brien, B.A. Harley, I.V. Yannas, L.J. Gibson, The effect of pore size on cell adhesion in collagen-GAG scaffolds, Biomaterials 26 (4) (2005) 433–441.

[18] P. Miranda, E. Saiz, K. Gryn, A.P Tomsia, Sintering and robocasting of beta-tricalcium phosphate scaffolds for orthopaedic applications, Acta Biomater 2 (4) (2006) 457–466.

[19] S. Michna, W. Wu, J.A. Lewis, Concentrated hydroxyapatite inks for direct-write assembly of 3-D periodic scaffolds, Biomaterials, 26 (2005) 5632–5639.

[20] S. Eqtesadi, A. Motealleh, P. Miranda, A. Pajares, A. Lemos, J.M.F. Ferreira, Robocasting of 45S5 bioactive glass scaffolds for bone tissue engineering, J Eur Ceram Soc 34 (2014) 113–124.

[21] M.C. Matesanz, J. Linares, M. Oñaderra, M.J. Feito, F.J. Martínez-Vázquez, S. Sánchez-Salcedo, D. Arcos, M.T. Portolés, M. Vallet-Regí, Response of osteoblasts and preosteoblasts to calcium deficient and Si substituted hydroxyapatites treated at different temperatures, Colloids and Surfaces B: Biointerfaces 133 (2015) 304–313.

[22] J.G. Dellinger, J. Cesarano III, R.D. Jamison, Robotic deposition of model hydroxyapatite scaffolds with multiple architectures and multiscale porosity for bone tissue engineering, J Biomed Mater Res A (2007) 383–394.

[23] C.F. Marques, F.H. Perera, A. Marote, S. Ferreira, S.I. Vieira, S. Olhero, P. Miranda, J.M.F. Ferreira, Biphasic calcium phosphate scaffolds fabricated by direct write assembly: Mechanical, anti-microbial and osteoblastic properties, J Eur Ceram Soc 37 (2017) 359–369.

[24] A. Lode, K. Meissner, Y. Luo, F. Sonntag, S. Glorius, B. Nies, C. Vater, F. Despang, T. Hanke, M. Gelinsky, Fabrication of porous scaffolds by three-dimensional plotting of a pasty calcium phosphate bone cement under mild conditions, J Tissue Eng and Regen Med 8(9) (2014) 682–693.

[25] J.A. Kim, J. Lim, R. Naren, H.S. Yun, E.K. Park, Effect of the biodegradation rate controlled by pore structures in magnesium phosphate ceramic scaffolds on bone tissue regeneration in vivo, Acta Biomater, 44 (2016) 155–167.

[26] A. Abarrategi, C. Moreno-Vicente, F.J. Martínez-Vázquez, A. Civantos, Ramos V, J.V. Sanz-Casado, R. Martínez-Corriá, F.H. Perera, F. Mulero, P. Miranda, J.L.López-Lacomba, Biological Properties of Solid Free Form Designed Ceramic Scaffolds with BMP-2: In Vitro and In Vivo Evaluation, PLoS ONE7(3) (2012) e34117.

[27] S. Nicolopoulos, J.M. Gonzalez Calbet, M.P. Alonso, M.T. Gutierrez Rios, M.I. De Frutos, M. Vallet Regi, Characterization by TEM of Local Crystalline Changes during Irradiation Damage of Hydroxyapatite Compounds, J. Solid State Chem, 116 (1995) 265–274

[28] D. Arcos, J. Rodriguez-Carvajal, M. Vallet-Regi, The effect of the silicon incorporation on the hydroxylapatite structure. A neutron diffraction study, Solid State Sci 6 (2004) 987–994.

[29] J.A. Norato, A.J. Wagoner Johnson, A Computational and Cellular Solids Approach to the Stiffness-Based Design of Bone Scaffolds, J Biomech Eng 133(9) (2011) 091003 1–8.

[30] G. Daculsi, R.Z. Legeros, E. Nery, K. Lynch, B. Kerebel, Transformation of biphasic calcium phosphate ceramics in vivo: ultrastructural and physicochemical characterization, J Biomed Mater Res 23 (1989) 883–894.

[31] G. Daculsi, R.Z. LeGeros, M. Heughebaert, I. Barbieux, Formation of carbonate-apatite crystals after implantation of calcium phosphate ceramics, Calcif Tissue Int 46 (1990) 20–27.

[32] Y.M. Shin, J.-S. Park, S.I. Jeong, S.-Jun An, H.-J. Gwon, Y.-M. Lim, Y.-C. Nho, C.-Y. Kim, Promotion of Human Mesenchymal Stem Cell Differentiation on Bioresorbable Polycaprolactone/Biphasic Calcium Phosphate Composite Scaffolds for Bone Tissue Engineering, Biotechnol Bioprocess Eng 19 (2014) 341–349.

[33] B. Pemmer, A. Roschger, A.Wastl, J.G. Hofstaetter, P.Wobrauschek, R. Simon, H.W. Thaler, P. Roschger, K. Klaushofer, C. Streli, Spatial distribution of the trace elements zinc, strontium and lead in human bone tissue, Bone 57 (2013) 184–193.

[34] X. Luo, D. Barbieri, N. Davison, Y. Yan, J.D. de Bruijn, H. Yuan, Zinc in calcium phosphate mediates bone induction: In vitro and in vivo model, Acta Biomater 10 (2014) 477–485.

[35] M. Schumacher, A. Lode, A. Helth, M. Gelinsky, A novel strontium(II)-modified calcium phosphate bone cementstimulates human-bone-marrow-derived mesenchymal stem cell proliferation and osteogenic differentiation in vitro, Acta Biomaterialia 9 (2013) 9547–9557.

[36] A.F. Lemos, J.D. Santos, J.M.F. Ferreira, Influence of characteristics of starting hydroxyapatite powders and of deagglomeration procedure, on rheological behaviour of HA suspensions, Mater Sci Forum 455–456 (2004) 361–365.

[37] L.M. Rodríguez-Lorenzo, M. Vallet-Regí, J.M.F. Ferreira, Colloidal processing of hydroxyapatite, Biomaterials 22(13) (2001)1847–52.

[38] L. Zhang, N. Hanagata, M. Maeda, T. Minowa, T. Ikoma, H. Fan, X. Zhang, Porous hydroxyapatite and biphasic calcium phosphate ceramics promote ectopic osteoblast differentiation from mesenchymal stem cells, Sci Technol Adv Mater 10 (2009) 025003 1–9.

[39] D.R. Carter, G.H. Schwab, D.M. Spengler, Tensile Fracture of Cancellous Bone, Acta Orthop Scand 51 (1980) 733–741.

[40] S. Pina, S.I. Vieira, P.M.C. Torres, F. Goetz-Neunhoeffer, J. Neubauer, O.A.B. da Cruz e Silva, E.F. da Cruz e Silva, J.M.F. Ferreira, In vitro performance

assessment of new brushite-forming Zn- and ZnSr-substituted β-TCP bone cements, J Biomed Mater Res B 94 B(2) (2010) 414–420.

[41] J. Caverzasio, Strontium ranelate promotes osteoblastic cell replication through at least two different mechanisms, Bone 42 (2008) 1131–1136.

[42] C.J. Wilson, R.E. Clegg, D.I. Leavesley, M.J. Pearcy, Mediation of biomaterial-cell interactions by adsorbed proteins: a review, Tissue Eng 11(1-2) (2005) 1–18.

[43] Y. Lai, C. Xie, Z. Zhang, W. Lu, J. Ding, Design and synthesis of a potent peptide containing both specific and non-specific cell-adhesion motifs, Biomaterials 31 (2010) 4809–4817.

[44] M. Cicuéndez, M. Malmsten, J.C. Doadrio, M.T. Portolés, I. Izquierdo-Barba, M.Vallet-Regí, Tailoring hierarchical meso–macroporous 3D scaffolds: from nano to macro, J Mater Chem B 2 (2014) 49–58.

[45] S.N. Rath, L.A. Strobel, A. Arkudas, J.P. Beier, A.-K. Maier, P. Greil, R.E. Horch, U. Kneser, Osteoinduction and survival of osteoblasts and bone-marrow stromal cells in 3D biphasic calcium phosphate scaffolds under static and dynamic culture conditions, J Cell Mol Med 16(10)(2012) 2350–2361.

[46] F.N. Syed-Picard, G.A. Shah, B.J. Costello, C. Sfeir, Regeneration of periosteum by human bone marrow stromal cell sheets, J Oral Maxillofac Surg. 72 (2014) 1078–1083.

[47] Y.Li, W. Weng, K.C. Tam, Novel highly biodegradable biphasic tricalciumphosphates composed of alpha-tricalcium phosphate and beta-tricalcium phosphate, Acta Biomater 3 (2007) 251–254.

[48] T. Jiang, B. Zhou, L. Huang, H. Wu, J. Huang, T. Liang, H. Liu, L. Zheng, J. Zhao, Andrographolide exerts pro-osteogenic effect by activation ofWnt/beta-catenin signaling pathway in vitro, Cell Physiol Biochem 36 (2015) 2327–2339.

[49] S. Peng, G. Zhou, K.D.K. Luk, K.M.C. Cheung, Z. Li, W.M. Lam, Z. Zhou, W.W. Lu, Strontium promotes osteogenic differentiation of mesenchymal stem cells through the Ras/MAPK signaling pathway, Cell Physiol Biochem 23 (2009) 165–74.

[50] X. Luo, D. Barbieri, N. Davison, Y. Yan, J.D. de Bruijn, H. Yuan, Zinc in calcium phosphate mediates bone induction: In vitro and in vivo model, Acta Biomater 10(1) (2014) 477–485.

Supplementary Tables

Table 1. Statistical analysis of data from Fig. 8, metabolic activities of hMSCs on BCP and BCP-7Sr3Zn. Statistically significant differences are marked with * ($p < 0.05$), ** ($p < 0.01$), *** ($p < 0.001$) or **** ($p < 0.0001$), n.s. means not statistically significant.

BCP_120 _day1 Vs BCP_300 _day 1	n.s. 0.1145
BCP_120 _day1 Vs BCP_500 _day 1	** 0.0046
BCP_120 _day1 Vs BCP_120 _day 7	* 0.0239
BCP_120 _day1 Vs BCP_120 _day 14	*** 0.0007
BCP_120 _day1 Vs BCP-7Sr3Zn_120 _day 1	<0.0001
BCP_300 _day1 Vs BCP_500 _day 1	** 0.0016
BCP_300 _day1 Vs BCP_120 _day 7	<0.0001
BCP_300 _day1 Vs BCP_300 _day 7	<0.0001
BCP_300 _day1 Vs BCP_300 _day 14	<0.0001
BCP_300 _day1 Vs BCP-7Sr3Zn_300 _day 1	*** 0.0002
BCP_500 _day1 Vs BCP_500 _day 7	*** 0.0009
BCP_500 _day1 Vs BCP_500 _day 14	<0.0001
BCP_500 _day1 Vs BCP-7Sr3Zn_500 _day 1	<0.0001
BCP_120 _day7 Vs BCP_300 _day 7	<0.0001
BCP_120 _day7 Vs BCP_500 _day 7	<0.0001
BCP_120 _day7 Vs BCP_120 _day 14	** 0.0010
BCP_120 _day7 Vs BCP-7Sr3Zn_120 _day 7	*** 0.0002
BCP_300 _day7 Vs BCP_500 _day 7	n.s. 0.8503
BCP_300 _day7 Vs BCP_300 _day 7	<0.0001
BCP_300 _day7 Vs BCP-7Sr3Zn_300 _day 7	** 0.0056
BCP_500 _day 7 Vs BCP_300 _day 14	* 0.0356
BCP_500 _day 7 Vs BCP-7Sr3Zn_500 _day 7	<0.0001
BCP_120 _day14 Vs BCP_300 _day 14	** 0.007
BCP_120 _day14 Vs BCP_500 _day 14	*** 0.0001
BCP_120 _day14 Vs BCP-7Sr3Zn _120 _day 14	<0.0001
BCP_300 _day14 Vs BCP_500 _day 14	n.s. 0.1362
BCP_300 _day14 Vs BCP-7Sr3Zn _300 _day 14	n.s. 0.149
BCP_500 _day14 Vs BCP-7Sr3Zn_500 _day 1	<0.0001

BCP-7Sr3Zn _120 _day1 Vs BCP-7Sr3Zn _300 _day 1	n.s. 0.7575
BCP-7Sr3Zn _120 _day1 Vs BCP-7Sr3Zn _500 _day 1	<0.0001
BCP-7Sr3Zn _120 _day1 Vs BCP-7Sr3Zn _120 _day 7	<0.0001
BCP-7Sr3Zn _120 _day1 Vs BCP-7Sr3Zn _120 _day 14	<0.0001
BCP-7Sr3Zn _300 _day1 Vs BCP-7Sr3Zn _500 _day 1	<0.0001
BCP-7Sr3Zn _300 _day1 Vs BCP-7Sr3Zn _300 _day 7	<0.0001
BCP-7Sr3Zn _300 _day1 Vs BCP-7Sr3Zn _300 _day 14	<0.0001
BCP-7Sr3Zn _500 _day1 Vs BCP-7Sr3Zn _500 _day 7	<0.0001
BCP-7Sr3Zn _500 _day1 Vs BCP-7Sr3Zn _500 _day 14	<0.0001
BCP-7Sr3Zn _120 _day7 Vs BCP-7Sr3Zn _300 _day 7	<0.0001
BCP-7Sr3Zn _120 _day7 Vs BCP-7Sr3Zn _500 _day 7	<0.0001
BCP-7Sr3Zn _120 _day7 Vs BCP-7Sr3Zn _120 _day 14	<0.0001
BCP-7Sr3Zn _300 _day7 Vs BCP-7Sr3Zn _500 _day 7	<0.0001
BCP-7Sr3Zn _300 _day7 Vs BCP-7Sr3Zn _300 _day 14	<0.0001
BCP-7Sr3Zn _500 _day7 Vs BCP-7Sr3Zn _500 _day 14	<0.0001
BCP-7Sr3Zn _120 _day14 Vs BCP-7Sr3Zn _300 _day 14	<0.0001
BCP-7Sr3Zn _120 _day14 Vs BCP-7Sr3Zn _500 _day 14	<0.0001
BCP-7Sr3Zn _300 _day14 Vs BCP-7Sr3Zn _500 _day 14	<0.0001

Chapter 6

SINTERING-FREE SCAFFOLDS OBTAINED BY ADDITIVE MANUFACTURING FOR CONCURRENT BONE REGENERATION AND DRUG DELIVERY

C. F. Marques[1,2], S.M. Olhero[1], P.M.C. Torres[1], J.C.C. Abrantes[1,3], S. Fateixa[4], H. I. S. Nogueira[4], I.A.C. Ribeiro[5], A. Bettencourt[5], A. Sousa[2,6], P. Granja[2,6,7], J.M.F. Ferreira[1]

[1] Department of Materials and Ceramics Engineering, CICECO University of Aveiro, 3810-193 Aveiro, Portugal

[2] i3S – Instituto de Investigação e Inovação em Saúde

[3] UIDM, ESTG, Polytechnic Institute of Viana do Castelo, 4900 Viana do Castelo, Portugal

[4] Department of Chemistry- CICECO, University of Aveiro, 3810-193, Aveiro, Portugal

[5] Research Institute for Medicines (iMed.ULisboa), Faculty of Pharmacy, Universidade de Lisboa, Av. Prof. Gama Pinto, 1649-003 Lisbon, Portugal

[6] INEB – Instituto Nacional de Engenharia Biomédica, 4200-135, Portugal

[7] FEUP – Faculdade de Engenharia da Universidade do Porto, 4200-464, Portugal

Abstract

The present work reports on the fabrication of biphasic calcium phosphate/chitosan composite scaffolds using robocasting as additive manufacturing technique. Taking advantage of sintering step elimination, the possibility to obtain drug loaded scaffolds was also explored by adding levofloxacin to the extrudable inks. High amounts of solids (biphasic calcium phosphate powders, BCP) in inks and chitosan crosslinking by added genipin are the main factors responsible for the mechanical properties of the scaffolds after printing.

Three BCP powders containing different HA/β−TCP ratios were used. High percentage of solids (45 vol.%) in the final inks were attained, allowing successful extrusion behaviours during 3D porous structures printing. Adding levofloxacin induced slightly changes on the rheological behaviour of the inks and consequently, on the microstructure and on the mechanical properties of the final scaffolds. Drug delivery studies revealed a fast release of levofloxacin with a high burst of drug within the first 30 min. Levofloxacin loaded samples also presented bacteria growth inhibition ability, proving that antibiotic was not degraded during the fabrication process and its bactericidal efficacy was preserved.

The composite scaffolds fabricated constitute a promising approach joining both local bone regeneration and infection control.

Keywords: Sintering-free, composite scaffolds, robocasting, Biphasic CaP, bone regeneration, local-drug-delivery.

1. Introduction

Bone defects caused by several ways, such us traumatic accidents, tumour resection or osteoporosis, demand major health care challenges to biomedical science and repairing technologies. Also, therapies for bone associated infections often require the removal of infected bone, treating the infection around and filling the left bone space with a bio-regenerative material [1]. Combined efforts of medical practitioners and material scientists have been undertaken in enable fabrication of bone-regenerative scaffolds incorporating biomolecules with clinically important functionalities as reported in several recent works [2-9]. For instance, addition of antibiotics or chemotherapeutic drugs in the scaffolds could prevent bacterial infection and prevent cancer recurrence, respectively [2-9]. Therefore, as mentioned by Fernandes *et al.* [10], finding an implanted biomaterial that smartly combines both therapy functions of drug-eluting and regeneration will bring lots of benefits not offered by the conventional medical practice. This challenging approach is likely to become a compulsory target in the near future [10].

A number of biopolymers, such as polycaprolactone (PCL) and poly (lactic-co-glycolic acid, PLGA) have been studied for this purpose [11,12]. However, the exclusive use of polymer scaffolds has shown limited success because of their hydrophobicity, difficulty to control drug release, and low osteoconductivity [2]. Calcium phosphate (CaP) based materials are still the best choice to repair damaged bones [13]. CaP are osteoconductive, might acquire osteoinductive properties [14,15], being the most adequate type of material for controlled drug delivery. The trend is therefore finding an optimal combination of biomaterials to obtain tunable drug-delivery bone scaffolds with proper mechanical strength [1,2,12,16]. Biphasic calcium phosphates (BCP) have been widely investigated for several purposes [17]. As the name suggests, BCP consists of two calcium phosphate phases, commonly a more stable phase (HA) and a more soluble one (β-TCP), assorted in different proportions. This phase's combination offers some advantages over the pure phases, enabling a better control of bioactivity and biodegradation, and assuring the stability of the biomaterial while promoting bone ingrowth.

Besides based material, scaffold's architecture on the macro-, micro- and nanoscale is crucial for proper nutrient and waste transport, cellular interactions, mechanical

stability, drug delivery and ultimately functional tissue formation [1,11]. Additive manufacturing (AM) appears as an emergent and promising technique in regenerative medicine, essentially for bone substitute's fabrication, where a precise control of pore shape and size is possible, among other advantages [18-22]. Robocasting, also called direct write assembling (DWA) was developed for ceramics and uses extrudable aqueous ceramic inks at room temperature that are commonly obtained by mixing ceramic powders in water with few amounts of organic additives [19,21,22]. However, after printing, all green CaPs based scaffolds are commonly submitted to a sintering step at high temperatures (1100-1200 ºC) to obtain suitable mechanical properties. This hinders the incorporation of temperature sensitive bioactive molecules in the extrudable ink before sintering. Because of that, bioactive molecules for different therapeutic applications can only be added after sintering by soaking the scaffolds in suspensions with suitable concentrations of the desired biomolecules or drugs [3-5,7,8]. This means that impregnation process limits the amount of biomolecules incorporation to the absorption capacity of the scaffolds, as well as to their surface properties. However, the loading output of the process is very low, since a highly concentrated solution must be prepared in order to incorporate a small amount of drug in the scaffold, and hence the process is neither very well controlled and nor cost-effective. To overcome these difficulties, sintering-free scaffolds fabrication could be the ground-breaking solution. Martínez-Vázquez *et. al.* [16] published the first results related to the sintering-free drug-loaded Si-doped HA composite scaffolds fabricated by robocasting. The biological behaviour and biodegradabilty of these hybrid (Si-doped HA + gelatin) scaffolds was greater than that of sintered inorganic Si-doped HA scaffolds, but the overall targets are still far from being satisfactorily accomplished. The main drawback was related to the low inorganic contents of inks that strongly limited the filaments strength during printing process and the final mechanical properties of the scaffolds. Optimizing the rheological properties of the inks to obtain appropriate extruded filaments is a key step to fabricate scaffolds by robocasting.

Considering all the constraints stated in literature review and having ahead the future requirements to improve life quality of patients with bone diseases, the main goal of the present work is to develop calcium phosphate based scaffolds, with simultaneous activity on infection and regenerative therapies. This target will be achieved by

combining pioneering manufacture specifications, including: (1) preparation of drug-loaded high concentrated calcium phosphate based inks with proper rheological performance, (2) 3D-printing by robocasting technique and (3) sintering stage elimination. The model drug selected for this study was levofloxacin, an antibiotic successfully used in the treatment of bone infection, due to its ability to penetrate into trabecular and cortical bone minimizing the risk of resistance selection [23,24]. The drug delivery behaviour and the antibacterial activity of the resultant 3D scaffolds were also evaluated.

2. Experimental Procedure

2.1 Synthesis and characterization of biphasic calcium phosphate powders

The synthesis of CaP-based powders by aqueous precipitation requires a close control of many parameters such as, reaction pH, ripening time, temperature and stoichiometry of the raw materials [25]. Since the first step of this work was obtaining biphasic calcium phosphate powders (BCP) with different proportions of HA and β-TCP phases, and considering that higher Ca/P ratios and pH values promote the formation of HA phase [26,27], the initial Ca/P ratios and pH values were accordingly varied.

BCP powders with Ca/P ratios of 1.50, 1.59 and 1.65 were obtained via aqueous precipitation, according to a procedure described in a previous work [21]. Briefly, 1.2 M di-ammonium hydrogen phosphate solution [$(NH_4)_2HPO_4$, Panreac, Spain] was added to a calcium nitrate tetrahydrate [$Ca(NO_3)_2.4H_2O$, Panreac, Spain] solution with the concentration required for the planned Ca/P ratio. The reaction occurred at 90 ºC for 2 h under constant stirring conditions (1000 rpm) at pH 8, 8.5 and 9, for synthesis of BCP 1.50, 1.59 and 1.65, respectively. These pH values were maintained by adding the required amounts of 8 M ammonium hydroxide solution [NH_4OH, Sigma-Aldrich, Germany]. After the synthesis, the precipitates were separated through vacuum filtration and dried at 100 ºC overnight. The prepared powders were calcined at 1100 ºC in a Thermolab furnace (Pt30%Rh/Pt6%Rh thermocouple) using

a heating rate of 5 ºC min^{-1} and 2 h dwelling time at the maximum temperature, followed by cooling to room temperature (RT). The calcined powders were then dry milled for 45 min in a high energetic ball milling up to achieving a mean particle size ~1 μm.

The collection of XRD data for Rietveld refinement studies was performed using High Resolution X-ray Diffractometer (PANalytical X'Pert PRO) with Cu Kα radiation (λ = 1.5406 Å) produced at 45 kV and 40 mA, between 20º and 80º diffraction angles (2θ) with a step size of 0.013º and 200 s time per step. The software TOPAS version 4.2 (Bruker AXS, Karlsruhe, Germany) with the fundamental parameter approach, and the ICDD card numbers of # 04-015-7245 for HA [28] and # 04-006-9376 for β-TCP [29] were used for Rietveld refinements.

The particle size and particle size distributions of all powders were measured using a particle size analyser (COULTER LS230, UK) with Fraunhofer optical model. The specific surface area of the powders were measured by the Brunauer–Emmett–Teller (BET) method using a Micromeritics Gemini 2370 V5.00 (Norcross, USA) through the nitrogen gas adsorption after degassing the samples in a Micromeritics Flow Prep 060 (Norcross, USA). Powder morphology was also observed by Scanning Electron Microscopy (SEM, Hitachi S4100, Hitachi High-Technologies Europe, GmbH,Germany).

2.2 Inks preparation and characterization

The first step of ink preparation started with fine tuning the temperature and time dependent gelling/reticulation behaviour of the BCP/chitosan solution system in presence of the crosslinking agent genipin (Challenge Bioproducts, Taiwan) by rheological measurements. A chitosan (low molecular weight, Sigma-Aldrich, Germany) 3 wt.% solution was prepared in 0.5 vol.% of acetic acid glacial (Pronalab, Portugal) solution at room temperature (RT) overnight under constant stirring. Since cross-linking of chitosan can also occur in presence of only CaP powders [30], the inorganic component in these preliminary studies was fixed at 20 vol.% to assess the effects of the other variables. BCP-1.65 powder was selected for these experiments. The test methods employed included temperature, time, stress, and frequency sweeps in oscillatory mode at a constant temperature of 37 ºC, except for the temperature

sweep experiments that cover the temperature range from 20 to 90 ºC. The rheometer used is a Kinexus Pro^{+} instrument (Malvern, USA) coupled with plate and plate (20 mm diameter) as measuring system and 1000 μm gap. A solvent trap was used to prevent drying of the samples during experiments.

To select the most appropriate amount of crosslinking agent (wt.% genipin) for 3 wt.% chitosan solution, temperature sweep measurements of chitosan solution in presence of 0, 0.5, 1 and 2.5 wt.% of genipin, in absence and in presence of BCP-1.65 powder, was evaluated. In all measurements, 1 Hz frequency and shear stress values within the linear viscoelastic region (LVR) were selected. The dynamics of both viscoelastic characteristic functions (elastic storage modulus, G', and viscous loss modulus, G'') were employed to determine the gelation temperature, the instant at which G' intersects G''. The gel strength of resultant composite systems (80 vol.% chitosan solution + 20 vol.% BCP powder) in presence of different amounts of genipin (0, 0.5, 1 and 2.5 wt.%) was assessed by frequency sweeps at 37 ºC after 12 h maturation at a constant stress selected from LVR profiles. The reticulation ability of chitosan by the three as-synthetized BCP powders (without genipin) was analysed by measuring the time evolution of the viscoelastic (G´ and G´´) parameters. The results of these preliminary studies revealed that chitosan was rapidly reticulated by BCP-1.5 even at this low concentration, hindering the preparation of the inks. Therefore, only the BCP-1.59 and BCP-1.65 powders have been used for further studies.

Inks for robocasting containing 45 vol.% of inorganic components were prepared by mixing the powders (BCP-1.59, or BCP-1.65) with 3 wt.% chitosan solution. The powders were gradually added to chitosan solution using a planetary centrifugal mixer (ARE-250, Thinky Corp., Tokyo, Japan) to guarantee homogeneity of all components. The final ink preparation stage consisted of adding 1 wt.% of genipin (based on the mass of chitosan) followed by homogenization for further 2 min. Levofloxacin-loaded scaffolds were prepared using a similar procedure by adding 2 wt.% of levofloxacin (based on the mass of inorganic component) to the 3 wt.% chitosan solution just before mixing it with BCP powders. The final inks with 45 vol.% of solids without and with levofloxacin were characterized by amplitude sweep and frequency sweep modes.

For an easier identification, final inks were nominated as: Ink1.65 and Ink1.59; Ink1.65-LEV and Ink1.59-LEV, for inks prepared from BCP-1.65 and BCP-1.59 powders in absence and in presence of levofloxacin, respectively.

2.3 Scaffolds fabrication by robocasting

3D BCP scaffolds consisting of a mesh of ceramic rods were constructed layer-by-layer via direct write assembly of the ink using a robotic deposition device (3-D Inks, Stillwater, OK). The ink was deposited through cylindrical deposition nozzles (EFD Inc., East Providence, RI) with 410 μm diameter, at a printing speed of 10 mm s^{-1}. The external dimensions of the scaffolds were set at about 3×3×3 mm, being a total of 12 layers with 500 μm pore size. The deposition was at environment temperature and humidity. After printing, samples were placed at 37 ºC overnight with controlled humidity (80%) to promote chitosan crosslinking by genipin. Then, scaffolds were frozen at −80ºC and subsequently lyophilized (Telstar lyoQuest HT-40, Beijer Electronics Products AB, Malmoe, Sweden) at −80 ºC, keeping a sublimation pressure of 0.025 mbar to remove water.

Final scaffolds were nominated as: S1.65 and S1.59; S1.65-LEV and S1.59-LEV for scaffolds prepared from Ink1.65 and Ink1.59 in absence and in presence of levofloxacin, respectively.

2.4 Scaffolds characterization

2.4.1 *In vitro* cytotoxicity assessment

The cytotoxicity of the scaffolds was assessed according to ISO 10993-5 standard practices [31]. The hDNFs (human dermal neonatal fibroblasts) were routinely cultured in DMEM supplemented with 10% v/v FBS (Gibco), 1% v/v P/S (Biowest) and 1% v/v amphotericin B (Capricorn Scientific) and kept at 37 ºC in a humidified atmosphere of 5% CO_2. hDNFs were used up until passage 8. For cytotoxicity assays, hDNFs were seeded at a density of 1×10^4/well into 48-well plates and incubated in 500 μL of complete DMEM and allowed to reach full confluence. Sterilized scaffolds (S1.65 and S1.59) were incubated under the same conditions and after 24 h incubation time direct and indirect contact test were performed. For the direct contact assay samples were directly put into the wells containing fibroblasts and the medium was

refreshed. For the indirect contact assay the medium was replaced by the medium that had been incubated with the scaffolds to test the leachable substances thereof. All experiments were carried out in triplicate and cells that were not in contact with the materials were used as control. The resazurin-based assay was used to assess cytotoxicity after 24 h. Briefly, culture medium was removed and replaced with complete medium with 20% v/v resazurin (Sigma-Aldrich, Germany) and incubated at 37ºC in a humidified incubator with 5% CO_2 for 2 h, after which 100 μL per well was transferred to a 96-well black plate and fluorescence was measured (Ex 530 nm/Em 590 nm) using a micro plate reader spectrophotometer (Bioteck Plate Reader, Synergy MX).

2.4.1.1 Statistical analysis

Statistical significance analysis was conducted using analysis of variance (ANOVA), followed by the Greenhouse-Geisser test. Differences with p value <0.05 were considered significant.

2.4.2 Structural features

Morphological features and microstructure of the scaffolds were analysed by scanning electron microscopy (SEM, Hitachi S4100, Hitachi High-Technologies Europe, GmbH, Germany) and MetrologyCT system (μCT, Phoenix V|TOME|X, GE). μCT performs non-destructive imaging and allows the quantification of 3D micro architectural morphology of each scaffold. For that, samples were imaged with an X-ray tube voltage of 80 kV and a current of 80 mA. The scanning angular increment was 0.15 degrees and the voxel resolution 6.7 microns. Data sets were reconstructed and segmented into binary images (16-bit BMP images) for the subsequent image processing, namely dimensional measurements and 3D surface reconstructions using Volume Graphics 3.04 software (Volume Graphics).

The compressive strength of scaffolds was determined by uniaxial tests on cubic blocks of 3 mm per side cut from the 3D printed lyophilized scaffolds. Tests were carried out in air using a universal testing machine (AG-IS 5 kN, Shimadzu Corpor., Kyoto, Japan) in the perpendicular direction to the printing plane at a constant speed of 0.5 mm min^{-1}. Compressive strength was calculated as the maximum applied load

divided by the measured square section of the sample. A minimum of 15 samples was tested for each composition to obtain statistically reliable values. The apparent density values of scaffolds ($g \cdot cm^{-3}$) were calculated based on their weights and geometrical volumes.

2.4.3 Evaluation of levofloxacin distribution

Levofloxacin distribution, throughout 3D scaffolds obtained from Ink1.65-LEV and Ink1.59-LEV, was evaluated by Raman Imaging using a confocal Raman microscope (WITec alpha300 RAS+ (WITec, Ulm, Germany). An Nd:YAG laser operating at 532 nm were used as excitation source, with the power set at 8.5 mW (150 x 150 points per grid in a 50 x 50 μm area, 0.05 s). Raman images were produced by raster scanning the laser beam over the samples and by accumulating a full Raman spectrum at each pixel (in total 22500 spectra), with a spatial resolution of approximately 0.33 μm. The WITec software, WITec Project 4.0 (WITec, Ulm, Germany), was used to create the Raman images. The Raman images were generated using band integrals, in which the value of the absolute area underneath a band (e.g. at 1620 cm^{-1}) corresponds to a colour intensity in the scale, shown in the image at the respective pixels.

2.5 *In vitro* drug release and antimicrobial susceptibility testing

Levofloxacin (LEV) release from the different scaffolds was determined according to previously described methods [32,33]. Briefly, scaffolds accurately weighted (50 mg) were immersed in 25 mL of PBS (Phosphate Buffer Saline, Sigma-Aldrich) buffer (pH 7.4) in propylene tubes. Tubes were placed in a water bath at 37 ºC and shaken horizontally (30 strokes min^{-1}). At pre-determined time points (10 min, 30 min, 1 h, 2 h, 6 h, 8 h, 24 h) samples were collected and analysed for LEV content by UV-spectrophotometry (288 nm) (BMG Labtech FLUOstar Omega).

Agar disk diffusion tests (Kirby-Bauer test) were conducted to examine the antibacterial effect of levofloxacin-loaded materials [34]. For this, inks without and with 2% of levofloxacin (w/w) were prepared (as previously described in section 2.2) and used to obtain 8 mm diameter disks (1 mm height). Hereafter, these disks were

submitted to the same process as the scaffolds, i.e., placed at 37 ºC overnight under controlled humidity, frozen at −80 ºC and subsequently lyophilized. A methicillin susceptible *S. aureus* ATCC®25923 (MSSA) strain obtained from American Type Culture Collection (ATCC) and one clinical isolate methicillin resistant (MRSA) were used. Aliquots from frozen stocks at -80ªC were used to culture microorganisms on Tryptic Soy Agar (Biokar Diagnostics, France) plates for 24h. *S. aureus* inoculum of both strains (1×10^8 CFU mL^{-1}) was prepared by direct colony suspension in Mueller-Hinton Broth (Biokar Diagnostics, France) and swabbed uniformly across Mueller-Hinton Agar (Biokar Diagnostics, France) plates. The disks with and without levofloxacin and filter-paper disks with 5 mg of levofloxacin (control) were placed on the agar surface. Plates were incubated at 37 ºC for 20 h and the inhibition zone diameter was measured using a Vernier calliper. Three independent experiments were conducted.

3. Results and Discussion

3.1 Powders characterization

Particle size, size distributions and crystalline phase contents (HA and β-TCP in the BCP powders) are important factors determining the rheological behaviour of the inks and consequently the structural properties of scaffolds fabricated thereof. The mechanical integrity of the scaffolds depends essentially on a well-balanced formulation of the ink containing optimized proportions of gelling components and BCP powders with suitable particle size distributions. Hence, having BCP powders with similar particle size distributions will facilitate investigating the specific interactions between the different powders and the gelling system (chitosan/genipin).

Data on specific surface area (SSA), particle size distribution (D_{mean}, D_{10}, D_{50} and D_{90}) and crystalline phase assemblage of the three different BCP powders are presented in Fig. 1 (A). All powders presented similar particle size distribution parameters with mean particle sizes around 1.5 μm for BCP-1.65 and BCP-1.5 and slightly lower (1.4 μm) for BCP-1.59, with the same trend observed for D_{50} and D_{90}. Comparing the size data (Fig.1 A) with SEM micrographs in Fig. 1 (B) reveals that

individual particles are actually smaller than 1.5 μm. The high degree of particles agglomeration could be responsible for the higher values of mean particle size obtained by Coulter analysis.

A

Sample code	SSA(±0.3) (m^2 g^{-1})	Particle size distribution				Wt. % of phase composition (± 1)	
			D_x[a] (μm)				
		Mean (μm)	D_{10}	D_{50}	D_{90}	HA	β-TCP
BCP-1.65	2.17	1.548	0.194	1.276	3.432	87.13	12.87
BCP-1.59	1.40	1.372	0.173	1.057	3.127	46.40	53.70
BCP-1.5	1.88	1.558	0.158	1.239	3.597	22.96	77.04

[a] D_x is the particle diameter at or below which there is the amount x (vol.%) of particles in the cumulative (from 0 to 100%) particle size distribution curve.

B

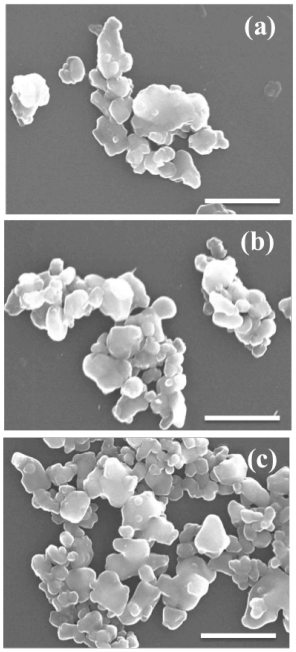

C

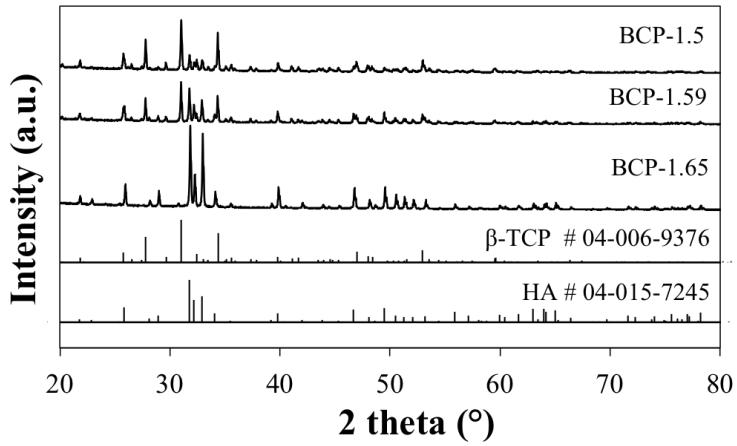

Fig. 1. Physical, chemical and morphological features of BCP powders heat-treated at 1100 ºC: (A) specific surface area, particle size distribution parameters and phase (HA+β-TCP) contents determined by Rietveld refinement (95% repeatability limits of the phase quantification should be considered to be close to ±1% [35]); (B) SEM micrographs of the BCP-1.65 (a), BCP-1.59 (b) and BCP-1.5 (c) powders (bar: 1.5 μm); (C) XRD patterns.

The biphasic nature (HA + β-TCP) of the powders is confirmed and, as expected, the amount of HA increased with increasing Ca/P ratios from 1.5 (~23%) to 1.59 (~46%) and 1.65 (87%). These results are in good agreement with XRD diffraction patterns of BCP powders displayed in Fig. 1 (C), showing clear intensity differences in the peaks of both HA and β-TCP phases according to the starting composition.

3.2 Inks characterisation

Colloidal inks for direct write assembly must satisfy two important criteria: (i) be able to flow through the fine deposition nozzle and then "set" immediately to facilitate shape retention of the extruded filaments even as they span gaps in the underlying layer(s); (ii) have a high solid volume fraction to minimize shrinkage during drying and assure mechanical integrity of the final scaffolds. In sintering-free scaffolds the viscoelasticity of the pastes and the structural reliability of the constructs will be assured by the gelling capacity of chitosan/BCP composite with genipin as crosslinking agent, as well as, the amount of inorganic components. Chitosan, a natural polymer obtained from the alkaline deacetylation of the chitin, is insoluble in aqueous solutions above pH 5.7. In dilute acids (pH <6) the free amino groups are protonated and the molecule becomes soluble, resulting in a relatively high viscosity solution. The reticulation of chitosan requires the addition of a crosslinking agent. Genipin is a natural crosslinking agent for chitosan, often preferred to several synthetic compounds as widely reported in literature [36]. It is also known that the polymerization/gelling process is somewhat faster in presence of CaPs due to the synergetic effect between the functional amine groups from chitosan and the phosphate groups of CaP powders [30]. Therefore, the first step of preliminary viscoelastic measurements aimed at establishing the maximum solids loading that could be used to investigate the effects of the other experimental variables. Fig. 2 plots the dynamic modulus (G′, G′′) as a function of temperature for BCP-1.65 system with 20 and 25 vol.% solids. It can be seen that G′ predominates over G′′ for the most concentrated system in BCP powder, contrarily to what is observed for the more diluted one. The higher stiffness of the paste containing 25 vol.% of BCP-1.65 is likely to derive from its higher solids loading, but an eventual more active contribution of the surface of the CaP particles and phosphorous leached ions towards chitosan reticulation cannot be discarded. Therefore, 20 vol.% of BCP (80 vol.% of chitosan) was the solids loading adopted for further studies involving temperature sweep measurements.

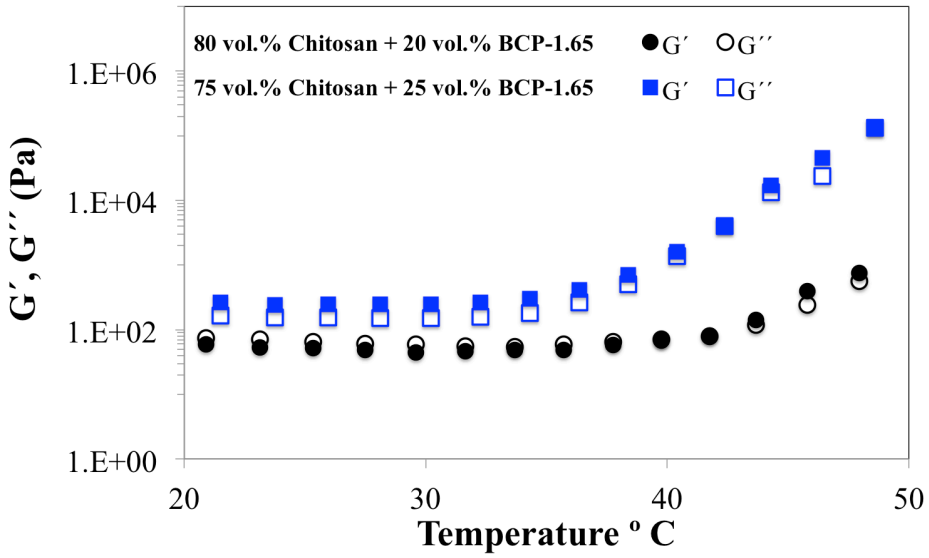

Fig. 2. Evolution of elastic modulus (G´) and viscous modulus (G´´) with temperature for BCP-1.65 suspensions with different solid loadings (20 and 25 vol.%) in the absence of genipin. The gelation temperature is defined as the temperature at which G´ and G´´ curves intersect each other.

The effects of the different added amounts of genipin on gelation behaviours of chitosan solutions in the absence and in the presence of BCP-1.65 powder, were investigated under temperature ramping. The results presented in Fig. 3 (a) and (b), respectively, indicate that gelation temperature decreases as the added amount of cross-linking agent increases. As expected, gelation process is faster in the presence of BCP-1.65 powders (Fig. 3b), with a significant decrease of gelation temperature for a given amount of genipin when compared to the chitosan solution in absence of BCP (Fig. 3a). In absence of genipin, gelation temperature decrease from 79ºC (only chitosan, Fig. 3a) to 42 ºC (chitosan + BCP-1.65, Fig. 3b) demonstrating the polymerization potential of BCP powder for chitosan chains. Surprisingly, for the composite systems the polymerization temperature apparently increases again for genipin additions >1 wt.% (Fig. 3b), oppositely to the behaviours observed in the absence of BCP-1.65 (Fig. 3a). In fact, the presence of BCP particles would cause local disruptions of the gel structure while reducing the freedom of polymeric chains of chitosan for searching an ordered binding with genipin. These unexpected behaviours are likely derived from the competition between the two polymerization

mechanisms, i.e., covalent crosslinking by genipin and ionic crosslinking by BCP powders [37].

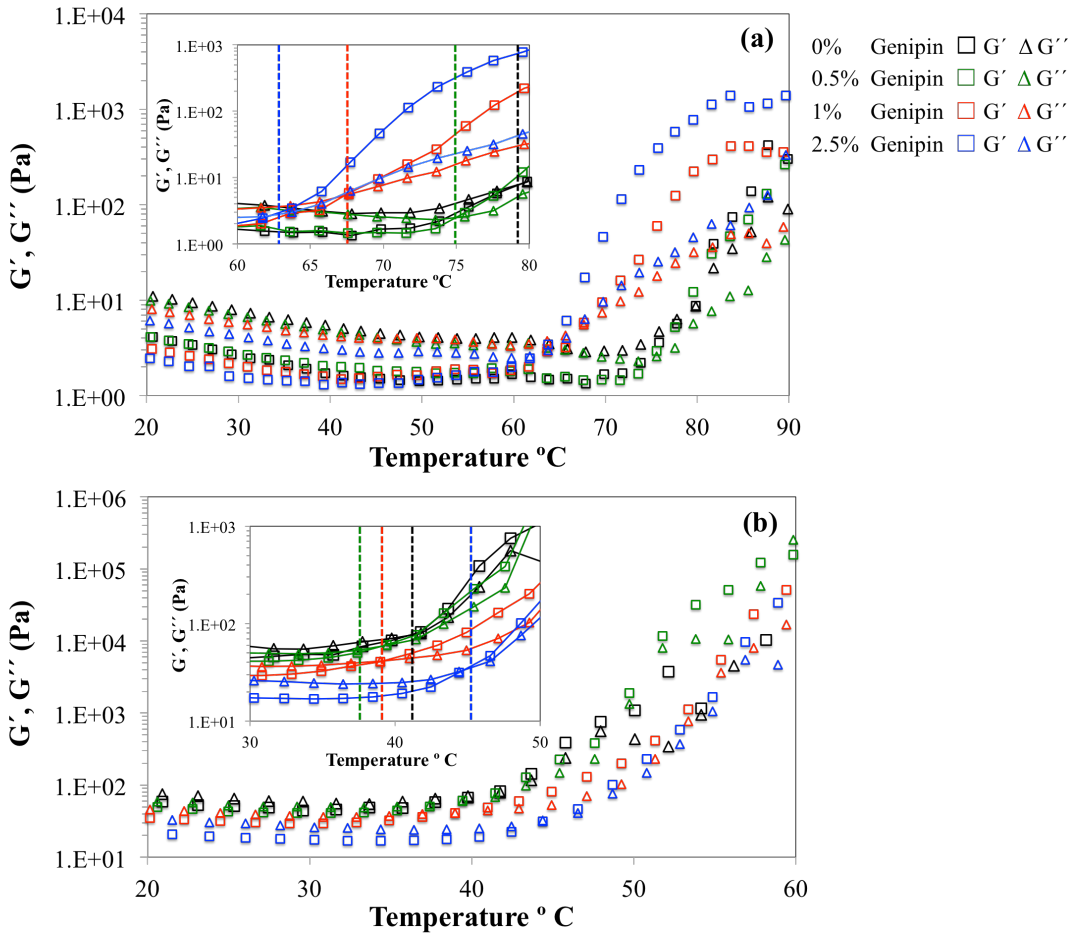

Fig. 3. Evolution of elastic modulus (G´) and viscous modulus (G´´) with temperature for: (a) 100 vol.% chitosan solution (3 wt.%); (b) 80 vol.% chitosan solution (3 wt.%) + 20 vol.% BCP-1.65) for different added amounts of genipin (0, 0.5, 1, 2.5 wt.%). The gelation temperature is defined as the temperature at which G´ and G´´ curves intersect each other. Zoomed areas of the plots in (a) and (b) are inserted for an easier observation of the gelation temperatures, also indicated by the vertical coloured dashed lines. The shear stress value used in each test was selected from linear viscoelastic region at RT.

These results allow concluding that a temperature in the range of 35–40 ºC could be adequate for BCP scaffolds reticulation in presence of genipin. To shed further light on the gelation kinetics and gel properties after BCP/chitosan composite maturation, a frequency sweep was carried out at 37 ºC. Fig. 4 presents the mechanical spectra of resultant gels. Due to the great differences in magnitude between G´ and G´´, the dynamic analysis was restricted to the elastic component (G´). In fact, measuring G´´ values under these conditions was no longer reliable as it depends on the instrumental resolution of the lag phase between sinusoidal stress and strain. Fig. 4 shows that all curves run almost parallel to the x-axis until 10 Hz, a characteristic behaviour of strong gels [38].

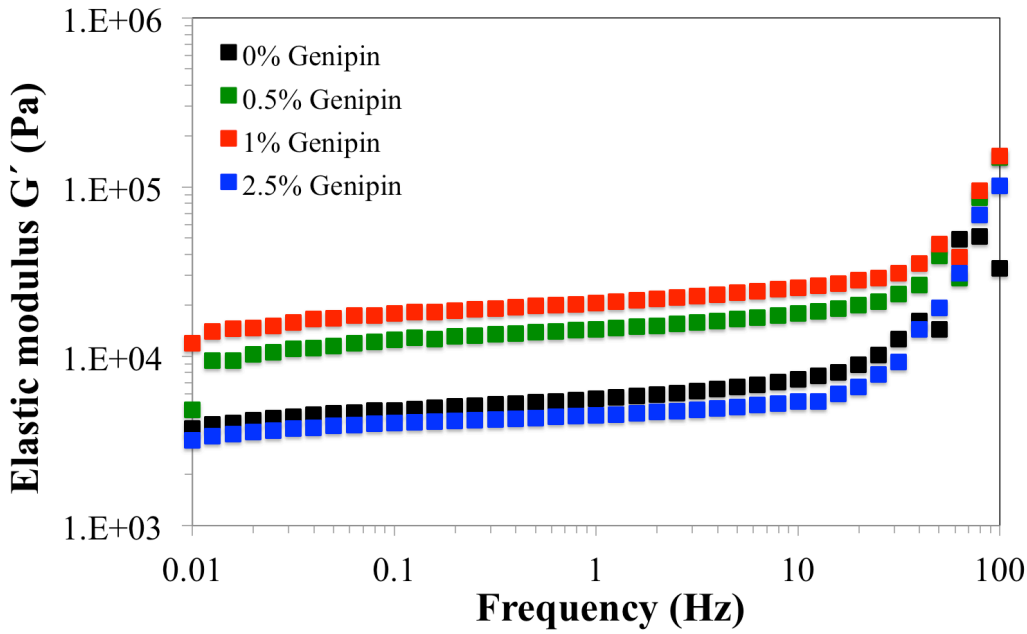

Fig. 4. Evolution of elastic modulus (G´) as a function of frequency at constant temperature (37 ºC) for the system containing 20 vol.% BCP-1.65 dispersed in 3 wt.% chitosan solution in the presence of different added amounts of genipin (wt.%) after 12 h of maturation. The shear stress value used in each test was selected from linear viscoelastic region.

Additions of 0.5 and 1 wt.% of genipin to BCP/chitosan suspensions enhanced G´ over the entire frequency range tested. This increase in G´ can be attributed to chitosan crosslinking with genipin/BCP, besides the particle-polymer network formation already present in the absence of crosslinking agent. Further increasing the added amount of genipin to 2.5 wt.% decreased gel strength, in good agreement with results presented in Fig. 3. This might be attributed to the saturation of free amine groups of chitosan molecules that could bond with genipin as proposed elsewhere [39]. The added amount of genipin also influences the swelling behaviour and pore size and size distribution of chitosan [40,41]. Increasing genipin concentration increased the total porosity and decreased pore size. A higher crosslinked density of chitosan gels is alleged to result in limited hydration, lower swelling and consequently smaller pore sizes [40]. All these trends could be slightly changed when BCP particles are presented as fillers, explaining the selection of 1 wt.% of genipin for the subsequent inks preparation for 3D printing.

The next step aimed to maximise the solid loadings while ensuring a suitable extrusion behaviour. This target was achieved for 45 vol.% solids for both BCP-1.59 and BCP-1.65 powders. Oppositely, increasing the volume fraction of BCP-1.5 to 45 vol.% turned the resulting ink too stiff and useless for printing as guessed from the results reported in Fig. 5. It can be seen from these time sweep results that the BCP-1.5 paste began turning into a gel-like system (G´>G´´) after 20 min, attributed to the crosslinking of chitosan promoted especially by this BCP powder. This stronger network formation effect of BCP-1.5 (richer in β-TCP, ~77 %) is likely related to the higher solubility of this phase and the resulting higher concentrations of Ca and P ions in solution for chitosan polymerisation. Accordingly, the BCP-1.5 powder was not further considered for the fabrication of scaffolds.

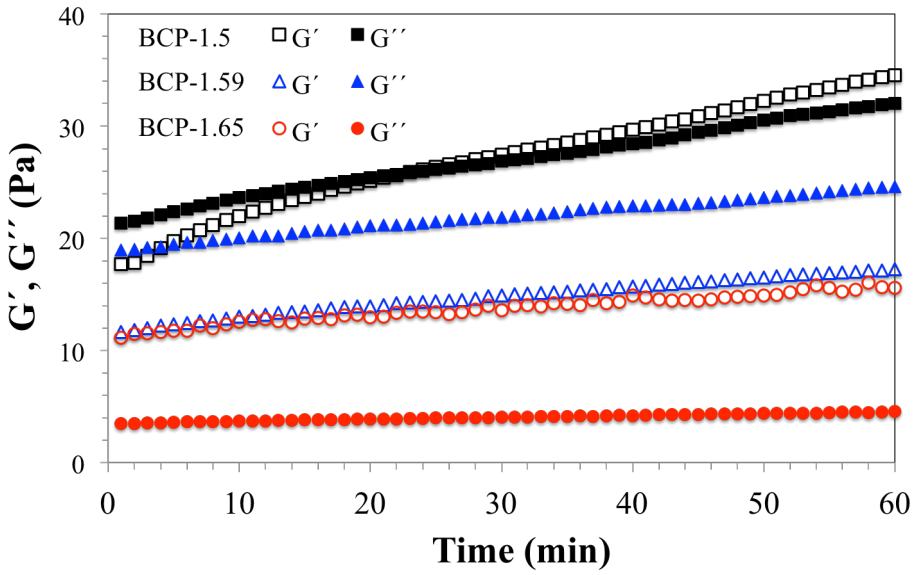

Fig. 5. Evolution of elastic modulus (G′) and viscous modulus (G′′) with time for pastes containing 20 vol.% of the different BCP powders dispersed in 3 wt.% chitosan solution. Time sweep was conducted at constant values of temperature (25 ºC), frequency (1 Hz) and shear stress selected from linear viscoelastic region.

Fig. 6 presents the elastic modulus (G′) *versus* complex shear stress (amplitude sweep) for both extrudable final inks, Ink1.65 and Ink1.59. They exhibit high elastic modules (G′ ~10^5 Pa) and remain stable along the entire shear stress range tested, suggesting that the deposited filaments will be mechanically stable and capable of fully support their own weight during assembling.

The mechanical spectra of Ink1.65 and Ink1.59 over the frequency range of 1–100 Hz in the absence and in the presence of levofloxacin are presented in Fig. 7. Within the lower frequency range up to ~0.2 Hz, G′ slightly increases with frequency, suggesting the occurrence of some structural relaxation. This is followed by trend to a plateau indicative of stable inks. The addition of LEV did not apparently disturb the structure of inks prepared from the BCP-1.65 powder for frequencies >0.2 Hz, but slightly decreased the elastic modulus of the inks derived from the BCP-1.59 powder, especially in the lower frequency range in which LEV seems to exert opposite effects on G'.

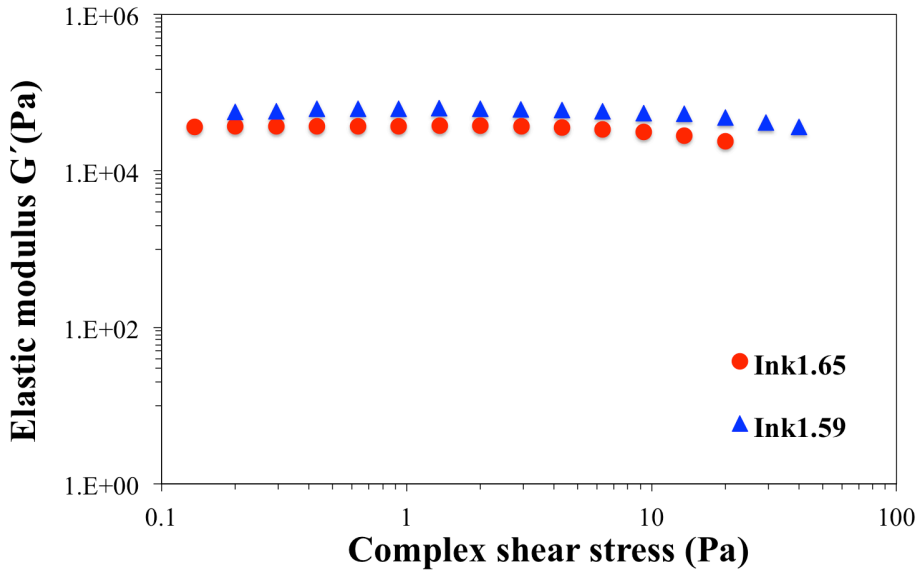

Fig. 6. Oscillatory amplitude sweep of final inks, Ink1.65 and Ink1.59.

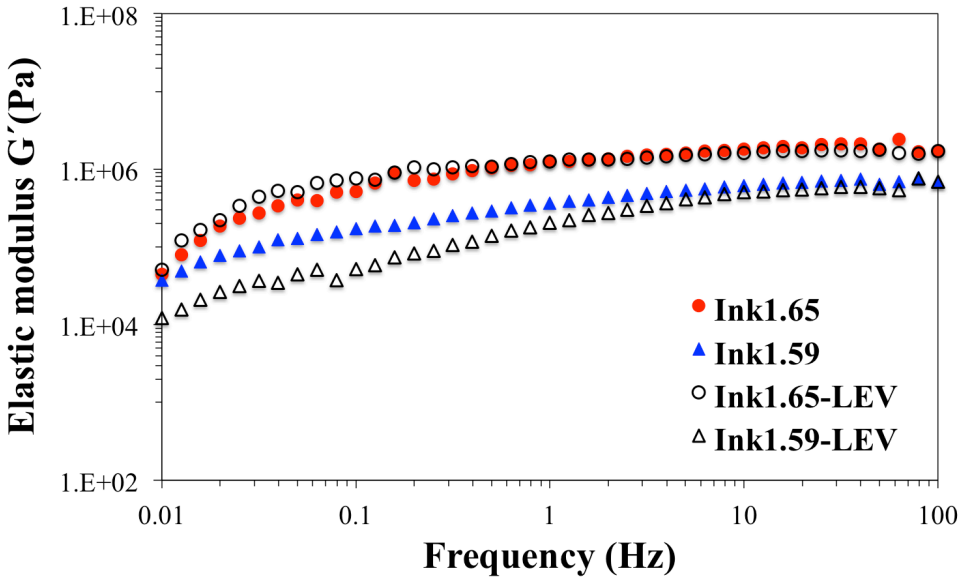

Fig. 7. Oscillatory frequency sweep of final inks without (Ink1.65 and Ink1.59) and with levofloxacin (Ink1.65-LEV and Ink1.59-LEV).

3.3. Scaffolds characterization

3.3.1 Cytotoxicity

Since acetic acid was used as solvent for chitosan and the final scaffolds were not submitted to any leaching procedure, assessing their cytotoxicity is essential. For that, direct and indirect contact tests were performed according to the ISO 10993-5 standard practice. Fig. 8 presents the metabolic activity normalized for cell number for scaffolds S1.65 and S1.59. The constructs proved to be non-cytotoxic as both direct and indirect contact assays showed cell metabolic activity values above the required 70% of the control's measured value. Moreover, the metabolic activity for direct contact with S1.65 was 60% higher than that of the control. These positive results seem promising for further future biological studies.

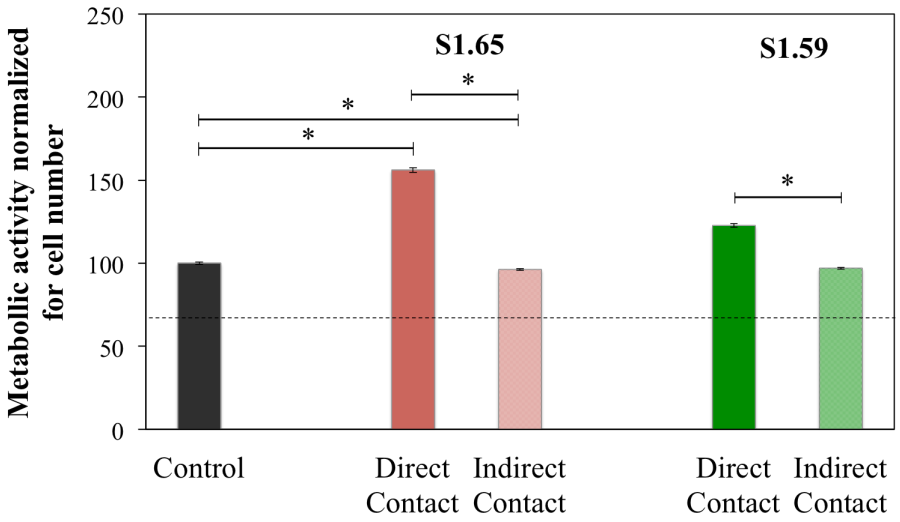

Fig. 8. Metabolic cell activity normalized for cell number for each assay (S1.65 and S1.59) of the cytotoxicity test. *statistically significant (p<0.05).

3.3.2 Structural

Scanning electron micrographs of scaffolds S1.65, S1.59, S1.65-LEV and S1.59-LEV are presented in Fig. 9. All constructs maintained their shapes after robotic deposition and no filament collapsing could be observed (Fig. 9 a-h). Keeping the structure (3D dimensions and pores grid) after printing is only possible for sintered-free scaffolds thanks to the high percentage of solids in the inks. High solid loading inks are also advantageous in decreasing shrinkage levels during drying avoiding shape distortions. In presence of levofloxacin, both scaffolds (S1.65-LEV and S1.59-LEV) showed an elliptical pore shape (Fig. 9 c,d,g,h), considerably more accentuated for S1.59-LEV, instead of squared shape visible in S1.65 and S1.59 (Fig. 9 a,b, e, f) as planed in CAD model. These results are in agreement with rheological properties of final inks (Fig. 7), being the less dominant elastic features of inks in presence of levofloxacin responsible for the interpenetration of filaments from consecutive layers and for the elliptical shape of macropores, more pronounced for Ink1.59-LEV (Fig. 9 g,h). According to mechanical spectra (Fig. 7), the inks exhibit a solid-like behaviour under high deformation rates during printing process. At low mechanical vibrations, upon depositing the subsequent layers, Ink1.59-LEV presents a weak gel-like structure where some structural relaxation occurs, explaining the partial collapsing of the macropores. The incorporation of levofloxacin seems also to affect the homogeneity of the pastes as deduced from the morphological features of rods, internal (Fig. 9 k, l) and surface (Fig. 9. o, p). The LEV containing scaffolds show higher microporosity when compared with respective scaffolds without drug (Fig. 9. i, j, m, n).

SEM observations were complemented by Metrology CT system (μCT) images shown in Fig. 10. The 2D and 3D μCT reconstructed structures of all sintering-free scaffolds (Fig. 10A) confirm the interconnected macro pore grids, as planned in CAD model. The size and fraction of micro pores in the filaments with added antibiotic increased (Fig. 10B) are in good agreement with SEM results. The drug effects on porous structure (pore amounts and size) are also more noticeable in S1.59-LEV as expected from the previous results. The overlapping of both 3D μCT reconstructed structures of S1.65 and S1.65-LEV (Fig. 10C) shows that they could not be totally superimposed due to the slightly different viscoelastic properties of the starting inks (Fig. 7). The more extensive structural relaxation of filaments extruded from Ink1.65-LEV induces small dimensional

variations upon depositing the subsequent layers and during the drying process. Accordingly, the percentages of macroporosity determined from μCT images presented in Fig. 10D reveal that scaffolds with added LEV are somewhat less porous in comparison to the ones without drug. This is in good agreement with the ellipsoidal shape of the pores visible in SEM (Fig. 9) and μCT pictures (Fig. 10A).

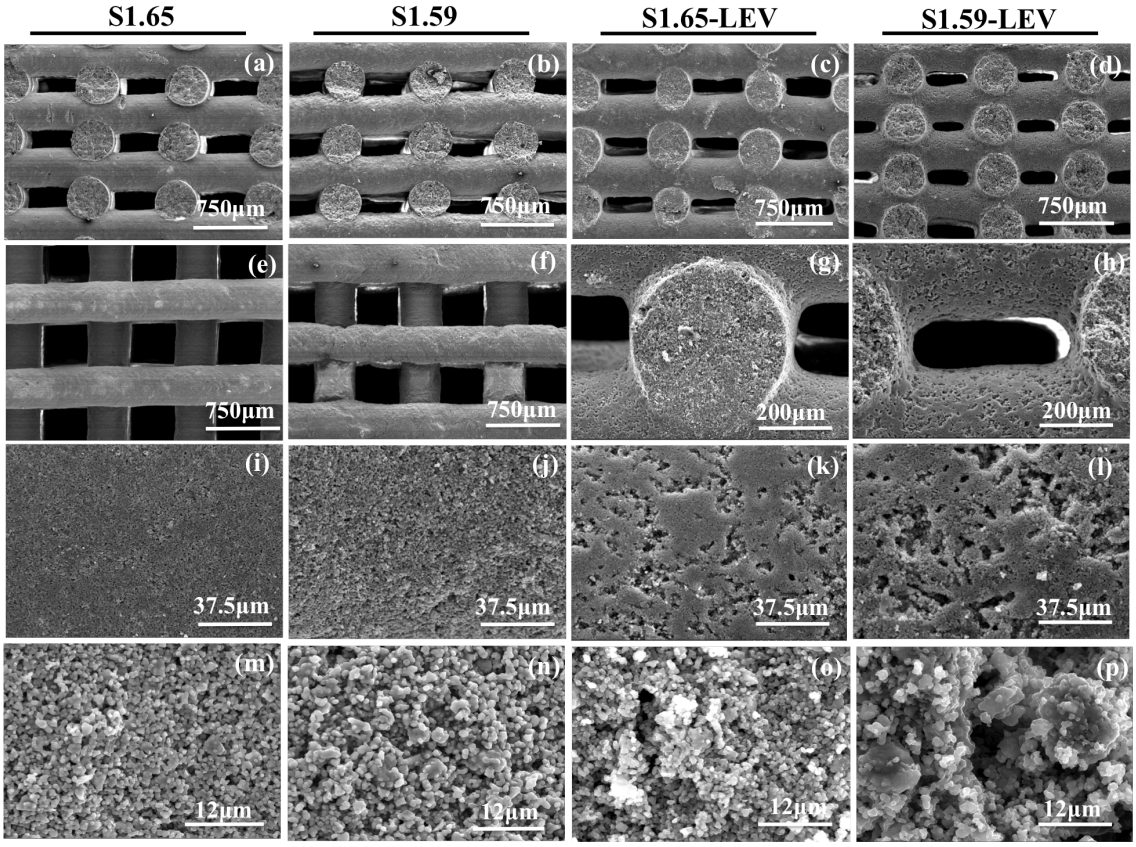

Fig. 9. SEM micrographs showing morphological aspects of S1.65 and S1.59 scaffolds with and without levofloxacin: (a, b, c, d) lateral views; (e, f) top-views; (g) rod detail, (h) pore detail; (i, j, k, l) rods' surface; (m,n,o,p) rods' inner fractured cross sections.

The compressive strength values of scaffolds (Fig. 10E) also concur to the consistency of the overall results discussed so far. The values appear in the following decreasing order: S1.65-LEV > S.165 > S1.59 > S1.59-LEV, which coincides with that of G´ in Fig. 7 under or near rest conditions. The lower compressive strength value of S1.59-LEV is also consistent with larger size (red colour in Fig. 10B) and fraction of micro pores (red and green colours) clearly noticeable from μCT images. Fig. 10E also replots the compressive strength values reported by Martínez-Vázquez *et al.* [16] for sintered-free composite (Si-doped HA + gelatin) scaffolds prepared from inks with only about 20 vol.% of the inorganic component, which seem analogous at a first glance. However, the extensive collapse of their scaffolds clearly evidenced by SEM lateral views.

Such extensive collapse is probably due to unsatisfactory rheological properties of the inks (not presented) that reduce the size of macropores, increases scaffolds density and consequently enhanced the apparent mechanical properties [16]. Moreover, the reported density values for composite scaffolds were already underestimated by the low density assumed for Si-doped HA (2.91 g cm^{-3}). The replacement of ~4.2 mol% P by Si is not expected to induce such significant changes in density of the Si-doped HA [42] in comparison to the theoretical value for pure HA (3.16 g cm^{-3}). The high solids loading of inks (45 vol.% BCP) used in the present study conferred to the extruded filaments enough stiffness for shape retention enabling to obtain almost perfect 3D porous scaffolds. The strains up to the maximum load are close to 10% and tend to be slight higher for the less rigid S1.59-LEV structure. Such relatively high strains demonstrate that the crosslinking of chitosan matrix by genipin was effective, conferring to scaffolds a considerable level of toughness.

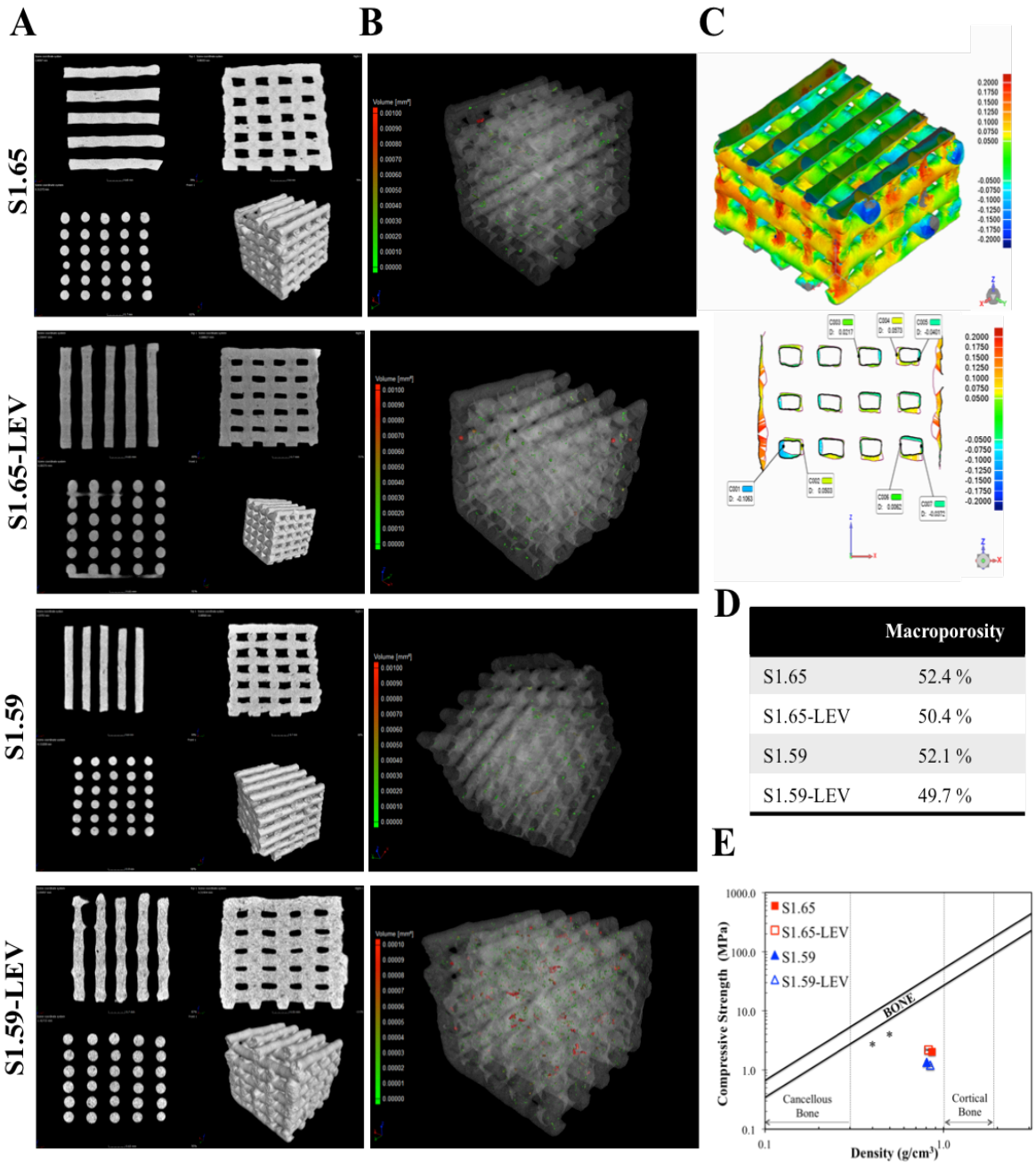

Fig. 10. (A) 2D (top plane and cross-section views) and 3D images of S1.65 and S1.59 scaffolds with and without levofloxacin obtained through Metrology CT. (B) 3D reconstruction of the scaffolds mapped with colour-coded for the internal porosity of rods. (C) 3D and 2D views of overlapped S1.65 and S1.65-LEV mapped with colour-coded. (D) Macroporosity (%) of the scaffolds determined from 3D μCT images in A; (E) compressive strength as a function of apparent density for S.165, S1.59 and S1.65-LEV, S1.59-LEV. *compressive strength values of composite scaffolds reported without drug by Martínez-Vázquez *et al.* [16], where the percentage of macroporosity is unknown. Graph illustration adapted from [16].

3.4. Levofloxacin release and in vitro bactericidal efficacy

The levofloxacin releasing profiles in PBS solution from S1.65-LEV and S1.59-LEV scaffolds along an immersion period of 24 h are shown in Fig. 11. The curves exhibit an initial burst release (at 10 min) more pronounced for S1.65-LEV (~75 % of total drug amount released, when compared with only ~27 % for S1.59-LEV), followed by more gradual increases towards plateaux trends. After 30 min, the percentages of LEV released were ~83% and ~62% for S1.65-LEV and S1.59-LEV, respectively, further increasing to ~88% and ~71% at 24 h time point, proving that antibiotic release is faster from S1.65-LEV scaffolds.

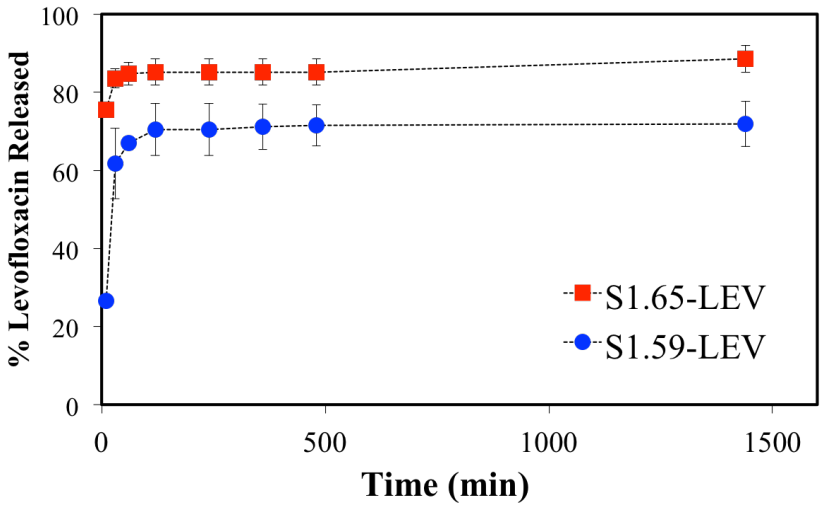

Fig. 11. Percentage of levofloxacin released in PBS solution from S1.65-LEV and S1.59-LEV scaffolds at 37 ºC throughout a period of 24 h. The data was obtained by UV spectrophotometry at 288 nm. Data is expressed as mean ± SD of at least three independent experiments.

The initial fast release of levofloxacin from both scaffold compositions could be explained due to the high surface area of the 3D structures, resulting not only from the macroporosity (~50 %), but also from the porosity on the rods themselves. In addition, it´s known that fluoroquinolones, namely levofloxacin, can interact with multivalent cations (Al^{3+}, Mg^{2+}, Fe^{2+}, Fe^{3+}, Ca^{2+}), forming ion-quinolone chelates [43]. Considering that S1.59-LEV is richer in the most soluble β-TCP phase than

S1.65-LEV, higher amounts of calcium ions will be available in solution to form chelates with levofloxacin, promoting the initial release of S.59-LEV three times lower than S1.65-LEV (Fig. 11). The Ca^{2+}–levofloxacin interactions could also help explaining the less predominating elastic character observed in rheological behaviour of I1.59-LEV (Fig. 7) and the consequent more extensive microstructural relaxation of the scaffolds.

The spatial distributions of levofloxacin molecules within the filaments of S1.65-LEV and S1.59-LEV evaluated by confocal Raman microscope are presented in Fig. 12. The integration of the absolute area underneath the calcium phosphate band at 964 cm^{-1} assigned to the symmetric stretching of the P–O bond [44] and of the levofloxacin band at 1620 cm^{-1} assigned to the C=C vibration of quinolone ring [45] were used to determine the colour intensity of the image pixels and create the Raman maps. Thus, the brighter colours in the images presented in Fig. 12A and Fig. 12B indicate regions with stronger Raman signals of BCP and antibiotic molecules, respectively. A well homogeneous spatial distribution of BCP can be inferred from Fig. 12A, while an overall fair distribution with some small aggregates is apparent for levofloxacin molecules in Fig.12B.

Strong differences can be observed when comparing the single Raman spectra obtained in the higher Raman levofloxacin signal spot on each S1.65-LEV and S1.59-LEV sample (Fig. 12C). The Raman spectrum of S1.65-LEV is equal to that of pure antibiotic, while the intensity of Raman peaks in the S1.59-LEV spectrum is much lower and similar to that found for a solution of levofloxacin in water or ethanol [45,46]. These results support the hypothesis of levofloxacin complexation with the more abundant Ca^{2+} cations suggested above (Fig. 11) due to the higher solubility of β-TCP phase in the case of S1.59-LEV. This is likely to induce polarization changes in the LEV molecule. These changes in the molecular structure of the antibiotic can induce chemisorption interactions with other components in the scaffold such as chitosan via a cleavable amide bond [47] or ion-quinolone chelates formation [43], leading to a slow release profile of the drug. Oppositely, levofloxacin is likely to be in its molecular solid state in the case of S1.65-LEV scaffold [48].

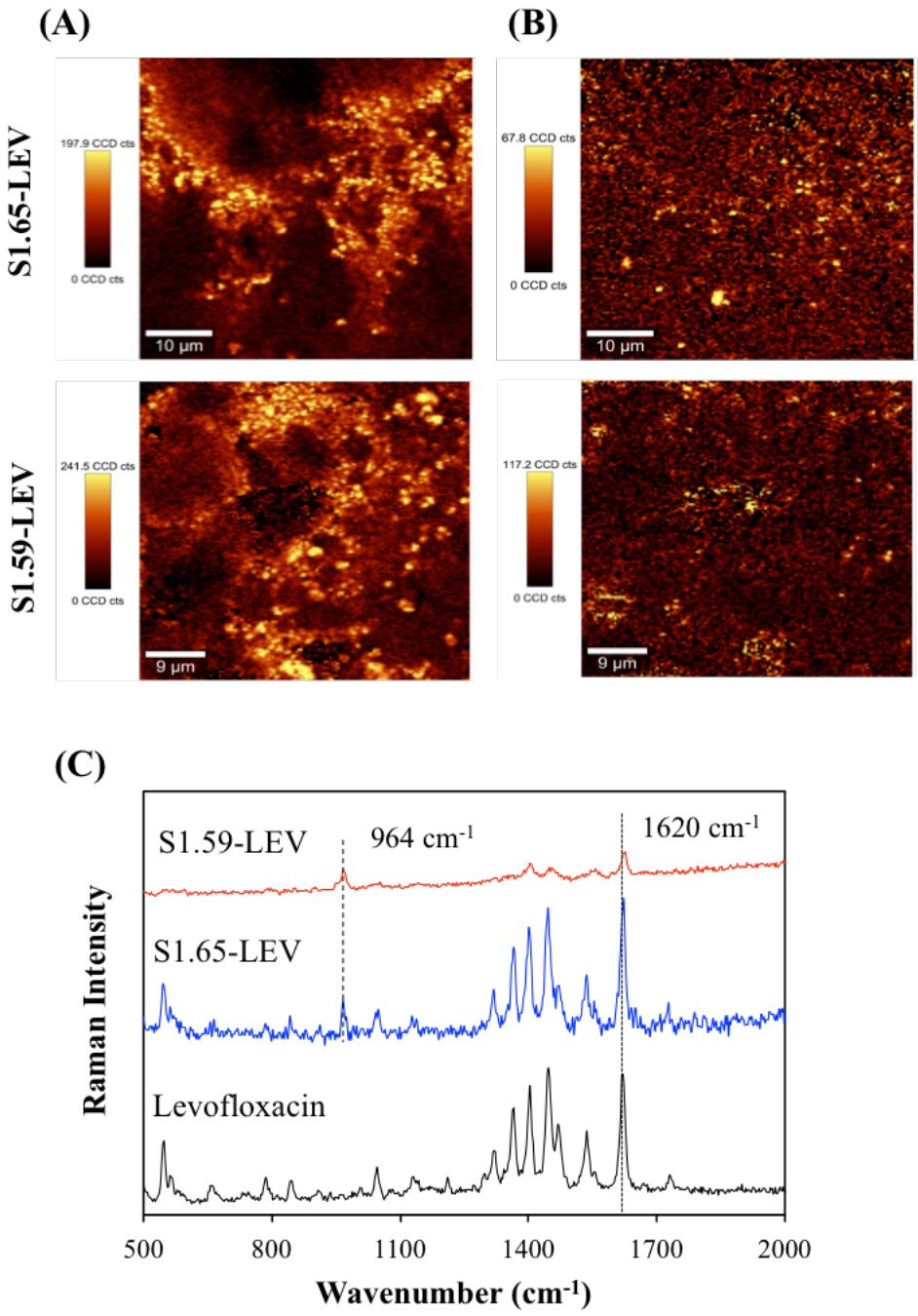

Fig. 12. Raman images were obtained using the integrated intensity of the bands at (A) 964 cm^{-1} and (B) 1620 cm^{-1} for the S1.65-LEV and S1.59-LEV scaffolds (excitation at 523 nm, 8.5 mW laser power, 150 points per line x 150 lines per image, 0.02 s). The coloured vertical bar represents the relative intensity scale. (C) Single Raman spectra (0.05 s and 1 acquisition).

Fig. 13 presents the results of bacterial growth inhibition, using the agar disk-diffusion test with two bacterial strains, *S. aureus* ATCC25923 and *S. aureus* clinic. Disks derived from Ink1.65-LEV and Ink1.59-LEV effectively inhibited bacterial growth, being the inhibition zone diameters of ~45 mm and ~36 mm against MSSA and MRSA, respectively. On the other hand, disks without antibiotic failed to inhibit bacterial growth, except for the Ink1.65 that presented an inhibition zone of ~24 mm against MSSA. This inhibition could be attributed to a smaller ionic contribution of chitosan reticulation by the less soluble BCP-1.65, leaving more chitosan available to play its antimicrobial role [49]. These results indicate that levofloxacin did not lose its bactericidal efficacy during the fabrication process. Moreover, the inhibition zone observed for the antibiotic control (5 µg of levofloxacin) was in accordance with the expected results for S. aureus ATCC 25923 (25–30 mm) and the MRSA (< 15 mm) (CLSI, 2014 [50])

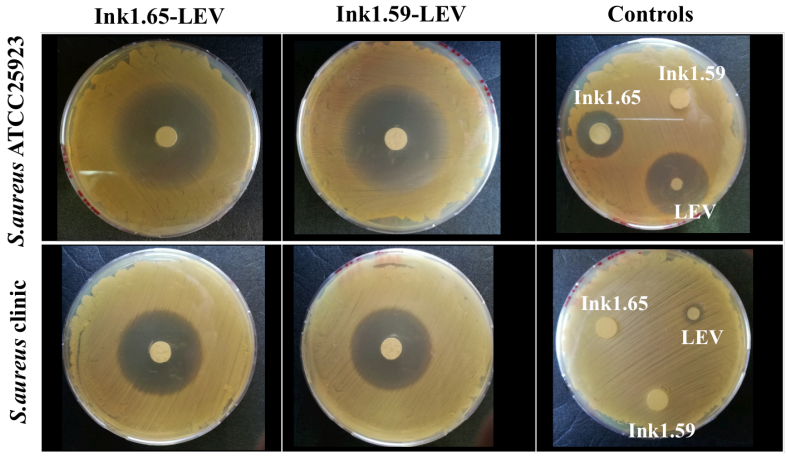

S.aureus ATCC25923	Inhibition zone (mm)
Control	28.31 ± 0.86
Ink1.65	24.35 ± 1.95
Ink1.65-LEV	45.15 ± 3.63
Ink1.59	0
Ink1.59-LEV	44.28 ± 1.06

S.aureus clinic	Inhibition zone (mm)
Control	8.66 ± 0.85
Ink1.65	0
Ink1.65-LEV	36.66 ± 1.44
Ink1.59	0
Ink1.59-LEV	35.78 ± 1.97

Fig. 13. Agar disk-diffusion test showing bacterial inhibition against two *S. aureus* strains (ATCC25923 and a clinic isolate).

The high initial burst and suitable porous structure of S1.65-LEV and S1.59-LEV scaffolds makes them very interesting and promising multifunctional devices for bone regeneration and *in situ* drug delivery to prevent local infections. They appear as a good alternative to systemic administration of antibiotic. As a matter of fact, achieving an effective antimicrobial concentration using intravenous antibiotics is

difficult, while systemic antibiotic treatment can lead to systemic toxicity. Furthermore, the on-site drug release can reduce the dose required to achieve a pharmacological response, when compared to the systemic delivery route. Moreover, a faster release rate after implantation could be desired in the case of scaffolds endowed with antimicrobial activity in order to respond to the elevated risk of infection from bacteria introduced during the surgical treatment [51,52].

5. Conclusions

The processing conditions to fabricate sintering-free composite scaffolds (BCP/Chitosan), containing high solids loading in the absence of any other processing additives (dispersant and binders) were established. Inks with proper rheological properties were successfully obtained and subsequently used for robocasting deposition.

The percentage of β-TCP in BCP powders (more soluble phase than HA) strongly influences the gelation behaviour of chitosan, being impossible to prepare extrudable inks for β-TCP contents >50 wt.%. The addition of levofloxacin modifies the viscoelastic behaviour of the inks, especially in the presence of BCP with higher amounts of β-TCP (I1.59-LEV, with ~50 wt.% β-TCP). Accordingly, the more extensive interactions between dissolved ions and levofloxacin induce rheological, morphological and structural changes along the fabrication process, with consequences in the mechanical performance of the final scaffolds. The obtained 3D LEV-loaded scaffolds exhibiting an early and fast drug release, opens a new path for local bone regeneration and infection treatments, since a more direct administration of drug might be a better solution than the conventional treatment strategies.

REFERENCES

[1] L. Roseti, V. Parisi, M. Petretta, C. Cavallo, G. Desando, I. Bartolotti, B. Grigolo, Scaffolds for Bone Tissue Engineering: State of the art and new perspectives, Materials Science and Engineering C 78 (2017) 1246–1262.

[2] M. Chen, D.Q.S. Le, S. Hein, P. Li, J.V. Nygaard, M. Kassem, J. Kjems, F. Besenbacher, C. Bünger, Fabrication and characterization of a rapid prototyped tissue engineering scaffold with embedded multicomponent matrix for controlled drug release, Int J Nanomed 7 (2012) 4285–4297.

[3] H. Ma, C. Jiang , D. Zhai , Y. Luo , Yu Chen , F. Lv , Z. Yi ,Y. Deng , J. Wang, J. Chang, C. Wu, A Bifunctional Biomaterial with Photothermal Effect for Tumor Therapy and Bone Regeneration, Adv Funct Mater 26 (2016) 1197–1208.

[4] H. Ma, J. Luo, Z. Sun, L. Xia, M. Shi, M. Liu, J. Chang, C. Wu, 3D printing of biomaterials with mussel-inspired nanostructures for tumor therapy and tissue regeneration, Biomaterials 111 (2016) 138–148.

[5] H. Wang, S. Zhao, J. Zhou, K. Zhu, X. Cui, W. Huang, M.N. Rahaman, C. Zhang, D. Wang, Biocompatibility and osteogenic capacity of borosilicate bioactive glass scaffolds loaded with Fe_3O_4 magnetic nanoparticles, J Mater Chem B 3 (2015) 4377–4387.

[6] K.-F. Lin, S. He, Y. Song, C.-M. Wang, Y. Gao, J.-Q. Li, P. Tang, Z. Wang, L. Bi, G.-X. Pei, Low temperature additive manufacturing biomimic threedimensional hydroxyapatite/collagen scaffolds for bone regeneration, Appl Mater Interfaces 8 (11) (2016) 6905–6916.

[7] Y. Zhang, D. Zhai, M. Xu, Q. Yao, J. Chang, C. Wu, 3D-printed bioceramic scaffolds with a Fe_3O_4/graphene oxide nanocomposite interface for hyperthermia therapy of bone tumor cells, J Mater Chem B 4 (2016) 2874–2886.

[8] U. Hess, S. Shahabi, L. Treccani, P. Streckbein, C. Heiss, K. Rezwan, Co-delivery of cisplatin and doxorubicin from calcium phosphate beads/matrix scaffolds for osteosarcoma therapy, J Mater Sci and Eng C 77 (2017) 427–435.

[9] Z.-J. Rong, L.-J. Yang, B.-T. Cai, L.-X. Zhu, Y.-L. Cao, G.-F. Wu, Z.-J. Zhang, Porous nano-hydroxyapatite/collagen scaffold containing drug-loaded ADM–PLGA microspheres for bone cancer treatment, J Mater Sci: Mater Med (2016) 1–12.

[10] R. Fernandes, P. Siegel, S. Komarova, J. Hilton, C. Addison, M. F. K. Ibrahim, J. Werier, K. Dennis, G. Singh, E. Amir, V. Jarvis, U. Emmenegger, S. Mazzarello, M. Clemons, Future directions for bone metastasis research – highlights from the 2015 bone and the Oncologist new updates conference (BONUS), J Bone Onc 5 (2016) 57–62.

[11] L.G. Bracaglia, B.T. Smith, E.Watson, N. Arumugasaamy, A.G. Mikos, J.P. Fisher, 3D printing for the design and fabrication of polymer-based gradient scaffolds", review article, Act Biomaterialia (2017) 3–13.

[12] E. Wenk, A.J. Meinel, S. Wildy, H.P. Merkle, L. Meinel, Microporous silk fibroin scaffolds embedding PLGA microparticles for controlled growth factor delivery in tissue engineering, Biomaterials 30(13) (2009) 2571–2581.

[13] W. Habraken, P. Habibovic, M. Epple, M. Bohner, Calcium phosphates in biomedical applications: materials for the future?, Materials Today 19 (2016) 69–87.

[14] G. Daculsi, R.Z. Legeros, E. Nery, K. Lynch, B. Kerebel, Transformation of biphasic calcium phosphate ceramics in vivo: ultrastructural and physicochemical characterization, J Biomed Mater Res 23 (1989) 883–894.

[15] G. Daculsi, R.Z. LeGeros, M. Heughebaert, I. Barbieux, Formation of carbonate-apatite crystals after implantation of calcium phosphate ceramics, Calcif. Tissue Int. 46 (1990) 20–27.

[16] F.J. Martínez-Vázquez , M.V. Cabañas, J.L. Paris, D. Lozano, M. Vallet-Regí, Fabrication of novel Si-doped hydroxyapatite/gelatine scaffolds by rapid prototyping for drug delivery and bone regeneration, Act Biomaterialia 15 (2015) 200–209.

[17] O. Gauthier, E. Goyenvalle, J.-M. Bouler, J. Guicheux, P. Pilet, P. Weiss, *et al.*, Macroporous biphasic calcium phosphate ceramics versus injectable bone substitute: a comparative study 3 and 8 weeks after implantation in rabbit bone, J Mater Sci Mater Med 12 (2001) 385–390.

[18] I. Sopyan, T.A. Rahim, Recent progress of the development of porous bioactive calcium phosphate for biomedical applications. Recent Patents on Biomedical Engineering 1 (2008) 213–229.

[19] L. Sun, S.T. Parker, D. Syoji, X. Wang, J.A. Lewis, D.L. Kaplan, Direct-Write Assembly of 3D Silk/Hydroxyapatite Scaffolds for Bone Co-Cultures, Adv. Healthcare Mater 1 (2012) 729–735.

[20] R.L. Truby, J.A. Lewis, Printing soft matter in three dimensions, Nature 540 (2016) 371–378.

[21] C. Marques, F.H. Perera, A. Marote, S.I. Vieira, S. Ferreira, S. Olhero, P. Miranda, J.M.F. Ferreira, Biphasic calcium phosphate scaffolds fabricated by direct write assembly: mechanical, anti-microbial and osteoblastic properties, J Europ Ceram Soc 37 (2017) 359–368.

[22] S. Eqtesadi, A. Motealleh, A. Pajares, F. Guiberteau, P. Miranda, Influence of sintering temperature on the mechanical properties of -PCL-impregnated 45S5 bioglass-derived scaffolds fabricated by robocasting, J Europ Ceram Soc 35 (2015) 3985–3993.

[23] Ferreira M, Rzhepishevska O, Grenho L, Malheiros D, Gonçalves L, Almeida AJ, Jordão L, Ribeiro IA, Ramstedt M, Gomes P, Bettencourt A. Levofloxacin-loaded bone cement delivery system: Highly effective against intracellular bacteria and Staphylococcus aureus biofilms. Int J Pharm. 2017 Oct 30;532(1):241-248.

[24] R.N. Greenberg, M.T. Newman, S. Shariaty, R.W. Pectol, Ciprofloxacin, lomefloxacin or levofloxacin as treatment for chronic osteomyelitis, Antimicrob Agents Chemother 44 (2000) 164–166.

[25] M. Descamps, J.C. Hornez, A. Leriche, Effects of powder stoichiometry on the sintering of β-tricalcium phosphate, J Europ Ceram Soc 27(6) (2007) 2401–2406.

[26] A. Destainville, E. Champion, D. Bernache-Assollant, E. Laborde, Synthesis, characterization and thermal behavior of apatitic tricalcium phosphate, Mat Chem and Phys 80(1)(2003) 269–277.

[27] Sergey V. Dorozhkin, Calcium Orthophosphate-Based Bioceramics, Materials 6 (2013) 3840–3942.

[28] S. Nicolopoulos, J.M.G. Calbet, M.P. Alonso, M.T. Gutierrez Rios, M.I. De Frutos, M. Vallet-Regi, Characterization by TEM of Local Crystalline Changes during Irradiation Damage of Hydroxyapatite Compounds, J Solid State Chem 116 (1995) 265–274.

[29] D. Arcos, J. Rodriguez-Carvajal, M. Vallet-Regi, The effect of the silicon incorporation on the hydroxylapatite structure. A neutron diffraction study, Solid State Sci 6 (2004) 987–994.

[30] M.R. Finisie, A. Josué, V.Y. Fávere, M.C.M. Laranjeira, Synthesis of calcium-phosphate and chitosan bioceramics for bone regeneration, An Acad Bras Cienc 73 (2001) 525–532.

[31] ISO 10993-5. Biological evaluation of medical devices - Part 5: Tests for in vitro cytotoxicity, (2009) 34.

[32] A.C. Matos, C.F. Marques, R.V. Pinto, I.A. Ribeiro, L.M. Gonçalves, M.A. Vaz, J.M.F. Ferreira, A.J. Almeida, A.F. Bettencourt, Novel doped calcium phosphate-PMMA bone cement composites as levofloxacin delivery systems, Int J Pharm 490 (2015) 200–208.

[33] Marques CF, Matos AC, Ribeiro IA, Gonçalves LM, Bettencourt A, Ferreira JM (2016). Insights on the properties of levofloxacin-adsorbed Sr- and Mg-doped calcium phosphate powders. J Mater Sci Mater Med 2016 Jul;27(7):123

[34] Clinical and Laboratory Standards Institute, CLSI, 2009. Performance standards for antimicrobial disk susceptibility tests. Approved Standard: 10th ed. CLSI, Wayne, USA. M02–A10.

[35] N. Döbelin, Interlaboratory study on the quantification of calcium phosphatephases by Rietveld refinement, Powder Diffr 30 (3) (2015) 231–241.

[36] S.C. Chen, Y.C. Wu, F.L. Mi, Y.H. Lin, L.C. Yu, H.W. Sung, A novel pH-sensitive hydrogel composed of N,O-carboxymethyl chitosan and alginate cross-linked by genipin for protein drug delivery, J Control Release 96 (2004) 285–300.

[37] M.J. Moura, H. Faneca, M.P. Lima, M.H. Gil, M.M. Figueiredo, In situ forming chitosan hydrogels prepared via ionic/covalent Co-cross-linking, Biomacromolecules 12 (9) (2011) 3275–3284.

[38] S.M. Olhero, G. Tarí, M.A. Coimbra, J.M.F. Ferreira, Synergy of polysaccharide mixtures in gelcasting of alumina, J Eur Ceram Soc 20 (2000) 423–429.

[39] L. Gao, H. Gan, Z. Meng, R. Gu, Z. Wu, L. Zhang, X. Zhu, W. Sun, J. Li, Y. Zheng, G. Dou, Effects of genipin cross-linking of chitosan hydrogels on cellular adhesion and viability, Colloids and Surfaces B: Biointerfaces 117 (2014) 398–405.

[40] R.M. Schek, A.J. Michalek, J.C. Iatridis, Genipin-Crosslinked Fibrin Hydrogels As A Potential Adhesive To Augment Intervertebral Disc Annulus Repair, Europ Cells and Mater 21 (2011) 373–383.

[41] N. Siddiqui, K. Pramanik, E. Jabbari, Osteogenic differentiation of human mesenchymal stem cells in freeze-gelled chitosan/nano β-tricalcium phosphate porous scaffolds crosslinked with genipin, Mat Sci and Eng: C 54 (2015) 76–83.

[42] R. Astala, L. Calderín, X. Yin, M.J. Stott, Ab Initio Simulation of Si-Doped Hydroxyapatite, Chem Mater 18 (2006) 413–422.

[43] M.P. Pai, S.E. Allen, G.W. Amsden, Altered steady state pharmacokinetics of levofloxacin in adult cystic fibrosis patients receiving calcium carbonate, J Cystic Fibrosis 5(3) 82006) 153–157.

[44] S. Saber-Samandari, K. Alamara, S. Saber-Samandari, K.A. Gross, Micro-Raman Spectroscopy Shows how the Coating Process Affects the Characteristics of Hydroxylapatite, Act Biomaterialia 9 (2013) 9538–9546.

[45] I.J. Hidi, M. Jahn, K. Weber, D. Cialla-May, J. Popp, Droplet based microfluidics: spectroscopic characterization of levofloxacin and its SERS detection, Phys Chem Chem Phys 17 (2015) 21236–21242.

[46] L. Yanga, M. Gong, X. Jiang, Y. Chen, X. Han, K. Song, X. Sun, Y. Zhang, B. Zhao, SERS investigation and detection of levofloxacin drug molecules onsemiconductor TiO2: Charge transfer contribution, Colloids and Surfaces A: Physicochem Eng Aspects 508 (2016) 142–149.

[47] J. Jalvandi, M. White, Y. Gao, Y.B. Truong, R. Padhye, I.L. Kyratzis, Polyvinyl alcohol composite nanofibres containing conjugated levofloxacin-chitosan for controlled drug release, Mat Sci and Eng C 73 (2017) 440–446.

[48] S.S. Singh, T.S. Thakur, New crystalline salt forms of levofloxacin: conformational analysis and attempts towards the crystal structure prediction of the anhydrous form, CrystEngComm 16 (2014) 4215–4230.

[49] E.I. Rabea, M.E.T. Badawy, C.V. Stevens, G. Smagghe, W. Steurbaut, Chitosan as antimicrobial agent: Applications and mode of action, Biomacromolecules 4(6) (2003) 1457–1465.

[50] Clinical and Laboratory Standards Institute, CLSI, 2014. Performance Standards for Antimicrobial Susceptibility Testing. Twenty-Fourth Informational Supplement. CLSI, Wayne, USA M100-S24.

[51] M. Zilberman, J.J. Elsner, Antibiotic-eluting medical devices for various applications, J Control Release 130 (2008) 202–15.

[52] Mourinõ V, Boccaccini AR. Bone tissue engineering therapeu- tics: controlled drug delivery in three-dimensional scaffolds. J R Soc Interface. 2010;7:209–27.

Chapter 7

GENERAL CONCLUSIONS AND FUTURE WORK

GENERAL CONCLUSIONS

The main goal of this PhD thesis was to develop novel 3D porous scaffolds similar to the human cancelous bone for bone regeneration using robocasting technique. Their porosity was tailor-made in order to evaluate the influence of porous structure on the formation of bone tissue in a cellular environment thus enabling the prediction of scaffolds' behaviour after implantation. Thereby, all the relevant properties (chemical, structural, mechanical and biological) were considered and balanced in order to obain the best compromise for the proposed aim.

Biphasic calcium phosphates (BCP) both undoped and co-substituted with different ions (shown to have important roles in biological processes) were successfully synthesized by precipitation. The crystalline phase assemblages and the biological performances were strongly dependent on the specific dopant ions as all the used ions present a tendency for preferentially entering into the β–TCP's lattice rather than into the HA's one, increasing the percentages of β–TCP phase in the resulting BCP. Sr^{2+} was the only one capable of totally enter the lattice structures of both HA and β–TCP phases, replacing calcium ions. The *in vitro* biocompatibility with pre-osteoblasic cells was proven for all synthesized powders, while only the silver-doped powders exhibited antimicrobial activity.

The prepared BCP powders have shown proper behaviour for colloidal processing enabling the preparation of suspensions with very high solids concentrations, around 50 vol.% for all compositions. The rheological properties of the suspensions were properly adjusted to enable the successful production of 3D structures appropriate for bone tissue engineering by robocasting. The size and morphology of the powder particles and the concentrations of the processing additives were shown to play major roles in inks performance during extrusion process by robocasting. Scaffolds with different pore sizes and a rod diameter of 410 μm were fabricated and sintered at 1100 ºC and, finally, characterised in terms of their physical and mechanical properties. For all pore sizes tested, compressive strength of scaffolds was comparable to or even higher than that of cancellous bone, and mechanical data could be systematically correlated with the porosity fraction. Since scaffolds for bone tissue engineering must have sufficient mechanical properties that match those of the host

tissue, it could be concluded that BCP scaffolds developed under this PhD thesis present the required properties for the target application.

It is known that the microstructural characteristics, i.e., porosity, pore size, pore shape, and interconnectivity of the pores can influence the performance of a tissue engineering scaffold. To study the effect of a single parameter such as pore size, other parameters should be identical in all scaffold designs. Biphasic calcium phosphate (HA/β-TCP) based scaffolds revealed to be appropriate matrices for *in vitro* cell culture. Furthermore, it could be demonstrated that hMSCs are capable not only to survive, proliferate and produce extracellular matrix components but also to differentiate into the osteogenic lineage upon induction. The behaviour of the cells on the scaffolds with pore size between rods around 500 μm demonstrates the positive effect of a bigger pore size on cell differentiation.

Avoiding sintering step allowed the introduction of drug molecules during ink preparation step for fabricating biphasic calcium phosphate/chitosan composite scaffolds by robocasting. The 3D scaffolds obtained exhibited an early and fast release of levofloxacin, opening a new strategy for local bone regeneration and infection treatments, since a more direct administration of drug might be a better solution than the conventional treatment of systemic administration.

The results presented and discussed along this PhD Thesis demonstrated this direct write assembling technique (robocasting) is a particularly suitable alternative to the currently used production methods, showing an extraordinary potential for creating adequate support structures for new bone tissue engineering strategies. The attractive advantages of this technique for fabricating 3D porous scaffolds include: (i) the ability to fabricate devices with complex shapes providing great design flexibility and the possibility to manipulate the macroporosity of the scaffolds; (ii) the technique is rapid, simple, repeatable and versatile.

Giving all the above mentioned findings, it is possible to conclude that the tissue engineering strategy proposed in this thesis allowed to obtain a bone substitute with osteogenic potential and opening new possibilities for the development of antibiotic-releasing tissue engineering scaffolds with the potential of a single stage surgical treatment of bone infection treatment.

FUTURE WORK

Although the present work has contributed to progresses in the state-of-the art by disclosing new biphasic calcium phosphate compositions and devices to mimic the structure, the mineral composition and the properties of bone, additional work still needs to be done. Concerning calcium phosphate powders composition, testing doped powders with new ions and/or different ions combinations and select the best quantity of each phase in the perspective of bone regeneration is still desirable.

Additionally, to achieve a material that might be qualified for bone tissue engineering applications and since the scaffolds manufacturing by robocasting allows great level of accuracy in tailoring the pore size/porosity, different architectures should be designed and fabricated in an attempt to devise an "ideal scaffold". Moreover, it would be important to investigate the degradation rate of scaffolds *in vitro* and how that affects its mechanical properties.

In vivo studies will be required in order to evaluate the biological performance of scaffolds manufactured under this PhD thesis, testing the materials in animal models to confirm their suitability for intended applications in bone regeneration. Degradation study should be carried out to determine the period of time that scaffolds continue to maintain its biomechanical properties upon implantation.

Printing composite scaffolds without sintering offers new opportunities to design biomaterials with new functionalities, which can act as synthetic bone substitutes and as drug delivery systems. However, plenty of future work needs to be carried out to study the release kinetics. Since the addition of organic molecules such as levofloxacin in aqueous CaP pastes changes viscoelastic properties of the inks, drug encapsulation before its addition to the paste system would be a good approach to overcome this problem.